Computational Methods for Infrared Spectroscopy of Airless Planetary Bodies

A thesis approved for the academic degree of
Doktor der Naturwissenschaften (Dr. rer. nat.)

at the
Faculty of Electrical Engineering and Information Technology

TU Dortmund University

by

Kay Stephan Wohlfarth, M.Sc.

Supervisor:	Prof. Dr. Christian Wöhler, TU Dortmund University
Co-advisor:	Prof. Dr. Josef Pauli, University of Duisburg-Essen
Day of Oral Examination:	April 9, 2025

Abstract

Planetary science attempts to understand how planetary bodies developed and what mechanisms act on the planets today. Because planetary bodies are far away, telescopic observations and remote sensing are the primary sources of information about these distant worlds. Further, the long timespans and extreme conditions on which planetary processes often occur make them inaccessible to direct interaction. Because of these limitations, computer models for remote sensing data analysis have become crucial tools for planetary research.

This thesis presents three computational models that simulate infrared spectra of airless planetary bodies - mainly the Moon, Mercury, and the airless exoplanet LHS 3844b. The models help calibrate the infrared spectra of airless bodies and address science questions about the mineralogical composition, the character and distribution of volatiles, and the structural and thermophysical properties.

First, a thermal model for the Moon, Mercury, and LHS 3844b was developed that takes the geometry and surface albedo and outputs the spectral radiance for arbitrary observation and illumination conditions. The model was validated with disk-resolved lunar measurements under two phase angles (-30° and 27°), acquired by the Gaofen-4 satellite around 3.77 μm. The model and the measurements agree exceptionally well with a root mean squared error relative to the maximum signal of around 3 % measured along sixteen profiles evenly distributed across the visible disk. The average surface roughness is $\overline{\theta} \approx 22°$. The model was further validated with the nadir and off-nadir measurements of channel 4 (8.25 μm) and 7 (25–41 μm) of the Diviner lunar radiometer. Again, the model and data agree well for the nadir case and the off-nadir cases, predicting roughness values of $\overline{\theta} \approx 20°$ and $\overline{\theta} \approx 30°$, respectively. The model can estimate the excess thermal radiation that occurs longward of 2.5 μm on the Moon and thus helps access the 3 μm absorption band that is diagnostic for OH/H_2O. Because all former thermal removal schemes had shortcomings, the new model was used to reprocess the global spectral data cube of the Moon mineralogy mapper (0.6–3.0 μm). The resulting diurnal, latitudinal, and compositional hydration patterns agree with previous results and recent observations of the SOFIA airborne telescope. Reprocessing the model with different bolometric hemispherical emissivities yielded similar fitting results with slightly more realistic parameter estimates.

The new thermal model has multiple future applications: (1) The thermal model was compared to lunar flyby data of the Mercury Radiometer and Thermal Infrared Spectrometer (MERTIS) onboard the BepiColombo probe. Despite challenging observation conditions, the model agrees with the data. This comparison serves as a dress rehearsal for the calibration of MERTIS emissivity spectra after orbit insertion in 2025. (2) Computing phase curves of the airless exoplanet LHS 3844b with the new thermal model indicates that surface roughness considerably increases the signal of the phase curve near the secondary eclipse. This effect turned out to be detectable with the NIRSpec instrument onboard the James Webb Space Telescope and is scheduled for measurement in July 2024. The thermal model will be a crucial tool for phase curve analysis. (3) The lunar trailblazer mission planned for 2024 carries the High-Resolution Volatiles and Minerals Moon Mapper (HVM^3) and the Lunar Thermal Mapper (LTM) that will measure infrared spectra to understand lunar OH/H_2O, mineralogy,

and thermophysical properties better. Data analysis of these instruments will also require a thermal model, such as presented in this thesis. (4) The model may also aid the absolute calibration of Earth-observation satellites. (5) Future research should address directional emissivity effects in the mid-infrared, which might explain the discrepancy between $\overline{\theta} \approx 20^\circ$ and $\overline{\theta} \approx 30^\circ$ for different observation geometries. Another promising research direction is the combination of the thermal roughness model with a heat conduction model, which has successfully been tailored to planet Mercury for future MERTIS data analysis.

Second, a model was devised that combines light scattering theory and the Hapke model to simulate the spectral effects of submicroscopic iron particles that form in the upper lunar regolith through space weathering. Model characterization shows that small iron particles lead to spectral reddening in the near-infrared, and larger iron particles cause more complex spectra that, on average, cause spectral darkening. Both effects agree with observations. Further analyses show that iron particles have only a small influence on the integrated band-depth of the $3\,\mu$m absorption band. The model was applied to fresh lunar mare and highland spectra from the M^3 instrument and compared to mature spectra sampled nearby. The model generally reproduces the shape of mature M^3 spectra. However, the $2\,\mu$m absorption band in lunar mare regions cannot be explained with the model, hinting at different processes that affect this band. Extending the model with a T-matrix approach also shows that clusters of tiny iron particles can cause spectral darkening. Consequently, tiny iron particles in agglutinitic rims do not only cause reddening but also darkening. The space weathering model proved to be useful for spectral unmixing of lunar near-infrared spectra and photometric analysis of lunar swirls.

Third, telescopic observations of Mercury in the near-infrared were revisited. Previous campaigns found a correlation between the normalized spectral slope of the planet and the emission angle. However, the analyses never considered wavelength-dependent atmospheric effects in the optical path. This thesis combined a reflectance model of Mercury with an atmospheric seeing model. The reflectance was constrained with albedo maps derived from data acquired by the Mercury Dual Imaging System (MDIS) onboard the MESSENGER spacecraft. The simulation shows that wavelength-dependent seeing indeed changes the normalized spectral slope and can explain all effects previously thought to be caused by changing emission angle.

Acknoledgements

First and foremost, I would like to thank my advisor, Prof. Dr. Christian Wöhler, for supporting this project, providing helpful knowledge and experience, valuable discussions, and the freedom to pursue new ideas. I would also like to thank co-advisor Prof. Dr. Josef Pauli for providing his time and expertise.

My thanks go to the MERTIS team led by Prof. Dr. Harry Hiesinger and Dr. Jörn Helbert and all the scientific collaborators listed on the next page with whom I had the privilege of working. I also acknowledge the use of the RELAB database and all other datasets (see chapter 4) without the studies, would not have been possible.

Moreover, I would like to thank my present and former colleagues and students, especially Mirza Arnaut, Dr. Arne Grumpe, Dr. Marcel Hess, Dr. Malte Lenoch, Dr. Lubaba Migdadi, Dr. Robert Nowak, Tom Sander, Moritz Tenthoff, and Dr. Thorsten Wilhelm for countless discussions and a pleasant working atmosphere.

Finally, I would like to thank all my friends and important people in my life who supported me along the way - especially my parents, Dr. Herbert, and Dr. Susanne, who embarked on a similar journey some years ago.

Related publications

This thesis is based on the publications listed below, primarily on the three peer-reviewed first-author journal publications: Wohlfarth et al. [2023], Wohlfarth and Wöhler [2022], and Wohlfarth et al. [2019]. Other journal articles and conference contributions of the author that are not part of this thesis are given thereafter.

Peer-reviewed journal articles

- K. Wohlfarth, C. Wöhler, H. Hiesinger, and J. Helbert. An advanced thermal roughness model for airless planetary bodies. Implications for global variations of lunar hydration and mineralogical mapping of Mercury with the MERTIS spectrometer. *Astronomy & Astrophysics*, 674:A69, 2023. doi: 10.1051/0004-6361/202245343

- K. Wohlfarth and C. Wöhler. Wavelength-Dependent Seeing Systematically Changes the Normalized Slope of Telescopic Reflectance Spectra of Mercury. *Remote Sensing*, 14(2):405, 2022. doi: 10.3390/rs14020405

- M. Hess, T. Wilhelm, C. Wöhler, and K. Wohlfarth. Uncertainty Introduced by Darkening Agents in the Lunar Regolith: An Unmixing Perspective. *Remote Sensing*, 13 (22):4702, 2021. doi: 10.3390/rs13224702

- M. Hess, C. Wöhler, M. Bhatt, A. A. Berezhnoy, A. Grumpe, K. Wohlfarth, A. Bhardwaj, and V. V. Shevchenko. Processes governing the VIS/NIR spectral reflectance behavior of lunar swirls. *Astronomy and Astrophysics*, 639:A12, 2020a. doi: 10.1051/0004-6361/201937299

- K. S. Wohlfarth, C. Wöhler, and A. Grumpe. Space Weathering and Lunar OH/H2O - Insights from Ab Initio Mie Modeling of Submicroscopic Iron. *The Astronomical Journal*, 158(2):80, 2019. doi: 10.3847/1538-3881/ab26af

Conference contributions and proposals

- M. Tenthoff, K. Wohlfarth, C. Wöhler, N. Schmedemann, K. E. Bauch, N. Verma, T. M. Powell, B. Greenhagen, M. Knollenberg, M. D'Amore, S. Adeli, H. Hiesinger, J. Helbert, and MERTIS Team. Thermal modeling of Mercury's surface: Parameter estimation from MERTIS flyby data. *Lunar and Planetary Science Conference*, 56: 2272, 2025

- K. Wohlfarth, M. Martinot, T. Panambur, T. Sander, S. Zorzan, M. Arnaut, J. L. Bishop, M. Parente, and C. Wöhler. Seeking Relationships Between Lunar Hydration and Surface Composition. *AGU24*, 2024:P41C–02, 2024

- T. Panambur, T. Sander, K. Wohlfarth, M. Martinot, S. Zorzan, M. Arnaut, J. L. Bishop, M. Parente, and C. Wöhler. Using machine learning to find relationships between different lunar maps: A case study of lunar hydration. *AGU24*, 2024:IN51B–06, 2024

- M. Seifert, K. Wohlfarth, T. Müller, S. Adriaensen, D. Nuyts, J. Léon-Tavares, J. Blommaert, F. Kahil, J. Mollière C1, Gottfriedsen, M. Langer, and D. Rio Fernandes. Lunar calibration of Earth observation thermal infrared imagers using cross-calibration and thermo-physical models. *VH-RODA*, 2024

- M. Tenthoff, K. Wohlfarth, C. Wöhler, S. Zieba, and L. Kreidberg. Reflectance and Emission Modelling of Airless Exoplanets. *European Planetary Science Congress*, pages EPSC2024–649, 2024. doi: 10.5194/epsc2024-649

- A. M. Dapremont, J. L. Bishop, C. Wöhler, K. S. Wohlfarth, M. Parente, R. Klima, and J. Flahaut. Comparing Thermally Corrected Spectra from the Moon Mineralogy Mapper (M3). *56th Lunar and Planetary Science Conference*, 56:2337, 2024

- S. Zieba, L. Kreidberg, R. Hu, C. Morley, K. Wohlfarth, M. Tenthoff, and C Wöhler. The search for regolith on the airless exoplanet LHS3844b. *James Webb Space Telescope Proposal*, Cycle 2(4008), 2023. URL `https://www.stsci.edu/jwst/phase2-public/4008.pdf`. Online; accessed December 4, 2023

- M. Tenthoff, K. Wohlfarth, S. Zieba, L. Kreidberg, and C. Wöhler. How does Surface Roughness affect the Phase Curve of Airless Exoplanets? *Thermal Modeling for Planetary Science IV (TherMoPS IV)*, 4:71, 2023b

- K. S. Wohlfarth and C. Wöhler. Computational Techniques for Fractal Rough Thermal Models. *Thermal Modeling for Planetary Science IV (TherMoPS IV)*, 4:15, 2023

- K. S. Wohlfarth, M. Tenthoff, and C. Wöhler. How does small-scale roughness influence thermal infrared spectra around Mercury's north pole? *Thermal Modeling for Planetary Science IV (TherMoPS IV)*, 4:57, 2023a

- K. Wohlfarth, M. Tenthoff, J. Wright, V. Galluzzi, C. A. Wöhler, H. Hiesinger, J. Helbert, J. Zender, and J. Benkhoff. Computational Models for Mercury Surface Analysis. *Mercury Exploration Assessment Group (MExAG) Annual Meeting 2023*, 2023

- K. S. Wohlfarth, C. Wöhler, J. Helbert, and H. Hiesinger. A New Thermal Roughness Model for the Moon and Mercury: implications for the diurnal lunar hydroxyl cycle and mineralogical mapping with MERTIS onboard Bepicolombo. *Thermal Modeling for Planetary Science IV (TherMoPS IV)*, 4:47, 2023b

- J. L. Bishop, C. Wöhler, K. Wohlfarth, R. L. Klima, A. Dapremont, J. Flahaut, and M. Parente. Characterizing Variations in the Hydrous Components of the Moon. *AGU Fall Meeting Abstracts*, 2022:P41A–05, 2022

- O. Groussin, K. Wohlfarth, P. Vernazza, H. Hiesinger, and J. Helbert. Thermal modelling of Mercury's surface for the MERTIS instrument. *European Planetary Science Congress*, pages EPSC2022–202, 2022. doi: 10.5194/epsc2022-202

- K. Wohlfarth, C. Wöhler, K. E. Bauch, M. D'Amore, H. Hiesinger, J. Helbert, A. Maturilli, A. Morlok, M. P. Reitze, N. Schmedemann, A. N. Stojic, I. Varatharajan, and I. Weber. Mercury is hot: A fractal thermal roughness Model for MERTIS spectral calibration. *Mercury 2022*, pages 102–103, 2022a

- K. Wohlfarth and C. Wöhler. A Mystery solved: Wavelength-dependent Seeing changes the normalized spectral slope of Mercury. *Mercury 2022*, pages 100–101, 2022

- K. S. Wohlfarth, C. Wöhler, J. Helbert, H. Hiesinger, and Mertis-Team. Disk-Resolved Validation of a Fractal Rough Thermal Model for the Moon. *Lunar and Planetary Science Conference*, 53:2431, 2022b

- C. Wöhler, K. Wohlfarth, and A. A. Berezhnoy. Time-of-Day-Dependent Behavior of Lunar Surficial Hydroxyl on a Rough Regolith Surface. *Lunar and Planetary Science Conference*, 53:1492, 2022

- I. Varatharajan, C. Tsang, K. Wohlfarth, C. Wöhler, N. Izemberg, and J. Helbert. Surface Mineralogy of Major Geochemical Terranes of Mercury: Results from NIR (0.7-4.2 microns) Ground Based IRTF/SpeX Spectroscopy. *Lunar and Planetary Science Conference*, 52:1359, 2021

- M. Arnaut, K. Wohlfarth, and C. Wöhler. The interaction between multiple nanophase iron particles changes the slope of lunar reflectance spectra. *European Planetary Science Congress 2021 , Abstract No. 770*, 2021. doi: 10.5194/epsc2021-770

- H. Hiesinger, J. Helbert, K. Bauch, M. D'Amore, M. Maturilli, A. Morlok, M. Reitze, A. N. Stojic, I. Varatharajan, I. Weber, K. Wohlfarth, and C. Wöhler. The Mercury Radiometer and Thermal Infrared Spectrometer (MERTIS) at the Moon — First Results and Status Report. *Lunar and Planetary Science Conference*, page 1494, 2021

- N. Schmedemann, H. Hiesinger, K. Wohlfarth, C. Wöhler, K. Bauch, M. D'Amore, J. Helbert, A. Maturilli, A. Morlok, M. Reitze, A. Stojic, I. Weber, I. Varatharajan, and the MERTIS Team. BepiColombo - Correction of MERTIS Geometry. *Lunar and Planetary Science Conference*, 52:1290, 2021

- K. Wohlfarth, C. Wöhler, K. Bauch, M. D'Amore, H. Hiesinger, J. Helbert, A. Maturilli, A. Morlok, M. P. Reitze, N. Schmedemann, A. Stojic, I. Varaharajan, and I. Weber. A Fractal Rough Thermal Model for Emissivity Retrieval of MERTIS Lunar Flyby Spectra. *Lunar and Planetary Science Conference*, 52:1241, 2021b

- I. Varatharajan, C. Tsang, K. Wohlfarth, C. Wöhler, N. Izenberg, and J. Helbert. Simulation of combined reflectance and emittance spectra in the thermal infrared band on mercury. *European Planetay Science Congress 2019, Abstract No. 1331*, 2019

- K. Wohlfarth, C. Wöhler, and A. Grumpe. How Does Space Weathering Affect the Detection of Lunar OH/H2O? Insights from Ab-Initio Mie Modeling of Submicroscopic Iron. *Lunar and Planetary Science Conference*, 50:2584, 2019b
- K. Wohlfarth, A. Grumpe, C. Wöhler, A. Stojic, A. Morlok, and H. Hiesinger. Simulation of Space-Weathered TIR Spectra on Mercury. *European Planetary Science Congress*, pages EPSC2018–649, 2018
- A. Grumpe, K. S. Wohlfarth, and C. Wöhler. Simulation of Space Weathering based on Mie Theory. *Lunar and Planetary Science Conference*, 49:2533, 2018

Other journal articles

- B. P. Coy, J. Ih, E. S. Kite, D. D. B. Koll, M. Tenthoff, J. L. Bean, M. Weiner Mansfield, M. Zhang, Qiao Xue, E. M. R. Kempton, K. Wolhfarth, R. Hu, X. Lyu, and Wöhler. Population-level hypothesis testing with rocky planet emission data: A tentative trend in the brightness temperatures of m-earths. *arXiv*, 2024. doi: 10.48550/arXiv.2412.06573
- R. M. Marshal, O. Rüsch, C. Wöhler, K. Wohlfarth, and S. Velichko. Photometry of LROC NAC resolved rock-rich regions on the Moon. *Icarus*, 394:115419, 2023a. doi: 10.1016/j.icarus.2022.115419
- M. Hess, M. Tenthoff, K. Wohlfarth, and C. Wöhler. Atmospheric Correction for High-Resolution Shape from Shading on Mars. *Journal of Imaging*, 8(6), 2022. doi: 10.3390/jimaging8060158
- O. Ruesch, M. Hess, K. Wohlfarth, T. Heyer, C. Wöhler, T. R. R. Bontognali, C. Orgel, E. Sefton-Nash, J. L. Josset, and J. L. Vago. Synthetic topography from the decameter to the centimeter scale on Mars for scientific and rover operations of the ESA-Roscosmos ExoMars mission. *Planetary and Space Science*, 205:105301, 2021. doi: 10.1016/j.pss.2021.105301
- M. Tenthoff, K. Wohlfarth, and C. Wöhler. High Resolution Digital Terrain Models of Mercury. *Remote Sensing*, 12(23):3989, 2020. doi: 10.3390/rs12233989
- T. Wilhelm, M. Geis, J. Püttschneider, T. Sievernich, T. Weber, K. Wohlfarth, and C. Wöhler. DoMars16k: A Diverse Dataset for Weakly Supervised Geomorphologic Analysis on Mars. *Remote Sensing*, 12(23):3981, 2020. doi: 10.3390/rs12233981

Other contributions

- I. Krüll, K. Wohlfarth, M. Tenthoff, C. Wöhler, V. Galluzzi, J. Wright, J. Benkhoff, and J. Zender. Shape and Albedo from Shading with Planetary Flyby Images of Mercury and the Moon. *European Planetary Science Congress*, pages EPSC2024–247, 2024. doi: 10.5194/epsc2024-247

- M. Tenthoff, M. Arnaut, T. Barot, N. Elkhouly, M. Faizan, A. Gulati, D. Hallmann, M. Karam, A. Nedungadi, J. Ravikumar, M. Hess, K. Wohlfarth, and C. Wöhler. 3D Models of the Martian Surface in Virtual Reality. *AAS/Division for Planetary Sciences Meeting*, 55:212.04, 2023a

- R. M. Marshal, O. Rüsch, C. Wöhler, K. Wohlfarth, S. Velichko, and M. Patzek. Photometry of rock-rich surfaces on airless bodies. *EGU General Assembly Conference*, pages EGU–14255, 2023c. doi: 10.5194/egusphere-egu23-14255

- M. Arnaut, K. Wohlfarth, and C. Wöhler. Yet Another Scattering Framework: Simulation of Light Scattering Interaction Between Spherical Particles Using the T-Matrix. *54th Lunar and Planetary Science Conference*, 54:2997, 2023

- K. E. Bauch, A. Morlok, H. Hiesinger, M. P. Reitze, N. Schmedemann, A. N. Stojic, I. Weber, J. H. Pasckert, M. D'Amore, J. Helbert, A. Maturilli, K. Wohlfarth, and C. Wöhler. Unmixinig of Laboratory IR Spectral Reflectance Measurements of Low-Mg Northern Volcanic Plains Analogs. *54th Lunar and Planetary Science Conference*, 54:2247, 2023

- R. M. Marshal, O. Rüsch, C. Wöhler, K. Wohlfarth, S. Velichko, and M. Patzek. Photometry of Rock-Rich Surfaces on Airless Bodies. *54th Lunar and Planetary Science Conference*, 54:1650, 2023b

- R. M. Marshal, O. Rüsch, C. Wöhler, K. Wohlfarth, and S. Velichko. Photometry of rock-rich surfaces on the Moon. *European Planetary Science Congress*, pages EPSC2022–871, 2022c. doi: 10.5194/epsc2022-871

- M. Tenthoff, C. Wöhler, and K. Wohlfarth. Accurate 3D Reconstruction of Mercury with Shape from Shading. *Mercury 2022*, pages 98–98, 2022

- R. M. Marshal, O. Rüsch, C. Wöhler, and K. Wohlfarth. Estimating Lunar Rock Abrasion Stage using Photometric Studies. *EGU General Assembly Conference*, pages EGU22–12217, 2022b. doi: 10.5194/egusphere-egu22-12217

- M. Arnaut, K. Wohlfarth, and C. Wöhler. Space Weathering Simulation of Interacting Nanophase Iron Particles in the Thermal Infrared Region. *53rd Lunar and Planetary Science Conference*, 53:2184, 2022

- K. E. Bauch, A. Morlok, H. Hiesinger, M. P. Reitze, N. Schmedemann, A. N. Stojic, I. Weber, J. H. Pasckert, M. D'Amore, J. Helbert, A. Maturilli, K. Wohlfarth, and C. Wöhler. Unmixing of Laboratory IR Spectral Reflectance Measurements of Smooth Plains Analogs. *53rd Lunar and Planetary Science Conference*, 53:1989, 2022

- R. M. Marshal, O. Rüsch, C. Wöhler, and K. Wohlfarth. Estimating Lunar Rock Abrasion Stage Using Photometric Studies. *53rd Lunar and Planetary Science Conference*, 53:1108, 2022a

- A. Morlok, M. P. Reitze, I. Weber, A. N. Stojic, K. E. Bauch, K. Wohlfarth, C. Wöhler, H. Hiesinger, and J. Helbert. FTIR Studies of Planetary Materials: The Impact of Temperature and Vacuum on Spectral Features. *84th Annual Meeting of the Meteoritical Society*, 84:6184, 2021b

- A. Maturilli, K. Wohlfarth, G. Alemanno, C. Woehler, M. D'Amore, J. Helbert, and H. Hiesinger. Spectral Signatures of Glass on Lunar Analogue Rocks. *52nd Lunar and Planetary Science Conference*, 52:2085, 2021

- A. Morlok, B. Charlier, M. P. Reitze, C. J. Renggli, S. Klemme, O. Namur, M. Sohn, D. Martin, I. Weber, A. N. Stojic, K. E. Bauch, K. Wohlfarth, C. Wöhler, K. H. Joy, R. Wogelius, C. Carli, H. Hiesinger, and J. Helbert. BepiColombo and MERTIS @Moon: A Very First Comparison of Mid-Infrared (7-14 µm) Spectra. *52nd Lunar and Planetary Science Conference*, 52:1964, 2021a

- K. E. Bauch, A. Morlok, H. Hiesinger, M. P. Reitze, N. Schmedemann, A. N. Stojic, I. Weber, M. D'Amore, J. Helbert, A. Maturilli, I. Varatharajan, K. Wohlfarth, and C. Wöhler. Unmixing of Laboratory IR Spectral Reflectance Measurements of Labradorite-Enstatite-Glass Mineral Mixtures. *52nd Lunar and Planetary Science Conference*, page 1567, 2021

- R. Marshal, K. Wohlfarth, and O. Ruesch. Insights on Pixel and Sub-Pixel Scale Rock Abundance on the Moon with LROC/NAC. *52nd Lunar and Planetary Science Conference*, 52:1457, 2021

- K. Wohlfarth, C. Wöhler, K. Bauch, M. D'Amore, H. Hiesinger, J. Helbert, A. Maturilli, A. Morlok, M. P. Reitze, N. Schmedemann, A. Stojic, I. Varaharajan, and I. Weber. The Lunar EPI-Regolith — A Hypothesis to Explain the Lunar Flyby Data of MERTIS. *52nd Lunar and Planetary Science Conference*, 52:1236, 2021a

- M. Hess, K. Wohlfarth, C. Wöhler, A. A. Berezhnoy, M. Bhatt, and A. Bhardwaj. Space Weathering Trends at the Mare Moscoviense Swirl. *European Planetary Science Congress*, pages EPSC2020–716, 2020c. doi: 10.5194/epsc2020-716

- A. Kosak, M. Arnaut, S. Beck, H. Schippers, K. Wohlfarth, T. Wilhelm, and C. Wöhler. Geomorphologic Feature Extraction and Clustering of Martian DTM Data. *51st Annual Lunar and Planetary Science Conference*, 51:3044, 2020

- M. Arnaut, K. Wohlfarth, and W. Wöhler. A Study of Hyperspectral Clustering - How to Speed Up Spectral Unmixing of Moon Mineralogy Mapper Data. *51st Annual Lunar and Planetary Science Conference*, 51:3008, 2020

- M. Hess, K. Wohlfarth, and C. Wöhler. Quantifying Lunar Spinel-Rich Lithologies with Nonlinear Spectral Unmixing Considering Space-Weathering Effects. *51st Annual Lunar and Planetary Science Conference*, 51:1863, 2020b

- M. Hess, K. Wohlfarth, O. Ruesch, C. Wöhler, and A. Grumpe. High Resolution Digital Terrain Model for the Landing Site of the Rosalind Franklin (ExoMars) Rover. *EPSC-DPS Joint Meeting 2019*, 2019:EPSC–DPS2019–1533, 2019c
- I. Varatharajan, C. Tsang, K. Wohlfarth, C. Wöhler, N. Izenberg, and J. Hebert. Surface Composition of Mercury from NIR (0.7-4.2 μm) Ground-Based IRTF/SpeX Spectroscopy. *EPSC-DPS Joint Meeting 2019*, 2019:EPSC–DPS2019–1331, 2019
- M. Hess, K. Wohlfarth, A. Grumpe, C. Wöhler, O. Ruesch, and B. Wu. Atmospherically Compensated Shape from Shading on the Martian Surface: Towards the Perfect Digital Terrain Model of Mars. *ISPRS - International Archives of the Photogrammetry, Remote Sensing and Spatial Information Sciences*, 4213:1405–1411, 2019b. doi: 10.5194/isprs-archives-XLII-2-W13-1405-2019
- M. Arnaut, K. Wohlfarth, A. Grumpe, and C. Wöhler. Mineralogical Maps of Mars from Hapke Modeling and Spectral Unmixing. *50th Annual Lunar and Planetary Science Conference*, 50:2661, 2019
- M. Hess, K. Wohlfarth, A. Grumpe, C. Wöhler, O. Ruesch, and B. Wu. Overcoming Troublesome Stereo Artifacts: Towards the Perfect Digital Terrain Model of Mars. *50th Annual Lunar and Planetary Science Conference*, 50:2565, 2019a
- K. Wohlfarth, A Grumpe, C. Wöhler, J. Maturilli, A. andHelbert, A. Morlok, and H. Hiesinger. Combined Reflectance and Emittance Model for Spectral Unmixing. *Thermal Modeling for Planetary Science III (TherMoPS III)*, 3, 2019a
- K. Wohlfarth, C. Schröer, M. Klaß, S. Hakenes, M. Venhaus, S. Kauffmann, T. Wilhelm, and C. Wöhler. Dense Cloud Classification on Multispectral Satellite Imagery. *2018 10th IAPR Workshop on Pattern Recognition in Remote Sensing (PRRS)*, pages 1–6, 2018. doi: 10.1109/PRRS.2018.8486379
- K. S. Wohlfarth, A. Grumpe, C. Wöhler, A. Morlok, and H. Hiesinger. Combined Reflectance and Emittance Spectroscopy in the Thermal Infrared Band: Implications for Mercury. *49th Annual Lunar and Planetary Science Conference*, 49:2519, 2018a
- K. S. Wohlfarth, W. C. Liu, B. Wu, A. Grumpe, and C. Wöhler. High Resolution Digital Terrain Models of the Martian Surface: Compensation of the Atmosphere on CTX Imagery. *49th Annual Lunar and Planetary Science Conference*, 49:2498, 2018b

Supervised theses

The author supervised fourteen Bachelor's and Master's theses during the preparation of this thesis.

- N. Elkhouly. Tailoring a Thermal Model to Planet Mercury. *Master's thesis, TU Dortmund University*, 2023
- M. Tenthoff. Reflectance and Emission Models for Airless Planetary Bodies: Application to Solar System Objects and Exoplanets. *Master's thesis, TU Dortmund University*, 2023
- I. Krüll. Shape from Shading with Planetary Fly-By Images. *Bachelor's thesis, TU Dortmund University*, 2023
- M. Arnaut. Light Scattering of Small Particles on Planetary Surfaces. *Master's thesis, TU Dortmund University*, 2021
- A. Bowkunnyj. Simulation der elektromagnetischen Streuung im oberen Mondregolith. *Master's thesis, TU Dortmund University*, 2021
- D. Schauten. Thermische Modellierung von planetaren Oberflächen: Modellierung und Analyse verschiedener Rauigkeitsskalen. *Bachelor's thesis, TU Dortmund University*, 2021
- A. Bartsch. Lokale Analyse von lunaren Hydroxylvorkommen bezogen auf topografische und geologische Effekte. *Bachelor's thesis, TU Dortmund University*, 2020
- J. Beck. Implementierung eines Verfahrens zur Erkennung von Spielkarten. *Bachelor's thesis, TU Dortmund University*, 2020
- N. Bergmann. Spektrales Reddening und Darkening von planetaren Oberflächen. *Bachelor's thesis, TU Dortmund University*, 2020
- M. Tenthoff. 3D-Rekonstruktion der Merkuroberfläche mit Shape from Shading. *Bachelor's thesis, TU Dortmund University*, 2019
- T. Harnisch. Entwurf eines mikrocontrollerbasierten Systems zur Anwendung moderner Bilderkennungsalgorithmen. *Bachelor's thesis, TU Dortmund University*, 2019
- R. Mbakop. Methode zur Bestimmung von Endgliedern in Mineralmischungen. *Bachelor's thesis, TU Dortmund University*, 2019
- M. Hess. Shape from Shading Applied to the Martian Surface: Compensation of Atmospheric Effects. *Master's thesis, TU Dortmund University*, 2019
- M. Arnaut. Unmixing of CRISM Hyperspectral Data. *Bachelor's thesis, TU Dortmund University*, 2018

Contents

Chapter 1

Introduction

1.1 Epistemological and methodological context

This thesis presents computational methods for infrared spectroscopy that help analyze the surface composition of airless planetary bodies, especially the Moon, Mercury, and the exoplanet LHS 3844b. These methods do not stand for themselves but help answer broader questions about the formation history of the Moon and Mercury and are related to research about various surface processes of the Moon and LHS 3844b. The author believes a doctoral thesis should embed his endeavors into the broad scientific and methodical context. Before addressing individual research questions, this chapter reviews the scientific methodology of planetary science and astronomy and discusses how engineering, applied physics, and computer simulation enable planetary research.

The primary question is: How can we explore planetary bodies? We start from the general aims of the scientific endeavor and arrive at the specific methodic challenges of planetary science, remote sensing, infrared astronomy, and computer modeling that motivate this thesis. Science generally attempts to describe, explain, and eventually predict the objects and phenomena under study. Scientific explanations stem from causal models of phenomena, and scientists attempt to develop these models through reasoning and the scientific method. Many phenomena are unique, and the perspective of describing and explaining the unique by a chain of reasons is often referred to as *ideographic*, initially coined by Windelband [1904]; Windelband et al. [2021]. It is typically, but not exclusively, found in the historical sciences, archaeology, social sciences, anthropology, paleontology, and many more. If reoccurring scenarios or patterns are present, explaining them by general rules or laws that apply to the individual case is possible. This perspective is often called *nomothetic* [Windelband, 1904] and is prevalent in physics, chemistry, biology, and many more.

However, ideographic and nomothetic approaches are often intertwined. Parts of a unique phenomenon may exhibit regularities that stem from a regular cause system. The unique phenomenon may result from a sequence of otherwise regular processes. Therefore, many scientific fields take ideographic and nomothetic perspectives. The major challenge of inferring the cause system of the unique phenomenon is that the experimental access and the interaction are limited due to uniqueness. It is not, or hardly, possible to carry out repeated experiments, which may impair the scientific method. However, what explanations are present in planetary science? Are there specific challenges that arise from planetary bodies? And: What methods are necessary to conduct fruitful planetary research after all?

Planetary science shares aspects of Earth science and astronomy because the field investigates planetary objects in space. We unravel characteristics, challenges, and methodologies pertinent to planetary research by looking at theoretic insights from Earth science [Kleinhans et al., 2010] and astronomy [Anderl, 2016]. Both fields attempt to explain the history of the objects under study and identify general causal relations that act in similar situations or on similar classes of objects. Consequently, both fields embrace ideographic and nomothetic perspectives. This frame seamlessly extends to planetary science, which aims to explain the formation history of the bodies, a wide variety of unique properties of the planetary objects (such as composition and surface features), and general processes that act on many planetary bodies in a similar way (such as cratering, space weathering, planetary dynamos, atmospheric processes and many more). Eventually, insights from planetary science will help us understand the formation of the solar system and the grounds we are walking on and even apply to extrasolar planets and planetary systems.

Planetary science is challenging and cumbered with twofold inaccessibility. First, similar to the Earth and astronomical objects, we cannot directly access the past and the causal processes that shape the planetary bodies. Second, similar to astronomic objects, it is hard to access a planet because it is far away. Together with the complex and contingent nature of the planetary bodies, these challenges give rise to five methodic fields central to planetary science. (1) The method of narrative explanation, (2) generalized but not universal causal relations, (3) remote sensing instrumentation, (4) laboratory experiments and fieldwork, and (5) computer models.

Inaccessibility of the past prohibits the researcher from conclusively testing a hypothesis on the formation history and forming a continuous and rigorous chain of causal explanations. This situation is almost always the case when reconstructing a unique phenomenon only from the remaining manifestations that are still there, somewhat similar to a crime scene with an unknown course of events. However, does this circumstance prohibit explanations in astronomy and planetary sciences? Anderl [2016] counters and states that the astronomer, or here, the planetary scientist, applies a *"Sherlock Holmes"* strategy and collects clues for a consistent story that is the best way to describe the observations. More specifically, two principles and some heuristics guardrail narrative explanations for planetary bodies: The geologic principles of actualism and universalism assume the uniformity of causes and conclude that a process behaves similarly at different times and places. These principles allow for comparing well-known processes today with manifestations of past events and comparisons between planets. Further, universalism is the basis for drawing analogies between controlled experiments in the laboratory and processes of manifestations of past processes somewhere else. Even though working hypotheses on past processes and events cannot be conclusively tested with a controlled experiment, the implications of hypothetical explanations can be evaluated on how they relate to other observations, narrations, and physical constraints. As Rossi et al. [2018] point out, a narrative explanation or working hypothesis should be consistent, coherent, and consilient. Consistency means that the narrative model must not contradict other observations about the phenomenon under study. A hypothesis must be coherent because it provides enough explanation that aligns with similar phenomena at other places. Consilience is not mandatory, but good explanations often combine previously unrelated observations under one causal model. The cornerstones of the narrative planetological method are sound, but it may require heuristics, and best practices are not theoretically grounded. Further, if not appropriately conducted, the narrative explanation may be susceptible to fallacies such as ad-hoc modifications, confirmation bias, formation of camps, historical fallacies, moving the goalposts, and more. It is vitally important to remember this, gather enough evidence through measurements, experiments, and simulations, judge confirming and opposing evidence, and always consider the physical plausibility to arrive at sound explanations. However, it might be essential to deliver a bold statement at times to move things forward. Two examples of narrative explanations in planetary science and the Sherlock Holmes strategy are the Moon's and Mercury's formation histories [Rossi et al., 2018; Hauck II et al., 2018]. The commonly accepted theory for lunar formation history tells the story of another planetary body that struck the Earth. Debris remained in orbit and accreted to form the Moon, then a hot pebble with differentiated layers of mineral components. Magma oceans cooled and formed a solid crust, but impacts during the late heavy bombardment struck the surface and triggered volcanism that formed the dark and basaltic lunar maria. This narrative explanation results from audacious sample return missions, hundreds of detailed laboratory and theoretical studies, and computer simulations. The formation history of Mercury needs to be more detailed. The current model proposes a buoyant carbon crust, extensive resurfacing through widespread volcanism, and ongoing bombardment that excavated deeper layers. The upcoming BepiColombo mission will likely provide new insights, such as the MErcury Radiometer and Thermal Infrared Spectrometer (MERTIS), which will map the mineralogy and thermal environment, delivering clues for the greater narrative [Hiesinger et al., 2020].

Planetary bodies are not unique but exhibit regularities resulting from higher-level processes and causal relations that can be generalized and applied to similar situations or other planetary bodies. As Kleinhans et al. [2010] state for the Earth, these generalizations cannot be reduced to more universal laws. They have the character of "*generalized – but not universally valid—descriptions of contingent processes*" [Kleinhans et al., 2010]. Here, contingency refers to a singular manifestation of a process under specific constellations. These principles cannot be summarized as a single equation of a rigorous set of rules. However, they must be formulated as an ideal scenario for which the individual realizations may differ. Space weathering on airless bodies is an example of a very general, ubiquitous, and comparatively well-understood process. The fresh ejecta material is usually bright but darkens as the harsh space environment erodes the surface and alters the makeup of the regolith. Space weathering has been around for millions of years and has only been inferred through comparing different sites of different maturity, analyzing samples, controlling laser irradiation and shock experiments in the laboratory, and computer simulation [Hapke, 2001; Pieters and Noble, 2016]. A general theory of space weathering must explain variations between individual bodies. As stated by Anderl [2016], causal astrophysical explanations can be inferred from the astronomical laboratory: "*The accessible cosmic sample of objects in various evolutionary stages is then reassembled as a self-consistent time series within a given evolutionary model, augmented and aided by simulations.*" In the case of lunar space weathering, sites with different maturity stages can be brought into a time series showing how the surface darkens.

Direct spatial access and measurement of phenomena are possible on Earth but exceptionally rare for planets. It is limited to rovers and a few astronauts. Therefore, planetary science must rely on telescopes and space-borne remote sensing instruments that measure electromagnetic radiation emerging from the object. Electromagnetic radiation and matter are known to interact in many possible ways. Consequently, a battery of different measurement principles has been devised that exploit various physical principles of light-matter interaction to measure planetary surfaces and subsurfaces. Among the most common techniques are optical cameras, spectrometers, and radiometers in the ultra-violet, visible and infrared regions, Radar devices, Lidar systems, X-ray fluorescence spectrometers, and Gamma-ray spectroscopes; for a detailed explanation of these techniques, see, for example, Bishop et al. [2019]. Raw remotely sensed data do not speak for themselves. In virtually all cases, data reduction and calibration are performed before the data is interpreted, often in the context of a physical model. This process requires a thorough understanding of the instrument, the calibration routines, and the models involved. Special care must be taken to decide whether variations in the data are an artifact of the measurement process or an actual phenomenon. An example of the interpretation of remote sensing data in the context of a physical model is the global mapping of lunar hydroxyl [Wöhler et al., 2017]. Thermal emission contaminates the near-infrared spectra of the lunar surface. Therefore, a thermal model that removes the emission component and reveals an absorption band specific for hydroxyl in minerals is employed. Well-tested physical theory and in-situ temperature measurements of the Moon support the thermal emission modeling, which the author investigates in this thesis [Wohlfarth et al., 2023].

Laboratory facilities serve two purposes: analyzing returned samples for direct insight into the body's composition and replicating planetary conditions for controlled experiments. Earth itself acts as an outdoor laboratory offering direct access to similar processes on other planets. Examples include any endogenic process, such as tectonics, mass wasting, and volcanism, which can be analyzed directly or, in rare cases, even controlled. Results from the laboratory or field studies can be transferred to the planetary body by analogy.

Computer models have long been productive tools across science. They use assumptions and simplifications to recreate a defined outcrop of reality. Changing the input parameters or adapting the model components allows for control of the simulation output. Other than laboratory experiments, computer simulations are not restricted by the feasibility of any experimental setup, only by ever-growing computational complexity and memory capacity. In principle, computer models allow access to extreme system sizes, periods, and unfriendly conditions and thus overcome many accessibility issues that complicate planetary and astrophysical research in the real world or the laboratory. However, computer models in astrophysics and planetary science exhibit several issues that make it difficult to relate the model to reality, thus limiting its epistemological power. Following Anderl [2022], the author identifies four culprits: modeling complex systems, model plasticity, modeling choices, and limited data prone to post-hoc theorizing.

A computer model always builds on a specific set of assumptions and thus idealizes reality. Simplifications are necessary if the model attempts to recreate a complex system stretching across many scales, such as a planetary surface, interior, or the entire cosmos. Batterman [2013], Anderl [2022], and Massimi [2018] distinguish between bottom-up and top-down modeling: Bottom-up models start at the microphysical level with relatively detailed assumptions and let the overall system behavior result from these interactions. In contrast, the top-down approach makes assumptions about the general model behavior and then uses theoretical or empirical relations that constitute the overall behavior. Cosmological bottom-up models tend to have upscaling problems, while top-down models have explanatory problems because they can be adjusted to describe anything [Anderl, 2022]. In planetary science, the reflectance of a planetary regolith has been modeled with bottom-up and top-down approaches (see also Section 3.4). Light scattering theory is rigorous and simulates the light-matter interactions at small scales. However, it remains computationally complex and has yet to be successfully up-scaled to describe the reflectance behavior of planetary surfaces. More computing resources and more efficient codes may address this problem. The Hapke model [Hapke, 2012] boldly assumes that the radiative transfer equation applies to a planetary regolith, producing good fits with actual measurements but eventually running into explanatory problems relating the internal model parameters to meaningful physical quantities. Validation of sub-systems may overcome explanatory problems but prove problematic in the case of the Hapke model.

A crucial point is guaranteeing that a computer model describes reality. Anderl [2022] discusses two opposing views. Ruphy [2011] analyzed computer models for galaxy evolution and uttered skepticism that accurately reproducing the data with a model is a sign that the model is true. Model plasticity makes parameter variations fit any given data, generating no epistemological value. Model components are often chosen without testing alternative paths, making the model no compelling but arbitrary build. Boyd [2014] counters with a more optimistic argument. Model components are not an arbitrary choice because they are subject to the laws of physics and can be refined step by step. Insofar as the models become better with time, and if the model and data disagree, something must be wrong with the initial modeling theory.

Another common problem in astrophysical model testing is post-hoc theorizing. It occurs when testing a model or theory the data suggests, i.e., adjusting a model to a given dataset and using the same data to test if the modeling theory is adequate. Strictly speaking, post-hoc theorizing prohibits any statement about the theory's validity. Unfortunately, astrophysical campaigns often yield only a limited amount of data, which are used repeatedly and thus become prone to post-hoc theorizing. If there is only one dataset and an isolated theory, post-hoc theorizing becomes a problem. Fortunately, theories and related models are rarely isolated, usually follow the laws of physics, and model components can be tested independently.

Even if a model is well validated, it may remain complicated to solve the inverse problem, i.e., determining the suitable model parameters that fit an observation. In the sense of

Hadamard [1902], the inverse problem is well-posed if a unique solution exists that continuously depends on the input. Unfortunately, astrophysical and planetary computer models are often ill-posed because they often depend on multiple interchangeable parameters, which leads to non-unique solutions, e.g., Schmidt and Fernando [2015] and Hess et al. [2023]. At best, these cases only allow for the determination of a parameter space with plausible solutions. Sometimes, suitable regularizations narrow down this parameter space. Bayesian formulation provides uncertainties and reveals which parameter combinations are compatible. Spectral unmixing of mineral components is an ill-posed inverse problem in planetary science that can be best managed with prior information and Bayesian theory, e.g., Hess et al. [2021].

All in all, computer models are no cure-all to inaccessibility issues of celestial objects and do not guarantee definite answers. However, computer models may impose physical constraints, simulate what-if scenarios, guide other analyses, and support or refute an overarching explanation. Often, computer models are crucial parts of calibration routines. Consequently, computer models aid planetary research but must always be contextualized and critically discussed.

In conclusion, uncovering knowledge about planetary bodies and other astronomical objects is not straightforward. Accessibility issues of the target almost entirely prevent experimental and causal interaction. Researchers must resort to alternative approaches to infer consistent, coherent, and consilient narratives that explain how a celestial body evolves. Adopting a Sherlock-Holmes-like investigation, researchers combine clues from remote measurements and draw from analogy conclusions with laboratory experiments and computer models. All these tasks come with specific pitfalls that must be avoided to arrive at sound conclusions. Remote sensing and telescopic measurements require knowledge of the entire optical path and robust calibration. Laboratory setups are limited by physical and financial feasibility.

Computer models may overcome accessibility issues, but ensuring they adequately describe reality is complicated. Ultimately, planetary and astronomical science questions involve various mechanisms and require many fields of expertise. Planetary science becomes a multi- and transdisciplinary approach: Geology, Geophysics, Geochemistry, Astronomy, Astrophysics, Engineering, Computer Science, and more work together to explain planetary bodies.

This work focuses on computational models to calibrate infrared spectra better and understand the surface processes of airless planetary bodies. The models and techniques touch almost all topics presented here. The following section introduces the detailed contributions and how they relate to the broader questions.

1.2 Motivation and outline

Many questions in astronomy and planetary science revolve around the structure and the mineralogical composition of planetary bodies: What is the mineralogical composition of a planetary surface? What is the distribution of volatiles on the body, and how do they interact with the exosphere? What is the (micro-) physical structure of the planetary surface? Answering these questions gives clues that constrain the greater narrative of a body's formation history or the processes that govern planetary surfaces. To infer a body's mineral composition and other physical properties of the surface, planetary scientists primarily rely on infrared remote sensing probes or infrared telescopes that measure wavelengths typically longer than 0.75 mum. An infrared detector measures reflected solar light and thermally emitted light that emerges from a planetary body. Depending on the wavelength region, one component, the other component, or a superposition of both arrive at the sensor. The reflected spectrum may contain crystal field absorptions, and the emitted light may exhibit vibrational bands that help to identify and differentiate between rock-forming minerals and volatiles such as hydroxyl/water. However, the infrared spectra do not present the compositional information right away. Reflected light depends on multiple variables, such as the illumination conditions, regolith properties, and the solar spectrum. Emitted light depends on the surface's temperature distribution, the thermal properties, and the micro-physical structure of the surface, such as surface roughness. Consequently, extracting compositional and structural information from infrared spectra is a complex problem involving many processes. This endeavor necessitates a view that combines light scattering, thermal emission, and compositional aspects. This thesis approaches methodic challenges for calibrating and analyzing infrared measurements of airless planetary bodies that aid a broad scope of science questions. In particular, this thesis contributes in three ways:

Contribution 1: Thermal radiance modeling. In the first chapter, the author develops, validates, and applies a state-of-the-art thermal model for airless planetary bodies that simulates the directional emission of infrared radiation. The thermal model extends the approaches of Rozitis and Green [2011], Rozitis and Green [2012], Davidsson et al. [2015], and Grumpe et al. [2019] using fractal rough surface elements constrained by lunar in-situ observations attempt to model a planetary regolith realistically. The model validation uses two datasets: First, the Chinese weather satellite Gaofen-4 (GF-4) acquired disk-resolved lunar infrared spectra from 3.5–4.1 μm [Wu et al., 2021] that allow validation under moderate phase angles. Second, the Diviner Lunar Radiometer onboard the Lunar Reconnaissance Orbiter (LRO) performed emission phase function (EPF) off-nadir measurements for a broad range of infrared wavelengths [Bandfield et al., 2015]. In both cases, the model and the measurements agree nearly exactly. Reprocessing the model with different bolometric hemispherical emissivities also yielded similar fitting results with slightly more realistic parameter estimates. The thermal model is used to address several topics that help to address four science questions:

What is the global distribution of superficial lunar OH/H_2O? Lunar reflectance spectra have a vibrational absorption band around 2.8–3.0 μm, which indicates superficial OH/H_2O.

However, radiance spectra acquired in this spectral region consist of a reflected and a thermally emitted component. The excess thermal radiation has to be removed to uncover and correctly interpret the absorption feature of the reflectance spectrum. Even though several thermal correction methods exist, they have yet to be thoroughly tested. The newly devised thermal model allows for evaluating the performance of the thermal correction of Wöhler et al. [2017]; Grumpe et al. [2019] and analyzing the fidelity of lunar OH/H_2O maps. The author also computes new global lunar hydration maps from Moon Mineralogy Mapper (M^3) data that confirm lunar hydration's spatial, temporal, and compositional patterns.

What is Mercury's mineralogy? The geologic history of Mercury still needs to be fully understood. The mineralogy remains unknown to date, which is an essential constraint to the planet's geologic evolution and, ultimately, the development of the inner Solar System. The MErcury Radiometer and Thermal Infrared Spectrometer onboard the BepiColombo mission is on its way to Mercury to acquire highly resolved global coverage in the mid-infrared. The scientific objective of the MERTIS instrument is to identify rock-forming minerals, provide mineralogic maps, and characterize the planet's thermophysical properties. Accurate calibration of the thermal emissivity spectra requires a thermal roughness model. The author compares the model to lunar spectra from 7.0–14.0 μm that were acquired by MERTIS during a flyby-maneuver on 10^{th} April 2020, showing good agreement. The author further models the thermal emission of Mercury, which prepares for the first Mercury flyby in late 2024 and the data arriving after orbit insertion in late 2026.

What is the surface structure of the airless exoplanet LHS 3844b? The newly discovered exoplanets LHS 3844b [Kreidberg et al., 2019; Diamond-Lowe et al., 2020], TRAPPIST-1b [Greene et al., 2023], and TRAPPIST-1c [Zieba et al., 2023] likely lack an atmosphere and can be regarded as the first known rocky exoplanets. If the exoplanet's regolith were comparable to the Moon or Mercury, the thermal emission would behave similarly. Due to surface roughness, the airless body may appear hotter than predicted by a smooth body of the same size. This effect is known as thermal beaming in the asteroid community, and in the case of an exoplanet, roughness may alter the thermal phase curve. Applying the thermal model developed in this thesis to LHS 3844b shows that surface roughness alters the planet's phase curve, and the effect is strong enough to be detected with Near-Infrared Spectrograph (NIRSpec) onboard the James Webb Space Telescope (JWST). Hence, the author initiated and co-authored an application (General Observer Program (GO) 4008, Zieba et al. [2023]) for the James Webb's GO Cycle 2, which is scheduled for July 2024. The subsequent study will be the first of its kind for an exoplanetary surface. The author further issued a Master's thesis that explored the combined thermal emission and reflectance phase curves of LHS 3844b and found ways to reveal information about the planet's surface structure (Tenthoff [2023]).

What are the thermophysical properties of planet Mercury? Infrared emission of a planetary nightside declines with time because the surface receives no radiation and cools down. Comparing temperature evolution with a one-dimensional heat conduction model allows for retrieving the body's thermophysical parameters. These parameters (such as conductivity, porosity, thermal inertia, and thermal skin depth) characterize the upper regolith and indicate boulders and other features. Hayne et al. [2017] derived these parameters from Diviner measurements and presented state-of-the-art global lunar thermophysical parameter maps. Bauch et al. [2021] adapted a one-dimensional heat-conduction model to Mercury to prepare for the upcoming MERTIS radiometer measurements. However, none of the heat conduction models assume roughness. The author taylors the heat-conduction model of Hayne et al. [2017] to Mercury to prepare the combination of surface roughness and heat-conduction models. Further analysis of the bolometric hemispherical albedo indicated that this quantity is not constant and likely plays a crucial role in the thermal analysis of Mercury.

Contribution 2: Space weathering simulation. Cosmic erosion processes, termed space weathering, alter the physical and chemical structure of the uppermost layer of airless planetary bodies. Space weathering is not fully understood, but the gradual accumulation of nanometer-sized iron particles in the upper layer of the regolith is known to considerably affect the shape and obstruct the mineral absorption bands of near-infrared (NIR) spectra of the Moon. Modeling and understanding the spectral effects of space weathering is crucial to estimating the mineral composition, the presence of volatiles, and the age of the surface. In this thesis, the author critically reviews the reflectance modeling of planetary surfaces and presents a light scattering model of submicroscopic iron induced by lunar space weathering. The model is compared with thermally corrected NIR spectra of the M^3, showing good agreement. The space weathering model is applied in the context of three research questions.

How does submicroscopic iron of different sizes influence the shape of infrared reflectance spectra? Small iron particles of several nanometers in size are believed to redden the spectrum, and particles of several tens to several hundred nanometers in diameter tend to darken the material. Previous models have mostly omitted the iron particles' phase function, and a broad particle size range has not been systematically analyzed. The newly developed space weathering simulation framework addresses these points and characterizes the spectral effects of varying particle sizes and amounts of submicroscopic iron in detail. The results show a more complex spectral behavior than previous models, but superposing various large particle sizes leads to spectral darkening and can recreate the spectral trends on the Moon well.

How does submicroscopic iron influence the detection of lunar OH/H_2O? Space weathering generates submicroscopic iron that subdues the mineral absorption bands and the diagnostic band for OH/H_2O around 2.8–3.0 μm. The space weathering model helps to analyze the influence of tiny iron particles on the absorption band. The analysis shows that space weathering effects on the integrated band-depth are small, which is an important constraint for lunar hydroxyl analysis with M^3 (0.6–3.0 μm), the Imaging Infrared Spectrometer (IIRS) (0.8–5.0 μm) and the upcoming High-Resolution Volatiles Mineral Moon Mapper (HVM^3) (0.6–3.6 μm).

How does the interaction between neighboring iron particles influence the infrared spectrum? Previous frameworks implicitly assumed that submicroscopic iron particles are well separated, spectral reddening is due to small particles, and spectral darkening comes from larger iron spheres. However, Tunneling Electron Microscope (TEM) imagery [Pieters and Noble, 2016, and references therein] suggests that the nanometer-sized iron particles in vaporized rims are often closely packed and form layers with lateral extents of hundreds of nanometers. The author issued a master's thesis [Arnaut, 2021] that models inter-particle light scattering interaction with the T-matrix method. Based on the methods developed in the thesis, this work explores the spectral effects of submicroscopic iron particle clusters. The results suggest that particle clusters spectrally behave similarly to large particles, which leads to a new understanding of spectral space weathering effects that the author critically discusses.

How does the space weathering simulation help determine mineral abundances? Spectral unmixing is a technique that predicts the mineral abundances from spectral measurements. Because space weathering flattens the diagnostic absorption bands, it hampers the proper determination of mineral abundances. Hess et al. [2021] devised a Bayesian spectral unmixing approach that employs the newly developed space weathering simulation technique and elemental priors. They find that Bayesian unmixing successfully yields mineral abundances and requires nanophase and microphase iron with abundances up to approximately 2 wt%, consistent with previous studies.

Contribution 3: Telescopic measurements of Mercuy After Mariner 10 imaged one side of Mercury, and before the Mercury Surface, Space Environment, Geochemistry and Ranging (MESSENGER) spacecraft acquired high-resolution global datasets, all spectrophotometric constraints came from telescopic measurements across multiple wavelength ranges. Several NIR measurements report variations of the spectral slope that are allegedly associated with the planet's emission angle. Previous interpretations mainly focussed on photometric effects. However, none of the telescopic studies considered that atmospheric seeing distortions of the target depend on the wavelength. The third contribution of this thesis combines a photometric model of Mercury with wavelength-dependent atmospheric seeing and simulates Mercury as seen at the time of the telescopic observations. Simulation results help to investigate if wavelength-dependent seeing influences the spectral slope of telescopic measurements of Mercury. The study re-analyzes telescopic measurements of the past three decades and finds that wavelength-dependent seeing largely explains all changes in the spectral slope previously thought to have other reasons.

Chapter 2

The surface of airless planetary bodies

Rocky airless planetary bodies are sheeted with a layer of regolith ($\grave{\rho}\tilde{\eta}\gamma o\zeta$ = colored, $\lambda\acute{\iota}\theta o\zeta$ = stone), i.e., the *“unconsolidated, weathered, broken rock debris, mineral grains, and superficial deposits which overlie the unaltered bedrock”* [Mayhew, 2009]. This layer results from various erosion processes in the harsh space environment that acted on the bedrock for geologic timescales. The composition of the regolith largely resembles the underlying bedrock [Jolliff et al., 2006], but it may also contain alteration products or material that originates from other parts of the surface or space. The regolith is also interspersed with boulders and rocks and may cover various geologic surface features formed by impact cratering, tectonics, or volcanism. Consequently, the regolith is the window to the structure and formation history of the whole planetary body. This chapter summarizes the current state of research about the surface structure and composition of the Moon, Mercury, and recently discovered airless exoplanets.

2.1 The Moon

2.1.1 A brief geologic history

The prevailing hypothesis is that the Moon resulted from a cataclysmic event 4.5 Ga ago in which a protoplanet of the size of Mars impacted the proto-Earth [Rossi et al., 2018]. The impactor disintegrated, partly recombined with the early Earth, and partly stirred up material from Earth’s crust and mantle. The debris re-accreted in Earth’s orbit and subsequently differentiated, resulting in a new body. During the differentiation of the primary silicate mantle, light plagioclase material rose to the top, eventually solidifying and forming the primary lunar crust [Rossi et al., 2018]. The theory assumes the Late Heavy Bombardment phase between 4.0 and 3.9 Ga ago, in which giant planet migration caused a disproportionally high influx of asteroids to the inner Solar System [Neukum, 1983]. In the lunar case, giant impacts caused several hundred to thousands of kilometers sized basins [Rossi et al., 2018]. Subsequent melting and volcanic events between 3.9–1.2 Ga ago [Hiesinger et al., 2003] flooded the impact basins with several layers of basaltic material that emerged from the lunar mantle that was still molten. These processes lead to a manifest morphologic and compositional dichotomy: The lunar highlands appear bright and comparatively rugged, with lots of craters from the Late Heavy Bombardment. The unaltered mineral composition is dominated by plagioclase feldspar and only small fractions of pyroxenes, olivine, and ilmenite [Taylor et al., 2010]. The mare regions are generally darker and younger than the highlands and exhibit more complex units due to 2.7 Ga of volcanism. The mare material is basaltic, with higher fractions of pyroxenes, olivines, and ilmenite than the highlands. For a thorough review of lunar geology and mineralogy, the author refers to the compendia following the Apollo mission [Taylor, 1982; Heiken et al., 1991]. For a detailed discussion of lunar highland composition, see Taylor et al. [2010]; for mare basalts, see Taylor et al. [2001], Basaltic Volcanism Study Project [1981], and Hiesinger et al. [2003]. After the Late Heavy Bombardment, impactor flux remained constant and produced craters up to this day, which can be statistically analyzed to determine the relative surface age [Neukum, 1983]. Comparatively, young crater systems are Copernicus and Tycho, which excavated bright material from the subsurface, forming extensive ejecta systems. On local scales, the lunar formation left traces visible as geologic features resulting from endogenic processes such as volcanism and tectonic activity. For a detailed discussion, see Taylor [1982], Heiken et al. [1991], Jolliff et al. [2006], Rossi and van Gasselt [2018], and Rossi et al. [2018]. Many aspects of the lunar formation and its surface are well understood and can be transferred and applied to other bodies, such as Mercury. The Moon can work as a reference object or test bench to answer questions about other airless bodies. However, some properties of the lunar surface remain to be understood. Despite this, global mineral abundance maps have yet to be generated, for example, with spectral unmixing techniques.

2.1.2 The weathered lunar regolith

The lunar surface does not consist of a solid crust but of a layer of so-called regolith that results from the harsh space environment acting on the lunar surface for billions of years. Right after the outer surface cooled down, asteroid bombardment crumbles the uppermost bedrock of the primary crust, resulting in a growing layer of rock fragments and mineral grains accumulating at the surface. This layer is termed regolith. For a definition, see Section 2 or Mayhew [2009]. The thicker the layer becomes, the better it shields the underlying bedrock from impacts such that the layer levels at approximately 4–5 m in lunar maria and 10–15 m in lunar highlands [McKay et al., 1991]. For a more detailed note on regolith characteristics and formation, see McKay et al. [1991].

Various physical and chemical mechanisms alter the regolith, commonly summarized under the umbrella term *space weathering*. The harsh space environment that acts on the lunar surface over geologic timescales processes the regolith into a complex layer of tiny mineral grains, rock fragments, alteration products, and a small fraction of implanted material. Space weathering mechanisms are numerous and complex and roughly form two groups. Pieters and Noble [2016] distinguish between micrometeorite impacts on the one hand and irradiation through atoms, ions, or electromagnetic radiation from the Sun or elsewhere on the other hand. Micrometeorite impacts shatter the mineral grains into smaller fragments (comminution). The impact energy can also vaporize or melt grains. Impacts may also deliver material from external sources (contamination) and displace material deeper into the regolith, known as *gardening a soil* [Pieters and Noble, 2016] — energetic atoms or ions from the solar wind cause sputtering, which alters the outermost components. Cosmic rays and solar ultraviolet radiation may also damage and melt the mineral grains. Energy from impacts and irradiation produces melt that may clog minerals and rock debris into agglutinate particles and other products that regularly amount to one-half of the lunar regolith volume fraction. Further, regolith may re-solidify into rocks, such as the lunar breccias.

What stands out most in the space-weathered lunar regolith is the spectral effects. Early studies of Gold [1955] already recognized that ejectas darken with time. Apollo samples revealed that the lunar regolith is darker and has shallower absorption features compared to crushed lunar rock [Cassidy and Hapke, 1975]. The precise reasons for these spectra sparked a longstanding debate [Hapke, 2001; Pieters and Noble, 2016]. Cassidy and Hapke [1975] proposed that solar wind sputtering and micrometeorite impacts lead to coatings of mineral grains that host tiny particles of elemental iron with varying sizes. The iron is reduced from the FeO of the minerals. TEM studies [Keller and McKay, 1993, 1997] confirmed the presence of very small nanophase iron (npFe^0) particles of approximately 1–10 nm in diameter that primarily accumulate in dispositional and amorphous rims and larger iron particles of several hundred nanometers in agglutinitic glass [Pieters and Noble, 2016] termed microphase iron (mpFe^0). Both types of iron (npFe^0 and mpFe^0) are summarized as submicroscopic iron (smFe^0). Hapke [2001] modeled the spectral effects of nanophase iron on lunar spectra with radiative transfer and effective media theory, finding that nanophase iron alone reddens the regolith spectra but induces slopes that are too steep. Laboratory work of Noble et al. [2007] and the radiative transfer modeling of Lucey and Riner [2011] indicate that a second group of larger iron particles (mpFe^0) could explain spectral darkening without reddening. However, the experimental particle sizes ($\approx$ 50 nm) and the simulatory particle sizes ($\approx$ 200 nm) disagree. However, the prevailing view is that nanophase iron particles in depositional rims cause spectral reddening, and larger particles, only present in agglutinates, are responsible for spectral darkening. Both particle types subdue the absorption bands and may be complemented with other optically active particles [Pieters and Noble, 2016]. Most recently, Yasanayake et al. [2018], Denevi et al. [2021], and Yasanayake et al. [2024] manually sorted agglutinates and mineral grains and measured the reflectance spectra of each fraction. Surprisingly, the spectral slope of the agglutinates was redder than the spectral slope of the mineral remainders. This finding contradicts the established view that the nanophase iron particles in the mineral rims are the predominant reason for reddening and large iron particles in the agglutinates. Further modeling appears to be necessary to understand this effect.

Space weathering simultaneously behaves as a *friend and a foe.* On the one hand, the regolith is a pristine record of the lunar bedrock's mineralogy and the surface formation and external mechanisms that acted on the Moon. Deciphering these effects helps understand the history of lunar formation and other airless bodies such as Mercury. On the other hand, the spectral effects obstruct the mineral spectra, complicating compositional and volatile analysis. Therefore, simulation models are a useful tool for approaching these tasks. Space weathering simulation models are reviewed in Section 3.4.5 and further developed in Chapter 6 of this thesis.

2.1.3 The lunar thermal environment

The Sun heats the lunar surface, which causes the Moon to heat up. Because the Moon has no atmosphere, there is no heat redistribution through convection and advection - only radiative and conductive heat transfer on smaller scales. Consequently, the Moon cycles through a strong temperature amplitude throughout the lunar day, which takes around 29.5 Earth days: At the lunar midday, the equatorial temperature rises to the radiative equilibrium temperature of around 390 K, gradually decreases during the afternoon due to increasing oblique illumination, and falls off after lunar sunset. How fast the surface cools after sunset depends on the local thermophysical properties, such as heat conductivity, which also carries information about the surface structure. Further, the Moon does not isotropically emit thermal radiation. Rough and highly isolating regolith leads to complex temperature distributions on lateral spatial scales of several millimeters to centimeters. The thermal emission caused by the different temperatures in these distributions superimposes and blends into a complex anisotropic thermal emission that depends on the illumination and viewing geometry. Those anisotropies are helpful for determining the surface roughness, but also disturbing for mineralogical analysis and must thus be compensated when calibrating any thermal emission data.

The Moon's surface temperature and thermophysical properties have been mainly inferred through in-situ measurements, remote sensing, and simulation studies. Astronauts of the Apollo 11 mission measured the temperature over one and a half days, well agreeing with predictions from the equilibrium temperature [Hickson, 1970]. The Apollo 15 and 17 astronauts deployed heat sensors that measured the temperatures and the heat flow at different depths for several years [Langseth et al., 1976; Nagihara et al., 2018]. Regolith heat conductivity was derived through modeling [Keihm and Langseth Jr., 1973; Langseth et al., 1976]. Later analyses showed that higher derived conductivity values might be due to regolith compaction near the probe's borehole [Grott et al., 2010]. Further, Paige and Siegler [2016] interpret higher heat flows as a local phenomenon likely caused by radiogenic elements. The Diviner lunar radiometer onboard the LRO has three compositional channels around $8\,\mu$m and several radiometer channels [Paige et al., 2010a] that measure the Moon's thermal emission and revolutionized the view of the lunar thermal environment. Most notably, Hayne et al. [2017] applied a complex sub-surface heat conduction model to Diviner data and mapped the thermal properties of the Moon. The thermal properties of the Moon appear remarkably homogeneous, which might be due to a rapid homogenization of the regolith due to impact gardening [Hayne et al., 2017]. The average global thermal conductivity at the surface is $7.4 \cdot 10^{-4}\,\mathrm{Wm^{-1}\,K^{-1}}$. When going deeper into the regolith, the conductivity increases up to $3.4 \cdot 10^{-3}\,\mathrm{Wm^{-1}\,K^{-1}}$, assuming a surface density of $1,100\,\mathrm{kg\,m^{-3}}$ and a density of $1,800\,\mathrm{kg\,m^{-3}}$ in a depth of 1 m. However, local features exhibit significant variations, such as crater ejecta that bear higher thermal inertia values. The younger the crater, the higher the thermal inertia. Further, thermal inertia positively correlates with rock abundance or geologic features where bedrock has been exposed.

Another remarkable property of airless planetary bodies is surface roughness and associated effects. Early observation of the lunar thermal phase curve in the infrared could not be brought in line with a simple thermal equilibrium model [Pettit and Nicholson, 1930]. Smith [1967], Buhl et al. [1968], and Sexl et al. [1971] repeated those observations and proposed a spherical crater model that reproduced the rugged lunar surface. Their results suggested that local shadows and altered temperature distributions could explain the lunar thermal phase curve [Wohlfarth et al., 2023]. The Apollo missions also revealed that the lunar regolith is rough [Gold, 1969]. Consequently, the Sun does not illuminate a flat surface from afar but a region where the incidence angle varies on small scales and thus receives different levels of incidence radiation. Because the regolith is isolating, it can sustain strong thermal gradients, and regions only millimeters away can exhibit temperatures that differ by several tens to hundreds of degrees Kelvin [Bandfield et al., 2015; Grumpe et al., 2019]. The resolution of a remote sensing detector is usually limited to several meters, so it cannot resolve the fine temperature distribution of the Moon. It measures the superposition of the thermal emissions that stem from vastly different temperatures. Shadowing, mutual heating, and scattering also play a role, leading to thermal emission, which is a complex function of the incidence and the viewing direction. It could also be the case that thermal gradients in the uppermost micrometers, such as those modeled by Millán et al. [2011], affect the directional characteristics of the emissivity, but that still needs to be thoroughly investigated. Bandfield et al. [2015] derived lunar surface roughness using Diviner nadir and off-nadir measurements. In the nadir setting, the detector sees the Moon from above, but the solar incidence angle may vary according to the local time. For small incidence angles, the brightness temperatures derived from Diviner channel four ($8.25\,\mu$m) and channel seven ($25–41\,\mu$m) are similar but deviate by up to 70 K as the incidence angle increases. Diviner ran an off-nadir campaign where the instrument performed so-called emission phase function (EPF) measurements - complex choreographies that measured the surface under various azimuth and emission angles up to 80°. Bandfield et al. [2015] then employed a thermal roughness model with a Gaussian slope distribution. A root mean square slope (RMSL) of 20° best fits the nadir observations, and an RMSL of 20-35° best explains twelve EPF measurements. Rubanenko et al. [2020] re-analyzed Diviner data and telescopic data of Sinton [1961], finding a bi-directional RMSL of $30.2\,^\circ \pm 5.9\,^\circ$ for maria and $36.8\,^\circ \pm 4.4\,^\circ$ for highlands.

2.1.4 Lunar hydroxyl and water

The historical assumption that the Moon hosts large water oceans was once eponymous for the lunar maria, but it turned out that they were, in fact, rocky and extremely dry. However, research in the past two decades revealed that the Moon does have water, albeit not to the same extent as once assumed [e.g. Clark, 2009; Pieters et al., 2009b]. The Moon hosts a complex hydroxyl (OH) and water (H_2O) cycle with constant exosphere regolith interactions, and evidence intensified that permanently shadowed regions at the lunar poles host water ice deposits. For the structure of polar ice deposits and the current state of research, the reader is referred to Cannon et al. [2020] and references therein. The diurnal surficial lunar water/hydroxyl cycle has been inferred from neutron spectroscopy and evaluation of infrared spectra. The current view is that solar wind implants protons into the lunar regolith and reacts with the regolith's oxygen, forming hydroxyl and water [Farrell et al., 2015]. Subsequent processes such as diffusion, photodissociation, and burial may explain diurnal variations of the associated spectral bands. The diurnal lunar hydroxyl/water cycle is subject to ongoing research because neither the abundance pattern nor the formation and circulation model is fully understood. For a current review, see Grumpe et al. [2019], Schörghofer et al. [2021], and Wohlfarth et al. [2023].

Lunar OH/H_2O can be detected by assessing spectral signatures of hydrogen via neutron spectrometry or the vibrational bands of OH via infrared spectroscopy. Early studies detected traces of hydrogen in the lunar poles from neutron fluxes of the Lunar Prospector Neutron Spectrometer [Feldman et al., 1998; Starukhina and Shkuratov, 2000], later confirmed by the Lunar Exploration Neutron Detector [Sanin et al., 2017]. Livengood et al. [2015] report a diurnal pattern in the global hydrogen from this dataset.

The stretching vibrations (v_1 and v_3) of the hydroxyl (OH) bond cause absorption lines around 3 μm [Tennyson, 2019]. Depending on the bounding state, the attached molecule, the surrounding conditions, and other factors, the absorption lines may shift or blend into one smooth and broad absorption feature. Consequently, a broad spectral absorption feature of lunar minerals around 2.8–3.0 μm has been interpreted as a sign of hydration [Pieters et al., 2009a; Li and Milliken, 2017; Wöhler et al., 2017; Bandfield et al., 2018; Grumpe et al., 2019; Schörghofer et al., 2021]. However, analyzing the feature alone can hardly distinguish between hydroxyl and water and determine the exact bounding mechanisms. Furthermore, lunar spectra longward of 2.5 μm exhibit a thermal emission signal, which obscures the OH-absorption band. Thus, thermal excess radiation must be removed to assess the absorption band under discussion. The resulting band depth and any derived hydroxyl/water abundance crucially depend on the thermal removal method, e.g., [Wöhler et al., 2017; Bandfield et al., 2018]. Despite these challenges, the 2.8–3.0 μm absorption band remains the best indicator of lunar hydration.

Sunshine et al. [2009] analyzed global data of the 1.05–4.5 μm spectrometer onboard the DeepImpact probe [Hampton et al., 2005] and removed the excess thermal radiation with the thermal model of Groussin et al. [2007]. They found a diurnal pattern with similar absorption depths in the lunar morning and evening and shallower absorption bands during midday. They do not find a compositional correlation with the absolute levels, but the depletion of the absorption bands is stronger in mare regions compared to highlands. The M^3 instrument onboard the Chandrayaan-1 probe acquired hyperspectral data from 461 to 2936 nm to map the mineralogical surface composition and to detect surficial lunar water/hydroxyl [Pieters et al., 2009a]. Pieters et al. [2009b] employed the thermal correction method of Clark [1979] and found that an OH/H_2O-absorption is only present for high latitudes approximately above 55°. The original dataset was reprocessed with three different approaches, consistently finding that Clark [1979] underestimates the temperatures, which leads to weaker absorption bands in the derived data. Li and Milliken [2016] devised an empirical thermal correction method based on an average global reflectance spectrum. Li and Milliken [2017] employed the correction of Li and Milliken [2016] and reported only a small absorption in the equatorial region but increasing absorption with latitude. Further, they found diurnal variations strongest for latitudes between $30 - 60°$.

They also reported that the absorption weakly changes between maria and highlands but appears to be associated with maturity. Bandfield et al. [2015] devised a thermal model with Gaussian roughness of $\overline{\theta} = 20°$, initially to explain the off-nadir measurements of the Diviner Lunar Radiometer. Bandfield et al. [2018] employed their model to correct selected regions of the M^3 measurements thermally. They detect an absorption band with only slight temporal and spatial variations and conclude the widespread presence of lunar hydroxyl/water. Wöhler et al. [2017] and Grumpe et al. [2019] developed an iterative thermal correction that uses a thermal roughness model with $\overline{\theta} = 9°$ and $\overline{\theta} = 20°$. They present global maps of the continuum-removed and integrated band-depth of the 2.8–3.0 μm absorption band. The band exhibits latitudinal, compositional, and diurnal variations — the band depth increases with latitude, most visible in the far-side highlands. The overall band depth is the strongest in the lunar morning, drops until the lunar midday, and rises in the afternoon. The cycle's amplitude is higher for mare regions compared to highlands. However, the band does not entirely vanish during midday, which suggests some form of permanently bound hydration component [Wöhler et al., 2017].

As reviewed by Wohlfarth et al. [2023], Honniball et al. [2020] used the Spectrograph at the IRTF facility (SpeX) instrument of the Infrared Telescope Facility (IRTF) at Hawaii [Rayner et al., 2003]. They corrected the excess thermal radiation that has previously been used to remove thermal radiation on asteroids [Rivkin et al., 2005; Reddy et al., 2009; Takir and Emery, 2012]. Honniball et al. [2020] find an OH/H_2O absorption feature across the entire Moon that varies with latitude, lunar time of day, and surface composition, which agrees with Wöhler et al. [2017], Grumpe et al. [2019], and Wohlfarth et al. [2023]. In a follow-up study, Honniball et al. [2021] used the Stratospheric Observatory for Infrared Astronomy (SOFIA) to measure the diagnostic H_2O-absorption around 6.1 μm caused by the v_2 bending vibration. The analysis confirms the presence of surficial lunar H_2O. However, given the local analysis, no global pattern can be derived.

The Imaging Infrared Spectrometer IIRS spectrometer onboard the Indian lunar probe Chandrayaan-2 [Chowdhury et al., 2020] currently maps the lunar surface from 0.8 to 5.0 μm. Further, the Lunar Trailblazer mission of the National Aeronautics and Space Administration (NASA) is scheduled for launch in early 2024 and carries the High-Resolution Volatiles Mineral Moon Mapper HVM^3 [Ehlmann et al., 2022] that will map the lunar surface from 0.6 to 3.6 μm. Both instruments access the full 2.8–3.0 μm absorption band, which will help understand the lunar hydration cycle.

2.2 Mercury

Mercury's origin remains elusive, and the planet's crustal formation and surface composition are not yet fully understood. However, the Mercury Surface, Space Environment, Geochemistry and Ranging (MESSENGER) spacecraft of NASA carried a battery of remote sensing instruments that imposed essential constraints on the formation and composition of the innermost planet. Future data from BepiColombo mission, which is a joint project of the European Space Agency (ESA) and the Japan Aerospace Exploration Agency (JAXA), will likely reveal more about Mercury's surface and composition, advancing our knowledge about the origin and the formation history of the innermost planet.

2.2.1 The elusive origin and a preliminary formation model

How Mercury came into place is still not understood. Ebel and Stewart [2018] summarize the current discussion given recent findings from MESSENGER: Mercury is dense, Mg-rich, Fe-poor, and anomalously reduced but not depleted in volatiles. To explain this, various hypotheses have been proposed, assuming a chaotic formation through one or many collisions or a more orderly formation inside a protoplanetary disk. No model conclusively explains the formation of Mercury. Likely, the planet is the result of multiple processes. In the future, numeric simulations that combine the collision dynamics with chemical and petrological models might prove helpful. Further, investigation of the innermost edge of protoplanetary disks may shed light on the conditions in these regions, which can be transferred to the formation environment of Mercury in the early solar system.

Hauck II et al. [2018] aggregate the findings derived from the MESSENGER data and discuss the current understanding of Mercury's global formation history, which is summarized below. The early crust formation can be accessed by looking at the low-reflectance material and the dichotomy between the smooth and the intercrater plains. The Mercury Dual Imaging System (MDIS) revealed that extensive regions in low and southern latitudes host exceptionally dark material termed Low-reflectance material (LRM) [Robinson et al., 2008; Denevi et al., 2009; Murchie et al., 2015; Klima et al., 2018]. The darkening agent is associated with impact ejecta [Denevi et al., 2009; Klima et al., 2018] and is inferred to be elemental carbon, likely in the form of graphite [e.g. Klima et al., 2018]. Chondritic carbon was buoyant enough to form a flotation crust on Mercury's early magma ocean [Vander Kaaden and McCubbin, 2015]. After solidification, Mercury experienced extensive resurfacing through volcanism, which buried the graphite layer under several kilometers of magma — subsequent impacts unearthed parts of the LRM that blended into the volcanic deposits [Vander Kaaden and McCubbin, 2015; Denevi et al., 2018]. However, the LRM was not thoroughly mixed with the rest of the material. Experimental analysis and discussion of planetary differentiation models suggest that Mercury once had a magma ocean that underwent differentiation and later experienced remelting at different layers, which explains compositional heterogeneities between volcanic deposits [Vander Kaaden and McCubbin, 2015]. Mercury's surface can be divided into two geologic units, i.e., smooth plains or intercrater plains [Denevi et al., 2018]. The smooth plains are sparsely cratered and exhibit distinct boundaries with surrounding regions. They are located mainly in the northern hemisphere in the northern smooth plains and in and around the Caloris basin. Smooth plains are assumed to result from effusive volcanism that floods the existing topography [Hauck II et al., 2018, and references therein]. The underlying surface acted as an embankment for the magma floods and left sharp boundaries. Ghost craters are a typical example of such a flooded structure. Crater chronology suggests that the largest units in the Northern Smooth Plaines, Caloris, and Rembrandt formed 3.8–3.7 Ga ago, and the effusive volcanism of the smooth plains ceased 3.5 Ga ago [Hauck II et al., 2018, and references therein]. Intercrater plains are less understood but likely result from effusive volcanism 4.1–4.0 Ga ago and subsequent impact processes [Hauck II et al., 2018, and references therein]. They might be similar to smooth plains, only older, thus heavily cratered, and more textured. This view agrees with the observation that compositional heterogeneity does not always correlate with morphological heterogeneity [Weider et al., 2015]. The end of effusive volcanism largely completed crust formation. However, local events continued to shape Mercury's surface. Explosive vulcanic events continued up to approximately 1 Ga ago, forming, for example, pit craters. The presence of contractional features indicates that Mercury shrunk by several kilometers in diameter [Byrne et al., 2018] and shrinking carried on within recent geologic times [Man et al., 2023], which makes it the only other tectonically active body besides Earth.

2.2.2 Constraints on the surface mineralogy

Mercury's mineralogy needs to be better understood. Elemental abundance measurements and spectral reflectance measurements impose constraints that paint the picture of a magnesium-rich, iron-poor silicate mineralogy that formed under reducing conditions. McCoy et al. [2018] present a geochemical analysis of Mercury based on the X-ray Spectrometer and the Gamma-Ray and Neutron-ray Spectrometer onboard MESSENGER. The instruments mapped the elemental abundance of U, K, and Th and the elemental ratios of Na, Mg, Al, S, Cl, Ca, Ti, Cr, Mn, Fe, and C to Si. These results allow constraining Mercury's mineralogy and define geochemical terranes. Mercury exhibits a Mg-rich but Fe-poor crust that likely formed under reducing conditions and is depleted in volatiles [McCoy et al., 2018]. Elemental mapping does not yield a mineralogical composition, but the Cross Iddings, Pirsson, Washington (CIPW) normative calculation method can estimate possible mineralogy from the elemental abundances. McCoy et al. [2018] find high levels of pyroxene, some olivines, and sulfides and construct four distinct and spatially continuous geochemical terranes for $> 20°$ latitude: the Northern Terrane, the Caloris Interior Plains Terrane, the High-Magnesium Terrane, and the Low-Fast Terrane. Murchie et al. [2018] summarize and discuss the spectral reflectance constraints of Mercury. As already anticipated by telescopic studies [e.g. Sprague et al., 2007], it was finally confirmed by the MDIS instrument onboard the MESSENGER spacecraft: Mercury is comparatively dark, red-sloped, and lacks diagnostic absorption features in the visible and near-infrared (VNIR). A reduced iron-poor silicate mineralogy explains the absence of any strong absorption feature in the MDIS data [Izenberg et al., 2014]. A subtle absorption feature in the Mercury Atmospheric and Surface Composition Spectrometer (MASCS) at 0.6 μm, and the neutron spectroscopy data analysis indicated that the hermean darkening agent is likely carbon in the form of graphite [Klima et al., 2018]. Unlike the Moon, where a strong geomorphological and spectral dichotomy is apparent between maria and highlands, the spectral reflectance variations are more ambiguous at Mercury. The slope and brightness of the reflectance spectra vary across Mercury.

The spectra are comparatively bright in the smooth volcanic plains and exhibit dark regions at lower latitudes and in the south. Murchie et al. [2018] defined five reflectance units: Red units, high reflectance material (HRP), intermediate plains (IP), low reflectance blue plains (LBP), and LRM. Besides the Caloris basin and the northern plains, reflectance and geomorphology only weakly correlate. Different regions only differ in spectral slope and brightness. Some regions exhibit exceptionally dark material. Mercury further hosts some remarkable phenomena that sparked subsequent research: Radar bright deposits, which have been attributed to water ice in permanently shadowed regions, have been found in the north and south Pole. For a review, see Chabot et al. [2018]. MESSENGER further found surprising structures termed hollows - depressions with an undulating boundary and apron of bright material. They are reviewed by Blewett et al. [2018].

Domingue et al. [2014] review how space weathering interacts with Mercury's surface: The small distance to the Sun and the different magnetic fields change the makeup of space weathering mechanisms on Mercury compared to the Moon. Mercury's regolith likely experienced more overturn and underwent higher melting, vaporization, and irradiation levels. The character of submicroscopic iron is still poorly constrained. Mercury generally hosts a mineralogy with a very low FeO content [e.g. Izenberg et al., 2014], but space weathering may have still formed reduced iron in silicates into small particles of elemental iron [Domingue et al., 2014]. Strong space weathering has likely altered Mercury's surface, possibly more substantial than the Moon, and left a layer that obscures remote sensing compositional analysis.

2.2.3 Future investigations

The compositional studies and the formation model are marked with considerable uncertainty that only new data can overcome. The BepiColombo mission is a joint mission of the European Space Agency (ESA) and the Japan Aerospace Exploration Agency (JAXA) and comprises two independent orbiters. The Mercury Planetary Orbiter (MPO) and the Mercury Magnetospheric Orbiter (MIO), formerly MMO, are on their way to planet Mercury and arrive in December 2025. The MPO carries several instruments to acquire more data and constrain the mineralogy. For this purpose, the Mercury Imaging X-ray spectrometer (MIXS) and the Mercury Gamma-ray and Neutron Spectrometer (MGNS) will map the elemental composition and provide better coverage of the southern hemisphere. The MErcury Radiometer and Thermal Infrared Spectrometer (MERTIS) is planned to acquire hyperspectral data from 7–14 μm where diagnostic mineral absorption features are located unaffected by an iron-poor silicate mineralogy [Hiesinger and Helbert, 2010; Hiesinger et al., 2020]. MERTIS aims are to identify rock-forming minerals, map the mineralogic composition, and derive the thermophysical parameters of Mercury's surface [Hiesinger and Helbert, 2010; Hiesinger et al., 2020]. MERTIS will likely reveal more about the space weathering products on the uppermost regolith layer. The results of MERTIS are expected to revolutionize the understanding of Mercury's mineralogy, thus imposing crucial constraints on global evolution. The thermal model presented in this thesis will be crucial for calibrating MERTIS spectra.

2.3 Minor bodies, dwarf planets, Moons, and exoplanets

Many other airless planetary bodies host a regolith layer, bear a water/hydroxyl cycle, and still hide many secrets. Recent missions visited asteroids Ryugu and Bennu, the double asteroid system Didymos and Dimorphos, comets like 67P/Churyumov-Gerasimenko, and dwarf planets Ceres and Pluto. Future missions will return to the Moon and visit Phobos, Deimos, Psyche, and the Jovian and Saturnian moons. All these bodies are not in the scope of this thesis, but the methods developed here can, in principle, be adapted to these targets.

Extrasolar planets were discovered more than twenty-five years ago and sparked a whole new scientific field that currently delivers one pioneering discovery after another. In recent years, three exoplanets, namely LHS 3844b, TRAPPIST-1b, and TRAPPIST-1c, have been discovered that likely have no atmosphere [Kreidberg et al., 2019; Diamond-Lowe et al., 2020; Greene et al., 2023; Zieba et al., 2023]. The name LHS derives from the Luyten Half-Second star catalogue, and TRAPPIST comes from the Transiting Planets and Plenetesimals Small Telescope at the La Silla observatory in Chile. Almost nothing is known about their planetary surfaces, but new JWST measurements may provide clues about the surface structure and composition. This thesis presents thermal models that help analyze the surface of LHS 3844b with JWST data and help answer whether this planet hosts a regolith similar to what we know from the Solar System.

Chapter 3

Methods for planetary infrared spectrosopy

As discussed in the previous section, the regolith is the key to a planetary body's structure and formation history. Consequently, one aim of modern planetary remote sensing is to infer compositional and structural information about the planetary regolith, which is possible with several spectroscopic techniques. Neutron, Gamma-ray, and X-ray spectroscopy primarily detect elemental abundances with a coarse resolution, as reviewed by Prettyman et al. [2019]. These techniques are not part of this thesis. Instead, the focus lies on infrared spectroscopy, which measures a planet's reflected and thermally emitted radiation that contains information about the mineralogical composition. This chapter introduces the fundamental theory and practical techniques for reflectance and emittance spectroscopy and briefly summarizes how to access the planetary regolith's mineralogy, structure, and thermal properties.

Theoretically, planetary infrared spectroscopy requires a sound understanding of the physical interaction processes between electromagnetic waves and planetary regolith. The Sun (or host star) emits incoherent electromagnetic waves that reach the Sun-facing parts of a planetary body. The incoming electromagnetic waves interact with the mineral grains of the regolith. Essentially, the surface partly scatters and partly absorbs the incoming light. Quantum mechanical light-matter interactions generally produce spectral absorption features as diagnostic markers for individual mineral components. Further, complex light scattering processes between individual mineral grains lead to anisotropic light reflection that varies with regolith properties such as packing density, particle size, and many more. Consequently, the reflected light varies directionally and with wavelength. The absorbed light, however, heats the regolith, which warms up and eventually emits thermal radiation. Thermal emission also varies according to wavelength and direction. The overall spectral shape indicates the surface temperature, and the individual absorption bands stem from the mineralogy. The directional variations result from surface roughness and regolith structure, and thermal conductivity governs temporal variation.

From a practical perspective, planetary spectroscopy requires detectors that translate electromagnetic radiation to actual observables and viable models and techniques that allow correctly interpreting the measurements of the planetary body and relating them to compositional, structural, and thermal properties. Reflected and thermally emitted light are often partially superimposed and must thus be disentangled for proper analysis.

This chapter introduces the fundamental theory and practical techniques for airless bodies' infrared reflectance and emittance spectroscopy. Section 3.1 establishes the microphysical foundation of planetary remote sensing and introduces the fundamental observables and the general framework of planetary remote sensing 3.2. Light scattering and thermal emission each have their own theory section (Section 3.4 and Section 3.5).

3.1 Observables and electromagnetic foundation of remote sensing

In principle, there is a phenomenological and a microphysical approach to define the radiometric observables of (planetary) remote sensing. The phenomenological approach to radiation has been prevalent for more than a century and serves as a simple yet problematic foundation of remote sensing theory. As Mandel and Wolf [1995] state, the branch of (phenomenological) radiometry and radiative transfer theory *developed quite independently of modern theories of radiation, and in spite of their long history, their foundations have not been fully clarified*. Mishchenko et al. [2006], Mishchenko [2014a], and Mishchenko [2014b] discuss why the phenomenological approach is incompatible with fundamental physics and rigorously derive radiative transfer theory and related detector observables from classical electrodynamics that can be regarded as state-of-the-art. The author shortly sketches the microphysical approach and attempts to link other light scattering theories, including less rigorous planetary reflectance models, within the correct frame.

Astronomic objects emit and reflect electromagnetic waves that carry information about the object's temperature, composition, and many other properties. Unfortunately, the electromagnetic field in the optical and infrared region fluctuates with frequencies in the THz region, which are extremely difficult to measure directly. Further, averaging the field quantities over a time interval much larger than the wave period yields a vanishing result because of the time-harmonic nature of light waves. Consequently, classic optical devices such as telescopes and remote sensing detectors cannot immediately measure the electromagnetic field's instantaneous state (magnitude, orientation, polarization). Instead, a detector acts as a wavefront filter. The wavefront passes through the detector entrance, spanning a small solid angle $\Delta\Omega$, and falls onto the optically active sensor with area ΔA. The sensor finally outputs a signal proportional to the time-averaged intensity of the collected waves. Depending on whether the detector resolves the object or not, the observed signal has two different meanings. For a detailed discussion on measuring the directional energy flow of electromagnetic waves, see Chapter 11 in Mishchenko [2014b].

In the case of a distant light source such as a star, the target's angular resolution is smaller than the acceptance solid angle of the detector, and hence, the target cannot be resolved. The signal strength measured by the detector is proportional to the intensity of the field at the detector, multiplied by the sensitive detector area. The signal decreases with $\propto 1/r^2$ as the source moves away from the detector. The measured quantity has the dimension of energy flux per unit area [$\mathrm{W\,m^{-2}}$] and is denoted with J_0. The spectrally resolved quantity is termed spectral irradiance or coherent specific intensity in the notion of [Mishchenko et al., 2006], is denoted with J, and has the unit [$\mathrm{W\,m^{-2}\,m^{-1}}$].

In the case of a resolved light source, such as a planetary surface, the detector observes only a fraction of the target. If the detector moves farther from the target, the received intensity decreases, but the detector also collects radiation from a larger area. Both effects cancel out such that the detector receives a constant signal. This effect is termed *conservation of radiance* and holds regardless of the scaling performed by the optical system, the distance between the source and detector, and the aperture size. For a detailed discussion, see Smith [2000] (pp. 225–227) and also Hapke [2012] (pp. 186–187). Conservation of radiance can intuitively be understood: I could observe my wood-chip wallpaper with a magnifying glass, and it would appear as bright as if I stood meters away. Because the target is resolved, the received intensity depends on the size of the solid angle spanned by the detector. Consequently, the measured quantity has the dimension of energy flux per unit area per unit solid angle [$\mathrm{W\,m^{-2}\,sr^{-1}}$]. It is termed diffuse intensity or radiance and is denoted by I_0. If the detector spectrally resolves the measured light, the measured quantity has the dimension [$\mathrm{W\,m^{-2}\,m^{-1}\,sr^{-1}}$]. It is then termed diffuse specific intensity or spectral radiance and denoted by I. The quantities I_0 and I encode the principle of how optical devices work and represent the primary observable of (planetary) remote sensing. Note that the diffuse specific intensity, as clarified by Mishchenko et al. [2006], can only be understood as the energy transport averaged over a sufficiently long period.

An electromagnetic wave has a specific state of polarization that cannot be determined by measuring only the intensity. Stokes introduced a formalism (see, e.g., Hapke [2012]; Mishchenko et al. [2006]) that collects four specific intensities into a vector. Each component passes a linear polarizer that lies in the plane perpendicular to the direction of propagation with a specific orientation ($0°, 90°, +45°, -45°$, measured with respect to a vector in that plane, usually the laboratory coordinate system [Chapter 2 Mishchenko et al., 2006]). Together, the vector components describe the polarization state of the entire wave. For a detailed mathematical description, see Section 3.4.1.

It is important to note that the observable I has been defined through a time-averaged electromagnetic field that enters a detector. This modern definition must be contrasted against the older phenomenological approach still prevalent in remote sensing literature, which uses the same notation but does not have the same meaning. The *phenomenological* radiance in the remote sensing literature is derived from phenomenological radiometry that postulates a field that gives the instantaneous directional radiative power at any given point in space at any time. The radiative flux that falls into the detector opening $\Delta\Omega$ onto the sensor ΔA is then defined as the phenomenological radiance. Mishchenko [2014a,b] pointed out that postulating such a field with instantaneous directional power flow and any derivative quantities, such as the phenomenological radiance, is unphysical. Further, the phenomenological radiance might be identified with the time-averaged Poynting vector of the field integrated over the detector opening. That is not the case either because the detector primarily filters the wavefronts, as clarified by Mishchenko [2014a,b]. Even though the rigorous definition of the diffuse specific intensity I implies that it does not necessarily equal the time-averaged Poynting vector, it helps determine the energy budget of a scattering scenario and understand the directional scattering effects. Thus, the quantities I and J are well suited to characterize a resolved planetary surface illuminated by a distant stellar source. This thesis often uses the term radiance for brevity instead of diffuse specific intensity but always refers to the modern rigorous definition in contrast to the old phenomenological approach.

Different schemes exist that define and subdivide the infrared wavelength region. This thesis adheres to the wavelength regions defined in the ISO 20473:2007 standard. The visible ranges from 380–780 μm, the near-infrared (NIR) ranges from 0.78–3 μm, and the mid-infrared (MIR) comprises 3–50 μm. The mid-infrared (MIR) is also termed thermal infrared (TIR).

3.2 Standard scenario of planetary remote sensing

If an infrared detector points at an airless planetary body and resolves the target, the device measures the diffuse specific intensity that emerges from the surface. For the most generic case of a horizontally stratified medium, the total diffuse specific intensity Stokes vector $\mathbf{I}$ is modeled as the superposition of the specific intensity from solar reflection and thermal emission:

$$\mathbf{I}(i, e, \psi, \lambda) = \underbrace{\mathbf{R}_{\mathrm{m}}(i, e, \psi, \lambda)\mathbf{J}_0(\lambda)}_{\text{reflected light}} + \underbrace{\mathbf{E}_{\mathrm{m}}(e, \lambda)\mathbf{I}_{\mathrm{t}}(i, e, \psi, \lambda)}_{\text{thermal emission}}. \tag{3.1}$$

The vector $\mathbf{J}_0$ is the specific intensity of the stellar illumination source, usually the Sun or a host star. The matrix $\mathbf{R}_{\mathrm{m}}$ describes the surface's spectral and angular reflectance and polarization behavior. The vector $\mathbf{I}_{\mathrm{t}}$ is the specific intensity of a surface for unit emissivity, and the matrix $\mathbf{E}_{\mathrm{m}}$ characterizes the angular and spectral emissivity behavior of the surface. All quantities $\mathbf{I}$, $\mathbf{R}_{\mathrm{m}}$, $\mathbf{J}_0$, $\mathbf{E}_{\mathrm{m}}$, and $\mathbf{I}_{\mathrm{t}}$ depend on the wavelength λ. Figure 3.1 shows the spatial relations of the incidence angle i, the emission angle e, and the azimuth angle ψ. A useful assumption is that spectrometers are polarization agnostic in that they only measure the total intensity, which equals the first component of the Stokes vector. This assumption might not hold for every operation scenario, especially in Earth science, where polarization correction is sometimes required [e.g. Meister et al., 2005]. For planetary surface analysis, however, it is a standard approach, and the Equation 3.1 becomes a scalar equation, which reads

$$I(i, e, g, \lambda) = \underbrace{r_{\mathrm{d}}(i, e, g, \lambda)J_0}_{\text{reflected light}} + \underbrace{\epsilon_{\mathrm{d}}(e, \lambda)X(i, e, g, \lambda)}_{\text{thermal emission}}. \tag{3.2}$$

In this notation, the source J_0 is given by the irradiance of the host star. The bi-directional reflectance function r_{d} commonly models the reflected component and depends on the illumination geometry and the wavelength. It is often sufficient to use the phase angle g instead of the azimuth angle ψ. The absorbed and re-emitted radiation is the product of the emissivity ϵ_d and the blackbody radiation X, which models the spectral emission for unit emissivity. In the most general case, X may not be a Planck function but could be the superposition of many. The emissivity ϵ_d mitigates X's directional and spectral characteristics of X, depending on the material properties.

The detector measures the superposition of reflected and thermally emitted spectral radiance. The solar temperature controls the spectral bulge of J_0, and the surface temperature controls the spectral bulge of X. Consequently, there are spectral regions in which only solar reflection dominates, only thermal emission dominates, or reflection and emission mix. This thesis takes an integrated view of combined reflectance and emittance spectroscopy and explicitly treats purely reflectance, purely emission, and the transition regions with reflected and thermally emitted light. To illustrate the spectral context, Wohlfarth et al. [2023] provided a plot extended to the spectral regions of all instruments discussed in this thesis. For illustration, the author models the lunar surface at 1 AU, constant reflectance of $r_\mathrm{d} = 0.1$, constant directional emissivity of $\epsilon_\mathrm{d} = 0.95$, and constant bolometric hemispherical emissivity $\bar{\epsilon}_\mathrm{h} = 1$. The solid black line in Figure 3.1 (left) indicates the spectrum of the reflected component, and the solid red line represents the thermal emission.

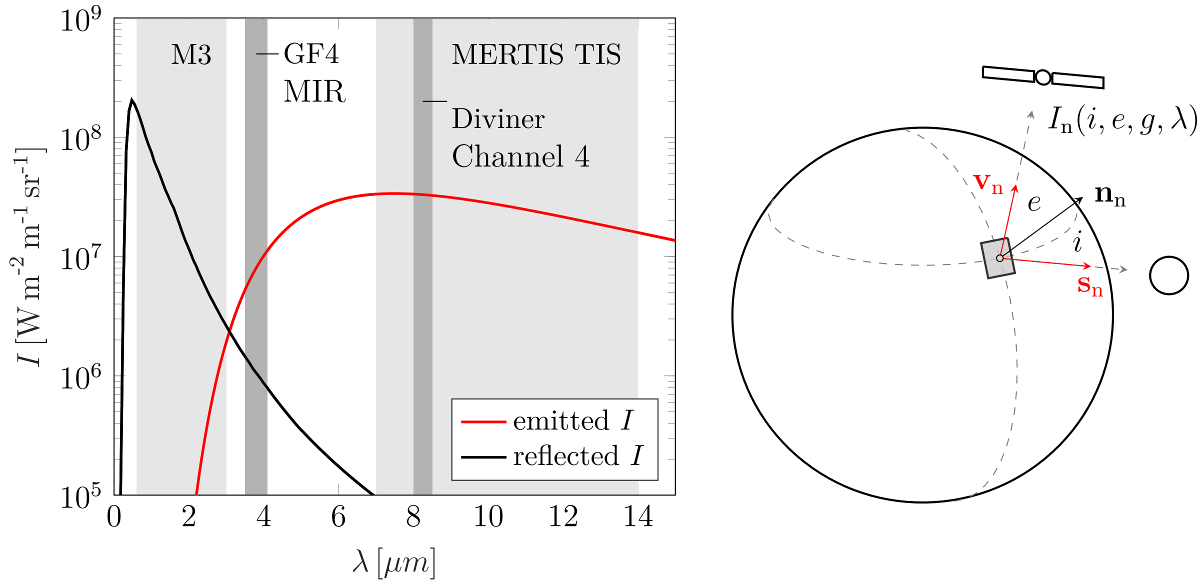

Figure 3.1. Spectral and spatial relationships for thermal modeling. Left: Reflected solar spectral radiance (black) and thermally emitted spectral radiance (red) emerging from the subsolar point at lunar noon, given a constant reflectance of $r_\mathrm{d} = 0.1$, a directional emissivity of $\epsilon_\mathrm{d} = 0.95$, a bolometric hemispherical emissivity of $\bar{\epsilon}_\mathrm{h} = 1$, and a directional-hemispherical albedo of $A_\mathrm{dh} = 0.07$. The spectral regions for the M^3 instrument (0.6–3.0 μm), GF-4 (3.5–4.1 μm), MERTIS thermal infrared spectrometer (7–14 μm), and Diviner channel 4 (8.10–8.40 μm) measure different combinations of reflected and emitted radiation. Right: Geometric relations. The quantity of interest is the spectral radiance I_n that emerges from the n^th facet. The vectors $\mathbf{s}_\mathrm{n}$, $\mathbf{v}_\mathrm{n}$, and $\mathbf{n}_\mathrm{n}$ denote the illumination vector, the viewing vector, and the surface normal vector at the facet. The incidence angle i spans between $\mathbf{n}_\mathrm{n}$ and $\mathbf{s}_\mathrm{n}$, the emission angle e between $\mathbf{n}_\mathrm{n}$ and $\mathbf{v}_\mathrm{n}$. The phase angle g is measured between $\mathbf{s}_\mathrm{n}$ and $\mathbf{v}_\mathrm{n}$ (not displayed), and the azimuth ψ is the angle between the projection of $\mathbf{s}_\mathrm{n}$ and $\mathbf{v}_\mathrm{n}$ onto the gray plane (not displayed). Figure and caption adapted from Wohlfarth et al. [2023].

3.3 Celestial mechanics and planetary shape models

Reflected and thermally emitted light depends on the illumination, viewing directions, and the light source's distance. These quantities, in turn, depend on the position of the target body, the Sun, and the observer in space. If the target is disk-resolved, the shape of the planetary body (usually spherical, but more anisotropic for some asteroids) and the local topography must also be considered. Celestial mechanics are not part of this thesis. For an introductory text, see Curtis [2015]. All practical applications discussed in this thesis draw the solar, target, and observer positions either from the Spacecraft, Planet, Instrument, Camera-matrix, Events (SPICE) system [Acton, 1996] of the corresponding mission or the Horizon ephemeris (`https://ssd.jpl.nasa.gov/horizons/`) provided by NASA. This information allows constructing a solar illumination vector $\mathbf{s}$ that points from the target toward the Sun and a viewing vector $\mathbf{v}$ that points from the target toward the observer at the time of the observation.

As shown in Figure 3.1 (right), a planet can be modeled with N surface elements, each bearing an individual normal vector $\mathbf{n}_\mathrm{n}$ that characterizes the surface's orientation. Adding topography onto a large body such as the Moon and Mercury requires superimposing a digital elevation model (DEM) onto a sphere with the average planetary radius. The author derived a method to compute the normal vector for a DEM on a spherical planet, as outlined in Appendix A. A triangular mesh might better suit smaller bodies that significantly deviate from a sphere, such as comets or asteroids. Section 4.9 lists the DEMs used in this thesis.

3.4 Light scattering and reflectance theory

There is no light scattering model that is physically rigorous and viable for photometric and compositional studies simultaneously. Instead, the field is marked by methodic pluralism, which is dominated mainly by two approaches.

One branch attempts to start from the Maxwell equations and rigorously solves the electromagnetic scattering problem for a planetary regolith. Numerical solutions can hardly be carried out in a reasonable time, and *spherical cow problems* often hamper analytic models. These approaches, however, helped to understand the physical scattering processes inside the regolith for particular scenarios like polarization, coherent backscattering, and energy transport.

The other branch derived closed-form reflectance models, such as the Hapke or the Shkuratov model that compute the angular scattering behavior from specific material parameters. These models work well for photometric and compositional studies but have been repeatedly contested to have specific theoretical issues. Therefore, these reflectance models should not be regarded as a physically rigorous description of planetary light scattering that directly reveals the *true nature* of the regolith. Instead, the models should be considered viable approximations useful in specific contexts, such as photometry, comparative planetological studies, and compositional analysis. Future research must bridge the gap between rigorous but impractical models on the one hand and handy but actually untrue models on the other hand.

This section sketches the relationship between theoretical electrodynamics and radiative transfer theory and reviews the current rigorous light scattering models and the photometric models that are relevant to this thesis. The explanations come with a discussion of the scope and applicability of the methods.

The Maxwell equations comprise a set of four coupled partial differential equations that relate the electric and magnetic field quantities and their temporal and spatial derivatives. Together with the constituting relations and the Lorentz force, they fully describe the phenomena of classic electrodynamics. If the geometry, the material parameters, and the boundary conditions of any scenario are known in advance, Maxwell's equations yield the distribution of the electromagnetic field and its state. Consequently, the equations govern the wave propagation in any light-scattering scenario. However, finding solutions remains tedious, such that early works concentrated on simple spherical particles (Mie scattering) or abandoned electrodynamics and worked with the infamous radiative transfer equation. Later research addressed particle groups and nonspherical particles and bridged the gap between classic electrodynamics and radiative transfer theory. Only recently have computers been able to solve equations for realistic scenarios completely. Grynko et al. [2020] and Grynko et al. [2022] numerically solved Maxwell's equations for densely packed irregular particles resembling a planetary regolith. The resulting fields elucidate the scattering processes in the upper regolith that cause the energy transport between grains and the positive and negative branches of polarization. The uppermost layer of the regolith partly scatters the incoming electromagnetic waves — single scattering at the surface causes the positive branch of polarization. Grynko et al. [2022] inferred that coherent double scattering at the uppermost layer likely explains the negative branch of polarization — some parts of the incidence wave travel inside the regolith. The electromagnetic field appears localized between the grains and partly percolates along channels into the regolith [Grynko et al., 2020]. This transport mechanism contradicts ray optics, in which single and multiple scattering paths occur, or radiative transfer theory, in which an elementary scattering volume redistributes the radiance inside the medium. Further, Grynko et al. [2020] conclude that the elementary scattering volume is not valid for particulate media, thus falsifying the application of radiative transfer theory to planetary regolith. Grynko et al. [2020, 2022] solved the forward problem and related the material parameters and geometry to the electromagnetic waves' angular distribution and spectrum. However, photometric and compositional studies require inversion techniques to infer geometric or material properties from the angular and spectral intensity. It is unclear how to carry out the inversion and which parameters should characterize the regolith. Further, the numeric solver devours plenty of computational resources. Even for single-size parameters and single illumination geometries, running on the high-performance computers of the John von Neumann Institute for Computing and the Jülich Supercomputing Centre takes weeks. Even if inversion techniques existed, the available computational power limits spectral and multi-angular studies. In conclusion, the full-field method reveals the physical processes in the upper regolith but has yet to be suited for practical use.

Solving the Maxwell equations entails a high computational effort such that analytic models emerged. The Volume integral equation, the Lippmann-Schwinger equation, and the Foldy-Lax equations canonify the general scattering problem. Mishchenko et al. [2006] classify various scattering cases and review how to solve them. The Lorentz-Mie theory [Mie, 1908] tackles single spherical particles, and the T-matrix formalism [Waterman, 1965; Mackowski and Mishchenko, 2011] addresses multiple interacting particles of arbitrary shape. However, the T-matrix method becomes computationally expensive for larger clusters and multiple wavelengths, and model inversion is not well-established for these analytical methods. The mathematical branch of inverse scattering theory [Cakoni and Colton, 2013] attempts to invert comparable problems but has yet to provide any practical methods that could be transferred to planetary surfaces. Further, analytic light scattering theories are hampered by idealizations often referred to as *spherical cow problems*.

Radiative transfer theory (RTT) describes the energy propagation in tenuous media such as stellar or planetary atmospheres. Though viable for many practical applications, radiative transfer theory remained a phenomenologic island somewhat detached from *"mainland"* physics that lacks fundamental theory (Preisendorfer [1965] in Mishchenko [2014a]). Mishchenko [2003], Mishchenko et al. [2006], Mishchenko [2014a], and Mishchenko [2014b] clarified the physical foundations and showed that the vectorized radiative transfer equation (RTE) directly follows from the Foldy-Lax and the Maxwell equations. Planetary surfaces are not tenuous because the mineral grains are in contact, so strictly speaking, the RTE does not hold. Dense media radiative transfer simulations for planetary surfaces, however, remain relatively scarce, and only recently, Ito et al. [2018] applied dense packing modifications to model infrared spectra of laboratory regolith and Kolokolova et al. [2020] modeled infrared spectra of icy moons.

A successful yet controversial approach has existed since the early sixties. The scalar RTE was found to describe the angular scattering behavior of planetary surfaces reasonably well, treating the regolith as if it were a medium of sparse single scatterers. Most notably, the work of Hapke, starting in the early sixties for the Apollo mission, established a closed-form model that relates a set of parameters, the Hapke parameters, to the measured diffuse specific intensity. Other photometric models, such as the Lommel-Seeliger law, the Buratti-Veverka model [Buratti and Veverka, 1985], the Lumme-Bowell model [Lumme and Bowell, 1981], and the Kaasalainen-Shkuratov model [Kaasalainen et al., 2001; Shkuratov et al., 2011], also follow from the RTE but build on their own individual assumptions. The advantage of closed-form models is that they are relatively simple compared to rigorous light-scattering approaches. However, issues arise when relating the model parameters to the actual physical properties of the regolith. Hapke [1981, 2012] originally derived the model from the Ambratsumian invariance principle to describe the bi-directional reflectance of a plane parallel homogeneous atmosphere. The single scattering contribution is modeled anisotropically, but the multiple scattering component was assumed to scatter isotropically [Hapke, 1981] (isotropic multiple scattering approximation). Over the years, Hapke introduced a correction for macroscopic roughness [Hapke, 1984], the shadow-hiding opposition effect (SHOE) [Hapke, 1986], the coherent backscatter opposition effect (CBOE) [Hapke, 2002], the anisotropic multiple scattering approximation (AMSA) [Hapke, 2002], and a model for surface porosity [Hapke, 2008]. The full Hapke model is one equation that computes the bi-directional reflectance from three geometrical parameters and up to nine parameters that describe the surface properties. The Hapke model has widely been used in the planetary science community but has several caveats that limit its power. The practitioner must be aware of these aspects to avoid overinterpretations.

The Hapke model has been tested multiple times, but the results were mixed. It was questioned whether the parameters relate meaningfully to the physical characteristics of the planetary regolith and whether it has any advantage over a purely empirical approach [Shkuratov et al., 2012]. Mishchenko [1994] argued that given the size of regolith particles, the phase function of mineral grains must be forward scattering. This prediction contradicts the results from the Hapke model, which consistently finds phase function parameters of laboratory and lunar regolith that describe backward scattering. Mishchenko [1994] further concluded that the phase function parameters are likely an artifact of an insufficient model. Hapke [1996] responded that experiments with mineral powders indicate backward scattering, and the phase function instead describes the scattering properties of a fundamental volume element consisting of multiple closely packed particles. Some works (e.g., Ito et al. [2018]) assume such a fundamental volume element, but simulations of Grynko et al. [2022] ruled out its existence. Shepard and Helfenstein [2007] compared the Hapke model with particulate laboratory samples and retrieved individual Hapke parameters. They find that the single scattering albedo is *"the most robust parameter"* in the Hapke model [Shepard and Helfenstein, 2007]. Still, the Hapke parameters are, in general, neither independent nor can they directly be related to the physical properties of the regolith [Shepard and Helfenstein, 2007]. However, this study does not consider advanced retrieval methods such as modern Markov chain Monte Carlo approaches and does not systematically assess the mutual parameter dependency. Shkuratov et al. [2012] also compared the Hapke model with laboratory samples. They list fifteen shortcomings of the model that question its physical plausibility and the Hapke parameters' meaning concerning particulate media's measurable properties. In a subsequent response paper, Hapke [2013] acknowledges that the Hapke model utilizes approximations, just like every other model, highlights the empirical adequacy of his model, and claims that several physical argumentations of Shkuratov et al. [2012] are wrong. Shkuratov et al. [2013] respond again and clarify that most of Hapke's physical arguments are wrong. Going into a manageable amount of detail, the author concludes that Shkuratov's physical assumptions are more in line with rigorous light scattering theory. Ciarniello et al. [2014] further compared the Hapke model with a Monte-Carlo raytracer in the geometric optics regime and concluded that the Hapke model could accurately fit the angular scattering behavior of the simulated medium.

In conclusion, the Hapke model can accurately fit the photometric behavior of planetary surfaces, but it cannot withstand critical tests for the physical plausibility of all model parameters. Strictly speaking, it has no more explanatory power than an empirical model, and thus, the Hapke parameters must not be taken as a direct indicator for physical surface properties to avoid overinterpretation. Nevertheless, the Hapke model can be a productive tool in planetary surface analysis if the practitioner applies it within certain boundaries and only for specific cases. First, the model is applicable whenever an accurate model for the angular scattering properties of a planetary surface is required, which includes simple surface rendering, intensity-based 3D reconstruction, and photometric normalization. Secondly, the Hapke parameters are not orthogonal and mutually exchangeable, making model inversion ambiguous. Markov chain Monte Carlo approaches provide suitable statistical inversion techniques that yield a single parameter value and the entire uncertainty. Because the single scattering albedo appears to be the most robust and dominant model parameter, keeping all other model parameters fixed and varying only the single scattering albedo became a best practice. This simplification treats the Hapke model as purely empirical but works well. Thirdly, the Hapke model allows for comparative studies. Mapping the variations of the Hapke parameters on a single body and between bodies may give insight into spatial variations on single bodies, between different bodies, and between the laboratory and a planet. Fourthly, there is empirical evidence that the model works to constrain the mineralogical composition of regolith material [Liu et al., 2016; Rommel et al., 2017; Hess et al., 2021].

Unfortunately, no model exists that is rigorous, well-validated, practically useful, and yields unambiguous inversion results at the same time. The best practice employs the most rigorous simulation methods to understand the physics in a planetary regolith. Approximative reflectance models are the best choice for practical applications such as photometric normalization, structural and compositional studies, and any task involving angular-dependent light scattering. Still, they must strictly operate within their scope and boundaries to avoid overinterpretations. Future research must connect both poles and clarify the relevant and physically reasonable model parameters. Section 3.4.1 gives the mathematical foundations of light scattering theory, and Sections 3.4.3 and 3.4.4 present the technical details of the Hapke model and the Kaasalainen-Shkuratov model, respectively.

3.4.1 Light scattering formalism

Light scattering relates the scattered field to the incidence electromagnetic field and the scattering target. This relationship allows solving the forward problem and predicting the scattering behavior of the target or the inverse scattering problem that constrains the target from the scattered fields. Analytic light scattering has been successful for relatively well-constrained targets such as spheres or collections of simple geometric shapes, even though arbitrary shapes are possible. In this thesis, scattering theory simulates submicroscopic iron particles that accumulate in the upper regolith through space weathering. The scattering properties subsequently enter a simulation pipeline that outputs the spectral effects of space weathering. This section briefly reviews light scattering theory and sketches the T-matrix approach as a general case for light scattering of multiple interacting scattering targets. The conclusions of Mie [1908], who solved scattering at single spheres for the first time, are then embedded in the T-matrix approach as a special case. For brevity, the text contains no derivations but references to the relevant literature, mostly Bohren and Huffman [1998]; Mishchenko et al. [2002, 2006]; Sun et al. [2020a,b].

Light scattering theory knows three matrices that relate the incoming to the scattered light: The Amplitude scattering matrix $\mathbf{S}$ links the electromagnetic fields that enter and leave the scene. The Stokes matrix $\mathbf{Z}$ combines the Stokes vectors of the incoming and the scattered radiation. The Stokes vector contains specific intensities and often results from practical measurements. The **T**-matrix builds a relationship between expansion coefficients of incidence and scattered fields, which forms the basis for further theoretical studies and derivate quantities. In the standard light scattering geometry, the electric field at point $\mathbf{r}$ and time t of a monochromatic electromagnetic plane wave that travels through a vacuum along the direction $\mathbf{k} = k\mathbf{n}_{\text{wave}}$ reads

$$\mathbf{E}^{\text{inc}}(\mathbf{r}, t) = \mathbf{E}_0^{\text{inc}} \exp\left(i\mathbf{k} \cdot \mathbf{r}\right) \exp(i\omega t) = \mathbf{E}^{\text{inc}}(\mathbf{r}) \exp(i\omega t). \tag{3.3}$$

Here, $k = \omega\sqrt{\epsilon\mu_{\text{mag}}}$ denotes the wave number of the medium that depends on the angular frequency ω, the permittivity ϵ, and the permeability μ_{mag}. The wave elastically scatters at the scattering target, which means that the frequency of the monochromatic incident wave remains the same after scattering. The field $\mathbf{E}(\mathbf{r})$ above the scattering target is now the superposition of the scattered and the incidence field

$$\mathbf{E}(\mathbf{r}) = \mathbf{E}^{\text{inc}}(\mathbf{r}) + \mathbf{E}^{\text{sca}}(\mathbf{r}). \tag{3.4}$$

The factor $\exp(i\omega t)$ with the time dependency was omitted for simplicity. It is often convenient to express the scattering problem with the amplitude scattering matrix $\mathbf{S}$, which establishes a relationship between the angular field components of the incoming plane wave and the scattered field. The $\mathbf{S}(\mathbf{n}^{\text{sca}}, \mathbf{n}^{\text{inc}})$ matrix characterizes the change in amplitude and polarization for all geometric configurations and thus fully determines any scattering problem:

$$\begin{pmatrix} E_\theta^{\text{sca}} \\ E_\phi^{\text{sca}} \end{pmatrix} = \frac{\exp(i\mathbf{kr})}{||\mathbf{r}||} \begin{pmatrix} S_{11}S_{12} \\ S_{21}S_{22} \end{pmatrix} \begin{pmatrix} E_\theta^{\text{inc}} \\ E_\phi^{\text{inc}} \end{pmatrix}. \tag{3.5}$$

In principle, this matrix fully determines the scattering problem. However, the electromagnetic field components E_θ and E_ϕ, which depend on the angular components (θ, ϕ) of spherical coordinates, are not directly accessible because the electromagnetic field in the visible and infrared wavelength regions fluctuates with frequencies in the tera-Hertz region, which is extremely difficult to measure directly. Instead, optical devices usually act as a wavefront filter. The wavefront passes through the detector entrance, spanning a small solid angle $\Delta\Omega$, and falls onto the optically active sensor with area ΔA. The sensor finally outputs a signal proportional to the time-averaged intensity I of the collected waves without any information about the polarization state. Stokes discovered a formalism with a four-element vector to recover the polarization state and intensity simultaneously. The Stokes vector directly follows from the field components (Equation 3.5), and the quantities Q, U, and V practically result from measurements with polarizers and retarders. For more details, see Mishchenko et al. [2006]; Mishchenko [2014b].

$$\mathbf{I}^{sca} = \begin{pmatrix} I^{sca} \\ Q^{sca} \\ U^{sca} \\ V^{sca} \end{pmatrix} = \frac{1}{2}\sqrt{\frac{\epsilon}{\mu_{\mathrm{mag}}}} \begin{pmatrix} E_\theta^{\mathrm{sca}}[E_\theta^{\mathrm{sca}}]^* + E_\phi^{\mathrm{sca}}[E_\phi^{\mathrm{sca}}]^* \\ E_\theta^{\mathrm{sca}}[E_\theta^{\mathrm{sca}}]^* - E_\phi^{\mathrm{sca}}[E_\phi^{\mathrm{sca}}]^* \\ -E_\theta^{\mathrm{sca}}[E_\phi^{\mathrm{sca}}]^* - E_\phi^{\mathrm{sca}}[E_\theta^{\mathrm{sca}}]^* \\ i\left(E_\phi^{\mathrm{sca}}[E_\theta^{\mathrm{sca}}]^* - E_\theta^{\mathrm{sca}}[E_\phi^{\mathrm{sca}}]^*\right) \end{pmatrix} \tag{3.6}$$

The Stokes phase matrix $\mathbf{Z}(\mathbf{n}^{\mathrm{sca}}, \mathbf{n}^{\mathrm{inc}})$ then relates the Stokes vector of the incidence field to the Stokes vector of the scattered field and thus fully determines the scattering behavior in terms of physically measurable quantities

$$\mathbf{I}^{\mathrm{sca}} = \mathbf{Z}(\mathbf{n}^{\mathrm{sca}}, \mathbf{n}^{\mathrm{inc}})\mathbf{I}^{\mathrm{inc}} \tag{3.7}$$

and directly relates to $\mathbf{R}$ in Section 3.1 [Mishchenko et al., 2006]. This thesis only comprises detectors that do not measure polarization but only the total intensity. Consequently, only the first matrix element is relevant, and the problem reduces to

$$I^{\mathrm{sca}} = Z_{11} I^{\mathrm{inc}} = \frac{1}{2}(|S_{11}|^2 + |S_{12}|^2 + |S_{21}|^2 + |S_{22}|^2) I^{\mathrm{inc}}. \tag{3.8}$$

For detailed theoretical analysis of scattering problems, the spherical vector wave function (SVWF) have proven useful. These functions satisfy orthogonality and completeness on the unit sphere, meaning any square-integrable vector field defined on the unit sphere can be decomposed into SVWFs (see Kristensson [2014] and references therein). Consequently, the incidence field and the scattered field outside the scattering target ($r > r_{\mathrm{target}}$) can be decomposed into a superposition of SVWFs, which reads

$$\mathbf{E}(\mathbf{r})^{\mathrm{inc}} = \sum_{n=0}^{\infty} \sum_{m=-n}^{n} \left[a_{\mathrm{mn}} \mathrm{Rg}\mathbf{M}_{\mathrm{mn}}(k\mathbf{r}) + b_{\mathrm{mn}} \mathrm{Rg}\mathbf{N}_{\mathrm{mn}}(k\mathbf{r})\right] \tag{3.9}$$

$$\mathbf{E}(\mathbf{r})^{\mathrm{sca}} = \sum_{n=0}^{\infty} \sum_{m=-n}^{n} \left[p_{\mathrm{mn}} \mathbf{M}_{\mathrm{mn}}(k\mathbf{r}) + q_{\mathrm{mn}} \mathbf{N}_{\mathrm{mn}}(k\mathbf{r})\right], \tag{3.10}$$

where $k = 2\pi/\lambda$ indicates the wave number of the medium and a_{mn}, b_{mn}, p_{mn}, and q_{mn} denote expansion coefficients of the fields. Appendix B lists the SVWFs $\mathbf{M}_{mn}$, $\mathrm{Rg}\mathbf{M}_{mn}$, $\mathrm{Rg}\mathbf{N}_{mn}$, $\mathbf{N}_{mn}$. The internal field unfolds inside the scattering sphere and decomposes into the SVWFs, but is not discussed here. For an arbitrary scattering scenario, the coefficients of the scattered field become a linear combination of the incidence field coefficients. The eponymous $\mathbf{T}$-matrix [Waterman, 1965] formalizes this relationship:

$$\begin{pmatrix} p_{mn} \\ q_{mn} \end{pmatrix} = \sum_{n'=1}^{\infty} \sum_{m'=-n'}^{+n'} \begin{pmatrix} T^{11}_{mnm'n'} & T^{12}_{mnm'n'} \\ T^{21}_{mnm'n'} & T^{22}_{mnm'n'} \end{pmatrix} \begin{pmatrix} a_{m'n'} \\ b_{m'n'} \end{pmatrix}. \tag{3.11}$$

In many practical scenarios in which the electromagnetic fields are not directly accessible, derived quantities that indicate power balance are practically useful. Disassembling the fields into the SVWF components allows constructing these quantities like piecing together Lego bricks. The extinction cross-section describes how much power W^{ext} is removed from the incidence light I^{inc} through electromagnetic interaction with the scattering target. It follows from the optical theorem [Jackson, 1998; Mishchenko et al., 2006] and reads

$$C_{\text{ext}} = \frac{W^{\text{ext}}}{I^{\text{inc}}} = \frac{4\pi}{k|\mathbf{E}_0^{\text{inc}}|^2}\text{Im}\left[\mathbf{E}_1^{\text{sca}}(\mathbf{n}^{\text{inc}}) \cdot \mathbf{E}_0^{\text{inc}}\right] \tag{3.12}$$

$$= -\frac{1}{k^2|\mathbf{E}_0^{\text{inc}}|^2}\sum_{n=1}^{\infty}\sum_{m=-n}^{+n}\text{Re}\left[a_{mn}(p_{mn})^* + b_{mn}(q_{mn})^*\right], \tag{3.13}$$

where $\mathbf{E}_1^{\text{sca}}$ is the radial-free field with $\mathbf{E}_1^{\text{sca}}(\mathbf{r}) = \mathbf{E}_1^{\text{sca}}(\mathbf{n}_r)\exp(i\mathbf{kr})/||\mathbf{r}||$ along the unit-vector $\mathbf{n}_r$ that points into the same direction as $\mathbf{r}$ [Mishchenko et al., 2006].

The scattering cross section specifies how much power W^{sca} has been scattered in all directions compared to the incidence intensity I^{inc}

$$C_{\text{sca}} = \frac{W^{\text{sca}}}{I^{\text{inc}}} = \frac{1}{|\mathbf{E}_0^{\text{inc}}|^2}\int_{4\pi} d\mathbf{n}|\mathbf{E}_1^{\text{sca}}(\mathbf{n})|^2 \tag{3.14}$$

$$= \frac{1}{k^2|\mathbf{E}_0^{\text{inc}}|^2}\sum_{n=1}^{\infty}\sum_{m=-n}^{+n}\left[|p_{mn}|^2 + |q_{mn}|^2\right]. \tag{3.15}$$

Dividing the scattering and extinction cross-sections by the geometric cross-section G of the scattering target yields the scattering and extinction efficiencies:

$$Q_{\text{ext}} = \frac{C_{\text{ext}}}{G}, \quad Q_{\text{sca}} = \frac{C_{\text{sca}}}{G}. \tag{3.16}$$

The single scattering albedo w finally defines the fraction of the power that is scattered from the power that is lost from the incidence beam in total:

$$w = \frac{C^{\text{sca}}}{C^{\text{ext}}} = \frac{Q^{\text{sca}}}{Q^{\text{ext}}}. \tag{3.17}$$

Even though $\mathbf{S}$ and $\mathbf{Z}$ already fully determine the scattering behavior of the target, some applications require a dimensionless and normalized function. This function is termed phase function $p(\mathbf{r}, \mathbf{n}^{\text{inc}})$ and can either be expressed via the differential cross-section $dC_{\text{sca}}/d\Omega$ or the radial-free scattered field [Arnaut, 2021] $\mathbf{E}_1^{\text{sca}}$:

$$p(\mathbf{r}, \mathbf{n}^{\text{inc}}) = \frac{4\pi}{C_{\text{sca}}}\frac{dC_{\text{sca}}}{d\Omega} = \frac{4\pi}{C_{\text{sca}}}\frac{|\mathbf{E}_1^{\text{sca}}(\mathbf{n}_r)|^2}{|\mathbf{E}_0^{\text{inc}}|^2}. \tag{3.18}$$

If the scattered field is rotationally symmetric, the phase function only depends on the scattering angle θ or the phase angle g, such that $p(g) = p(\mathbf{r}, \mathbf{n}^{\text{inc}})$. Here, $\mathbf{r}$ denotes the scattering direction, $\mathbf{n}_r$ is the normal vector that points into the scattering direction, and $\mathbf{n}^{\text{inc}}$ is the normal vector that indicates the direction in which the incident plane wave propagates. The normalization condition then reads

$$\frac{1}{2}\int_0^{2\pi} p(g)\sin(g)dg = 1. \tag{3.19}$$

3.4.2 Light scattering at single and multiple spherical particles

The scattering of electromagnetic plane waves from perfectly spherical particles is ubiquitous in astrophysics and planetary science and has been well-studied for over a century. Lorentz [1880], Mie [1908], and Debye [1909] analyzed the scattering of single non-interacting spheres, and the theory is commonly referred to as Lorentz-Debye-Mie-Theory. Mie [1908] expanded the incidence and the scattered field into SVWFs and enforced several boundary conditions at the particle's surface. The coefficients a^{Mie} and b^{Mie} follow from extended algebraic calculations when inserting the field expansions in the boundary conditions. For a detailed derivation, see Mie [1908] and Bohren and Huffman [1998]. The Mie coefficients for the scattered field are

$$a_{\mathrm{n}}^{\mathrm{Mie}} = \frac{\mu s^2 j_{\mathrm{n}}(sx)[xj_{\mathrm{n}}(x)]' - \mu_1 j_{\mathrm{n}}(x)[sxj_{\mathrm{n}}(sx)]'}{\mu s^2 j_{\mathrm{n}}(sx)[xh_{\mathrm{n}}^{(1)}(x)]' - \mu_1 h_{\mathrm{n}}^{(1)}(x)[sxj_{\mathrm{n}}(sx)]'} \tag{3.20}$$

$$b_{\mathrm{n}}^{\mathrm{Mie}} = \frac{\mu_1 j_{\mathrm{n}}(sx)[xj_{\mathrm{n}}(x)]' - \mu j_{\mathrm{n}}(x)[mxj_{\mathrm{n}}(sx)]'}{\mu_1 j_{\mathrm{n}}(sx)[xh_{\mathrm{n}}^{(1)}(x)]' - \mu h_{\mathrm{n}}^{(1)}(x)[sxj_{\mathrm{n}}(sx)]'}, \tag{3.21}$$

where μ and μ_1 are the permeabilities of the surrounding medium and the particle, respectively. The symbol $x = 2\pi Nr/\lambda$ is the size parameter for a particle with radius r, $s = N_1/N = k_1/k$ is the relative refractive index, and N and N_1 are the refractive indices of the surrounding medium and the particle, respectively. The variable k_1 denotes the wave number of the particle's material, and k stands for the wave number of the surrounding medium. The function $j_{\mathrm{n}}(x)$ denotes the spherical Bessel functions and $h_{\mathrm{n}}^{(1)}(x)$ stands for the spherical Hankel functions (Appendix B). For single particles, Equation 3.11 no longer depends on the index m. The T-matrix formalism then reduces to the Lorentz-Debye-Mie [Mishchenko et al., 2002] solution because the scattered field coefficients now only depend on the Mie coefficients and the plane wave expansion coefficients

$$p_n = -b_n^{\mathrm{Mie}} a_n \tag{3.22}$$

$$q_n = -a_n^{\mathrm{Mie}} b_n. \tag{3.23}$$

The cross-section readily follows from the Mie coefficients

$$C_{\mathrm{ext}} = \frac{2\pi}{k^2} \sum_{n=1}^{\infty} (2n+1) \mathrm{Re} \left[(a_n^{\mathrm{Mie}})^* + (b_n^{\mathrm{Mie}})^* \right] \tag{3.24}$$

$$C_{\mathrm{sca}} = \frac{2\pi}{k^2} \sum_{n=1}^{\infty} (2n+1) \left[|a_n^{\mathrm{Mie}}|^2 + |b_n^{\mathrm{Mie}}|^2 \right]. \tag{3.25}$$

For spherical particles, the phase function p (Equation 3.18) can be defined as [Mishchenko, 2014b]

$$p(\theta) = \frac{2\pi}{C_{\mathrm{sca}}} \left(|S_{11}(\theta)|^2 + |S_{22}(\theta)|^2 \right), \tag{3.26}$$

where the amplitude scattering matrix elements S_{11} and S_{22} are defined as

$$S_{11}(\theta) = \sum_{n=1}^{\infty} \frac{2n+1}{n(n+1)} \left\{ a_n^{\mathrm{Mie}} \tau_n(\cos(\theta)) + b_n^{\mathrm{Mie}} \pi_n(\cos(\theta)) \right\} \tag{3.27}$$

$$S_{22}(\theta) = \sum_{n=1}^{\infty} \frac{2n+1}{n(n+1)} \left\{ a_n^{\mathrm{Mie}} \pi_n(\cos(\theta)) + b_n^{\mathrm{Mie}} \tau_n(\cos(\theta)) \right\}. \tag{3.28}$$

The angle $\theta = 180° - g$ is the scattering angle. Note that the off-diagonal elements S_{12} and S_{21} of the amplitude scattering matrix (Equation 3.5) vanish for spherical particles. The functions π and τ depend on the associated Legendre polynomials P_n^1:

$$\pi_n(\cos(\theta)) = \frac{1}{\sin(\theta)} P_n^1(\cos(\theta)) \tag{3.29}$$

$$\tau_n(\cos(\theta)) = \frac{d}{d\theta} P_n^1(\cos(\theta)). \tag{3.30}$$

Now, N non-overlapping spherical particles at positions $\mathbf{r}_i \in \mathbb{R}^3$ with radii r_i are considered. Following Egel et al. [2017], it is convenient to simplify the notation in Equation 3.11 and introduce a combined index l that summarizes n, m, and τ. The polarization index τ decides whether to use the a_{mn} and p_{mn} ($\tau = 1$) or b_{mn} and q_{mn} ($\tau = 2$). The T-matrix in single index notation reads

$$p_l^i = \sum_{l'} T_{ll'}^i a_l^i. \tag{3.31}$$

For multiple particles, interaction comes into play. The incidence field at the i$^{\text{th}}$ particle is the incidence field of the entire scene and the superposition of the scattered fields of all other ($i' \neq i$) particles:

$$\mathbf{E}_{\mathrm{inc}}^i(\mathrm{r}) = \mathbf{E}_{\mathrm{inc}}(\mathrm{r}) + \sum_{i' \neq i} \mathbf{E}_{\mathrm{sca}}^{i'}(\mathrm{r}). \tag{3.32}$$

Because the fields superpose linearly, the expansion coefficients a_l^i of the field at each particle i are the expansion coefficients $a_{\mathrm{inc},l}^i$ of the incidence field and the expansion coefficients of the scattered fields of all other particles

$$a_l^i = a_{\mathrm{inc},l}^i + \sum_{i' \neq i} \sum_{l'} W_{ll'}^{ii'} p_{l'}^{i'}. \tag{3.33}$$

The expansion coefficients of particle l belong to a set of SVWFs extending around the center of the particle. In the case of multiple particle scattering, each particle has its own origin, and the coefficients $p_{l'}^{i'}$ are incompatible. The translation operator $W_{ll'}^{ii'}$ alleviates this issue and translates the coefficients of all $l' \neq l$ particles to particle l and its coordinate system. The matrix $W_{ll'}^{ii'}$ appears in Appendix B. Combining Equation 3.31 and 3.33 and eliminating a_l^i leads to a coupled system of linear equations that fully determines the multiple-scattering problem:

$$\sum_{i'}\sum_{l'} M_{ll'}^{ii'} p_l^{i'} = \sum_{l'} T_{ll'}^{i} a_{\mathrm{inc},l}^{i}, \text{ with} \tag{3.34}$$

$$M_{ll'}^{ii'} = \delta_{ii'}\delta_{ll'} - \sum_{l''} T_{ll''}^{i} W_{l''l'}^{ii'}. \tag{3.35}$$

The plane wave expansion $a_{\mathrm{inc},l}^{i}$ of the incidence field is known as a-priori. The translation operators $W_{l''l'}^{ii'}$ follow from the particle arrangement, and each T-matrix $T_{ll'}^{i}$ contains the expansion coefficients for the i^{th} sphere, which come from the Mie solution (Equation 3.23). The symbol δ denotes the Kronecker-delta. The problem is now fully constrained such that common matrix-inversion techniques yield p_l^{i}, which are the expansion coefficients of the scattered field of the i^{th} particle after considering multiple scattering. Adding up the individual scattered fields at each particle yields the total scattered field. Arnaut [2021] derived expressions for Q_{ext}, Q_{sca}, and found a way to compute the phase function $p(\mathbf{r}, \mathbf{n}^{\mathrm{inc}})$ from the far field. The extinction cross-section of the particle cluster is simply the sum of the extinction cross-sections of all particles

$$C_{\mathrm{ext}} = \sum_{t=1}^{N} C_{\mathrm{ext}}^{t}. \tag{3.36}$$

The scattering cross-section is more intricate and requires summing over all combinations of two particles in the cluster and considering the translation operator $\mathcal{R}$, as shown by Arnaut [2021]:

$$C_{\mathrm{sca}} = \frac{1}{k^2 |\mathbf{E}_0^{\mathrm{inc}}|^2} \sum_{u=1}^{N}\sum_{v=1}^{N}\sum_{l=1}^{\infty}\sum_{m=-l}^{+l} \left[p_{uml}\mathcal{R}_{u\leftarrow v} p_{vml}^{*} + q_{uml}\mathcal{R}_{u\leftarrow v} q_{vml}^{*}\right]. \tag{3.37}$$

The translation operator $\mathcal{R}_{u\leftarrow v}$ is defined in Appendix B. Finally, the phase function can be evaluated numerically from the far-field expansion of the scattered field and inserted into Equation 3.18. The angular component of the scattered field of the t^{th} particle is

$$\mathbf{E}_{1,t}^{\mathrm{sca}}(\mathbf{n}_{\mathrm{r}}) = \frac{1}{k}\sum_{l=1}^{\infty}\sum_{m=-l}^{+l} (-i)^{l+1}\gamma_{ml}\left[p_{ml}^{t}\mathbf{C}_{ml}(\theta,\phi) - i q_{ml}^{t}\mathbf{B}_{ml}(\theta,\phi)\right], \tag{3.38}$$

and the total scattered far-field is the superposition of all individual fields

$$\mathbf{E}_{1}^{\mathrm{sca}}(\mathbf{n}_{\mathrm{r}}) = \sum_{t=1}^{N} \frac{r}{r_t} \exp(ik(r_t - r))\mathbf{E}_{1,t}^{\mathrm{sca}}(\mathbf{n}_{\mathrm{r,t}}). \tag{3.39}$$

3.4.3 Hapke model

The Hapke model computes the bi-directional reflectance of a planetary regolith, given a set of parameters that attempt to characterize various regolith properties. The most advanced version of the Hapke model described in Hapke [2012] is given by

$$
\begin{aligned}
r_{\mathrm{d}}(i,e,g,w) =& \frac{w}{4\pi}\frac{\mu_{0,\mathrm{e}}}{\mu_{0,\mathrm{e}}+\mu_{\mathrm{e}}}\{p(g)B_{SH}(g)+L_1(\mu_{0,\mathrm{e}})[H(\mu_{\mathrm{e}})-1] \\
&+L_1(\mu_{\mathrm{e}})[H(\mu_{0,\mathrm{e}})-1]+L_2[H(\mu_{\mathrm{e}})-1] \\
&\cdot[H(\mu_{0,\mathrm{e}})-1]\}B_{CB}(g)S(i,e,g,\overline{\theta}).
\end{aligned}
\tag{3.40}
$$

The geometric parameters are the phase angle g and $\mu_{0,\mathrm{e}}$ and μ_{e}, which are the modified cosines of the incidence angle i and the emission angle e (Appendix C). The single scattering albedo w and the phase function $p(g)$ characterize, in theory, the single scattering properties of the mineral grains. The single scattering albedo w (Equation 3.17) is the dominant material parameter that indicates the fraction of how much power a single particle removes from the incidence light through scattering at a specific wavelength. Thereby, the single scattering albedo encodes most information about the spectral shape and how bright the surface is, independent of the illumination and observation conditions. The single-particle phase function models the angular scattering behavior of a single grain and can be expressed by the empirical double-lobed Henyey-Greenstein (DHG)-function that always integrates to unity:

$$
p(g)=\frac{1+c}{2}\frac{1-\xi^2}{(1-2\xi\cos(g)+\xi^2)^{3/2}}+\frac{1-c}{2}\frac{1-\xi^2}{(1+2\xi\cos(g)+\xi^2)^{3/2}}. \tag{3.41}
$$

The DHG-function can be expressed in terms of Legendre polynomials, which reads

$$
\begin{aligned}
p(g) &= 1+\sum_{n=1}^{\infty} b_n P_n(g) && (3.42)\\
&= 1+\sum_{n=1}^{\infty} b_n[P_n(\mu_0)P_n(\mu)+2\sum_{m=1}^{\infty}\frac{(n-m)!}{(n+m)!}P_{nm}(\mu_0)P_{nm}(\mu)\cos m\phi]. && (3.43)
\end{aligned}
$$

The cosine causes the third term to vanish. The Legendre coefficients are thus

$$
b_n=\left[\frac{1+c}{2}(2n+1)(\xi)^n+\frac{1-c}{2}(2n+1)(-\xi)^n\right], \tag{3.44}
$$

where the asymmetry factor ξ describes how strong the scattering lobes deviate from isotropy, and c indicates forward or backward scattering. Planetary regolith is primarily backscattering, such that the phase function usually has parameters $b\approx 0.2$, and $c>0$ [Hapke, 2012; Sato et al., 2014]. The Ambartsumian-Chandrasekhar H-function is a direct result of the Ambratsumian invariance relation and is defined as

$$
H(x)=1+\frac{w}{2}xH(x)\int_0^1\frac{H(x')}{x+x'}dx', \tag{3.45}
$$

where w is the single scattering albedo, and x is a placeholder for either μ_0 or μ, the cosines of the incidence angle i or the emission angle e, respectively. It cannot be solved analytically, but Hapke [2012] found an analytical expression that is a viable approximation

$$
H(x)=\left\{1-wx\left[r_0+\frac{1-2r_0x}{2}\ln\frac{1+x}{x}\right]\right\}^{-1}, \tag{3.46}
$$

where

$$\gamma = \sqrt{1-w} \tag{3.47}$$

$$r_0 = \frac{1-\gamma}{1+\gamma}. \tag{3.48}$$

The L_1- and L_2-terms are defined by:

$$L_1(\mu) = 1 + \sum_{n=1}^{\infty} A_n b_n P_n(\mu) \tag{3.49}$$

$$L_1(\mu_0) = 1 + \sum_{n=1}^{\infty} A_n b_n P_n(\mu_0) \tag{3.50}$$

$$L_2 = 1 + \sum_{n=1}^{\infty} A_n^2 b_n. \tag{3.51}$$

A Legendre expansion of the DHG-function yields the coefficients b_n. The coefficients A_n for even n follow from a recursion:

$$A_0 = 0 \tag{3.52}$$

$$A_\mathrm{n} = \frac{(-1)^{(n+1)/2}}{n} \frac{1 \cdot 3 \cdot 5 \cdots n}{1 \cdot 2 \cdot 4 \cdots (n+1)}, \; n \in \{2k | k \in \mathbb{N}^+\}. \tag{3.53}$$

For odd n, A_n is always zero. The terms B_SH and B_CB describe the shadow-hiding and the coherent backscatter opposition effect. For small phase angles g, planetary regolith reflects light comparatively strongly because of two overlapping effects. Near opposition, the illumination and observation direction are similar, and small shadows in the rough and rugged structure of the regolith vanish. This effect is termed the SHOE, and Hapke [1986] introduced the following factor

$$B_\mathrm{SH}(g) = 1 + B_\mathrm{S0} \frac{1}{1 + \tan(g/2)/h_\mathrm{s}} \tag{3.54}$$

that accounts for the effect, where B_S0 describes the amplitude and h_s the angular width. Usually, the SHOE acts within phase angles $g < 10°$. For small phase angles, usually $g < 1°$, multiply scattered light constructively interferes and causes a signal around two times higher than for slightly larger g. Hapke [2002] introduces another term that models the CBOE

$$B_\mathrm{CB}(g) = 1 + B_\mathrm{C0} \frac{1 + \frac{1-\exp((1/h_\mathrm{c})\tan(g/2))}{(1/h_\mathrm{c})\tan(g/2)}}{2(1 + (1/h_\mathrm{c})\tan(g/2))^2}, \tag{3.55}$$

where B_C0 describes the effect's amplitude. The angular width is defined as

$$h_\mathrm{c} = \frac{\lambda}{4\pi\Lambda}, \tag{3.56}$$

where Λ is the average distance a photon travels between multiple scattering events. Because the CBOE is comparatively sharp, difficult to measure, and not captured in most geometries, it will be omitted in this thesis.

Planetary surfaces are rough, meaning the regolith has a microscopic topography such that the illumination and observation geometry varies at small scales, and the surface shadows itself. The roughness of planetary surfaces can be defined in many ways [Helfenstein and Shepard, 1999]. The Hapke-$\overline{\theta}$ and the root mean square slope (RMSL) are two standard definitions. The Hapke-$\overline{\theta}$ [Hapke, 2012] is defined via a slope distribution function $a(\vartheta)$, where ϑ is the zenith angle with respect to the vertical direction. The tangent of the $\overline{\theta}$ is the weighted average of the tangent of each possible zenith angle ϑ:

$$\tan(\overline{\theta}) = \frac{2}{\pi} \int_0^{2\pi} a(\vartheta) \tan(\vartheta) d\vartheta. \tag{3.57}$$

The RMSL is defined via the slope of a surface Z at point (x, y) weighted with the total area ΔA:

$$\text{RMSL} = \sqrt{\frac{1}{\Delta A} \int_\Omega \left(\frac{\partial Z}{\partial x}\right)^2 + \left(\frac{\partial Z}{\partial x}\right)^2 dA}. \tag{3.58}$$

The fractal dimension D [Helfenstein and Shepard, 1999] is also a suitable measure for surface roughness but is not discussed in this thesis. Hapke [1984] accounted for macroscopic roughness and introduced the modified cosines of the incidence and emission angles $\mu_{0,\mathrm{e}}(i, \overline{\theta})$ and $\mu_{\mathrm{e}}(e, \overline{\theta})$, respectively, and the shadowing function $S(i, e, \overline{\theta})$ that are listed in Appendix C. Surface roughness will also play an essential role in thermal modeling (Section 5.2).

3.4.4 Kaasalainen-Shkuratov model

The Kaasalainen-Shkuratov (KS) model [e.g. Shkuratov et al., 2011; Domingue et al., 2016] has been developed independently of the Hapke model and provides an alternative for computing the bi-directional reflectance. The model combines two components, the equigonal albedo A_{eq} and the disk function D [Domingue et al., 2016]. The disk function depends on the incidence and emission angles and simulates the directional light scattering behavior. The equigonal albedo only depends on the wavelength and the phase angle g and thus mainly accounts for the material properties independent of topography and the exact lighting conditions. The equigonal albedo is defined as the normal albedo $A_{\vec{\mathrm{n}}}$, and the phase function $f(g)$ [Shkuratov et al., 2011; Domingue et al., 2016]:

$$\begin{align} \pi r_{\mathrm{d}}(i, e, g, A_{\vec{\mathrm{n}}}) &= A_{\mathrm{eq}}(g) D(i, e, g) \tag{3.59} \\ &= A_{\vec{\mathrm{n}}} f(g) D(i, e, g). \tag{3.60} \end{align}$$

The terms $f(g)$ and D can be modeled in different ways. Domingue et al. [2016] presents six formulations of the KS model that they used for photometric analysis of Mercury:

$$KS_1(i,e,g,A_{\vec{n}}) = A_{\vec{n}} e^{-a_0 g} \frac{2\mu_0}{\mu_0+\mu} \tag{3.61}$$

$$KS_2(i,e,g,A_{\vec{n}}) = A_{\vec{n}} e^{-a_0 g} \cos\frac{g}{2} \cos\left[\frac{\pi}{\pi-g}\left(\gamma_\mathrm{p} - \frac{g}{2}\right)\right] \frac{(\cos\beta_\mathrm{p})^{g/(\pi-g)}}{\cos\gamma_\mathrm{p}} \tag{3.62}$$

$$KS_3(i,e,g,A_{\vec{n}}) = A_{\vec{n}} e^{-a_0 g} \left[c_\mathrm{l}\frac{2\mu_0}{\mu_0+\mu} + (1-c_\mathrm{l})\mu_0\right] \tag{3.63}$$

$$KS_4(i,e,g,A_{\vec{n}}) = A_{\vec{n}} e^{-a_0 g} \mu_0^{k_\mathrm{m}} \mu^{k_\mathrm{m}-1} \tag{3.64}$$

$$KS_5(i,e,g,A_{\vec{n}}) = A_{\vec{n}} e^{-a_0 g} \cos\frac{g}{2} \cos\left[\frac{\pi}{\pi-g}\left(\gamma_\mathrm{p} - \frac{g}{2}\right)\right] \frac{(\cos\beta_\mathrm{p})^{\eta g/(\pi-g)}}{\cos\gamma_\mathrm{p}} \tag{3.65}$$

$$KS_6(i,e,g,A_{\vec{n}}) = A_{\vec{n}} \frac{e^{-a_1 g} + m e^{-a_2 g}}{1+m} \cos\frac{g}{2} \cos\left[\frac{\pi}{\pi-g}\left(\gamma_\mathrm{p} - \frac{g}{2}\right)\right] \frac{(\cos\beta_\mathrm{p})^{\eta g/(\pi-g)}}{\cos\gamma_\mathrm{p}}. \tag{3.66}$$

In all cases, exponential functions with the parameters a_0, a_1, a_2, and m model the phase function $f(g)$ dominated by the opposition surges. The disk function can be modeled with the Lommel-Seeliger law (KS1) [Shepard, 2017], Minnaert's law (KS4) [Shepard, 2017], the Lunar-Lambert model (KS3) [McEwen, 1996], and the semi-empirical version of the Akimov disk function (KS2,5,6) [Shkuratov et al., 2011]. Again, μ_0 and μ are the cosines of the incidence and emission angle. The parameters β_p and γ_p are the photometric latitudes and longitudes, respectively. They fulfill $\cos(i) = \cos(\beta_\mathrm{p})\cos(g-\gamma_\mathrm{p})$ and $\cos(e) = \cos(\beta_\mathrm{p})\cos(\gamma_\mathrm{p})$. The parameter c_l determines the relative strength of the Lommel-Seeliger and the Lambert contribution, and k_m is the Minnaert exponent that depends on the phase angle g via $k_\mathrm{m}(g) = (10^{-2}g+1)/2$. The parameter η is set to 0.34 or 0.52 for lunar maria or highlands. For a detailed description and derivation, the reader is referred to Domingue et al. [2016], Shkuratov et al. [2011], and references therein. Chapter 7 applies the KS3 model to Mercury because Domingue et al. [2016] found that it performs best on Mercury with MDIS data. The KS model has also been described by Wohlfarth and Wöhler [2022].

3.4.5 Space weathering models

Chapter 2.1.2 introduced nanometer-sized iron particles submicroscopic iron (smFe^0) that accumulate in mineral rims and agglutinates and cause spectral darkening, reddening, and obstruction of spectral features. Consequently, spectral space weathering effects are both *a friend and a foe*. On the one hand, those effects indicate how long the surface has been exposed to space weathering. On the other hand, feature obstruction inhibits compositional analysis, such as spectral unmixing. Therefore, modeling this effect is helpful for understanding, predicting, and removing it. Several models attempt to simulate the optical effects of these iron particles. Hapke [2001] uses the Maxwell-Garnett effective medium theory, which assumes that all soil components make up a single medium interspersed with nanophase iron particles. Hapke [2001] computes the absorption coefficients of iron particles that act as Rayleigh-scatterer and mixes them with the absorption of the regolith. The approach generally reproduces the spectral effects observed in lunar samples but overestimates spectral reddening, increasing deviations at lower wavelengths. Lucey and Riner [2011] extended the effective medium approach for npFe^0 by adding the absorption coefficient of mpFe^0 with sizes of 200 nm. The larger model particles successfully explain the darkening effect of weathered material but are too large compared to the implanted iron particles found by Noble et al. [2007] (200 nm vs. 50 nm). Penttilä et al. [2020] proposed a multiscale approach. First, they model individual iron particles embedded in a host material, which delivers the Mueller matrices and the cross sections of the npFe^0 inclusions. Second, they model individual Olivine grains of various sizes and add a rim interspersed with npFe^0. The resulting Mueller matrix and cross-sections are subsequently fed into the vectorized radiative transfer equation to model the bi-directional reflectance distribution function of the regolith. The model successfully predicts the spectral effects of space weathering but has not been extensively tested with remote sensing data.

The author developed and published [Wohlfarth et al., 2019] a space weathering model that directly works on remote sensing data. The model combines Mie scattering and Hapke modeling to simulate the spectral effects of submicroscopic iron. The author further suggested considering inter-particle interactions with T-matrix modeling, later implemented by Arnaut et al. [2021]. The core idea is to formulate the space weathering simulation as a mixing task, combining the smFe^0 inclusions and a bulk soil spectrum. Increasing the weight percentage of submicroscopic iron simulates the gradual accumulation of iron particles with time. The model has subsequently been used for hydration analysis [Wohlfarth et al., 2019], compositional analysis [Hess et al., 2021], and photometric studies of lunar swirls [Hess et al., 2020a]. This thesis describes the model of Wohlfarth et al. [2019] and presents further developments to better understand the spectral effects of space weathering.

3.5 Thermal emission theory

Airless planetary bodies reflect some of the electromagnetic radiation from the host star and absorb the rest. The absorbed electromagnetic radiation causes the planetary body to heat up, such that every point (x, y, z) of the body can be associated with a temperature T that evolves over time t. Consequently, the temperature of a planetary body can be described with a scalar temperature field $T(x, y, z, t)$. Bodies with a temperature of T, in turn, emit electromagnetic radiation, which can subsequently be measured with a remote sensing detector or telescope. Depending on the planet, the thermal structure is complex such that the emitted thermal emission becomes an intricate combination of emissions caused by various temperatures, heat transfer processes, and composition. The thermal emission thus becomes complex and ambiguous. However, it can reveal much about the planetary surface: Suitable physical models can simulate the planet's temperature distribution and the relevant mechanisms. Comparing the simulation results with measurements creates an inverse problem that constrains the target planet's composition, temperature, and other thermophysical properties, making thermal models so important for astronomy and planetary geoscience. This section first introduces temperature, thermal emission, and heat transfer. After that, it reviews the state of the art and various applications of thermal models to airless bodies. The section identifies current methodic challenges that will be later addressed in Chapter 3.5.2.

3.5.1 General relations

The temperature T is one of the fundamental state quantities of a thermodynamical system. According to the Zeroth law of thermodynamics, the temperature is defined via an equivalence relation: All systems in mutual thermodynamical equilibrium form an equivalence class. All thermodynamical systems within one of these equivalence classes can be associated with one common scalar state quantity named temperature T. The temperatures can be put in ascending order and form a strictly positive scale measured in Kelvin $[K]$. In terms of statistical physics, thermal equilibrium means that the joint phase space $\Omega_1(U_1)\Omega_2(U_2)$ of two individual systems with phase spaces $\Omega_1(U_1)$ and $\Omega_2(U_2)$ that were brought into thermal contact must be extremal. What follows from the extremality condition and other considerations is the statistical definition of the temperature that reads

$$\frac{1}{k_\mathrm{B}T} = \frac{\partial \ln \Omega_0(U_0)}{\partial U_0}, \tag{3.67}$$

where $k_\mathrm{B} = 1.381 \cdot 10^{-23}\, J\mathrm{K}^{-1}$ is the Boltzmann constant and U_0 is the internal energy of the system. Thus, the temperature determines how steeply the phase space, i.e., the entropy, grows with internal energy U_0. For an introduction to thermodynamics and a more thorough discussion, see Bartelmann et al. [2018b]. This temperature definition is fundamental and general but rather abstract and requires further contextualization to understand the role of T in a given scenario. At a planetary body, the target of this thesis, the temperature takes two roles: First, it determines the environment in which physical and chemical processes occur and thus constrains the thermal evolution and the formation of the planet, and what processes run at the surface (or atmosphere). Second, the temperature leads to thermal emission, which can be accessed with remote sensing devices and thus enable conclusions to be drawn about the thermal environment.

Planck's radiation law links the equilibrium temperature T of an ideal nonreflecting body, a blackbody, to its emitted diffuse spectral specific intensity $I_\mathrm{b}(T, \lambda)$. After several attempts to formalize blackbody radiation with classical physics, Planck [1900] made the first viable theoretical treatment. In an ad-hoc fashion, Planck replaced the assumption of a continuous energy distribution with discrete energy levels, later recognized as the birth of quantum mechanics. Mandel and Wolf [1995] work with a modern formalism to derive blackbody radiation that will not be treated here for brevity. Planck's law is defined as

$$U(T, \lambda) = \frac{2\pi h c_0^2}{\lambda^5} \frac{1}{e^{hc_0/\lambda k_\mathrm{B} T} - 1}, \tag{3.68}$$

where $h = 6.626 \cdot 10^{-34}\,\mathrm{m^2 kg\, s^{-1}}$ is Planck's constant and $c_0 = 299.792 \cdot 10^6\,\mathrm{m\, s^{-1}}$ is the speed of light. The diffuse spectral specific intensity (radiance) I_{b} emitted by a blackbody is

$$I_{\mathrm{b}}(T,\lambda) = \frac{1}{\pi}U(T,\lambda). \tag{3.69}$$

Integrating over the upper half-space Ω and all wavelengths, the total power per area that leaves the blackbody becomes what is known as the Stefan-Boltzmann law

$$\begin{aligned} dP(T) &= \int_{\lambda=0}^{\infty}\int_{\Omega} I_{\mathrm{b}}(T,\lambda)\cos(e)d\Omega d\lambda dA && (3.70)\\ &= \left(\frac{2\pi^5 k_{\mathrm{B}}^4}{15c_0^2 h_0^3}\right)T^4 dA && (3.71)\\ &= \sigma T^4 dA, && (3.72) \end{aligned}$$

where $\sigma = 5.671 \cdot 10^{-8}\mathrm{Wm^{-2}K^{-4}}$ is termed the Stefan-Boltzmann constant and $d\Omega = \sin(e)ded\phi$ is the differential surface element in spherical coordinates. The blackbody is an idealized body that does not reflect but absorbs radiation at every wavelength. Such bodies do not exist in nature. The thermal emission of real bodies observed under the emission angle e is operationalized with the spectral directional emissivity ϵ_{d} such that the measured diffuse specific intensity of the actual body becomes a function of the temperature T, the wavelength λ, and the emission angle e:

$$I(T,e,\lambda) = \epsilon_{\mathrm{d}}(e,\lambda)I_{\mathrm{b}}(T,\lambda) = \frac{1}{\pi}\epsilon_{\mathrm{d}}(e,\lambda)U(T,\lambda). \tag{3.73}$$

Consequently, the power per area that leaves a real body with an emissivity $\epsilon_{\mathrm{d}} < 1$ is defined as

$$\begin{aligned} dP(T) &= \int_{\lambda=0}^{\infty}\int_{\Omega} \epsilon_{\mathrm{d}}(e,\lambda)\cos(e)I_{\mathrm{b}}(T,\lambda)d\Omega d\lambda dA && (3.74)\\ &= \frac{\int_{\lambda=0}^{\infty}\int_{\Omega}\frac{\epsilon_{\mathrm{d}}(e,\lambda)}{\pi}\cos(e)I_{\mathrm{b}}(T,\lambda)d\Omega d\lambda}{\int_{\lambda=0}^{\infty}I_{\mathrm{b}}(T,\lambda)d\lambda}\int_{\lambda=0}^{\infty}\pi I_{\mathrm{b}}(T,\lambda)d\lambda dA && (3.75)\\ &= \frac{\int_{\lambda=0}^{\infty}\epsilon_{\mathrm{h}}(\lambda)I_{\mathrm{b}}(T,\lambda)d\lambda}{\int_{\lambda=0}^{\infty}I_{\mathrm{b}}(T,\lambda)d\lambda}\int_{\lambda=0}^{\infty}\pi I_{\mathrm{b}}(T,\lambda)d\lambda dA && (3.76)\\ &= \bar{\epsilon}_{\mathrm{h}}(T)\sigma T^4 dA, && (3.77) \end{aligned}$$

where $\bar{\epsilon}_{\mathrm{h}}$ is the bolometric hemispherical emissivity.

In radiative equilibrium, the surface absorbs and immediately re-emits the part of the solar flux that has not been reflected. Kirchhoff's law operationalizes this phenomenon and says that the directional emissivity ϵ_{d} relates to the hemispherical-directional reflection r_{hd} [Hapke, 2012] via

$$\epsilon_{\mathrm{d}}(e,\lambda) = 1 - r_{\mathrm{hd}}(e,\lambda). \tag{3.78}$$

Myhrvold [2018] points out that accurately accounting for this relationship is crucial for spectral regions in which reflected and emitted radiation are superimposed. The hemispherical-directional reflectance follows from integrating the bi-directional reflectance r_{d} over the upper half-sphere that collects all incidence directions:

$$r_{\mathrm{hd}}(e, \lambda) = \int_{i=0}^{\pi/2} \int_{\phi=0}^{2\pi} r_{\mathrm{d}}(i, e, g) \sin i \; d\phi di. \tag{3.79}$$

Integrating the bi-directional reflectance r_{d} over the entire half-space suppresses sensitivity to the illumination and observation geometry. The hemispherical-directional reflectance is independent of the incidence angle and only significantly changes for emission angles larger than 60°, which is backed by empirical studies of Maturilli et al. [2016] and Warren et al. [2019], as also discussed by Wohlfarth et al. [2023]. Appendix D contains a closed-form solution with the Hapke model.

A real body reflects a fraction A_{dh} of the incoming radiative power and absorbs a fraction $(1 - A_{\mathrm{dh}})$ that determines the body's temperature. The quantity A_{dh} is termed bolometric directional-hemispherical albedo, and Shkuratov et al. [2011] give a definition that reads

$$A_{\mathrm{dh}} = \frac{1}{S_{\odot}} \int_{0}^{\infty} J_0(\lambda) r_{\mathrm{dh}}(i, \lambda) d\lambda. \tag{3.80}$$

The solar spectral irradiance J_0 weighted by the directional-hemispherical reflectance gives the total spectral radiance that the surface reflects back into the upper hemisphere. Hapke [2012] proves that $r_{\mathrm{dh}}(i) = r_{\mathrm{hd}}(e)$ holds, i.e., the directional-hemispherical reflectance has the same behavior as the hemispherical-directional reflectance defined in Equation 3.79. Computing the bolometric integral of the reflected light over all wavelengths yields the total reflected power per unit area. Relating this result to the solar constant $S_{\odot}$ that specifies the power per unit area at 1 AU distance yields A_{dh}. The author notes that different albedo definitions are used in the thermal modeling literature, but only this formulation is physically sound [Wohlfarth et al., 2023].

Finally, combining equations 3.77 and 3.80 yields the heat balance equation for a surface with bolometric hemispherical emissivity $\bar{\epsilon}_{\mathrm{h}}$ and directional-hemispherical albedo A_{dh} at 1 AU distance, directly illuminated by the Sun

$$(1 - A_{\mathrm{dh}}) S_{\odot} = \bar{\epsilon}_{\mathrm{h}} \sigma T^4. \tag{3.81}$$

This equation forms the basis for all thermal modeling efforts in this thesis.

In most realistic cases, the thermal structure of a target is more complex than a simple blackbody. The rough surface of an airless planetary body is highly isolating such that the regolith surface may exhibit strong temperature gradients on centimeter and millimeter scales [Bandfield et al., 2015; Grumpe et al., 2019]. Consequently, the thermal emission is the sum of many Planck functions, each bearing an individual temperature. This blend of Planck functions causes considerable anisotropies of the thermal emission under oblique illumination and viewing geometries. Further, thermal gradients in semi-transparent layers may have a similar effect. The medium emits thermal radiation at different depths with different temperatures, which can be described with a superposition of multiple (attenuated) Planck functions. This effect occurs in planetary atmospheres [Stamnes et al., 2017] and possibly in the uppermost regolith layer [Millán et al., 2011].

In thermal equilibrium, the system has approached a common temperature value T that no longer changes. Outside thermal equilibrium, temperature differences drive processes that distribute the heat across the system, which leads to temperature changes. The fundamental mechanisms are radiative, conductive, and convective heat transfer. The first two mechanisms are relevant for the surfaces of airless bodies, while the last only occurs in atmospheres, oceans, and planetary interiors.

Radiative heat transfer occurs when matter exchanges heat through radiation. Each body has an individual temperature and thus emits thermal radiation, eventually heating other bodies. When a differential surface element dA_i has temperature T_i and heats the differential surface element dA_j, the latter receives a small amount d^2Q of heat energy per unit time

$$d^2Q_{\mathrm{i}\rightarrow\mathrm{j}} = \sigma T_\mathrm{i}^4 \underbrace{\frac{\cos(\phi_{\Delta,\mathrm{i}})\cos(\phi_{\Delta,\mathrm{j}})}{\pi d_{\mathrm{i,j}}^2} dA_\mathrm{i} dA_\mathrm{j}}_{f_\mathrm{i,j}} . \tag{3.82}$$

When two differential surface elements dA_i and dA_j heat each other, the net heat energy per unit time d^2Q flows from the hotter to the colder body and reads

$$d^2Q_{\mathrm{i}\Leftrightarrow\mathrm{j}} = \sigma(T_\mathrm{i}^4 - T_\mathrm{j}^4) \underbrace{\frac{\cos(\phi_{\Delta,\mathrm{i}})\cos(\phi_{\Delta,\mathrm{j}})}{\pi d_{\mathrm{i,j}}^2} dA_\mathrm{i} dA_\mathrm{j}}_{f_\mathrm{i,j}} . \tag{3.83}$$

The factor $f_\mathrm{i,j}$ is termed configuration factor, or view factor, and depends on the distance $d_\mathrm{i,j}$ between the surface elements and the angles $\phi_{\Delta,\mathrm{i}}$ measured between the normal of dA_i and the direction toward dA_j and $\phi_{\Delta,\mathrm{j}}$ is measured between the normal of dA_j and the direction toward dA_i. The configuration factors encode the geometry of a specific scene, and their computation imposes the real challenge of radiative heat transfer. For simple geometric cases, configuration factors are available, but realistic scenarios usually require numerical approaches. For a thorough discussion, see Howell et al. [2020]. Radiative heat transfer is how host stars heat their planets and how parts of a planetary surface heat each other and thus plays a central role in the thermal modeling of airless bodies. The main mechanism for self-heating of planetary regolith will be developed in Chapter 5.2. Conductive heat transfer generally appears in solid matter and can be modeled with the diffusion equation [e.g. Howell et al., 2020] that reads

$$\rho c_\mathrm{p} \frac{\partial T(x,y,z,t)}{\partial t} = \nabla \cdot \left(k_\mathrm{h}(x,y,z) \nabla T(x,y,z,t)\right) , \tag{3.84}$$

where ρ [$\mathrm{kg\,m^{-3}}$] is the density, c_p [$\mathrm{J\,kg^{-1}K^{-1}}$] is the specific heat capacity, and $k_\mathrm{h}(x,y,z)$ [$\mathrm{W\,m^{-1}K^{-1}}$] is the spatially variable heat conductivity. The heat conduction equation encodes the corollary from the second law of thermodynamics, which states that heat only flows from hotter to colder reservoirs until thermal equilibrium is reached. The diffusion equation is a partial differential equation, and its mathematical solution theory is well-developed. It was even the case for which Fourier first developed the ubiquitous harmonic analysis in 1822 [Fourier, 2009]. In the following decades, various numerical schemes have been developed for complex, realistic systems, as discussed by Minkowycz et al. [2006]. Heat conduction plays a crucial role on airless planetary surfaces. Some incoming radiation spreads into the surface's upper layer ($\approx 1\,m$). Radiometers can observe how fast the surface cools at night and determine the diffusion coefficient that encodes information about the surface material, such as density, conductivity, and other properties.

Convection describes a heat transfer process through combined diffusion and mass transport in a gravitation field. A hot surface conducts heat into a fluid that heats up and expands. In a gravitation field, the hot and less dense fluid moves upwards and is replaced by colder and denser fluid. The hot fluid eventually distributes its heat to the exterior at the upper boundary of the fluid, cools down, contracts, and sinks again, replacing the fluid that has just been heated and risen to the top. This process establishes cyclic convection currents responsible for several fascinating phenomena on planets: Mantle convection in the planetary interior causes a planetary dynamo, plate tectonics, and volcanism. Atmospheric convection drives global and local weather. However, this mechanism is outside of the scope of this thesis. Heat transport of a moving fluid alone is termed advection and is also out of the thesis's scope.

The preparatory thoughts finally allow the formulation of the radiation balance equation for a planetary surface. Following the Stefan-Boltzmann law (Equation 3.70), the surface temperature at a surface position $\mathbf{r}$ equals the total radiative power F_{total}, that arrives at this point plus the contribution through heat conduction

$$\bar{\epsilon}_{\text{h}}\sigma T^4(\mathbf{r}) = \underbrace{(1-A_{\text{dh}})F_{\text{sun}}(\mathbf{r}) + (1-A_{\text{dh}})F_{\text{sca}}(\mathbf{r}) + (1-A_{\text{dh,th}})F_{\text{rad}}(\mathbf{r})}_{F_{\text{total}}} + k_{\text{h}}\mathbf{n}\cdot\nabla T(\mathbf{r_0}). \tag{3.85}$$

The albedo $A_{\text{dh,th}}$ differs from A_{dh} (Equation 3.80) because it depends on the thermal emission $U(T)$ of the surface instead of the solar emission E_0. Computing this quantity in any scenario is difficult, so a common choice is $A_{\text{dh,th}} = 0.05$. The solar power F_{sun} primarily drives the temperature and reads

$$F_{\text{sun}}(\mathbf{r}) = \frac{S_{\odot} v(\mathbf{r}) \cos i(\mathbf{r})}{R^2(\mathbf{r})}, \tag{3.86}$$

where $S_{\odot}$ is the solar constant at 1 AU, v indicates if the Sun is visible at $\mathbf{r}$, and R is the solar distance in AU. The scattered component combines the single and multiple scattered sunlight from the surrounding area Σ

$$\begin{aligned} F_{\text{sca}}(\mathbf{r}) =& A_{\text{dh}} \int_{\Sigma} f(\mathbf{x},\mathbf{r}) F_{\text{sun}}(\mathbf{x}) d\mathbf{x} \\ &+ A_{\text{dh}}^2 \int_{\Sigma} f(\mathbf{x},\mathbf{r}) \int_{\Sigma} f(\mathbf{y},\mathbf{x}) F_{\text{sun}}(\mathbf{y}) d\mathbf{y} d\mathbf{x} \\ &+ \ldots, \end{aligned} \tag{3.87}$$

where f is the view-factor (Equation 3.83). Self-heating works similarly

$$\begin{aligned} F_{\mathrm{rad}}(\mathbf{r}) =& \int_{\Sigma} f(\mathbf{x},\mathbf{r}) \overline{\epsilon}_{\mathrm{h}} \sigma T^4(\mathbf{x}) d\mathbf{x} \\ &+ A_{\mathrm{dh,th}} \int_{\Sigma} f(\mathbf{x},\mathbf{r}) \int_{\Sigma} f(\mathbf{y},\mathbf{x}) \overline{\epsilon}_{\mathrm{h}} \sigma T^4(\mathbf{y}) d\mathbf{y} d\mathbf{x} \\ &+ \ldots . \end{aligned} \tag{3.88}$$

Most approaches omit the multiple integrals, and some even drop F_{sca} and F_{rad} entirely. In Section 5.2, the author develops a new solution approach to the discretized version.

3.5.2 Thermophysical models for airless planetary bodies

This subsection has been taken from Wohlfarth et al. [2023].

Thermophysical models (TPMs) of airless planetary bodies are used in astronomy and planetary geoscience. Nearly every science case and target has its own thermal model. This diverse landscape is motivated by two broad application scenarios: TPMs help astronomers characterize asteroids from telescopic observations. Planetary scientists employ TPMs to analyze planetary regolith and volatile stability from remote sensing data. The astronomical and geoscience perspectives overlap but are rarely reviewed together. For a review of (asteroid) thermal modeling, readers can refer to Delbo et al. [2015], who differentiate between equilibrium models and TPMs that include roughness, heat conduction, and sometimes scattering and self-heating. The first thermal asteroid models are often referred to as the standard thermal model (STM) of Lebofsky et al. [1978] and Lebofsky et al. [1986] that assumed a fixed shape, simple thermal equilibrium, and a beaming parameter that accounts for anisotropy due to roughness. In the literature, the surface roughness is operationalized in different ways, but the most common definitions are the Hapke-$\overline{\theta}$ and the RMSL (Appendix C). The near earth asteroid thermal model (NEATM) [Harris, 1998] and its modifications [Myhrvold, 2018] form the de facto standard for asteroid thermal modeling today if the data prohibit the use of a full TPM [Delbo et al., 2015]. Thermophysical models are more complex and are the method of choice if adequate data are available. Thermophysical models date back to the first lunar studies. Pettit and Nicholson [1930] found that a smooth surface in thermal equilibrium does not explain the thermal phase curve of the Moon. Smith [1967], Buhl et al. [1968], and Sexl et al. [1971] modeled the rugged lunar surface with spherical craters and suggested that shadows and an altered temperature distribution explain the shape of the thermal phase curve. Spencer et al. [1989] and Spencer [1990] adopted the lunar models for general airless bodies, thereby establishing the basis for most current asteroid TPMs [Delbo et al., 2015]. All these models [Spencer, 1990; Lagerros, 1996; Emery et al., 1998; Rozitis and Green, 2011, 2012, 2013; MacLennan and Emery, 2018; Rozitis et al., 2020] combined an equilibrium term, a thermal roughness model, and a heat conduction model. Nonresolved surface roughness controls the angular deviations of the emitted flux, which are responsible for the thermal beaming effect of asteroids or the non-Lambertian phase curve of the Moon. Roughness is commonly modeled by spherical segment craters [Smith, 1967; Spencer, 1990; Lagerros, 1996; Emery et al., 1998; Rozitis and Green, 2011, 2012, 2013; MacLennan and Emery, 2018], random Gaussian surfaces [Davidsson et al., 2015; Grumpe et al., 2019; Rubanenko et al., 2020], and by realistic fractal rough surface models [Davidsson et al., 2015; Rozitis et al., 2020]. Heat conduction becomes important if the rotational period of the body is comparatively fast or if the goal is to infer the thermal inertia from nightside measurements. Heat conduction can generally be neglected on the dayside if rotation is slow. Myhrvold [2018] reviews thermophysical asteroid modeling in the presence of reflected sunlight and points out how to correctly account for energy conservation in spectral regions, where thermal emission and solar reflection superimpose.

Since the early 2000s, several infrared detectors have visited airless bodies to map the thermal inertia, acquire emissivity spectra for mineralogical interpretation, and to determine the surface roughness: OTES on OSIRIS-REx for Bennu [Christensen et al., 2018], VIR on DAWN for Vesta [De Sanctis et al., 2012], TIR on Hayabusa2 for Ryugu [Okada et al., 2018], VIRTIS on Rosetta for 67P/Churyumov–Gerasimenko [Coradini et al., 2007], Diviner on LRO for the Moon [Paige et al., 2010a], the Moon Mineralogy Mapper (M^3) for the Moon on Chandrayaan 1 [Pieters et al., 2009a], and MERTIS on BepiColombo for Mercury [Hiesinger and Helbert, 2010]. The geophysical community is primarily interested in the thermophysical characteristics of the upper regolith and developed thermal heat conduction models, mostly in parallel to the asteroid thermophysical models. Keihm and Langseth Jr. [1973] first inferred the thermal conductivity of the lunar regolith near the Apollo 17 landing site. Vasavada et al. [1999] and Paige et al. [2010b] modeled lunar temperature stability to analyze the stability of polar volatiles with either a heat conduction model or an equilibrium model. Hayne et al. [2017] presented a detailed subsurface heat conduction model and derived the Moon's global thermal conductivity and thermal inertia maps from Diviner lunar radiometer measurements – again without roughness even though roughness has been thoroughly modeled for asteroids, Bandfield et al. [2015] were the first to derive roughness values from Diviner nadir and off-nadir measurements. The brightness temperatures inferred from Diviner channel four (8.25 μm) and channel seven (25–41 μm) are similar for small incidence angles but deviate for increasing incidence angles. Brightness temperature differences can be as high as 70 K in the early morning or late evening. Diviner further acquired off-nadir measurements (EPF functions) to cover a broad range of emission angles up to approximately 80°. Bandfield et al. [2015] found that an RMSL of 20° of a Gaussian slope distribution model best matches the nadir observations, and an RMSL of 20-35° best matches a small set of multiangle measurements. Bandfield et al. [2015] further employed a small-scale heat conduction model showing that those surface elements greater than $\sim$0.5–5 mm remain thermally isolated. Rubanenko et al. [2020] repeated a roughness study with telescopic measurements of Sinton [1961] and Diviner data and found a bi-directional RMSL of $30.2\,^\circ \pm 5.9\,^\circ$ for maria and $36.8\,^\circ \pm 4.4\,^\circ$ for highlands. Heat conduction models are used for other planetary bodies such as Ceres [Rognini et al., 2020] and Vesta [Capria et al., 2014]. Marshall et al. [2018] mapped the thermal inertia of 67P/Churyumov–Gerasimenko. Bauch et al. [2014, 2021] adapted a heat-conduction model for the planet Mercury that is planned to derive the thermal inertia from MERTIS measurements.

3.5.3 Thermal correction for lunar hydration analysis

This subsection has been taken from Wohlfarth et al. [2023].

Reflectance spectra of airless bodies may exhibit absorption features around 3 μm that provide valuable information on the spatiotemporal distribution of hydroxyl (OH) and water (H_2O). The spectral domain around 3 μm is characterized by the superposition of reflected solar flux and emitted thermal flux that obscures the absorption in the reflectance spectrum. The thermal emission component must be removed to access the 3 μm band, which is usually achieved by subtracting the modeled thermal emission from the total spectral radiance. Consequently, the thermal model directly controls the retrieved band depth around 3 μm, influencing the alleged abundance of OH/H_2O. As discussed in Section 2.1.4, previous studies employed different thermal models that yield observations that only partly agree on the temporal and spatial variations of lunar OH/H_2O. Li and Milliken [2017] used an empirical model, Bandfield et al. [2018] and Wöhler et al. [2017] used a thermal equilibrium model with Gaussian roughness, and Honniball et al. [2020] employed the excess thermal removal method for asteroids [Rivkin et al., 2005; Reddy et al., 2009; Takir and Emery, 2012]. Surprisingly, the models used for thermal correction neither take inspiration from the rich thermal model menagerie developed and tested over the past decades (see Section 3.5.2) nor have they been extensively tested for the lunar surface. Consequently, the current discourse on superficial lunar OH/H_2O will significantly benefit from assessing the quality of thermal correction methods.

3.5.4 Thermophysical models for emissivity mapping of the Moon and Mercury

This subsection has been taken from Wohlfarth et al. [2023].

Following Equation 3.73, the emissivity is retrieved by dividing the measured spectral radiance by the spectral radiance of a perfectly absorbing surface. For nadir observations at small incidence angles, the emissivity can be retrieved by simply dividing the measured flux by a single Planck function of unit emissivity. However, surface roughness is crucial at larger incidence angles during sunrise and sunset, larger emission angles during off-nadir observations, and large incidence and emission angles during flyby maneuvers. Different surface temperatures lead to a superposition of multiple Planck functions of different temperatures, which results in a non-linear function that is not a Planck function anymore [Davidsson et al., 2015]. The emissivity can only be retrieved by dividing the measured spectral radiance by this non-linear function. Consequently, emissivity retrieval requires a thermal roughness model. So far, emissivity spectra of Mercury have been extracted from coarse telescopic data with thermal roughness models, such as the model by Emery et al. [1998]. Section 5.2 presents the simulation results for various geometries, extending previous investigations of Davidsson et al. [2015] and preparing for the upcoming MERTIS data.

3.5.5 Thermophysical models for exoplanetary phase curves

Almost all exoplanets that have been detected bear some kind of atmosphere. Consequently, thermal models of exoplanets almost exclusively employ atmospheric heat models. Maurin et al. [2012] theoretically analyze thermal phase curves of airless exoplanets but without a detailed discussion of surface roughness. Only recently have a few atmosphere-less exoplanets been detected, and only since the JWST has been deployed can the subtle thermal signature of these worlds be measured. Consequently, no thermal roughness model has yet been applied for airless exoplanet analysis. The author initiated and co-applied for a JWST campaign to search for a regolith on the airless exoplanet Luyten Half-Second (LHS) 3844b as outlined in Section 5.

3.6 Infrared detectors

3.6.1 Spectrometer design

Infrared spectroscopy requires instruments that measure the electromagnetic radiation of planetary bodies (or any other celestial object) for a given wavelength range. Infrared measurement devices usually consist of three components: The optics that collect and redirect the electromagnetic radiation, a dispersing element that decomposes the light into its spectral components, and the actual detector that translates the electromagnetic intensity into digital numbers. The optics should minimize aberration, and if sent to space, they should be as compact as possible. Classical designs such as the Newton or Cassegrain reflectors gave way to more compact three-mirror systems that considerably reduced aberrations. Spectral decomposing is generally achieved with gratings or modifications such as grisms and echelles. Interferometer designs exist, such as the Fabry-Perot or the Fourier-transform spectrometer. The detectors are usually charge-coupled device (CCD) sensors for VNIR wavelengths or microbolometers for larger wavelengths in the MIR. For a detailed introduction to astronomical optics, see Schroeder [2000]; Heidt [2022]. Infrared spectroscopy has numerous applications in astronomy and planetary science that impose different requirements on wavelength range, operation mode, resolution, and dimensions, spawning multiple detector designs. Common causes are spectrographs attached to terrestrial, airborne, or space telescopes and imaging spectrometers that orbit the Earth or other astronomical objects. Four imaging spectrometers discussed in this thesis share a common design principle. They combine a three-mirror anastigmat telescope with an Offner system that consists of a mirror and a diffraction grating. The three-mirror telescope reduces coma, astigmatism, and spherical aberration. The Offner design further reduces aberrations and fits the dispersion grating into a compact format. The other instruments each have their own design. For details, see Section 4.

3.6.2 Calibration

Instrument characterization and calibration are intricate, so a significant part of infrared astronomy and planetary remote sensing revolves around instrumentation and calibration. The acquired infrared light takes a complex path through the instrument until it reaches the detector element. Meaningful data interpretation requires calibration that converts the raw measurement into a physical quantity (usually radiance) while correcting for any effect in the optical path. Every detector is unique and requires its calibration routine. However, most calibrations that involve a CCD or microbolometer array are essentially a variation of a basic sensor model that assumes a pixel grid with N rows and M columns. The calibrated spectral radiance I in the n^{th} row and m^{th} the column is an affine linear transform of the raw digital number DN with a factor g and an offset, often termed dark current DK. The factor g primarily converts between raw measurements and physical units, and the dark current is the offset of an individual pixel when not illuminated:

$$I_{\mathrm{n,m}} = g_{\mathrm{n,m}} DN_{\mathrm{n,m}} - DK_{\mathrm{n,m}}. \tag{3.89}$$

Real detectors may exhibit a non-linear characteristic and require more summation terms and models for smear, dwell, and illumination times, detector efficiencies, thermal effects, and many more. Infrared detectors often need ongoing re-calibration that can be achieved with any form of ground truth, such as calibration standards carried along or specific calibration targets. This thesis assumes that all data is radiometrically calibrated. For more details on infrared sensor calibration in astronomy, see Heidt [2022]. For thermal remote sensing detectors, see Künzer and Dech [2013].

3.6.3 Point spread function and atmospheric seeing

This subsection has been adapted from Wohlfarth et al. [2023].

The point spread function (PSF) and the modulation transfer function (MTF), which is the Fourier transform of the PSF, characterize any optical device. In terms of system theory, the PSF is an impulse response that describes the reaction of the optical system to a point-like disturbance. Atmospheric seeing affects terrestrial telescopic observations, which degrades the PSF and thus limits the target's resolution. Atmospheric turbulences lead to fluctuations of the atmospheric permittivity that constantly abberates the electromagnetic radiation toward the telescope. Light portions of the target, which have all been aberrated differently, reach the sensor, overlap, and produce a blurred version of the original radiance distribution. The point spread function of the atmosphere is then known as the seeing disk. Atmospheric seeing is known to be wavelength-dependent. The blurring is stronger for shorter wavelengths and weaker as the wavelength increases, where the full-width half maximum (FWHM) is $\sim \lambda^{-1/5}$ [Boyd, 1978]. Seeing can be modeled by a convolution of the original spectral radiance image I with the impulse response W of the atmosphere given by the PSF. Even though theoretically motivated derivations of complex atmospheric PSFs exist (e.g., Moffat [1969]), it is often sufficient to choose a Gaussian PSF. Consequently, the spectral radiance I_{S} measured by the telescope is a convolution of a wavelength-dependent PSF with the spectral radiance I that emerges from the surface

$$I_{\mathrm{S}}(x, y, \lambda) = PSF(x, y, \lambda) * I(x, y, \lambda). \tag{3.90}$$

Note that x and y denote the coordinates of the spectral radiance projected onto the image plane as seen by the telescope. In regions without thermal emission, dividing the spectral radiance by the solar spectral irradiance yields the reflectance

$$r_{\mathrm{d,s}}(x, y, \lambda) = PSF(x, y, \lambda) * r_{\mathrm{d}}(x, y, \lambda). \tag{3.91}$$

Therefore it is easily possible to work with reflectance images. The Gaussian PSF is defined as

$$PSF(x, y, \lambda) = \frac{1}{\sqrt{2\pi\sigma(\lambda)^2}} e^{-\frac{1}{2}\frac{x^2+y^2}{2\sigma(\lambda)^2}}. \tag{3.92}$$

As shown by [Boyd, 1978], the width of the Gaussian PSF is given by the standard deviation

σ modeled as

$$\sigma(\lambda) = b\lambda^{-\frac{1}{5}}, \tag{3.93}$$

where b is a calibration parameter adjusted to fit the current atmospheric conditions. The FWHM of the PSF is related to σ by

$$\mathrm{FWHM}(\lambda) = 2\sqrt{2\ln(2)}\sigma(\lambda). \tag{3.94}$$

There are several ways to limit seeing effects and increase the resolution. Airborne telescopes only see through a thin layer of the atmosphere, and space telescopes do not look through the air at all. However, they are expensive, restricted by spacecraft constraints, and maintenance is almost impossible. An alternative is adaptive optics, which can estimate and thus compensate for the atmospheric distortion at the cost of processing overhead.

3.7 Practical methods for remote compositional analysis

Mineral grains on planetary surfaces form an intimate mixture such that the resulting spectrum is a spectral superposition of the individual components (endmembers) and other components, such as alteration products. The author identifies qualitative and quantitative approaches for remote mineralogical analysis of planetary infrared spectra, often supported by reflectance models and statistical tools. The qualitative approach visually inspects planetary infrared spectra and draws qualitative conclusions based on experience and comparison with laboratory measurements. The position of spectral features gives a first impression of the mineralogy. Strong absorption bands near $1\,\mu$m and $2\,\mu$m generally indicate an iron-rich mineralogy. The spectral slope and the overall darkness give clues about the soil's maturity. For a summary, see Pieters et al. [2019]. In the MIR the Christiansen feature lies around $8\,\mu$m, and a shift to lower wavelengths indicates a feldspathic, and a shift to longer wavelengths indicates a mafic mineralogy [Greenhagen et al., 2010]. However, space weathering [Lucey et al., 2021] and thermal gradients [Millán et al., 2011; Donaldson Hanna et al., 2017] influence the position of the Christiansen feature. Thermal gradients and particle size also change the spectral contrast [Donaldson Hanna et al., 2017]. The position and shape of the Reststrahlen bands may also indicate the presence of individual minerals. Spectral unmixing techniques attempt to analyze the endmembers' spectral mixtures and output abundances quantitatively. In the MIR region, emissivity spectra mix linearly, which means that the resulting spectrum is a weighted sum of the end member spectra, and mineral abundances can be determined by simple least squares analysis [Ramsey and Christensen, 1998; Bandfield and Rogers, 2019]. In the NIR, however, the endmember reflectance spectra mix non-linearly [Farrand et al., 2019]. Spectral unmixing requires a reflectance model, such as the Hapke model, that normalizes and translates the spectral information into single scattering albedo spectra. The w-spectra can then be treated with linear unmixing [Mustard and Pieters, 1989; Liu et al., 2016; Rommel et al., 2017]. Several statistical tools help hyperspectral data and image analysis in planetary science. Recently, Hess et al. [2021] embedded a Hapke-based spectral unmixing approach into a Bayesian framework, which yields abundances and uncertainty values. Unsupervised clustering approaches such as support vector machines or self-organizing maps have proven useful in handling large datasets [Farrand et al., 2019]. Another approach is the Factor Analysis Target Transform (FATT) [Hopke, 1989], which decomposes the different measurements into a base of ideal factors that can subsequently be related to laboratory endmember spectra [Bandfield et al., 2000]. Linear spectral unmixing with Bayesian uncertainties and unsupervised classification techniques are best suited for analyzing the upcoming MERTIS MIR emissivity spectra. The Berlin Emissivity Database [Maturilli et al., 2008] and measurements from the IRIS lab [e.g. Weber et al., 2023] provide laboratory constraints for Mercury's environment.

3.8 Infrared spectroscopy of exoplanets

The previous sections focussed on (airless) planetary bodies in the solar system for which disk-resolved data are already available or can, in principle, be recorded with reasonable effort. Exoplanet imaging and spectroscopy techniques have yet to reach a level of precision to obtain disk-resolved measurements and likely will take a long time to come. There are a few rare cases in which exoplanets can be directly imaged with adaptive optics, but only if the planet is comparatively hot to emit a strong signal and the angular separation to the host star is large. The vast majority of exoplanets can only be accessed indirectly, monitoring subtle variations of the host stars. Early exoplanet detections determined the Doppler shift of the host star is caused by the gravitational pull of orbiting exoplanets. These measurements allow for determining an exoplanet's radial velocity and mass but provide no spectral information. If correctly aligned, an observer may also sense the transit of an exoplanet in front of its host star. The exoplanet blocks a fraction of the starlight, noticeable as a slight dip in the star's brightness. The transit time, the transit period, how long it takes to slide into the disk, and the relative darkening reveal the orbital period and the exoplanet's size. Exoplanetary transits also enable spectroscopy of planetary atmospheres. The solid part of the planet blocks the starlight, but the atmosphere attenuates the light depending on the wavelength. Consequently, the adequate exoplanet disk size (solid planet + opaque atmosphere) varies with wavelength and can be determined with the transit method. For comprehensive reviews of exoplanet detection methods, see Bozza et al. [2016], and for spectroscopic characterization methods, see Kreidberg [2017]; Parmentier and Crossfield [2018]. Another method for exoplanet spectroscopy is phase curve analysis. A phase curve is a disk-integrated radiation emerging from a planetary body as a function of the body's phase angle between the light source and the observer position. Historically, phase curves were important for solar system planet characterization before high-precision telescopes existed and still give information about faint solar system asteroids. Exoplanet phase curves are not directly accessible. However, measuring the combined flux of the host star and the orbiting exoplanet enables spectro-photometric studies of the planet. This method will be used to analyze exoplanet LHS 3844b.

Chapter 4

Instruments and datasets

This chapter presents specifications and further references for all infrared instruments used in this thesis. The chapter also lists the observation conditions of related datasets.

4.1 Gaofen-4

This subsection has been adapted from Wohlfarth et al. [2023].

The Chinese Government issued the China High-Resolution Earth Observation System Programme, which has launched twelve earth observation satellites since 2013 [Li, 2022]. The Gaofen-4 (GF-4) (高分四号) geostationary satellite was launched on December 28, 2015. It carries a five-band multispectral VNIR detector that covers the wavelengths from 0.45–0.9 μm and a MIR detector with one band between 3.5–4.10 μm around a center wavelength of 3.77 μm [Wu et al., 2021]. No detailed information about the instrument is publicly available. In the Summer of 2018, GF-4 pointed away from Earth and imaged the Moon for five days with a resolution of about 4 km/pixel at the lunar equator, yielding the first spaceborne high-resolution MIR images of the Moon [Wu, 2019; Wu et al., 2021]. Table 4.1 lists the observation conditions. This dataset is used to test the thermophysical roughness model (Section 5.2) in the NIR region, as presented in Section 5.4.2.

Table 4.1. The geometry of five lunar observations by the Gaofen-4 satellite [Wu et al., 2021].

Time (UTC)	Moon-Sun distance (AU)	Moon-Camera dist. (10^3 km)	Subsolar point (°)		Subcamera point (°)		Phase angle (°)
			Lat	Lon	Lat	Lon	
2018-03-02 04:00:25	0.991	407.98	-0.75	02.16	-1.68	2.37	-00.95
2018-07-25 02:49:02	1.016	444.37	-0.11	32.83	-5.68	3.21	-30.09
2018-07-28 04:49:00	1.015	445.81	-0.02	-04.77	-1.47	-1.17	03.88
2018-07-30 06:49:20	1.015	444.39	0.03	-30.18	2.08	-3.33	26.92
2018-08-04 12:25:20	1.015	420.63	0.18	-94.06	8.42	-5.00	89.04

4.2 Diviner

This subsection has been adapted from Wohlfarth et al. [2023].

The Diviner Lunar Radiometer onboard the Lunar Reconnaissance Orbiter (LRO) [Paige et al., 2010a] has been surveying the lunar surface since 2009. The instrument has considerable heritage from the Mars Climate Sounder, for which detailed optical descriptions exist [McCleese et al., 2007]. Diviner has two telescopes, A and B, each with an identical but mirror-symmetrical optical path. The optics do not contain a diffraction grating, but the filter bench directly lies in the focal plane of a three-mirror system. The radiometer has nine spectral channels with 21 pixels each that scan the lunar surface from 0.3–400 μm and are distributed across the two subsystems. Three narrowband mineralogical filters around 7.8 μm, 8.25 μm, and 8.55 μm (all on side A) constrain the position of the Christiansen feature at daytime temperatures. Two additional NIR channels on side A are designed to measure the solar reflectance. The broadband channels from 13–23 μm, 25–41 μm, 50–100 μm, and 100–400 μm (first channel on side A, rest on side B) measure the long wavelength tail of thermal emission and constrain the cold nighttime and polar thermal environment. The resulting datasets help to constrain the thermophysical properties of the Moon. The instrument can rotate around vertical and horizontal axes, allowing for off-nadir measurements. The so-called emission phase function (EPF) measurements [Bandfield et al., 2015] comprise a specific pattern of off-nadir pointings that take roughly four minutes. The solar incidence angle stays essentially constant during this short period, but the emission angle takes nine distinct configurations. In the first ninety seconds, the emission angle decreases in four steps from roughly 75° to 50°. In the next thirty seconds, Diviner observes in near-nadir view

Table 4.2. The geometry of eleven lunar off-nadir observations by the Diviner Lunar Radiometer [Bandfield et al., 2015].

Time (UTC)	Moon-Sun distance (AU)	Moon-Camera dist. (km)	Subsolar point (°)		Subcamera point (°)		Orbit (No.)
			Lat	Lon	Lat	Lon	
2010-09-03 19:26:52	1.008	52.60	-1.34	237.29	-9.90	263.72	5497
2010-09-03 19:31:50	1.008	51.66	-1.34	237.25	-25.67	263.97	5497
2010-09-03 21:09:57	1.007	54.23	-1.34	236.42	21.84	262.21	5498
2010-09-03 21:14:07	1.007	53.84	-1.34	236.38	8.64	262.42	5498
2010-10-13 17:10:00	0.997	64.13	-1.49	110.32	-61.88	98.86	6005
2010-10-13 17:13:47	0.997	63.09	-1.49	110.29	-71.23	99.97	6005
2010-10-13 18:36:14	0.997	57.76	-1.49	109.59	21.87	95.56	6006
2010-10-13 18:40:24	0.997	60.49	-1.49	109.55	8.74	95.80	6006
2010-11-09 22:44:25	0.989	62.72	-1.12	138.70	-9.83	97.86	6352
2010-11-09 22:49:23	0.989	64.04	-1.12	138.66	-25.41	98.16	6352
2010-11-09 00:27:30	0.989	57.55	-1.12	137.82	21.69	96.27	6353
2010-11-09 00:31:40	0.989	60.15	-1.12	137.79	8.56	96.52	6353

with $e \approx 0°$. After that, the emission angle jumps from 0° to approximately 50° and follows four steps up to around 75° in another ninety-second interval. During the first ninety seconds and the first four configurations, Diviner points up-track. During the last ninety seconds, the instrument looks down-track. Depending on the subsolar point, this leads to two groups of azimuth angles that are either below or above 90°, which means that the solar vector and the view vector roughly point in the same direction or in opposite directions. The EPF observations are well suited to validate thermal models because they comprise different combinations of incidence, emission, and azimuth angles in the MIR at which roughness effects come into play. This study uses the same EPF datasets as Bandfield et al. [2015] (see Table 4.2).

4.3 Moon Mineralogy Mapper (M^3)

This subsection has been adapted from Wohlfarth et al. [2023].

The M^3 instrument on board the Chandrayaan-1 probe combines a three-mirror anastigmat telescope with an Offner spectrometer, which allows for a compact and aberration-free build [Green et al., 2011]. The three-mirror telescope reduces coma, astigmatism, and spherical aberration. The Offner design further reduces aberrations and incorporates the dispersion grating into a compact design. M^3 mapped the lunar surface in the NIR domain primarily to detect mineral absorption bands [Pieters et al., 2009a]. The pushbroom grating spectrometer covered a wavelength range from 0.42–3 μm with 86 channels and provided a ground resolution of 140 m/pixel [Pieters et al., 2009a]. The spectrometer acquired nearly global coverage sampled at different times of the day until contact loss in the summer of 2009. Although no global coverage is available for every local time interval, many regions were observed at various times of day, allowing the study of diurnal patterns. This study used the level 1B radiance data available on the Planetary Data System (PDS) node, which the author processed according to photometric normalization with the method described by Wöhler et al. [2017] and Grumpe et al. [2019] extended by the thermal model in Chapter 5.

4.4 Current and upcoming lunar spectrometers

Beyond the instruments already mentioned, one other spectrometer is currently surveying the Moon, and two instruments are scheduled for launch in early 2024. Like the others, the IIRS onboard the Indian lunar probe Chandrayaan-2 combines a three-mirror anastigmat and an Offner spectrometer [Chowdhury et al., 2020]. The instrument currently maps the lunar surface from 0.8-5.0 μm, surpassing M^3's wavelength range. The first data release is, as of February 2025, expected soon. Further, NASA's Lunar Trailblazer is scheduled for launch in early 2025 and carries the HVM^3 and the Lunar Thermal Mapper (LTM). HVM^3 has a similar TMA and Offner mirror design as M^3 and will map the lunar surface from 0.6-3.6 μm [Ehlmann et al., 2022], continuing the work of its predecessor. The LTM [Bowles et al., 2020] is a miniaturized version of the Compact Modular Sounder (CMS) and will expand on Diviner's work. The instrument has eleven mineralogical narrow-band channels around 8 μm and four broadband thermal channels. IIRS and HVM^3 will acquire more data that may give new clues about the lunar hydroxyl/water distribution. All three instruments, especially LTM, will likely yield more insights about the lunar mineralogy and the thermal environment. Further, the company Ororatech is launching its satellite constellation for forest fire detection on Earth. Each satellite carries an infrared camera, which is calibrated with regular lunar acquisitions. The thermal model developed in this thesis can help calibrate these instruments by comparing the modeling results with the lunar measurements [Seifert et al., 2024].

4.5 MERTIS

This subsection has been taken from Wohlfarth et al. [2023].

MERTIS onboard BepiColombo combines a spectrometer with 78 spectral bands between 7–14 μm at a spectral resolution of $\lambda/\Delta\lambda = 78 - 156$ with a two-channel radiometer for 7 and 40 μm [Hiesinger and Helbert, 2010; Hiesinger et al., 2020]. The spectrometer's ground sampling interval (GSI) is expected to be better than 500 m, and the radiometer's GSI will be better than 5000 m. Like the above-mentioned devices, the instrument combines a three-mirror anastigmat with an Offner spectrometer. For more technical details, such as the calibration routines and onboard calibration targets, science modes, and more, see Hiesinger and Helbert [2010] and Hiesinger et al. [2020]. On April 9, 2020, the BepiColombo spacecraft performed a gravity-assist maneuver with Earth, and the MERTIS pushbroom sensors scanned the lunar disk at a distance of approximately 700,000 km [Hiesinger et al., 2021]. Table 4.3 provides the observation conditions. This dataset represents the first spaceborne hyperspectral infrared measurements of the Moon in this wavelength domain. Due to the stacked cruise configuration of BepiColombo, the planetary observation baffle of MERTIS was occluded, and the spectra were acquired through the deep space calibration baffle. The lunar surface is typically colder than the surface of Mercury, so the measured radiance is approximately ten times weaker, leading to a lower signal-to-noise ratio. The pushbroom sensor scanned the lunar disk from west to east, but due to the considerable distance between the spacecraft and the Moon, only six out of one hundred pixels captured the lunar disk. The ground interval of a pixel corresponds to 500 km, which also determines the distance between parallel tracks. MERTIS sampled approximately three thousand points along the track during the scan, resulting in a radiance profile across the entire disk. Altogether, the

Table 4.3. The geometry of lunar observations during MERTIS lunar flyby.

Time (UTC)	Moon-Sun distance (AU)	Moon-Camera dist. (10^3 km)	Subsolar point (°)		Subcamera point (°)		Phase angle (°)
			Lat	Lon	Lat	Lon	
2020-04-09 05:00:10	1.0039	734.25	-1.45	-12.68	0.77	-5.58	7.43
2020-04-09 05:59:24	1.0039	717.51	-1.45	-13.22	0.68	-5.77	7.75

MERTIS observed the Moon under challenging conditions but allowed for valuable checks of the geometric and radiometric calibration of MERTIS and the thermal model. Due to the challenging spectral calibration under these operational constraints, the author spectrally binned the data and limited the spectral resolution to four broad channels between $7\,\mu$m and $14\,\mu$m. The dataset allowed the radiance from the lunar surface to be traced for a broad range of incidence and emission angles, similar to the validation by GF-4 measurements. This situation allowed cross-checks between the measured and radiometrically calibrated data on the one hand and the model predictions on the other hand before the Mercury flyby in late 2024 and subsequent in-orbit operations.

4.6 MDIS

The Mercury Dual Imaging System (MDIS) onboard the MESSENGER spacecraft consisted of a narrow-angle camera (NAC) and a wide-angle camera (WAC). The NAC camera measures from 700–800 nm with a field of view of $1.5° \times 1.5°$. The WAC camera has a field of view of $10.5° \times 10.5°$ and a filter wheel with twelve different wavelength filters between 430–1040 nm. The cameras are mounted on a pivot platform, allowing a broad emission angle range. For more details, see Hawkins et al. [2007], who outlined the instrument design in detail. During its operational period in Mercury's orbit from 18 March 2011 to 30 April 2015, MDIS conducted various imaging campaigns that globally mapped the planet and acquired images under varying observation conditions [Denevi et al., 2017]. Becker et al. [2009] processed the MDIS WAC imagery into a near-global mosaic of Mercury for three wavelength bands (430 nm, 750 nm, 1040 nm). The author uses this dataset to estimate the directional hemispherical albedo for Mercury thermal simulations in Section 5.4.5 and for photometric studies of Mercury and the influence of wavelength-dependent seeing in Chapter 7.

4.7 Telescopic observations of Mercury

This subsection has been adapted from Wohlfarth and Wöhler [2022].

The Mariner 10 spacecraft did not acquire datasets that allowed a detailed compositional analysis. Before the MESSENGER spacecraft mapped Mercury with the multispectral MDIS camera, most compositional studies were based on telescopic spectra from various instruments in the NIR and the MIR range. Table 4.4 lists the telescopic campaigns in the VNIR wavelength region that have been conducted in the last three decades. The instrument abbreviations are Swedish Vacuum Solar Telescope (SVST), Nordic Optical Telescope (NOT), Alhambra Faint Object Spectrograph and Camera (ALFOCS), Infrared Telescope Facility (IRTF), New Technology Telescope (NTT), and Son of ISAAC (Sofi). Observations number 08, 11, 12, and 19 will be studied in depth in Section 7.3.2.

Table 4.4. Telescopic campaigns of Mercury in the visible and near-infrared. SELO: Sub-Earth Longitude, SELA: Sub-Earth Latitude, SSLO: Sub-Solar Longitude, SSLA: Sub-Solar Latitude is approximately zero and not displayed, ϕ: Phase angle in degree, AD: Angular Diameter in arcseconds, S: Seeing in arcseconds. The ephemerides are taken from the referenced publications. The values marked by ^{a} are taken from the HORIZON system `https://ssd.jpl.nasa.gov/horizons/app.html`. Table taken from Wohlfarth and Wöhler [2022].

Campaign	**No**	**Date**	**Time UTC**	**SELO**	**SELA**	**SSLO**	ϕ	**AD**	**S**
Warell and Limaye [2001]	01	20.10.1995	08:00	273.71	2.68	359.43	85.7	6.94	
SVST	02	22.10.1995	07:30	283.74	2.32	359.64	75.9	6.57	
550 - 940 nm	03	19.04.1996	15:00	91.43	-2.35	2.01	89.4	7.09	
	04	22.11.1997	17:30	213.22	-1.27	154.58	58.6	5.92	
	05	24.11.1997	16:30	222.82	-1.53	159.42	63.4	6.12	
	06	09.07.1998	19:00	307.68	6.34	223.69	84	6.98	
	07	27.04.1999	07:30	58.35	-1.41	143	75.6	6.59	
Warell [2003]	08	20.06.1999	20:41 - 21:02	291.8	4.8	207	84.8	7.0	
NOT with ALFOCS, 520 - 970 nm	09	22.06.1999	20:23 - 20:35	301.5	5.2	212.5	89.1	7.2	
Warell and Blewett [2004]	10	01.07.2002	05:57	277.1	5.3	354.7	60.7	6.5^a	
NOT with ALFOCS, 400 - 670 nm									
Warell et al. [2006]	11	26.06.2002	17:48 - 19:47	241	5.6^a	341	99.4	7.7	1
IRTF with SpeX	12	17.08.2003	18:06 - 21:41	197	8.2^a	102	95.3	7.8	1
700 - 5300 nm	13	17.08.2003	18:22 - 21:48	197	8.2^a	102	95.3	7.8	1
Vernazza et al. [2010]	14	28.02.2008	19:30 - 20:30	141	-7	27	89	7.5	1.5
IRTF with SpeX	15	29.02.2008	18:45 - 20:30	147	-7	27	87	7.4	1.5
900 - 2400 nm	16	22.03.2008	18:45 - 20:30	254	-4	21	53	5.6	1
	17	23.03.2008	18:30 - 20:30	258	-4	21	51	5.6	2
	18	13.05.2008	21:00 - 23:30	120	1	22	105	8.0	2
	19	14.05.2008	21:00 - 23:00	125	1	22	107	8.2	1.5
Erard et al. [2011]	20	16.06.2006	22:20 - 22:32	233.24	4.82	327.7	99.44	7.5^a	1.6
NTT with Sofi, 940 - 2500 nm									
Varatharajan et al. [2019]	21	16.12.2018	20:15	58.51	-3.92	348.06	70.50	6.4	
IRTF with SpeX, 700 - 2400 nm									

4.8 NIRSpec

The James Webb Space Telescope (JWST) carries four scientific instruments, one of which is the Near-Infrared Spectrograph (NIRSpec), a multi-purpose spectrograph that covers a spectral range from $0.6 - 5.3\,\mu m$. NIRSpec's optical path comprises seven elements: A periscope directs light from James Webb's primary optics into NIRSpec and onto a three-mirror anastigmat. An eight-position filter wheel blocks or selects light from a broad spectral region. The light further reaches a slit plane that carries three different slit types. A complex micro shutter array (MSA) with approximately 250,000 individual shutters, five fixed slits of varying sizes, and an integral field unit enables different observation modes. The masked-out light beam then traverses a collimator and reaches the grating wheel that selects one prism or one of seven gratings that vary in spectral resolution and wavelength range. The light finally enters the camera optics and reaches a detector with two Teledyne H2RG arrays named NRS1 and NRS2 with 2048 × 2048 pixels each. For a detailed description of NIRSpec, see Jakobsen et al. [2022]. NIRSpec can operate in four different modes: The multi-object spectroscopy mode uses the MSA and can observe up to one hundred different targets at once. The fixed-slit spectroscopy concentrates on a single target. The integral field unit spectroscopy determines the spectrum integrated over the field of view with a size of 3".1 × 3".2. The bright object time series (BOTS) mode observes a target through one of the five slits. It continually reads the detector to trace how the target changes with time. This mode helps study brightness variations caused by exoplanets. The author initiated and contributed to an application for the NIRSpec instrument, which was selected for the Cycle 2 General Observer Program (GO) as program number 4008 [Zieba et al., 2023]. In July 2024, NIRSpec will measure the phase curve of the airless exoplanet LHS 3844b in BOTS mode with the grating/filter configuration G395H/F290LP (see Table 4.5).

Table 4.5. The position of LHS 3844 with its exoplanet for the planned NIRSpec observation. Coordinates are given with respect to J2000.0.

Time (UTC)	Position		Proper Motion (mas/year)		Parallax
	R.A.	Dec.	R.A.	Dec.	
2024-07-05	$22^h41^m59.1203$	-69°10'19.95	334.419367	-726.985909	0.067212"

4.9 Digital elevation models

This subsection was taken from Wohlfarth et al. [2023].

The ground sampling interval of the measurements constrains the resolution of the shape model. The GSI of the GF-4 instrument is approximately 4 km/pixel. The lunar thermal model in Section 5 uses the LDEM_16ppd [Neumann, 2009] from the Lunar Orbiter Laser Altimeter (LOLA) because it has a GSI of < 2 km/pixel at the equator and hence fulfills

Shannon's sampling theorem. The resolution of the MERTIS observations is coarser compared to the GF-4 measurements with a GSI of about 500 km/pixel. Consequently, the author lowered the resolution of the simulated lunar disk to about 35 km per pixel, measured at the subspacecraft point. The M^3 instrument has a GSI of 140 m/pixel [Pieters et al., 2009a], which requires a finer shape model for targeted analyses. Hence, this thesis uses the Global Lunar DTM (GLD100) [Scholten et al., 2012] refined by the Shape from Shading procedure [Grumpe and Wöhler, 2014]. For the global hydroxyl analysis, the author downscaled the M^3 data so that the GLD100's resolution was sufficient. GF-4 and MERTIS viewed the entire lunar disk from space. Because the distance between the probe and the target was finite, the lunar disk appeared under a perspective projection in the image plane. The telescopic observations are too coarse, such that topography is not necessary. The author refers to several contributions [Hess et al., 2019b; Tenthoff et al., 2020; Hess et al., 2022] that consider Martian and Hermean digital elevation models but are out of the scope of this thesis.

Chapter 5

Contribution 1: Thermophysical roughness model

This chapter and many figures have been taken from or adapted from Wohlfarth et al. [2023]. The model characterization in Section 5.4.1, the exoplanet simulation, mainly in Section 5.4.6, and the heat conduction mode in Section 5.5 are new. During development, the computational techniques [Wohlfarth and Wöhler, 2023], the validation with GF-4 data [Wohlfarth et al., 2021b, 2022b], the application to MERTIS and M^3 *data [Wohlfarth et al., 2022a, 2023b], and the application to polar craters [Wohlfarth et al., 2023a] have been published and presented at conferences. The original publication [Wohlfarth et al., 2023] assumes a bolometric hemispherical emissivity of unity (*$\bar{\epsilon}_\mathrm{h} = 1.0$*). After submission (January 15, 2024), this thesis was extended to consider the effect of varying* $\bar{\epsilon}_\mathrm{h}$*. The thermal modeling results were recomputed with* $\bar{\epsilon}_\mathrm{h} = 0.95$ *and discussed (see Section 5.6). The numerical results are close to Wohlfarth et al. [2023].*

5.1 Introduction

This chapter presents a newly devised thermal roughness model for airless planetary bodies. The model undergoes extensive characterization and validation with disk-resolved mid-infrared images (3.5–4.1 μm) of the Moon acquired by the Gaofen-4 earth observation satellite and nadir and off-nadir measurements of the Diviner Lunar Radiometer at 8.25 μm and 25–41 μm. The new model has many applications. Four of them are investigated here in the context of the broader science questions: (1) The model helps remove excess thermal emission from M^3 hyperspectral data and thus allows the analysis of global and temporal patterns of lunar hydration. (2) The MERTIS spectrometer and radiometer are on their way to Mercury to investigate the planet's mineralogy and thermophysical properties. The thermal roughness model is tested with MERTIS lunar flyby data and will later be used for emissivity retrieval of Mercury's dayside thermal emission that aids mineralogical interpretation. (3) The author further tailors a heat conduction model to Mercury and devises strategies to connect it to the thermal roughness model. The combined model will be helpful for thermophysical parameter retrieval with MERTIS radiometer measurements of Mercury's night side. (4) The surface of airless exoplanet LHS 3844b remains elusive. To better understand this planet, the author co-applied for measurement time with NIRSpec onboard the James Webb Space Telescope, which is now scheduled for July 2024. The thermal roughness model will simulate the thermal phase curve of this planet, which is characterized in this thesis.

Thermophysical roughness models are an established tool. However, computational constraints required approximations. Therefore, many models simulate surface roughness with simplified spherical crater segments or Gaussian surfaces and omit higher-order effects such as shadowing and self-heating. Further, the albedo is usually assumed to be constant. However, the relevant physical quantity is the directional-hemispherical bolometric albedo. Increasing computational capabilities now allow for more realistic model components. Rozitis et al. [2020] consider fractal surfaces with self-heating and self-scattering, but only for very limited configurations. The author currently identifies no thermal roughness model in the literature comprising all effects. This thesis presents a radiance model for emissivity calibration and roughness characterization that consistently employs rough fractal surfaces with self-heating and self-scattering. Further, it takes the disk-resolved directional-hemispherical bolometric albedo. Numerical techniques speed up the procedure and allow for processing large regions of the Moon and Mercury within a reasonable time. The new thermal roughness model is thoroughly validated with lunar infrared measurements of the GF-4 satellite and the Diviner lunar radiometer. Delbo et al. [2015] list several studies that compared parameters derived from a thermophysical model with ground truth measurements of (21) Lutetia, (433) Eros, and (25143) Itokawa that suggest accurate results. A comparison of a thermal model to an entire highly resolved disk of emitted flux has yet to be carried out to date. The disk-resolved dataset of GF-4 imagery exhibits a wide range of incidence and emission angles and varying surface composition of a well-known atmosphere-less planetary body. Consequently, it represents a valuable complement to disk-integrated validation of Müller et al. [2021] or coarse phase function validation of older and recent studies [Smith, 1967; Rozitis and Green, 2011]. The new dataset further allows for regional analysis of albedo differences and a closer look at the limb of the disk. GF-4 acquired measurements around 3.77 μm, where thermal emission and solar reflection superimpose. This environment is comparable to the long-wavelength domain captured by M^3. Consequently, model validation with GF-4 data allows the assessment of thermal correction methods for M^3 data for lunar water and hydroxyl analysis. Diviner's EPF measurements cover longer wavelengths and contain multiple configurations of emission angles, phase angles, and different azimuth angles not observed by GF-4. Therefore, this work extended the model validation with the Diviner EPF dataset, and a small dataset of nadir measurements similar to Bandfield et al. [2015].

Absorption features of planetary reflectance spectra near 2.8–3.0 μm indicate the presence and the spatiotemporal distribution of surficial OH/H_2O. In the lunar case, the spectral range around 3 μm can be regarded as a transition zone in which reflected and thermally emitted radiation have the same order of magnitude. Consequently, the thermal emission component occludes the absorption feature in question, so a suitable thermal model becomes necessary to remove the excess thermal radiation and access the absorption band. The thermal model directly controls the retrieved band depth around 3 μm so that any model errors affect the inferred band depths, hence the alleged abundance of OH/H_2O. Despite their crucial role in OH/H_2O studies, all four thermal correction procedures [Wöhler et al., 2017; Li and Milliken, 2017; Bandfield et al., 2018; Honniball et al., 2020] have not been thoroughly tested. The newly devised thermal roughness model (Section 5.2) accounts for all dependencies on geometry, topography, roughness, composition, and other surface properties. Thorough model evaluations demonstrated that it is in excellent agreement with the GF-4-dataset at 3.7 μm, rendering it the most suitable thermal model for thermal excess correction on the Moon. Therefore, the author used the new thermal roughness model to reprocess the entire global dataset of level 1B M^3 imagery from the study of Wöhler et al. [2017] and analyzed the diurnal, latitudinal, and compositional behavior of the 3 μm band depth. The study then critically evaluates previous studies of Li and Milliken [2017], Wöhler et al. [2017], Bandfield et al. [2018], and Honniball et al. [2020] in the light of the new results, trying to proceed toward a better understanding of the actual patterns of lunar OH/H_2O variations.

The MERTIS instrument on board the BepiColombo space probe is destined to characterize Mercury's surface composition better, identify rock-forming minerals, map the surface mineralogy, and study the surface temperature variations and thermal inertia. The expected data will provide valuable constraints to understand Mercury's surface better and answer science questions related to hollows, polar deposits, and the mineralogical and geological history of the innermost planet. The spectrometer is designed to map the emissivity in a spectral domain that contains diagnostic mineral bands such as the Christiansen feature, Reststrahlen bands, and transparency features. The emissivity is retrieved by dividing the measured spectral radiance by the spectral radiance of a perfectly absorbing surface. For nadir observations at small incidence angles, the emissivity can be retrieved by simply dividing the measured flux by the thermal emission of the same body, assuming an emissivity of one. As described in 3.5.4, an airless planetary body does not necessarily emit isotropic blackbody radiation. Instead, the rough and highly isolating regolith causes a complex superposition of many Planck functions that are often anisotropic and sometimes cannot be approximated with a single Planck function. In preparation for MERTIS data analysis, the author tailors the new thermal model to Mercury with disk-resolved topography and directional-hemispherical albedo inferred from MESSENGER Mercury Dual Imaging System (MDIS) data [Becker et al., 2009]. The simulation results comprise various observation scenarios, which extend previous investigations of Davidsson et al. [2015] and prepare for the upcoming MERTIS data.

Like Diviner, the radiometer of MERTIS will measure how the thermal emission at Mercury's night side declines with time. Comparing the temporal behavior with a heat conduction model constrains the thermal inertia. For lunar Diviner data, the thermal model of Hayne et al. [2017] revealed global thermal inertia and thermophysical parameters maps, which are the current lunar standard. Bauch et al. [2014] prepared a heat conduction model for the Moon and later transferred it to Mercury [Bauch et al., 2021]. However, the model uses a constant albedo. As discussed earlier in this thesis, the directional-hemispherical albedo controls how much solar flux heats the surface. It varies locally and crucially depends on the incidence angle. Further, asteroid thermophysical models consistently combine surface roughness and heat conduction, which is currently not true for lunar or hermean heat conduction models. The author adapts the heat conduction model of Hayne et al. [2017] to planet Mercury and derives a realistic A_{dh} from MDIS data. A subsequent study estimates how strongly A_{dh} influences thermal emission. The chapter further introduces and discusses strategies for combining the mercurian conduction model and the newly devised thermal roughness model. Both serve as a preparatory study for MERTIS radiometer data analysis starting in late 2025.

The Transiting Exoplanet Survey Satellite (TESS) detected an earth-sized ($R = 1.32 \pm 0.02 R_{\mathrm{Earth}}$) planet that orbits the M dwarf LHS 3844 in 11 hours [Vanderspek et al., 2019]. The planet LHS 3844b bears no substantial atmosphere [Vanderspek et al., 2019; Kreidberg et al., 2019; Diamond-Lowe et al., 2020] and is likely a bare rock [Kreidberg et al., 2019]. The surface appears comparatively dark and has been hypothesized to consist of mafic silicates [Kreidberg et al., 2019], but the surface structure of LHS 3844b is currently unknown. If the surface hosts a rough regolith similar to the Moon, Mercury, or Asteroids, the thermal emission should exhibit surface roughness effects such as thermal beaming that could be visible in the planet's phase curve. Given the thermal environment of LHS 3844b, solid silicates can indeed occur at the planet's surface, at least at the limb of the illuminated disk, where thermal beaming is the strongest. Assuming that LHS 3844b hosts a rough regolith, this chapter computes the thermal emission of LHS 3844b, finding that thermal beaming significantly increases the phase curve near opposition configuration and shadowing decreases the phase curve above phase angles of $g = 90°$. Given this finding, the author initiated and co-authored an application for the JWST general observer program, selected as program GO 4005. The observations will target LHS 3844b in July 2024 and investigate whether surface roughness effects are visible for the planet. Further, the author issued a Master's thesis [Tenthoff, 2023] that explored the effect of combined reflectance and thermal emission on the phase curve of the exoplanet. The results will be presented at the end of the corresponding section.

5.2 Thermal model

Planetary surfaces are rough and highly anisothermal. Generally, the thermal emission is not given by a single Planck function. Instead, it is a superposition of thermal radiation that emerges from many differently oriented facets, each with a different temperature. The resulting thermal spectra may significantly deviate from the thermal emission of a corresponding smooth model [Rozitis and Green, 2011; Davidsson et al., 2015]. Roughness is responsible for thermal limb brightening and thermal beaming and, hence, has to be included for adequate thermal modeling. In the case of lunar observations, roughness is essential because it changes the thermally emitted spectral radiance and the effective brightness temperature, especially near the limb under oblique illumination or viewing conditions. For a thermal roughness model, this thesis adopted the approach of Rozitis and Green [2011], Rozitis et al. [2020], and Davidsson et al. [2015] and extended it to work with fractal surfaces. The author opted for fractal surfaces because they most naturally resemble the structure of planetary regolith.

Appendix E.1 describes the fractal surface generation method. As described in Section 3.3, the first step is to divide the lunar shape model into N surface elements, each of which is denoted by an index n and is associated with an individual illumination and viewing geometry according to Figure 3.1 (right). The aim is to compute the spectral emission X_n that reaches the sensor for a given surface element n. Therefore, the element n is again subdivided into M smaller facets that build up a rough fractal landscape (Figure 5.1 (left)). The thermal model computes the temperature T_m and the Planck function $U(\lambda, T_\mathrm{m})$ for each facet m of the fractal. Summing over the Planck functions $U(\lambda, T_\mathrm{m})$ of the individual facets m yields the spectral emission X_n of the surface element n. Note that the symbol X_n denotes an arbitrary thermal emission that might differ from blackbody emission I_b in equation 3.73. The following section reviews how to compute X_n and starts with the radiation balance of one single fractal facet m. In thermal equilibrium, which is a reasonable assumption given the slow rotation of the Moon, the radiant flux F_m emitted by the m^{th} facet equals the radiant flux brought by the solar light $F_\mathrm{m}^\mathrm{sun}$, scattered radiation $F_\mathrm{m}^\mathrm{sca}$ from neighboring facets, and thermally emitted flux $F_\mathrm{m}^\mathrm{rad}$ from neighboring facets (self-heating):

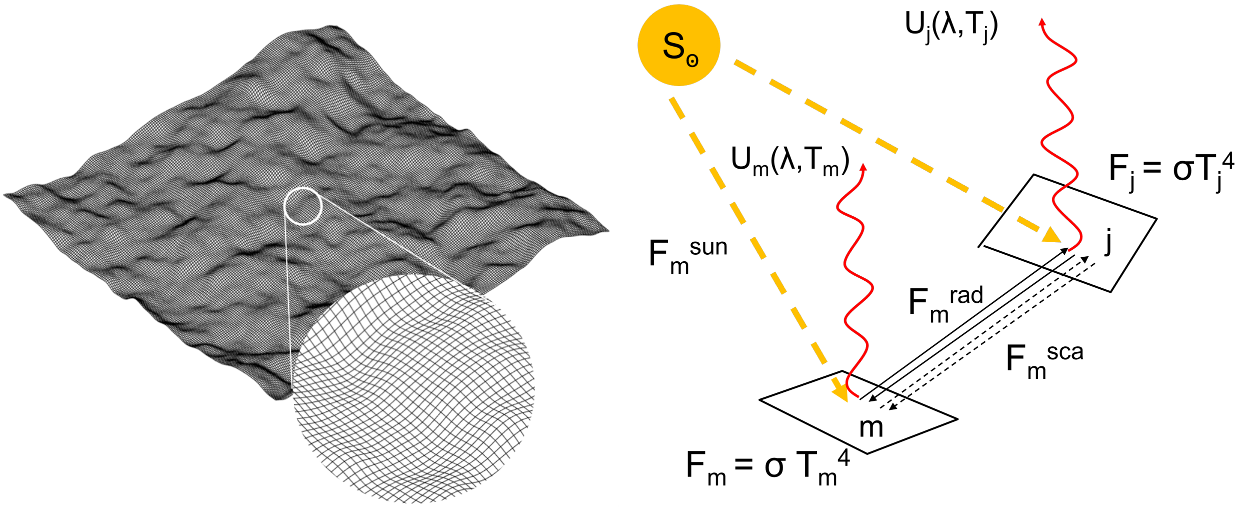

Figure 5.1. Geometric conventions for the fractal roughness model. Left: Simulated fractal surface with $M = 200 \times 200$ elements. The edge width is 1 mm. Right: Relationship between physical quantities. Adopted with changes from Rozitis and Green [2011]. Figure from Wohlfarth et al. [2023].

$$F_\mathrm{m} = F_\mathrm{m}^\mathrm{sun} + F_\mathrm{m}^\mathrm{sca} + F_\mathrm{m}^\mathrm{rad}. \tag{5.1}$$

The geometric relations between these quantities are given in Figure 5.1 (right). The Stefan-Boltzmann law relates the flux F_m to the temperature of the m^{th} surface element:

$$F_\mathrm{m} = \bar{\epsilon}_\mathrm{h} \sigma T_\mathrm{m}^4, \tag{5.2}$$

where σ is the Boltzmann constant and $\bar{\epsilon}_\mathrm{h}$ is the bolometric hemispherical emissivity. In the most generic case, the solar flux J_m strikes the surface. The directional-hemispherical albedo A_dh controls the fraction of scattered and absorbed radiation. The surface absorbs the majority $(1 - A_\mathrm{dh})$ of incoming radiation such that the directly absorbed component $F_\mathrm{m}^\mathrm{sun}$

becomes

$$F_{\mathrm{m}}^{\mathrm{sun}} = (1 - A_{\mathrm{dh}})J_{\mathrm{m}}. \tag{5.3}$$

This thesis assumes that the directional-hemispherical albedo A_{dh} is constant for all m within a facet n. The incoming solar irradiance J_{m} is given by

$$J_{\mathrm{m}} = \frac{S_{\odot}\nu_{\mathrm{m}}\cos i_{\mathrm{m}}}{r_{\mathrm{h}}^2}, \tag{5.4}$$

where $S_{\odot}$ is the solar constant, r_{h} is the heliocentric distance of the Moon, and i_{m} is the incidence angle of the facet. The variable v_{m} is a visibility switch that is either unity if the surface is directly illuminated by the Sun or zero if it is in shadow. The visibility switch is determined via raymarching that uses a variant of the Bresenham algorithm [Bresenham, 1965]. The surface scatters the remaining part A_{dh} of the incident radiation and reabsorbs a portion of $(1 - A_{\mathrm{dh,m}})$ when the light reaches the surface again. The component $F_{\mathrm{m}}^{\mathrm{sca}}$ becomes

$$F_{\mathrm{m}}^{\mathrm{sca}} = (1 - A_{\mathrm{dh,m}})A_{\mathrm{dh,m}} \sum_{j \neq m}^{M} f_{\mathrm{m,j}} J_{\mathrm{j}}. \tag{5.5}$$

The viewing factor $f_{\mathrm{m,j}}$ is essentially a discrete version of equation 3.83 and determines how much radiation from facet j reaches facet m and is expressed as

$$f_{\mathrm{m,j}} = \frac{\nu_{\mathrm{m,j}} A_{\mathrm{j}} \cos\phi_{\Delta,\mathrm{j}} \cos\phi_{\Delta,\mathrm{m}}}{\pi d_{\mathrm{m,j}}^2}. \tag{5.6}$$

Again, $v_{\mathrm{m,j}}$ is a boolean value that indicates whether facet m can see facet j and is determined via ray-tracing. The parameter A_{j} describes the surface area of a facet. The implementation adopted and refined the Bresenham [1965] algorithm for visibility checks. The mutually projected area of two different surface elements is given by the cosines of the angle between the surface normal and the connection vector between the facets. The angle $\phi_{\Delta,\mathrm{m}}$ is measured between the normal of facet m and the connection vector between facet m and j. The angle $\phi_{\Delta,\mathrm{j}}$ describes the mirrored case and is measured between the normal of facet j and the connection vector between facet m and j. $p_{\mathrm{m,j}}$ is the distance between the two facets, and b_{j} is the surface area. This geometry is illustrated in Figure E.1 in Appendix E.2. However, light can be scattered multiple times. Each scattering iteration corresponds to an additional application of the viewing factors and multiplication with $A_{\mathrm{dh,m}}$, such that $F_{\mathrm{m}}^{\mathrm{sca}}$ becomes

$$\begin{aligned} F_{\mathrm{m}}^{\mathrm{sca}} =& (1 - A_{\mathrm{dh}})A_{\mathrm{dh}} \sum_{j \neq m}^{M} f_{\mathrm{m,j}} J_{\mathrm{j}} + \\ & (1 - A_{\mathrm{dh}})A_{\mathrm{dh}}^2 \sum_{j \neq m}^{M} f_{\mathrm{m,j}} \sum_{k \neq j}^{M} f_{\mathrm{j,k}} J_{\mathrm{k}} + \dots \,. \end{aligned} \tag{5.7}$$

Parts of the thermal radiation F_m can also heat the surface, known as self-heating. Again, this process occurs repeatedly, such that the contribution $F_\mathrm{m}^\mathrm{rad}$ for self-heating becomes

$$\begin{aligned} F_\mathrm{m}^\mathrm{rad} =& (1 - A_\mathrm{dh,th}) \sum_{j \neq m}^{M} f_\mathrm{m,j} F_\mathrm{j} + \\ & (1 - A_\mathrm{dh,th}) A_\mathrm{dh,th} \sum_{j \neq m}^{M} f_\mathrm{m,j} \sum_{k \neq j}^{M} f_\mathrm{j,k} F_\mathrm{k} + \dots . \end{aligned} \tag{5.8}$$

The directional-hemispherical albedo $A_\mathrm{dh,th}$ of self-heating may not correspond to the value of A_dh of the initial scattering process. The directional-hemispherical albedos A_dh and $A_\mathrm{dh,th}$ are defined as

$$A_\mathrm{dh} = \frac{1}{S_\odot} \int_0^\infty J_0(\lambda) r_\mathrm{dh}(i, \lambda) d\lambda \text{ and} \tag{5.9}$$

$$A_\mathrm{dh,th} = \frac{1}{S_\mathrm{th}} \int_0^\infty X(\lambda) r_\mathrm{dh}(i, \lambda) d\lambda \approx 0.05, \tag{5.10}$$

where S_th is the thermal emission's total power per unit area, and X is the spectral emission for an emissivity of $\epsilon_\mathrm{d} = 1$. Wöhler et al. [2017] and Grumpe et al. [2019] numerically inferred disk-resolved A_dh values from M^3 measurements averaging around $A_\mathrm{dh} = 0.07$ for nadir illumination. Vasavada et al. [2012] and Keihm [1984] found larger values around $A_\mathrm{dh} = 0.12$ for nadir. Unfortunately, Mercury does not have any A_dh values. This study assumes that the thermal albedo is $A_\mathrm{dh,th} = 0.05$, which is a common value in the literature. The bolometric hemispherical emissivity $\bar{\epsilon}_\mathrm{h}$ is defined as

$$\bar{\epsilon}_\mathrm{h} = \frac{\int_0^\infty X(\lambda) \epsilon_\mathrm{h}(\lambda) d\lambda}{\int_0^\infty X(\lambda) d\lambda} \approx 0.95. \tag{5.11}$$

This value can, in principle, be derived from lunar mid-infrared emissivity spectra, for example, from Donaldson Hanna et al. [2017], but the value is not very well constrained. For the Moon, Müller et al. [2021] and Hayne et al. [2017] assume $\bar{\epsilon}_\mathrm{h} = 0.95$. A common value for asteroids is $\bar{\epsilon}_\mathrm{h} = 0.90$ [e.g. Rozitis and Green, 2011; Lagerros, 1996]. Other publications use $\bar{\epsilon}_\mathrm{h} = 1.0$, e.g., [Davidsson et al., 2015] and [Emery et al., 1998]. For simplicity, Wohlfarth et al. [2023] opted for $\bar{\epsilon}_\mathrm{h} = 1.0$, which will be the default for all analyses in Sections 5.3 and 5.4. Only the heat-conduction model for Mercury in Figure 5.13 assumes $\bar{\epsilon}_\mathrm{h} = 0.95$. In Section 5.6, the author reprocesses all modeling results with $\bar{\epsilon}_\mathrm{h} = 0.95$ and discusses the differences.

To solve Equations 5.1–5.8 for the surface temperature T_m, it is convenient to move to matrix-vector notation. The components F_m, $F_\mathrm{m}^\mathrm{sun}$, $F_\mathrm{m}^\mathrm{sca}$, $F_\mathrm{m}^\mathrm{rad}$, and J_m are summarized in the vectors $\mathbf{f}$, $\mathbf{f}_\mathrm{sun}$, $\mathbf{f}_\mathrm{sca}$, $\mathbf{f}_\mathrm{rad}$, and $\mathbf{j}$. The viewing factors $f_\mathrm{m,j}$ are collected in the viewing matrix $\mathbf{M}$ such that scattering and self-heating can be expressed through matrix-vector multiplication. The flux balance then becomes

$$\begin{aligned}
\mathbf{f} =&\mathbf{f}_{\mathrm{sun}} + \mathbf{f}_{\mathrm{sca}} + \mathbf{f}_{\mathrm{rad}} && (5.12)\\
\mathbf{f} =&(1 - A_{\mathrm{dh}})\mathbf{j} + (1 - A_{\mathrm{dh}}) \sum_{k=1}^{\infty} (A_{\mathrm{dh}}\mathbf{M})^k \mathbf{j} && (5.13)\\
&+ (1 - A_{\mathrm{dh,th}})\mathbf{M} \sum_{k=0}^{\infty} (A_{\mathrm{dh,th}}\mathbf{M})^k \mathbf{f}\\
\mathbf{f} =&\underbrace{(1 - A_{\mathrm{dh}}) \left[1 + \sum_{k=1}^{\infty} (A_{\mathrm{dh}}\mathbf{M})^k\right] \mathbf{j}}_{\mathbf{d}_0} && (5.14)\\
&+ \underbrace{(1 - A_{\mathrm{dh,th}})\mathbf{M} \sum_{k=0}^{\infty} (A_{\mathrm{dh,th}}\mathbf{M})^k}_{\mathbf{X_0}} \mathbf{f}.
\end{aligned}$$

Computing the power of matrix $\mathbf{M}$ in $\mathbf{d}_0$ and $\mathbf{X}_0$ (Equation 5.14) is computationally expensive. Because the spectral norm of $\mathbf{M}$ is already small, though, the author found it to be sufficient to neglect higher powers of $\mathbf{M}$ and introduce the average albedo $\overline{A_{\mathrm{dh}}}$, yielding

$$\mathbf{f} \approx (1 - A_{\mathrm{dh}}) \underbrace{\left(1 + \overline{A_{\mathrm{dh}}}\mathbf{M}\right) \mathbf{j}}_{\mathbf{d}} + \underbrace{(1 - A_{\mathrm{dh,th}})\mathbf{M}}_{\mathbf{X}} \mathbf{f}. \tag{5.15}$$

Rewriting this expression and calling for equality produces a fixed-point equation (Equation 5.16) of vector $\mathbf{f}$

$$\mathbf{f} = \mathbf{X}\mathbf{f} + (1 - A_{\mathrm{dh}})\mathbf{d}. \tag{5.16}$$

If the spectral norm of $\mathbf{X}$ is smaller than 1, the iteration rule

$$\mathbf{f}_{\mathrm{i+1}} = \mathbf{X}\mathbf{f}_{\mathrm{i}} + (1 - A_{\mathrm{dh}})\mathbf{d} \tag{5.17}$$

converges to the actual value, given an arbitrary start vector [Meister, 2015]. Here, $\mathbf{f}_0 = \mathbf{d}$ is chosen. The spectral norm of the matrix $\mathbf{X}$ is $\|\mathbf{X}\|_2 < 1$ for realistic surface geometries such that convergence is ensured for all practical applications. Good convergence is already achieved after five iterations in practically relevant settings. The iteration rule (Equation 5.17) can be rewritten as a sum

$$\mathbf{f} = (1 - A_{\mathrm{dh}}) \sum_{i=0}^{\infty} \mathbf{X}^i \mathbf{d}. \tag{5.18}$$

It becomes evident that the resulting $\mathbf{f}$ scales with $(1 - A_{\mathrm{dh}})$. This fact allowed us to set $A_{\mathrm{dh}} = 0$, precompute only the sum, and later multiply the result with any value for $(1 - A_{\mathrm{dh}})$. Further, one can summarize the vectors $\mathbf{d}$ and the resulting $\mathbf{f}$ for all N geometric configurations into matrices

$$\mathbf{F} = [\mathbf{f}_1 \mathbf{f}_2 ... \mathbf{f}_{\mathrm{N}}] \text{ and } \mathbf{D} = [\mathbf{d}_1 \mathbf{d}_2 ... \mathbf{d}_{\mathrm{N}}] \tag{5.19}$$

and run the iteration for all N geometries simultaneously with

$$\mathbf{F}_{\mathrm{i}+1} = \mathbf{X}\mathbf{F}_{\mathrm{i}} + \mathbf{D}. \tag{5.20}$$

Taking the fourth root of each element of $\mathbf{F}$ yields the temperature of the m^{th} facet:

$$T_{\mathrm{m}} = \left(\frac{F_{\mathrm{m}}}{\bar{\epsilon}_{\mathrm{h}}\sigma}\right)^{\frac{1}{4}}. \tag{5.21}$$

Planck's radiation law gives the diffuse specific intensity (radiance) that emerges from the m-th fractal element

$$P_{\mathrm{m}}(\lambda) = \frac{2hc_0^2}{\lambda^5}(\exp(hc_0/k_{\mathrm{b}}\lambda T_{\mathrm{m}}) - 1)^{-1}, \tag{5.22}$$

and the superposition

$$X_{\mathrm{n}}(\lambda) = \frac{\sum_{m=1}^{M} P_{\mathrm{m}}\nu_{\mathrm{m}}\cos e_{\mathrm{m}}}{\sum_{m=1}^{M} \nu_{\mathrm{m}}\cos e_{\mathrm{m}}} \tag{5.23}$$

yields the final thermal emission component $X_{\mathrm{n}}(\lambda)$. An edge-width of 200×200 pixels appears to be a viable size for the surface fractal, which leads to a $40,000 \times 40,000$ self-heating matrix. A surface of this size collects approximately 95 % of self-scattering and -heating radiation. Further, the implementation can be significantly accelerated by subsampling the feature space of geometric combinations. Parameter settings and implementation details for accurate self-heating modeling and accelerated processing are given in Appendix E.3.

5.2.1 Thermal correction and reflectance normalization for M^3 data

This study used the M^3 level 1B spectral radiance images available at the PDS. The level 2 data were not selected because the thermal correction is known to be incomplete [e.g., Li and Milliken, 2017]. In order to obtain thermally corrected and normalized reflectance spectra from 0.6–3.0 μm, the level 1B M^3 data were processed as described by Wöhler et al. [2017] and Grumpe et al. [2019] following four steps. First, an iterative updating scheme was employed to jointly estimate the thermally compensated reflectance r_{d} and the local temperature T. Second, the temperature compensated for roughness effects, so the thermal emission component could be entirely removed. Third, Hapke's model was employed to photometrically normalize the thermally corrected spectra to the standard geometry ($i = 30°, e = 0°, g = 30°$). Finally, the calibrated spectra were used to determine the continuum-removed integrated band depth of the 3 μm absorption band, an indicator for surficial OH/H_2O. These steps yielded thermally corrected and normalized reflectance spectra. The Integrated Band-Depth at 3 μm ($\mathrm{IBD}_{3\mu\mathrm{m}}$) parameter was introduced by Wöhler et al. [2017] to quantify the average relative absorption strength across the wavelength interval of 2.7-2.9 μm

$$\mathrm{IBD}_{3\mu\mathrm{m}} = \left[\int_{\lambda_{\min}}^{\lambda_{\max}} \left(1 - \frac{r_{\mathrm{d}}(\lambda)}{ct(\lambda)}d\lambda\right)\right] / \left[\lambda_{\max} - \lambda_{\min}\right], \tag{5.24}$$

where $\lambda_{\mathrm{min}} = 2697\,\mathrm{nm}$, $\lambda_{\mathrm{max}} = 2936\,\mathrm{nm}$, $r_{\mathrm{d}}(\lambda)$ is the bi-directional spectral reflectance, and $ct(\lambda)$ is the linear continuum fitted to the wavelength range of 2537 to 2657 nm. The absorption strength indicates the amount of surficial OH/H_2O, which means that the higher the $\mathrm{IBD}_{3\mu\mathrm{m}}$ value, the higher the amount of OH/H_2O present.

5.3 Model validation and application

With these methods at hand, the author performed seven studies for model characterization, model validation with GF-4 and Diviner data, independent tests for OH/H_2O calibration methods with M^3 global spectra, preparation for MERTIS emissivity calibration, and phase curve simulation for the exoplanet LHS 3844b. This section explains the experiments, and the results are presented in Section 5.4

5.3.1 Thermal model characterization

Before turning to actual observations, the author explores how the thermal roughness model behaves for different geometric configurations and roughness values. In the first case, the emission angle is always $e = 0$, and the incidence angle i varies between 0...90° with $\psi = 0°$. This configuration matches a point spectrometer in nadir view with an arbitrary Sun position. The second case always takes $i = e$ with $\psi = 0°$, such that the light source always illuminates the same region as the observer sees. This configuration corresponds to a planetary body seen in opposition configuration. The third case assumes $i = e$ but with $\psi = 180°$. For each case, the thermal model simulates the spectral radiance for five roughness values $\overline{\theta} = 0, 10, 20, 30, 40°$ averaged over ten different fractals each. The resulting spectral radiances stretch over a broad wavelength range from 0.5–15 μm.

5.3.2 Thermal model validation with GF-4 data

Because band six of the GF-4 satellite stretches from 3.5–4.1 μm with a center wavelength of 3.77 μm, the measured spectral radiance was subject to approximately 10–20 % of reflected solar light. Consequently, this condition necessitates a combined reflectance and emittance model. The thermal emission model and the reflectance model are evaluated on an equirectangular coordinate system and subsequently undergo perspective projection such that the resulting lunar disk matches the measurements of GF-4. Manual co-registration ensures that both model and measurements are well aligned. Further, the optical system of the GF-4 satellite has an unknown point spread function (PSF) that slightly blurred the target. Inspecting how the lunar disk's rim declines showed that a Gaussian with $\sigma = 1$ pixel could approximate the PSF. This PSF was applied to the modeled and projected radiance to ensure comparability between the modeled and the measured data. The radiance that emerges from a single surface element depends on the geometry defined by i, e, ψ (see Figure 3.1, right) and four parameters that characterize the surface: the bolometric hemispherical emissivity $\bar{\epsilon}_{\mathrm{h}}$, the directional-hemispherical albedo A_{dh}, the single scattering albedo w, and the surface roughness $\overline{\theta}$. This approach makes two simplifying assumptions. First, the bolometric emissivity $\overline{\epsilon}_{\mathrm{h}} = 1$ is set to unity, and second, the surface roughness $\overline{\theta}$ is assumed to be the same across the entire lunar surface. The bolometric albedo (A_{dh}) maps are derived from the M^3 according to equation 5.9 and the method described in Section 5.2. Because the single scattering albedo at 3.77 μm cannot be derived directly from the M^3 wavelength range, it must be estimated. The author found a robust ($r = 0.986$) correlation between the albedo at 2.5μm and 3.77μm of Apollo samples (see Figure E.3 in Appendix E.4).

Consequently, a linear function extrapolated the M^3-derived single scattering albedo at 2.5μm and estimated the albedo at 3.77 μm, which was then fed into the reflectance and the emissivity model. The results underwent a perspective projection to match the observation geometry. The optical system of the GF-4 satellite has an unknown point spread function (PSF) that slightly blurred the target. Inspecting how the lunar disk's rim declines showed that a Gaussian with $\sigma = 1$ pixel could approximate the PSF. This PSF was applied to the modeled and projected radiance to ensure comparability between the modeled and the measured data. Subsequently, the measured flux of GF-4 was compared with the modeled flux for phase angles of $-30.09°$ and $26.92°$. The study determined the roughness for maria and highlands, traced the model's behavior toward the limb, where roughness plays a crucial role, and looked at local variations between different surface areas. The disk-resolved validation is the first of this kind and complements the validation of Rozitis and Green [2011] and the disk-integrated validation of Müller et al. [2021]. As shown in Section 5.4.2, the modeling results agree exceptionally well with the GF-4 dataset, which justifies applying the model as part of a calibration routine in similar scenarios. The study did not consider the case near opposition ($g = 3.88°$) because the opposition effect is not well understood in this wavelength range, and it remains unclear how these effects can be included without introducing considerable uncertainty, rendering a model validation in the opposition configuration pointless.

5.3.3 Thermal model validation with Diviner nadir and off-nadir data

Thermal emission dominates the spectral region of Diviner channels 4 (8.25 μm) and 7 (25–41 μm) such that solar reflectance becomes negligible. In the NIR range, the emissivity followed from Kirchhoff's law and Equation 3.79. In the MIR, the lunar photometric properties are underconstrained such that the author refrained from this approach, which would require several unknown parameters. Instead, a simpler version of the emissivity curve [Hapke, 2012] proved helpful, which only takes the single scattering albedo as a free parameter. Similar to Bandfield et al. [2015], this study did not explicitly resolve the topography but assumed a spherical Moon with small-scale surface roughness.

A detailed topographic analysis of the EPF footprint is out of the scope of this study but remains an exciting question for future research. Here, the bolometric hemispherical emissivity was set to $\overline{\epsilon}_{\mathrm{h}} = 1.0$, and A_{dh} was determined from M^3 data according to equation 5.9 and the method described in Section 5.2.1. Consequently, two free model parameters were obtained for each of the eleven EPF maneuvers. The model ran for 22 roughness values from 19° to 40° with one-degree increments and 51 albedo values from 0 to 0.5, and the author performed a grid search to find the optimal parameter configuration. For comparison, an equilibrium model was also computed. The author introduced constant emissivity ϵ_d and scaled the equilibrium temperature to match the rough model brightness temperature near the nadir configuration in the middle of the maneuvers.

Further, Diviner's observations in nadir pointing were considered. Bandfield et al. [2015] provided the brightness temperature difference between Diviner channels four and seven, measured at different times of day at specific mare locations. Toward the early morning (06:00) and the evening (18:00), the brightness temperature inferred from channel four becomes up to 70 K higher than channel seven. The author derived the directional-hemispherical albedo A_dh for this scenario, simulated the thermal emission of both channels for three different roughness values ($\overline{\theta} = 10°, 20°, 30°$), derived the brightness temperatures, and compared it to Diviner data. Then, the fitting results were analyzed and compared with the GF-4 validation results. Diviner nadir and off-nadir validation extended the MIR model validation with GF-4 data to longer wavelengths.

5.3.4 Lunar hydration analysis with the M^3 global dataset

This study uses the TPM for thermal excess correction of lunar NIR reflectance spectra. This calibration process retrieved the 2.8–3.0 μm absorption band, a measure for surficial OH/H_2O, and allowed the analysis of its diurnal, latitudinal, and regional variations. The calibration used the existing processing pipeline for global level 1B data of the M^3 instrument [Wöhler et al., 2017; Grumpe et al., 2019] but replaced the old roughness correction with the new thermal roughness model. The calibration pipeline yielded the thermally corrected and normalized reflectance spectra for different lunar times of the day between latitudes of 80° S and 80° N that was uploaded to the supplementary material of Wohlfarth et al. [2023]. Subsequently, global maps were derived that show the integrated band depth around 2.8–3.0 μm in the lunar morning, midday, and evening, which was the basis for analyzing diurnal, latitudinal, and regional variations. The thermal correction methods of previous studies such as Wöhler et al. [2017], Li and Milliken [2017], Bandfield et al. [2018], and Honniball et al. [2020] have not been tested similarly, and the results did not entirely agree, such that the author discusses the previous results in the light of a new thermal model that has proven to be accurate.

5.3.5 Preparations for MERTIS data analysis

The first step compares the predicted thermal emission of the lunar disk to the MERTIS measurements acquired on April 9, 2020. MERTIS suffered a slight offset between the nominal and the real pointing direction, which can be corrected, as shown by Schmedemann et al. [2021]. Further, the instrument's PSF slightly blurred the emerging radiance and must be considered by the model. A parameter identification routine fine-tunes the pointing offset and determines the PSF parameter. This routine minimized the root mean squared error between the radiance model and the measured data. However, the radiance model has a uniform emissivity of one, but the spectral radiance that emerges from the Moon was modulated with the Moon's unique spectral emissivity spectrum that was not known in advance. However, the emissivity resulting from the whole calibration procedure was needed to fine-tune the calibration. To address this coupling of the quantities, an iterative optimization scheme is employed that concurrently estimates the mean spectral emissivity of the lunar disk and the model parameters. Initially, the spectral emissivity was assumed to have a constant value of 0.95, and a Bayesian optimization scheme was employed to retrieve the pointing offset and the width of the PSF. The Bayesian optimization comes from the MATLAB Statistics and Machine Learning Toolbox [The MathWorks Inc., 2022b], which implements Bull [2011], Snoek et al. [2012], and Gelbart et al. [2014]. For reference, see also Frazier [2018]. Bayesian optimization is well suited to optimize a small set of continuous variables of a problem that is computationally costly to evaluate. The first iteration then yielded a rough estimate of the parameters. The spectral emissivity was computed and averaged over the whole disk in the next step. The Bayesian optimization was rerun with the updated spectral emissivity. This step yielded an updated parameter set. The iteration runs for ten cycles, and the best fit is picked according to the objective function. This approach yields the pointing offsets of the MERTIS instrument, which were subsequently transformed into the coordinate system of MERTIS. Finally, the scanned profiles across the lunar disk were compared with the simulated profiles in the four wavelength regions, which is the first observation of a planetary target by MERTIS. This study ran the thermal model for 15 roughness values from $\overline{\theta} = 20°–34°$ and applied the parameter estimation to each.

The second step extended the investigation of Davidsson et al. [2015] to a realistic model of a planetary body to investigate in which cases surface roughness becomes necessary for emissivity retrieval of MERTIS spectra. First, the author presented the thermal radiance model of Mercury and traced the effects of surface roughness on the spectral shape for two phase angles of $g \approx 0°, 120°$. The topography came from the global digital terrain model of Becker et al. [2009], and the directional-hemispherical albedo was inferred from MESSENGER MDIS data as outlined in Appendix E.5. Further, the author sampled the spectral radiance from points near the limb, the middle of the illuminated part, and near the terminator. The spectral radiance of the rough model was then compared to the results of a smooth-surface equilibrium model. Then, the spectral radiance of the rough surface was approximated with a Planck function. This thermal model will later be used for MERTIS emissivity calibrations of Mercury.

The third step tailored the heat-conduction model of Hayne et al. [2017] to Mercury in preparation for future data analysis of MERTIS measurements. The Mercury model uses the orbit parameters of the NASA data archive [Williams, 2023] and an A_{dh} map inferred from MDIS data as described in the previous paragraph and Appendix E.5. Because the thermophysical properties of Mercury are still unknown, the values are approximated with the lunar parameters of Hayne et al. [2017]. The author issued a Master's thesis [Elkhouly, 2023] that validated the simulations and compared the results to Bauch et al. [2021]. Future work needs to explore combining the heat-conduction and roughness models and inversion techniques that extract thermophysical properties from MERTIS measurements.

5.3.6 Thermal phase curve simulation of exoplanet LHS 3844b

This study uses the thermal roughness model and the Hapke reflectance model to compute the phase curve for the airless exoplanet LHS 3844b. Given a spherical planet that orbits its host star, a distant observer sees the orthographic projection of the planet from one side. Consequently, the thermal model yields the radiation that emerges from an orthographically projected sphere for phase angles ranging from $g = 0°$ to $g = 180°$ in steps of $\Delta g = 10°$. Simple numerical integration collects the emission across the visible disk for each phase angle. Dividing the result by the thermal emission of the star yields the relative flux of the planet's phase curve. The author explored the effect of surface roughness on the thermal phase curve. Further, Tenthoff [2023] simulated the reflected component with the Hapke model and computed the combined thermal and reflectance phase curve. The results prepare for the upcoming measurements with NIRSpec onboard JWST.

5.4 Results

5.4.1 Thermal model characterization

This section presents how the thermal roughness model behaves under three different illumination and observation configurations with varying roughness values $\overline{\theta}$.

In case 1, the Sun illuminates the surface from the same direction as the spacecraft observes, such that the incidence and emission angles are equal ($i = e$). Figure 5.2 (top) shows the spectral radiance for three different incidence angles ($i = 0°, 40°, 70°$) and three different roughness values ($\overline{\theta} = 0°, 20°, 30°$). Two effects become immediately visible: The model predicts almost the same spectral emission for small incidence angles as the smooth equilibrium model, regardless of the roughness. With increasing incidence angle, the rough model outputs stronger emission spectra than the smooth model. The higher the roughness value is, the stronger this effect becomes. This finding can be explained in the following way: With increasing incidence angle, the Sun's direction becomes more oblique. Due to roughness, some surface areas are tilted toward the Sun and receive more direct radiation compared to a flat surface because the total power a point on the surface receives depends on the cosine of the local incidence angle. Because $e = i$, the observer always sees exactly the surface parts that are inclined toward the Sun, become hotter, and consequently emit more radiation. The total spectral radiance received from the rough surface is thus larger compared to a flat surface. A spherical body in opposition configuration with a distant source and observer will always fulfill $i = e$ everywhere on its surface. Toward the limb, the incidence angle grows and thus emits more spectral radiance toward the observer. Disk-integrating the rough spherical body's visible hemisphere yields a higher signal than a smooth sphere, where the rough body's limb contributes the most radiation. This effect is known as thermal beaming in the asteroid community [Delbo et al., 2015].

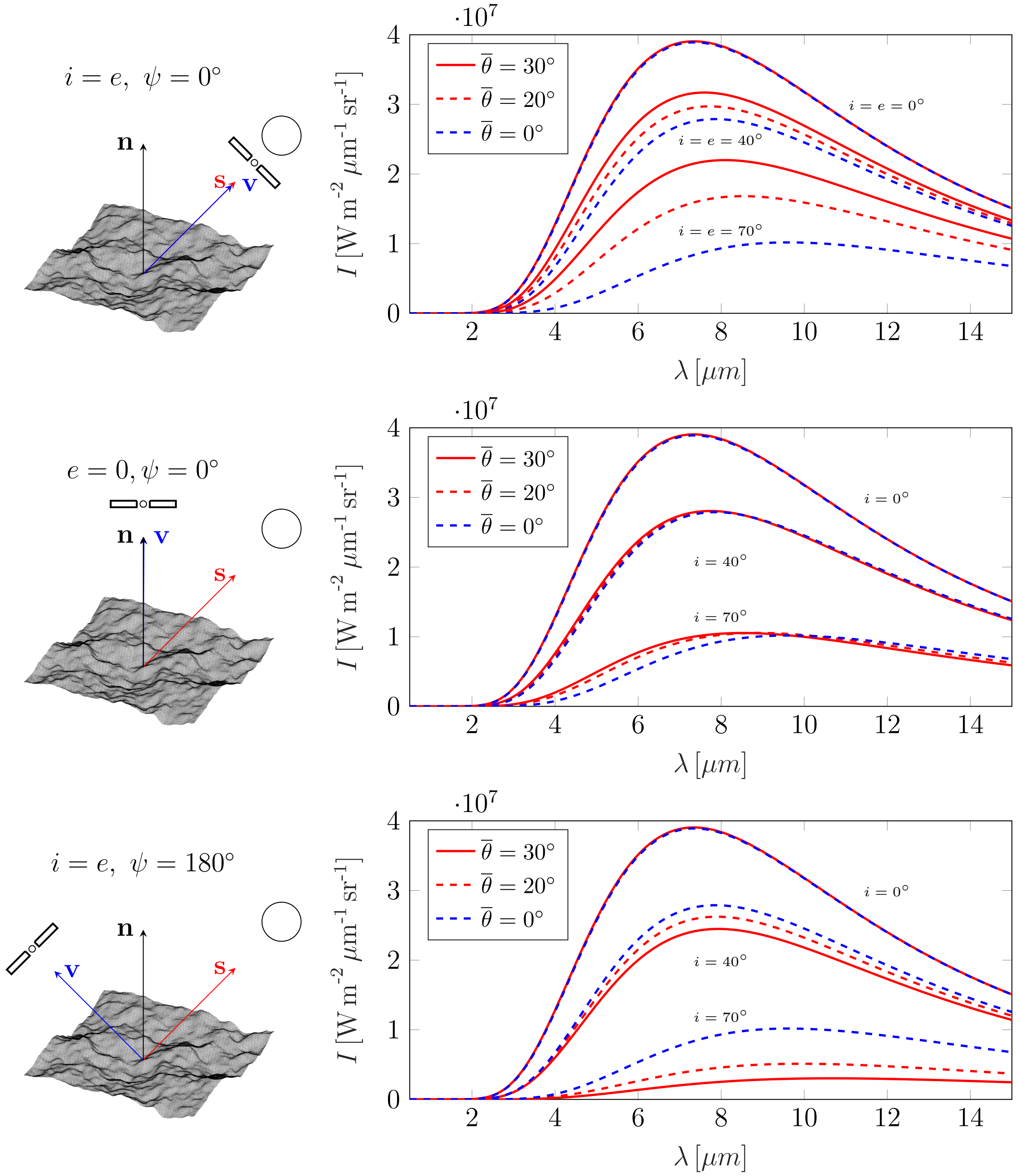

Figure 5.2. Three cases for thermal model characterization with $r = 1\,\mathrm{AU}$, $\epsilon_\mathrm{d} = 1$, $\bar{\epsilon}_\mathrm{h} = 1$, A_dh=0. Top: For $i = e$, the spacecraft observes facets tilted toward the Sun, and I increases. Center: In nadir view, only large i have an effect. Bottom: If $i = e$ and $\psi = 180°$, more shadows are seen, and I decreases.

In the nadir view (case 2), the spacecraft always sees all surface elements, but the incidence angle varies. Figure 5.2 (center) shows the spectral radiance for this case. In the nadir configuration ($i = e = 0$), the rough and equilibrium models predict similar values. For $i = 40°$, the thermal roughness and smooth equilibrium models still predict almost similar results. For larger incidence angles, e.g., $i = 70°$, the rough model outputs a spectral shape that is not a Planck function anymore. For wavelengths smaller than approximately

$\lambda = 9.5\,\mu$m, the rough model results surpass the smooth model results; for larger wavelengths, it is the other way around. The explanation is as follows: Again, surface roughness leads to some surface areas tilted toward the Sun and receiving more direct radiation than a flat surface. These regions become comparatively hot. However, some regions face away from the Sun or even fall in shadow and thus become cold. In case 1, the observer saw the same as the Sun and thus never observed shadowed regions. However, the observer sees both regions with enhanced and reduced temperatures in the nadir. Both effects largely cancel out for moderate incidence angles. Planck's law is a nonlinear function of the temperature. Consequently, the superposition of multiple Planck functions derived from different temperatures is no longer necessarily a Planck function. This effect occurs for large incidence angles in the nadir configuration, where the observer senses a complex temperature distribution (Figure 5.2 (center)). Case 2 resembles a spacecraft that orbits a planetary body and observes the surface from the nadir. Interestingly, a spectrometer in the NIR would sense enhanced thermal emission, while a MIR spectrometer would measure the opposite for large incidence angles.

Figure 5.2 (bottom) shows the spectral radiance for case 3, in which the Sun and observer point in opposite directions ($\psi = 180°$). In contrast to cases 1 and 2, the rough model predicts lower spectral radiance values than the smooth model. Higher surface roughness leads to even lower values. This effect is because the observer sees more shadows than before.

5.4.2 Radiance model for lunar measurements with GF-4

This section presents the modeling results of the lunar surface's combined reflectance and thermal emission at $3.77\,\mu$m and compares them to the GF-4 measurements acquired on July 25, 2018 and July 30, 2018. The author independently tested the thermal model, provided accurate roughness estimates, and demonstrated the performance of thermal roughness models. With the insights gained from thorough model characterization and validation, the author then analyzed the thermal model used for the detection of lunar hydration (Section 5.4.4), evaluated the MERTIS flyby measurements and prepared for MERTIS Mercury measurements (Section 5.4.5), and analyzed the phase curve of LHS 3844b (Section 5.4.6). This section follows Wohlfarth et al. [2023], who assume $\bar{\epsilon}_\mathrm{h} = 1.0$ and a global roughness estimate $\bar{\theta}$. Section 5.6 explores an updated model with $\bar{\epsilon}_\mathrm{h} = 0.95$ and regional albedo estimates for mare and highland.

The Moon on July 25, 2018

Figure 5.3 (top left) shows the radiance at $3.77\,\mu$m, measured on July 25, 2018. The subsolar point is located in the South of Mare Tranquilitatis (gray circle in Figure 5.3 (bottom left)). The satellite points almost at the center of the lunar disk (black dot in Figure 5.3 (bottom left)), spanning a phase angle of $-30.09°$ with the illumination vector. The terminator runs through Oceanus Procellarum, so approximately 93% of the disk is visible. The model takes the lunar shape model and outputs the spectral radiance for seven roughness levels ($\bar{\theta} = 18°, 20°, 22°, 24°, 26°, 28°, 30°$), averaging over ten random fractal surfaces, respectively.

The final result is the weighted superposition of the two roughness levels that best fit the data in the sense of a simple root mean squared error. The interpolation assumes linearity, and the average roughness with its 1-sigma error range was inferred to be $\overline{\theta} = 21.671° \pm 0.007°$ or RMSL= $22.410° \pm 0.007°$. The 1-sigma error range is comparatively small because the number of data points is large, pushing the numerical value down.

The modeled radiance in Figure 5.3 (bottom left) strongly resembles the measured radiance in Figure 5.3 (top left). The overall visual appearance is similar, the topographic features match, and the contrast between the maria and highlands has a similar trend. Figure 5.3 (bottom left) indicates horizontal and vertical profile positions for a detailed analysis. The measured and the modeled spectral radiance along the horizontal profiles 25_{R1}–25_{R4} and the four vertical profiles 25_{C1}–25_{C4} is given in Figure 5.3 (right). The horizontal profiles 25_{R1}–25_{R4} stretch from the terminator (around pixel position 100–200) to the rim (around pixel position 600–700). A linear slope occurs between the terminator and the subsolar point, and a downturn appears toward the limb (Figure 5.3 (right)). The vertical profiles 25_{C1}–25_{C4} nearly stretch from north to south and resemble symmetric arcs (Figure 5.3 (right)). The modeled and the measured curvatures of horizontal and vertical profiles resemble each other, which indicates that the roughness level is realistic and that the model correctly captures geometry-dependent spectral radiance variations. Profile 25_{C1} (pixels 400–600), 25_{C3} (pixels 200–700), and profile 25_{R4} (pixels 150–650) cover regions with prominent topographic features that lead to abrupt radiance variations. The rough model and the measurements match around these regions, indicating that the underlying topographic model is realistic. The model largely captures the contrast between maria and highland regions. Profile 25_{R3} exhibits a bump around pixel position 500, which can be associated with the transition between Mare Nectaris and the surroundings, mainly consisting of highland material. Profile 25_{R2} has a plateau-like shape around pixel 500 that stems from Mare Tranquilitatis, also present in profile 25_{C1} around pixel 300. The prominent notch in profile 25_{C2} around pixel position 250 results from the transitions between Mare Serenitatis and Sinus Honoris mixed with highland material. However, the model exhibits some deviations. An offset of up to approximately $1\,\mathrm{W\,m^{-2}\,\mu m^{-1}\,sr^{-1}}$ between modeled and measured data occurs for central highland material (see profile 25_{C2} from pixels 250 to 450 and profile 25_{R2} around pixel 500 and 600).

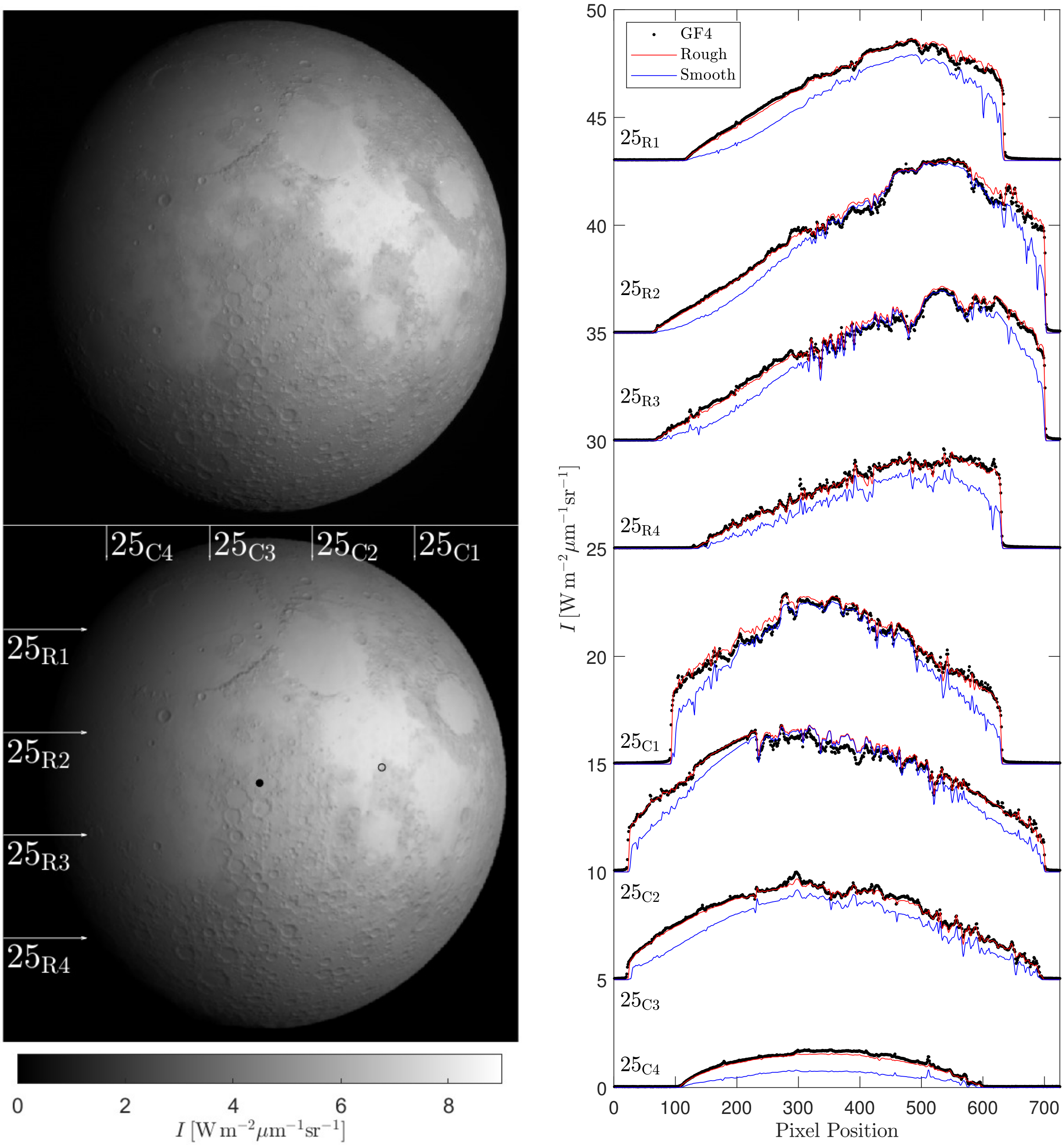

Figure 5.3. Comparison of the lunar data with the modeling results. Top left: Radiance I of the lunar disk at 3.77 μm measured on July 25, 2018, with the GF-4 satellite. Bottom left: Radiance of the lunar disk simulated with the new model. The arrows indicate the horizontal sampling profiles 25_{R1}–25_{R4} and the vertical sampling profiles 25_{C1}–25_{C4}. The subsolar point (gray circle) and the subcamera point (black dot) are given in Table 4.1. Right: Comparison of the measured spectral radiance (black) with the rough model (red) and the equilibrium model (blue) along the horizontal profiles 25_{R1}–25_{R4} and along the vertical profiles 25_{C1}–25_{C4} indicated in Figure 5.3 (bottom). Offsets for clarity. Figure from Wohlfarth et al. [2023].

The Moon on July 30, 2018

Figure 5.4 (top left) shows the spectral radiance at 3.77 μm, measured on July 30, 2018. The subsolar point lies in Oceanus Procellarum southwest of Copernicus (gray circle in Figure

5.4 (bottom left)). The satellite points almost at the center of the lunar disk (black dot in Figure 5.4 (bottom left)), spanning a phase angle of 26.92° with the illumination vector. The terminator runs through the area east of Mare Serenitatis and Mare Tranquillitatis, so approximately 95% of the disk is visible. Again, the model was evaluated for seven roughness levels with average slopes of $\overline{\theta} = 18°, 20°, 22°, 24°, 26°, 28°, 30°$. The best-fit result with its 1-sigma error range corresponds to a roughness of $\overline{\theta} = 22.870° \pm 0.008°$ or RMSL = $23.476° \pm 0.007°$.

The modeled spectral radiance in Figure 5.4 (bottom left) strongly resembles the measured spectral radiance in Figure 5.4 (top left). The measured and the modeled radiance along the horizontal profiles 30_{R1}–30_{R4} and the four vertical profiles 30_{C1}–30_{C4} (see Figure 5.4 (bottom left)) is given in Figure 5.4 (right). The horizontal profiles appear to be mirrored along the vertical axis, compared to profiles 25_{R1}–25_{R4} in Figure 5.3 (right). Again, the vertical profiles stretch from north to south, resembling a symmetric arc. The model accurately reproduces topographic features: compare profiles 30_{R4} (pixels 100–600), 30_{C2} (pixels 500–700), and 30_{C3} (pixels 500–650). However, the profiles exhibit slight systematic deviations near the limb. Parts of the modeled profiles 30_{R1}, 30_{R2}, and 30_{R3} between pixel positions 150–200 are up to approximately $1\,\mathrm{W\,m^{-2}\,\mu m^{-1}\,sr^{-1}}$ below the measured values. The same holds for profile 30_{C1} for pixels 100–450, which covers the same region. All these profiles cut through a region of Oceanus Procellarum that bears titanium-rich mare material [Lucey et al., 2000]. This material is known to be comparatively dark in the visible and the infrared, which means the infrared emissivity increases. Because there is no accurate emissivity map of the Moon, the estimation routine extrapolates the albedo w from M^3 measurements at $2.5\,\mu$m to $3.77\,\mu$m using Apollo samples. The A_{dh} and emissivity maps also follow from the albedo estimates. The correlation between the single scattering albedo at $2.50\,\mu$m and $3.77\,\mu$m (see Appendix E.4) is probably not adequate for titanium-rich mare material, such that deviations occur in these regions. A slight difference is also found in profiles 25_{R1}, 25_{R3}, and 25_{C4} but less strong because it is close to the terminator with its comparatively small spectral radiance. On the contrary, the modeled radiances at pixel positions 240–360 in 25_{R2} exhibit higher values than the measurements. This region was sampled from the bright ejecta material of crater Copernicus, which is comparatively fresh and bright. Likely, the interpolation routine does not accurately treat the anomalously bright ejecta material.

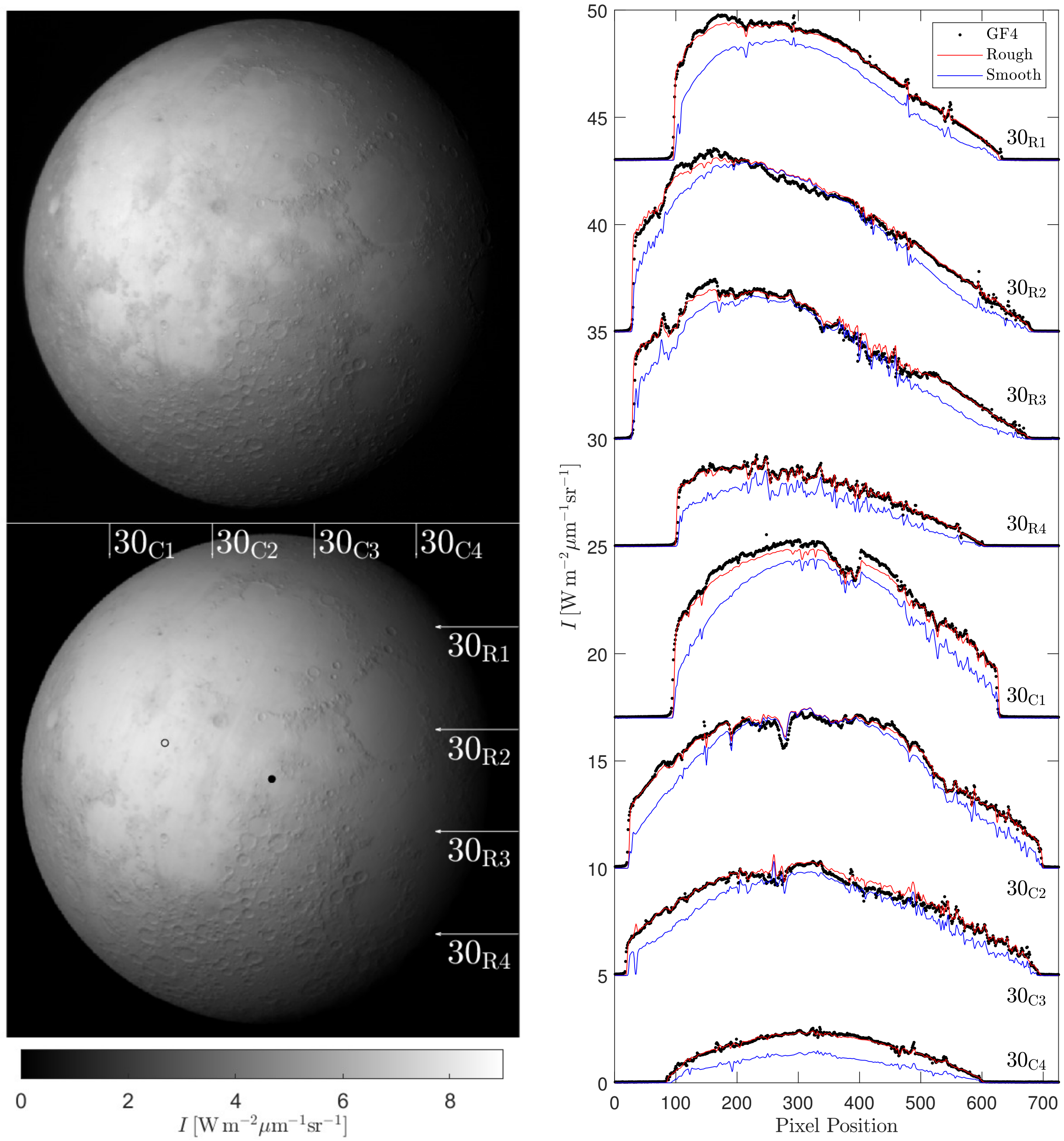

Figure 5.4. Comparison of the lunar data with the modeling results. Top left: Radiance I of the lunar disk at 3.77 μm measured on July 30, 2018, with the GF-4 satellite. Bottom left: Radiance of the lunar disk simulated with the new model. The dashed lines indicate the horizontal sampling profiles 30_{R1}–30_{R4} and the vertical sampling profiles 30_{C1}–30_{C4}. The subsolar point (gray circle) and the subcamera point (black dot) are given in Table 4.1. Right: Comparison of the measured spectral radiance (black) with the rough model (red) and the equilibrium model (blue) along the horizontal profiles 30_{R1}–30_{R4} and the vertical profiles 30_{C1}–30_{C4} indicated in Figure 5.4 (bottom). Offsets for clarity. Figure from Wohlfarth et al. [2023].

Accuracy analysis

Table 5.1 lists the root mean square error (RMSE) between the model and measurements of all sixteen profiles 25_{R1}–25_{R4}, 25_{C1}–25_{C4}, 30_{R1}–30_{R4}, and 30_{C1}–30_{C4}. The average RMSE

Table 5.1. Error analysis of all sixteen profiles from Figures 5.3 and 5.4. The values given in % indicate the ratio of the RMSE to the reference value of 8 W m^{-2} μm^{-1} sr^{-1}, close to the radiance maximum.

Profile	RMSE $[\frac{\mathrm{W}}{\mathrm{m}^2\mu\mathrm{m\,sr}}]$	rel. [%]	Profile	RMSE $[\frac{\mathrm{W}}{\mathrm{m}^2\mu\mathrm{m\,sr}}]$	rel. [%]
25_{R1}	0.2115	2.64	30_{R1}	0.1682	2.10
25_{R2}	0.2378	2.97	30_{R2}	0.2973	3.72
25_{R3}	0.2113	2.64	30_{R3}	0.2964	3.70
25_{R4}	0.1448	1.81	30_{R4}	0.1801	2.25
25_{C1}	0.2786	3.48	30_{C1}	0.3523	4.40
25_{C2}	0.2566	3.21	30_{C2}	0.2225	2.78
25_{C3}	0.1250	1.56	30_{C3}	0.2502	3.13
25_{C4}	0.1223	1.53	30_{C4}	0.0931	1.16
$\overline{x}$	**0.1985**	**2.48**		**0.2325**	**2.91**

between the modeled and measured profiles of July 25, 2018, are 0.1985 W m^{-2} μm^{-1} sr^{-1}, and of July 30, 2018, are 0.2325 W m^{-2} μm^{-1} sr^{-1}. None of the profiles exceeds a relative RMSE of 4.40 %. Relative to a reference value (8.0 W m^{-2} μm^{-1} sr^{-1}) close to the maximum spectral radiance of the disk, the profile-averaged relative RMSE is 2.48 % and 2.91 %, respectively. The RMSE between the model and the measurements averaged over the entire disk is 0.1985 W m^{-2} μm^{-1} sr^{-1} for July 25, 2018, and 0.2464 W m^{-2} μm^{-1} sr^{-1} for July 30, 2018. Both values closely agree with the profile-averaged values. Relative to a reference value (8.0 W m^{-2} μm^{-1} sr^{-1}) close to the maximum spectral radiance of the disk, the relative disk-integrated RMSE is approximately 2.8 %.

5.4.3 Radicance model for Diviner's emission phase function measurements

The new model agrees well with the twelve EPF measurements of Bandfield et al. [2015]. Table 5.2 lists the grid search results for the roughness and the single scattering albedo. The directional-hemispherical albedo was derived from the M^3 global mosaic. The average roughness for channel four is around $\overline{\theta} = 30.25°$ (RMSL= 29.61°). The single scattering albedos of both channels are comparatively low, which aligns with the fact that silicate spectra in the MIR have low reflectances and high emissivities. The single scattering albedos of measurements five and six deviate from the rest. The average best-fit roughness of channel seven is similar to channel four, which implies that the model behaves consistently over broader wavelength regions. Appendix F displays the geometries and model results for all twelve EPF measurements (Figures F.1–F.12 in Appendix F) and a lunar topographic map with EPF acquisition locations (Figure F.13 in Appendix F). Because most EPF measurements are similar, detailed evaluation is restricted to only one representative and one edge case.

Figure 5.5 (left) shows how the incidence, emission, and azimuth angle develop during the EPF maneuver 11 as explained in Section 4.2. The incidence angle (red circles) stays largely constant around 46°. The emission angle (blue dots) and the azimuth angle (black crosses) take nine distinct configurations. The emission angle successively takes the values 80°, 72°,65°,55°,0°,51°,61°,67°,74°. The first four configurations have azimuth angles around 110°, which means that the solar vector and the view vector roughly point in opposite directions. The last four configurations have an azimuth of around 65°, which means that the solar vector and the view vector roughly point into the same half-space.

Figure 5.5 (right) shows the brightness temperature derived from Diviner channel four (red circles) and channel seven (blue crosses). The data points exhibit a general trend from lower to higher temperatures but scatter strongly, likely due to local albedo and topographic variations. The equilibrium model (thin black line) predicts almost constant brightness temperatures around 352 K. However, the new roughness model (large black dots for channel four, smaller black dots for channel seven) captures the general trend and the stair-like increments of the brightness temperature during the entire maneuver. The model does not include topography, so it cannot reproduce the local temperature variations. However, the data points scatter symmetrically around the model predictions, which indicates that the model is unbiased. The excellent agreement between diviner EPF measurements and model predictions proves that the model accurately simulates how surface roughness impacts the brightness temperature for EPF geometries in the MIR.

Table 5.2. Best fit parameters for twelve EPF measurements of Diviner channels four and seven. See Table 4.2 for locations and geometries. The bolometric hemispherical emissivity is $\bar{\epsilon}_h = 1.0$ and the directional-hemispherical albedo A_{dh} is derived from M^3 measurements beforehand. The roughness $\bar{\theta}$ and the single scattering albedo w are inferred via a simple grid search. The last row provides the average values. Table adapted from Wohlfarth et al. [2023].

		Channel four (8.25 μm)			Channel seven (25-41 μm)		
No.	A_{dh}	$\bar{\theta}$ [°]	w	RMSE [K]	$\bar{\theta}$ [°]	w	RMSE [K]
01	0.085	37	0.11	28.91	35	0.18	21.56
02	0.084	28	0.17	25.40	29	0.18	23.04
03	0.076	34	0.26	5.75	34	0.20	5.90
04	0.067	37	0.12	5.23	31	0.16	4.27
05	0.075	28	0.00	43.44	28	0.00	43.14
06	0.081	19	0.42	6.29	19	0.16	7.98
07	0.067	29	0.17	4.88	32	0.15	4.14
08	0.047	34	0.20	3.90	36	0.17	3.31
09	0.074	34	0.20	24.50	27	0.19	18.10
10	0.075	29	0.11	27.02	26	0.13	27.31
11	0.063	28	0.18	5.60	27	0.18	6.11
12	0.050	26	0.31	6.44	27	0.23	6.67
$\bar{x}$	0.070	30.250	0.188	15.612	29.250	0.161	14.293

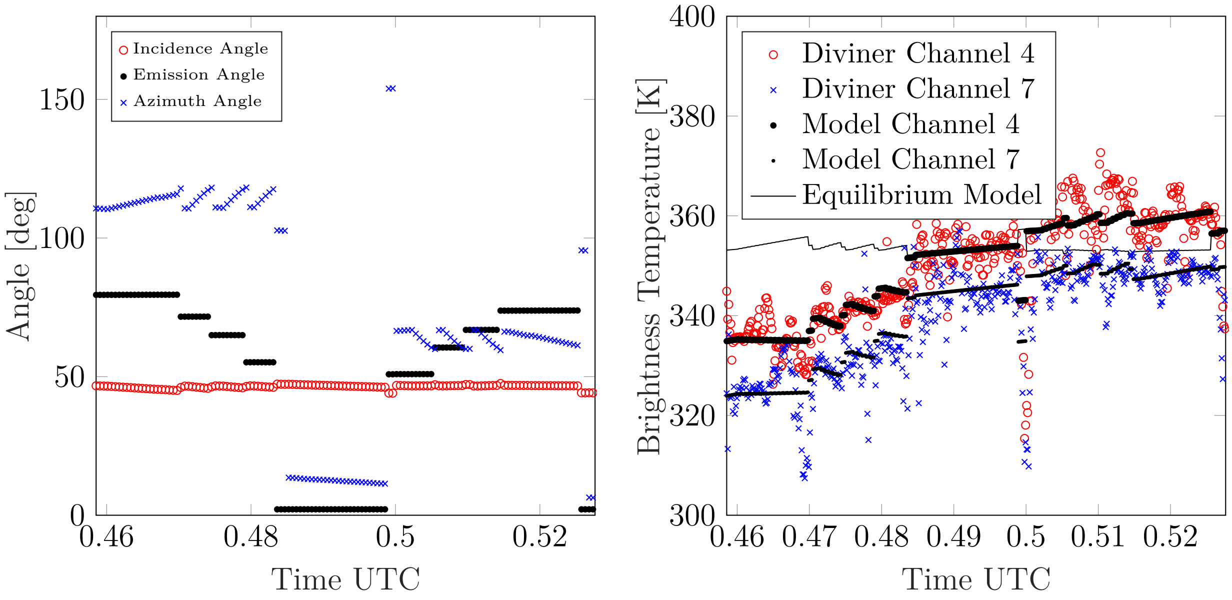

Figure 5.5. Analysis of EPF measurement no. 11. Left: Incidence, emission, and azimuth angle as a function of time during the EPF maneuver. Right: Brightness temperatures of the Diviner channels four and seven and the modeled brightness temperatures. Figure adapted from Wohlfarth et al. [2023].

Figure F.5 in Appendix F shows the brightness temperature of EPF observation number five. The incidence angle rises to $i = 69°$, and the grid-search result indicates a roughness of $\overline{\theta} = 28°$. EPF observation number six (Figure F.6 in Appendix F) covers a nearby region illuminated under $i = 67°$. However, the best fit yields $\overline{\theta} = 19°$, which is lower than all other roughness results. There are two possible explanations: Because the observation conditions of EPF observations five and six are similar, it may be true that the roughness at EPF site six is lower than at site five. However, the albedo values strongly differ among themselves and from the rest, which might also indicate that the fitting routine could not sufficiently decouple the roughness and albedo effects at these sites. Tailoring the thermal roughness model to the Diviner EPF data yields average roughness values around $\overline{\theta} = 30.25°$ (RMSL$=$ 29.61°) for channel four and $\overline{\theta} = 29.25°$ (RMSL$=$ 28.81°) for channel seven.

The diviner EPF measurements illustrate an essential result of rough surfaces: The MIR brightness temperatures measured under low azimuth angles appear significantly hotter than the equilibrium model. Under high azimuth angles, the brightness temperature appears significantly colder. The brightness temperature is the temperature of the best-fit Planck function that reproduces the radiance measured at a given wavelength interval. Consequently, the brightness temperature of a smooth surface equals its equilibrium temperature. In the case of rough surfaces where each surface facet sustains an individual temperature, the thermal emission is the superposition of the Planck functions of each surface facet. For small azimuth angles ($g < 90°$), the illumination and the viewing vectors roughly point in the same direction. The spacecraft observes the same facets inclined toward the Sun and obtains higher temperatures. Consequently, their thermal emission is higher than the equilibrium model, and the brightness temperature fit increases. This effect is consistent with thermal limb-brightening and thermal beaming and becomes stronger with increasing emission an-

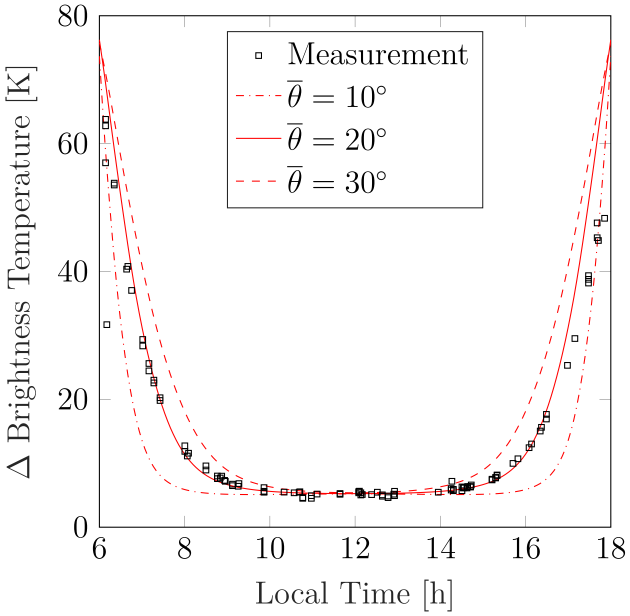

Figure 5.6. The brightness temperature of Diviner channel four minus channel seven. The measurements (squares) are taken from Bandfield et al. [2015] and are closest to a thermal model with a roughness of $\overline{\theta} = 20°$. Figure from Wohlfarth et al. [2023].

gle. The illumination and the viewing vectors point in opposite directions for large azimuth angles ($g > 90°$). The spacecraft primarily observes the facets that face away from the Sun and become colder. At large incidence angles, the rough surface may even exhibit shadows. The spacecraft then observes the colder and the shadowed facets such that the brightness temperature fit yields lower temperatures. See also Section 5.4.1.

Figure 5.6 compares the measurements of Bandfield et al. [2015] with the modeling results. Bandfield et al. [2015] find that mare brightness temperatures inferred from nadir observations of channels four and seven differ by time of day. Before 9:00 and after 15:00, the brightness temperature of channel four becomes up to 70 K hotter than channel seven. The brightness temperature difference is marked with squares. The model ran for three roughness values. Visual inspection indicates that roughness values close to $\overline{\theta} = 20°$ (solid red) better describe the brightness temperature anisotropy than $\overline{\theta} = 30°$ (dashed red) and $\overline{\theta} = 10°$ (dashed-dotted red).

All in all, this section reproduced the findings of Bandfield et al. [2015] that the nadir observations are best described by a roughness value close to $\overline{\theta} = 20°$ (RMSL 20.89°) and the best fit to model the EPF measurements spans between $\overline{\theta} = 19°$–$37°$ (RMSL 19.97°–35.02°) with $\overline{\theta} = 30.25°$ (RMSL 29.61°) being the mean value for channel four and $\overline{\theta} = 29.25°$ (RMSL 28.81°) being the mean value for channel seven. The EPF results found here are further consistent with other studies in this wavelength range [Rozitis and Green, 2011; Bandfield et al., 2015; Rubanenko et al., 2020].

5.4.4 Time-of-day dependent lunar hydration maps

The author reprocessed the global level 1B spectral radiance of the M^3 instrument with the method of Wöhler et al. [2017] and Grumpe et al. [2019] but using the new thermal roughness model setting the roughness to the rounded average of the GF-4 results ($\overline{\theta} = 22°$). The calibration yields normalized reflectance spectra used to compute the integrated and normalized band depth between 2697 and 2936 nm ($\mathrm{IBD}_{3\mu\mathrm{m}}$). Figure 5.7 shows global maps of the $\mathrm{IBD}_{3\mu\mathrm{m}}$ parameter in the morning, around noon, and in the evening. Three effects can be observed on a global scale. First, there are considerable diurnal variations. In the lunar morning, the $\mathrm{IBD}_{3\mu\mathrm{m}}$ parameter is mostly between 8 and 14, with an average of 10.79. The value decreases by 61.74 % at noon to 6.66 on average. In the evening, the $\mathrm{IBD}_{3\mu\mathrm{m}}$ value increases to 10.51 on average, corresponding to similar levels as in the morning. Secondly, the diurnal variations depend on the region. The amplitude of the diurnal variations is enhanced in the lunar maria, reaching higher $\mathrm{IBD}_{3\mu\mathrm{m}}$ values in the morning and evening and lower values around noon. The effect is pronounced in titanium-rich regions, such as western Oceanus Procellarum, central Mare Imbrium, and Mare Tranquilitatis. The amplitude in the lunar highlands is generally lower. On the lunar farside, the diurnal variations in the South Pole-Aitken basin appear to be enhanced compared to the remaining parts. Thirdly, the $\mathrm{IBD}_{3\mu\mathrm{m}}$ parameter appears to depend on the latitude. In the morning and evening, the $\mathrm{IBD}_{3\mu\mathrm{m}}$ parameter on the lunar farside clearly shows larger values toward the poles compared to the equatorial region and mid-latitudes. This effect can not be entirely separated from regional variations, but on the lunar nearside, the highland-dominated southern quarter exhibits increasing $\mathrm{IBD}_{3\mu\mathrm{m}}$ values toward the lunar south pole at all three times of the day. The diurnal variations are the smallest at the highest observed latitudes. The author provided the global calibrated reflectance maps for various times of day along with Wohlfarth et al. [2023].

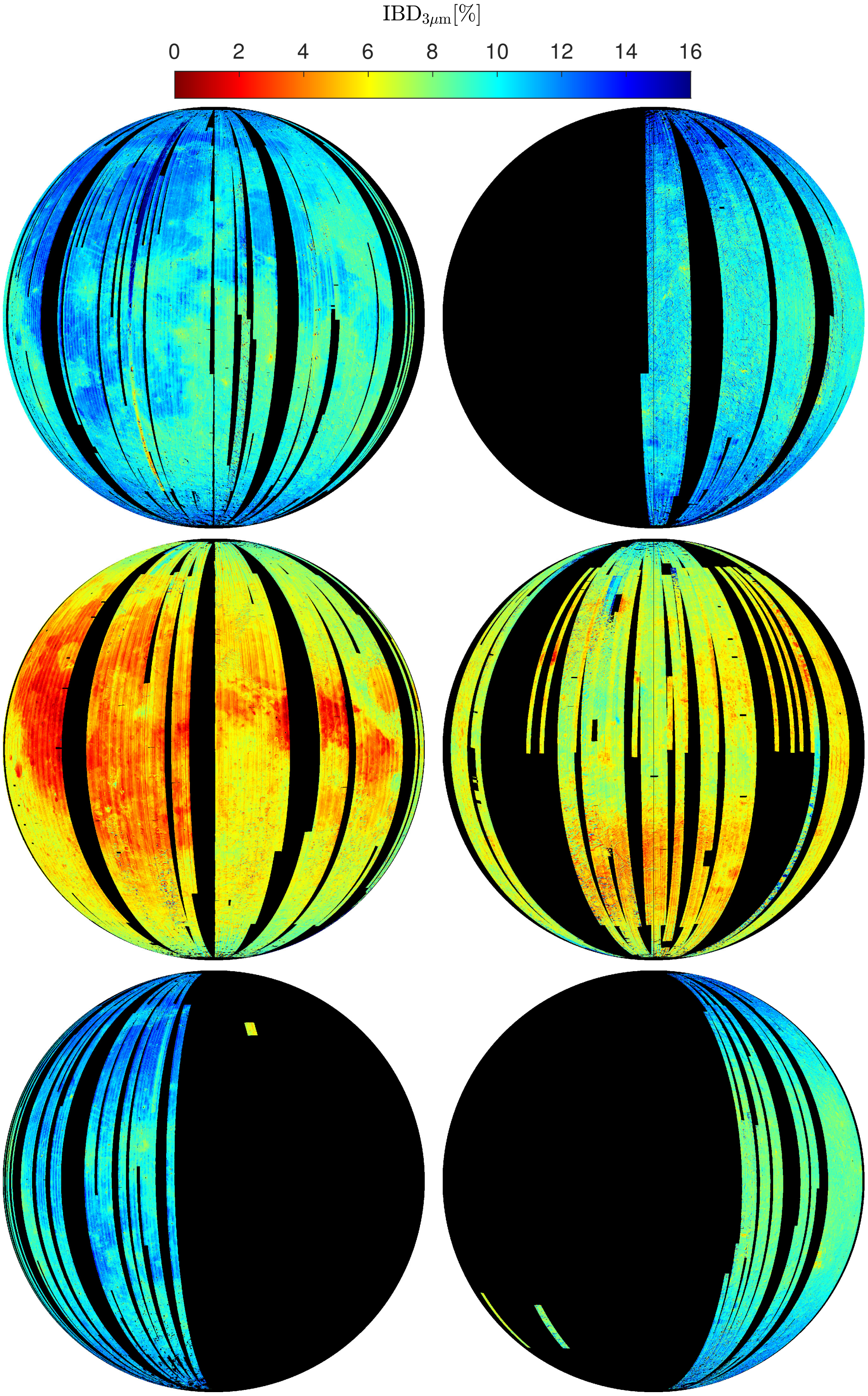

Figure 5.7. Global $IBD_{3\mu m}$ map in an orthogonal projection of the lunar nearside (left column) and the lunar farside (right column). Top row: $IBD_{3\mu m}$ maps in the morning (7:00–8:00). Central row: $IBD_{3\mu m}$ maps at noon (12:00–14:00 at the nearside and 10:00–12:00 at the farside). Bottom row: $IBD_{3\mu m}$ maps in the lunar evening (16:00–17:00). Black indicates missing data. Figure from Wohlfarth et al. [2023].

5.4.5 Preparations for MERTIS emissivity calibration and thermal analysis

Analysis of MERTIS lunar flyby data

MERTIS's push-broom-sensor consists of 100 pixels, six of which scanned the lunar disk from the northwest to the southeast through the calibration baffle from an average distance of 725,000 km. The pixel size and the instrument PSF limited the resolution such that the instrument effectively observed a blurry lunar disk at this distance, as shown in Figure 5.8. The yellow lines in Figure 5.8 represent the center positions of pixels 36–41 during MERTIS's scan across the lunar disk after pointing correction. These observation conditions were challenging, and parameter identification appears to be ill-posed. Figure 5.8 (right) shows the best results from the iterative parameter estimation scheme for each roughness value. The tilts in the east-west (EW) and north-south-direction (NS) of the instrument consistently scatter around $\Delta\mathrm{WE} = -0.19961$ mrad and $\Delta\mathrm{NS} = 0.33448$ mrad, respectively. The roughness values and the width of the point spread function appear to be correlated. The higher the roughness, the larger the width σ of the Gaussian PSF. Consequently, there seems to be no unambiguous minimum, and it was impossible to conclusively determine a single lunar roughness value from MERTIS lunar flyby measurements. Digital optical systems must fulfill Shannon's sampling theorem such that the full-width half maximum (FWHM) of the PSF equals two pixels. With a pixel size of approximately 500 km, the standard deviation of a Gaussian PSF must be around $\sigma = 2 \cdot \mathrm{FWHM}/(2\sqrt{2\ln 2}) = 425$ km. The fitting results

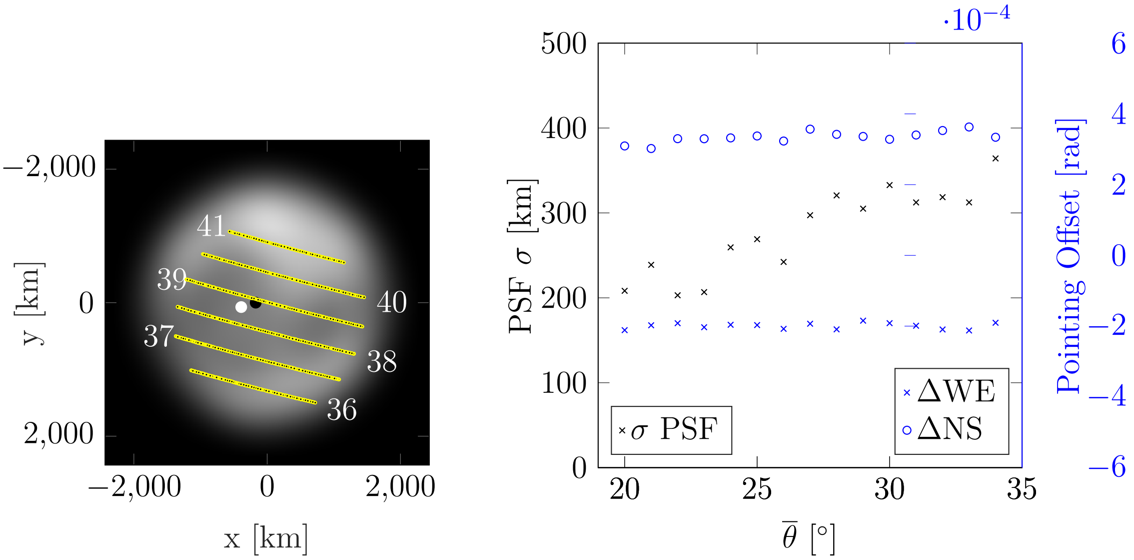

Figure 5.8. MERTIS lunar flyby data analysis. Left: Corrected center positions of MERTIS pixels 36–41 that scanned the lunar disk from west to east. Table 4.3 gives the subsolar point (white dot) and the subcamera point (black dot). Applying a Gaussian filter with $\sigma = 300$ km to the projected lunar disk simulates the instrument PSF. Right: Best fit parameter results for various roughness levels. The optimization scheme consistently retrieves a pointing offset in west-east-direction (ΔWE) and north-south direction (ΔNS). The width of the Gaussian PSF varies with roughness. Figure adapted from Wohlfarth et al. [2023].

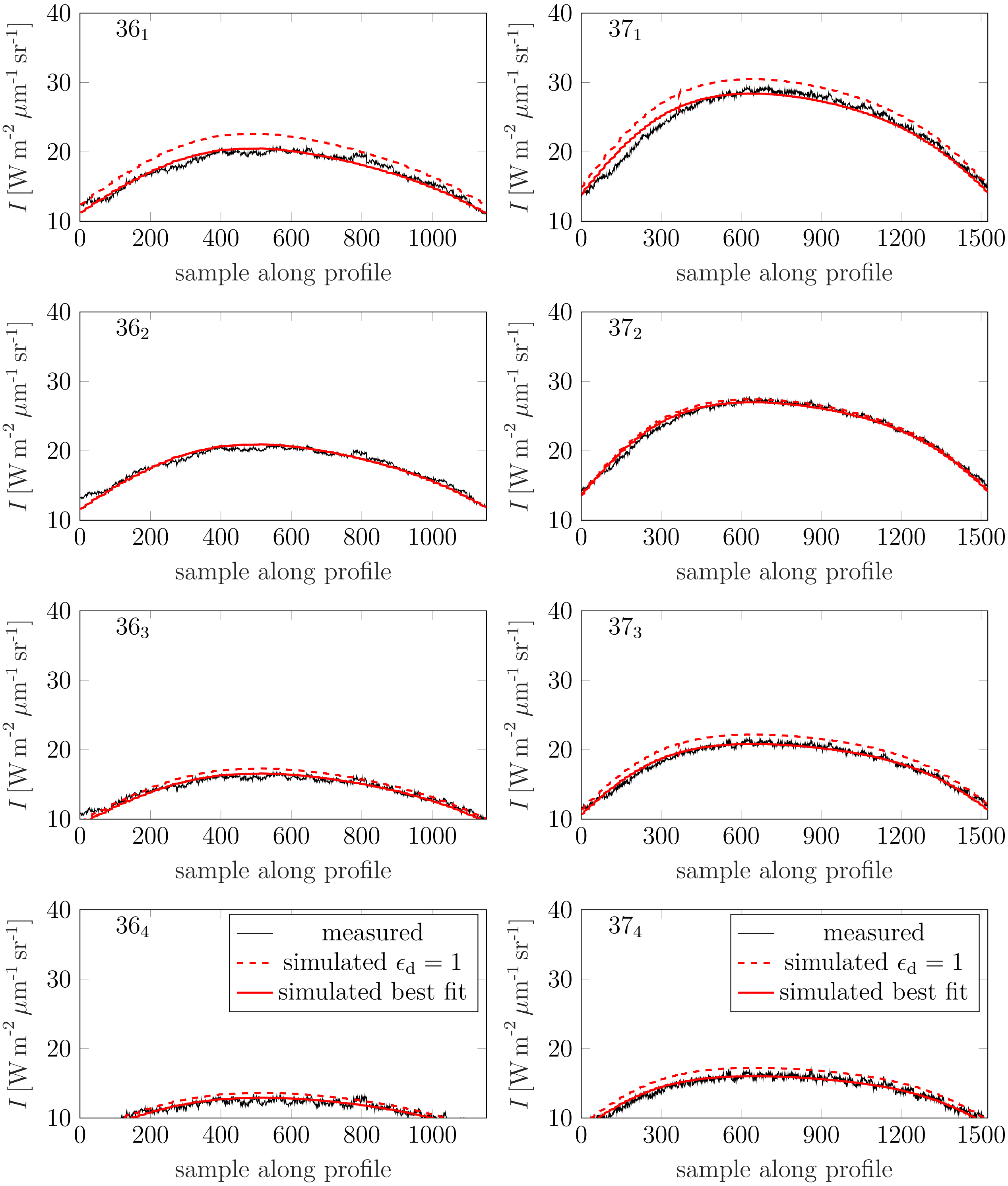

Figure 5.9. Radiance profiles for pixel 36 (left column) and 37 (right column) over four integrated wavelength channels, 7.00–8.62 μm, 8.79–10.41 μm, 10.59–12.21 μm, 12.38–14.00 μm. Figure based on Wohlfarth et al. [2023].

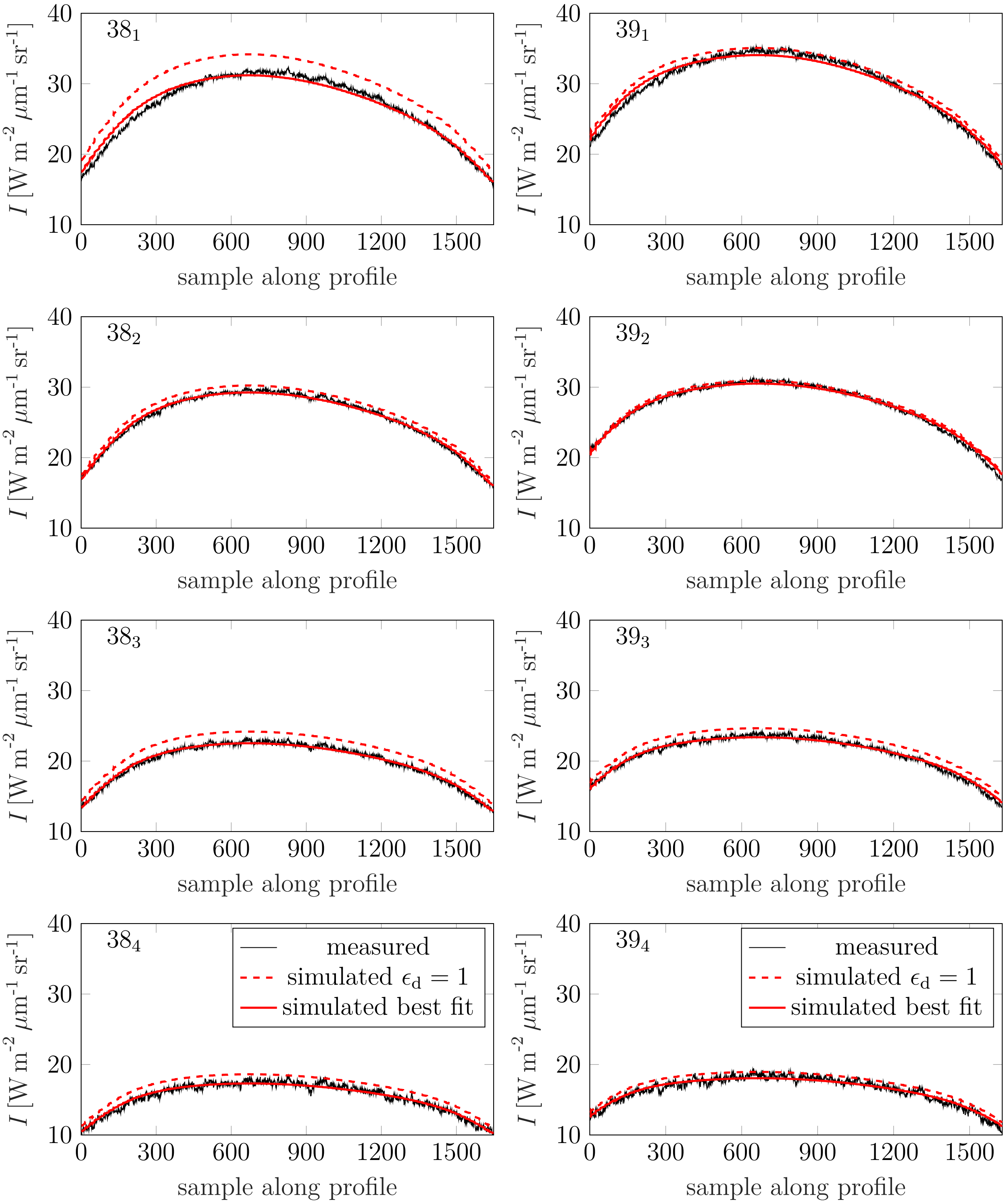

Figure 5.10. Radiance profiles for pixel 38 (left column) and 39 (right column) over four integrated wavelength channels, 7.00–8.62 μm, 8.79–10.41 μm, 10.59–12.21 μm, 12.38–14.00 μm. Figure based on Wohlfarth et al. [2023].

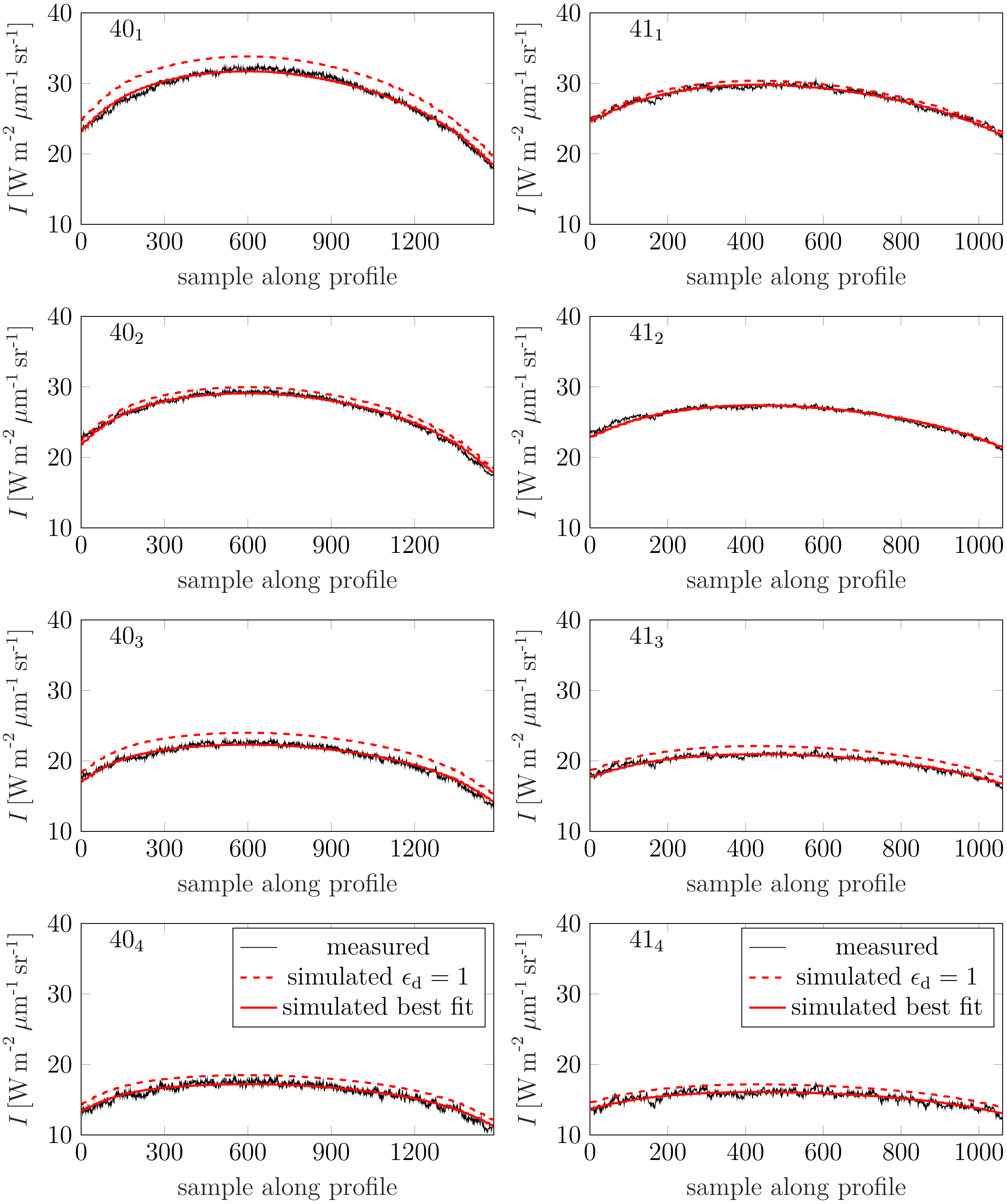

Figure 5.11. Radiance profiles for pixel 40 (left column) and 41 (right column) over four integrated wavelength channels, 7.00–8.62 μm, 8.79–10.41 μm, 10.59–12.21 μm, 12.38–14.00 μm. Figure based on Wohlfarth et al. [2023].

Table 5.3. Emissivity values of six profiles that scanned the lunar disk on April 9th, 2020. See the text for an explanation.

Profile	7.00–8.62 μm	8.79–10.41 μm	10.59–12.21 μm	12.38–14.00 μm
36	0.90	0.99	0.95	0.95
37	0.93	0.98	0.94	0.93
38	0.91	0.97	0.93	0.93
39	0.97	0.99	0.95	0.95
40	0.94	0.97	0.93	0.93
41	0.98	1.00	0.95	0.94

are, however, below this value, but given the theory, larger values are more plausible and point to roughness values of about $\overline{\theta} > 25°$. For the highest roughness values, however, the limb appears to be subtly elevated, which might be a hint that the thermal limb-brightening, and thus the roughness value, might be too large. Nevertheless, the fits agree well with the data. The author selected one representative case for $\overline{\theta} = 29°$. Figures 5.9, 5.10, and 5.11 show the measured and radiometrically calibrated spectral radiance profiles across the disk and compare them to the modeled spectral radiance for unit emissivity (dashed red) and the best-fit emissivity (solid red). Pixels at the limb that only partly contain the disk and the deep space are excluded. The rows from top to bottom show the pixels with numbers 36–41. The columns from left to right contain the spectral radiance averaged over the intervals 7.00–8.62 μm, 8.79–10.41 μm, 10.59–12.21 μm, and 12.38–14.00 μm. The spectral radiance of the unit emissivity model consistently lies above the measured profiles, which indicates that the energy balance is nearly always fulfilled. In profile 41_2, the emissivity lies marginally above unity with an estimated value of 1.0085. The best-fit emissivity values range from 0.90 to 1.00. The shortest-wavelength channel has emissivity values from 0.90–0.98 for all profiles. The second channel has almost unit emissivity. The two longest-wavelength channels have consistently lower emissivities, mostly between 0.93 and 0.95. The emissivity values are broadly consistent with the emissivity spectra of silicate mineralogy. The spatial shape of the best-fit model matches the measured spectral radiance; only pixel 37 exhibits a slight but systematic shift to the west. The spectral radiance between the rows varies. The spectral radiance is lowest for the southern and northern profiles 36 and 41 and highest for the center profile 39, whereas the spectral radiance profiles 37, 38, and 40 are in-between. This observation aligns with the trend that the temperature and thermal emission are highest in the disk's center and decrease toward the limb. See Table 5.3 for detailed numerical emissivity values.

Mercury thermal roughness model simulations

In preparation for future flybys and in-orbit operations, the author simulated Mercury for two phase angles of $g = 0°$ and $g = 120°$ and sampled the spectral radiance for $\bar{\epsilon}_{\mathrm{h}} = 1$ and $\epsilon_{\mathrm{d}} = 1$ at three locations assuming an arbitrary solar distance of 0.387 AU. Mercury's simulated disk for $g = 0°$ and $g = 120°$ at $5\,\mu$m is shown in Figure 5.12.

Near opposition ($g = 0°$), the surface roughness leads to higher spectral radiance values at the limb compared to the equilibrium model. Spectrum 0_1 in Figure 5.12 shows that the rough model predicts spectral radiance values more than twice as high as the smooth surface equilibrium model. Toward the disk's center, the smooth surface equilibrium and rough models predict nearly identical spectra (spectrum 0_3 in Figure 5.12). In this case, a single Planck function of an effective brightness temperature is able to approximate the spectral radiance of the rough-surface model. Between the center and limb of the disk, the rough surface leads to a radiance spectrum that looks slightly enhanced in comparison to a Planck spectrum (spectrum 0_2 in Figure 5.12). In addition, enhanced spectral radiance near the limb is the reason for the thermal beaming effect, as discussed by Rozitis and Green [2011].

A large phase angle ($g = 120°$) leads to a situation in which the smooth surface equilibrium model's spectral radiance is higher than the rough-surface model's result for most of the visible disk. Near the limb (120_1 in Figure 5.12), the spectral shape of the rough-surface model is similar to a Planck function, but near the terminator, the rough spectrum cannot be approximated by a Planck function (120_2 and 120_3 in Figure 5.12). These results suggest that different configurations (limb, center, terminator, opposition, near conjunction) lead to complex spectral effects. During a planetary flyby, the MERTIS instrument will scan the disk under various phase angles so that the thermal model can accurately account for these effects. In-orbit operations with oblique incidence angles or off-nadir observations also require this roughness model.

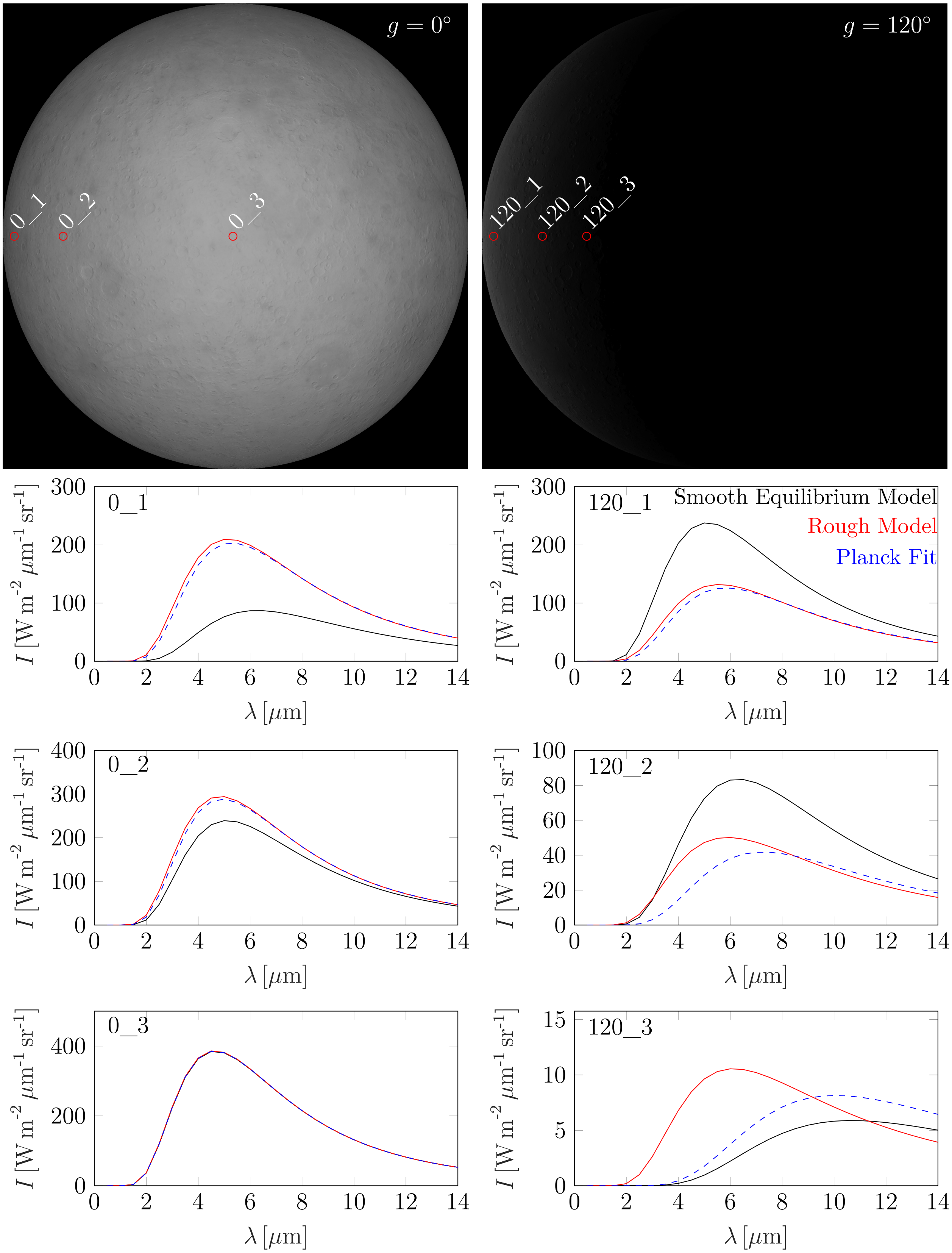

Figure 5.12. Simulated thermal emission of Mercury for two phase angles g at an arbitrary solar distance of 0.387 AU. Left: Simulated Mercury disk for $g = 0°$. The plots show the spectral radiance at the indicated locations. Right: Simulated Mercury disk for $g = 120°$. The plots show the spectral radiance at the indicated locations. Figure based on Wohlfarth et al. [2023].

Mercury heat conduction model simulations

This section explores the behavior of the one-dimensional heat-conduction model of Mercury. Figure 5.13 (top) shows the simulated temperature when Mercury passes perihelion. The day-side temperature around the sub-solar point ($0°N$, $0°E$) rises slightly above 700 K, and the night-side temperature decreases below 100 K. Figure 5.13 (bottom left) shows the temperature profiles sampled at six different latitudes on the prime meridian (Figure 5.13 (bottom left)). The temperatures reach their maximum when the sampling locations face the Sun. At sunset, the temperature falls below 200 K and slowly decreases until sunrise. The amplitude of the temperature curves decreases with increasing latitude. Figure 5.13 (bottom right) contains the temperature profiles sampled at various longitudes at the equator. At ($0°N$, $0°E$), the temperature curve approximately changes with $\sqrt[4]{\cos(i)}$, as known from the Moon (see Equation 3.70). For larger longitudes, the temperature curves show complex behavior. The orbit's eccentricity ($e = 0.2056$) leads to varying orbital velocities and solar distance. The 3:2 spin-orbit resonance causes two sideral Mercury years to equal three sideral Mercury days. Both properties may cause location-dependent retrograde solar motion across Mercury's skies, which explains the double bulges in profiles three and five in Figure 5.13 (bottom right). In locations close to $90°E$ (and $90°W$), an observer on Mercury sees the Sun rise and set before the main sunrise and after the main sunset, respectively. Further, varying solar distance generates hot poles at $0°E$ and $180°E$ with a maximum temperature above 700 K and cold poles at $90°E$ and $90°W$ with maximum temperatures less than 600 K. Under the supervision of the author, Elkhouly [2023] validated the thermal model again and found that the thermal curves are consistent with an independent orbital model and with Bauch et al. [2021]. However, Bauch et al. [2021] use a constant A_{dh}. With an A_{dh} that depends on the incidence angle, the maximum temperatures around $90°E$ and $90°W$ decrease by several percent.

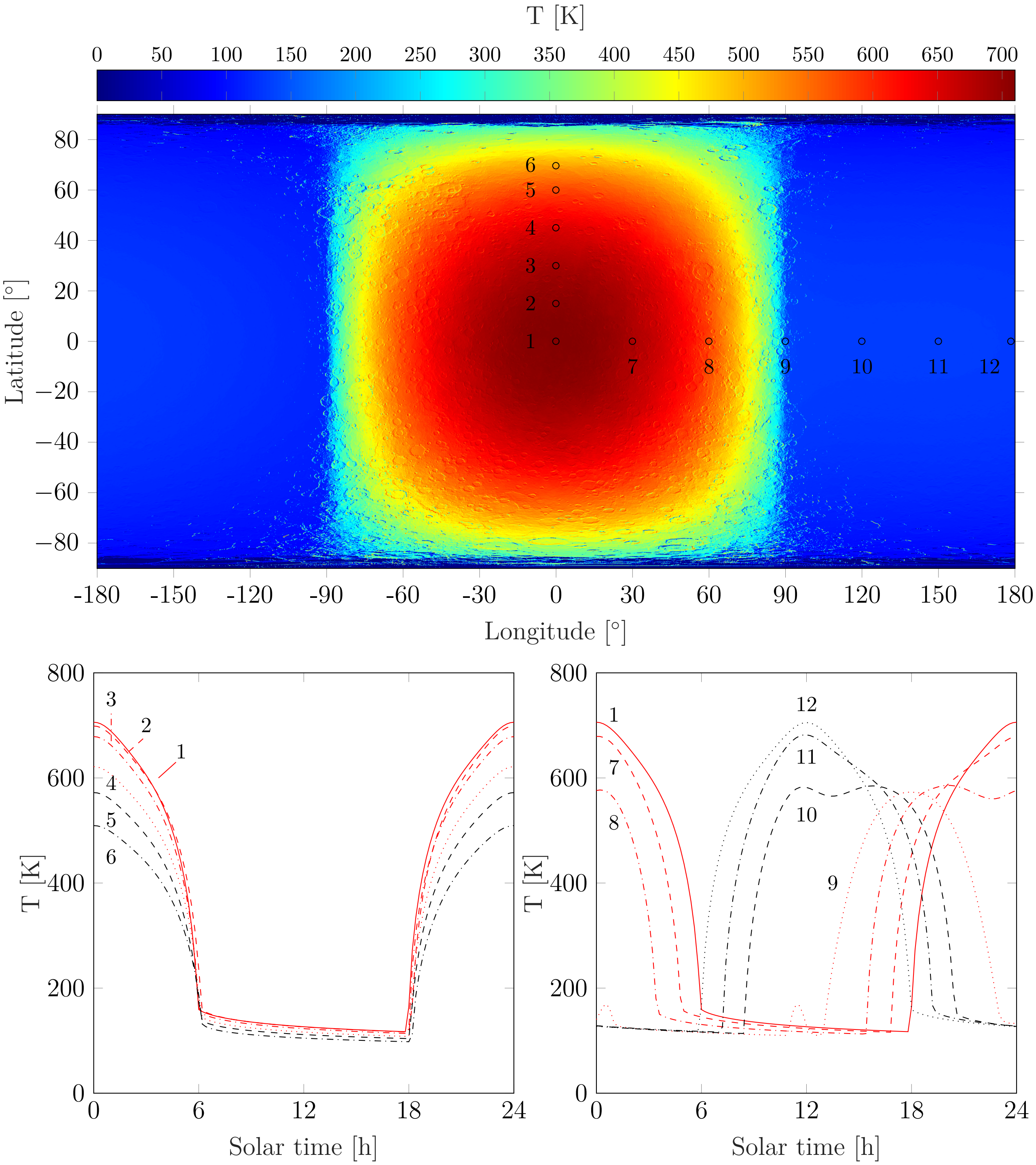

Figure 5.13. Heat conduction model simulations of Mercury. Top: Equirectangular projection of Mercury's brightness temperature at perihelion as seen by a distant observer. The black circles indicate the sampling points for the temperature evolution over an entire solar Mercury day. Bottom left: Temperature curves sampled from the prime meridian. Bottom right: Temperature curves sampled from the equator.

5.4.6 Thermal phase curve of LHS 3844b

Figure 5.14 shows the thermal phase curve of LHS 3844b for different wavelengths, roughness values, and albedos. The rough thermal model consistently predicts higher values for small phase angles than a smooth equilibrium model with $\overline{\theta} = 0°$. The higher the roughness, the higher the signal. This effect follows the thermal beaming effect discussed in Section 5.4.1. As the phase angle increases, the rough and the smooth model phase curves approach and eventually cross each other. The crossing point depends on the wavelength and lies near $g = 70°$ for $\lambda = 3\,\mu$m and around $g = 50°$ for $\lambda = 10\,\mu$m (Figure 5.14 top left, bottom left). For phase angles larger than the crossing point, the rough model gives lower values than the smooth model. This effect is due to shadowing, as explained in Section 5.4.1. Higher roughness values cause a stronger decrease. As A_{dh} increases, the thermal emission of both smooth and rough models decreases, and thus, the phase curves signal becomes smaller (Figure 5.14 bottom right). The phase curve enhancement at small phase angles through roughness can be detected with the JWST NIRSpec instrument [Zieba et al., 2023], which calls for further exploration. Supervised by the author, Tenthoff [2023] explored more parameter variations and computed phase curves that combine reflected and emitted thermal radiation. Figure 5.15 shows the combined phase curves. The rows show the phase curves integrated over the wavelength intervals of the NRS1 (2.7–3.7 μm) and NRS2 (3.8–5.2 μm) in G395H/F290LP mode of NIRSpec. The columns represent different initial albedo estimates resembling lunar maria or highlands. To obtain lunar-like albedos, Wohlfarth et al. [2023] and Tenthoff [2023] inverted M^3 spectra and spectral measurements of the Apollo samples [Taylor et al., 2010] from the RELAB database [RELAB, 2014] with the Hapke model and global lunar average parameters from Warell [2004]. The combined phase curves (Figure 5.15) indicate that the reflected component changes the shape of the phase curve and increases the overall signal. The effect is more pronounced for smaller wavelengths and higher initial albedos (highland case). LHS 3844b is likely very dark [Kreidberg et al., 2019], so the reflectance component will likely be small. Looking at Figure 5.14 (bottom right) and comparing Figures 5.15 (bottom left and bottom right), it becomes clear that the phase curve near the crossing point almost entirely depends on the albedo but not the roughness. Tenthoff [2023], therefore, proposed to first estimate the albedo from phase curve measurements near $g \approx 60°$ and subsequently extract the roughness value from the phase curve measurements near the secondary eclipse. This procedure might be helpful for data analysis of the upcoming JWST data, which will constrain its geophysical nature.

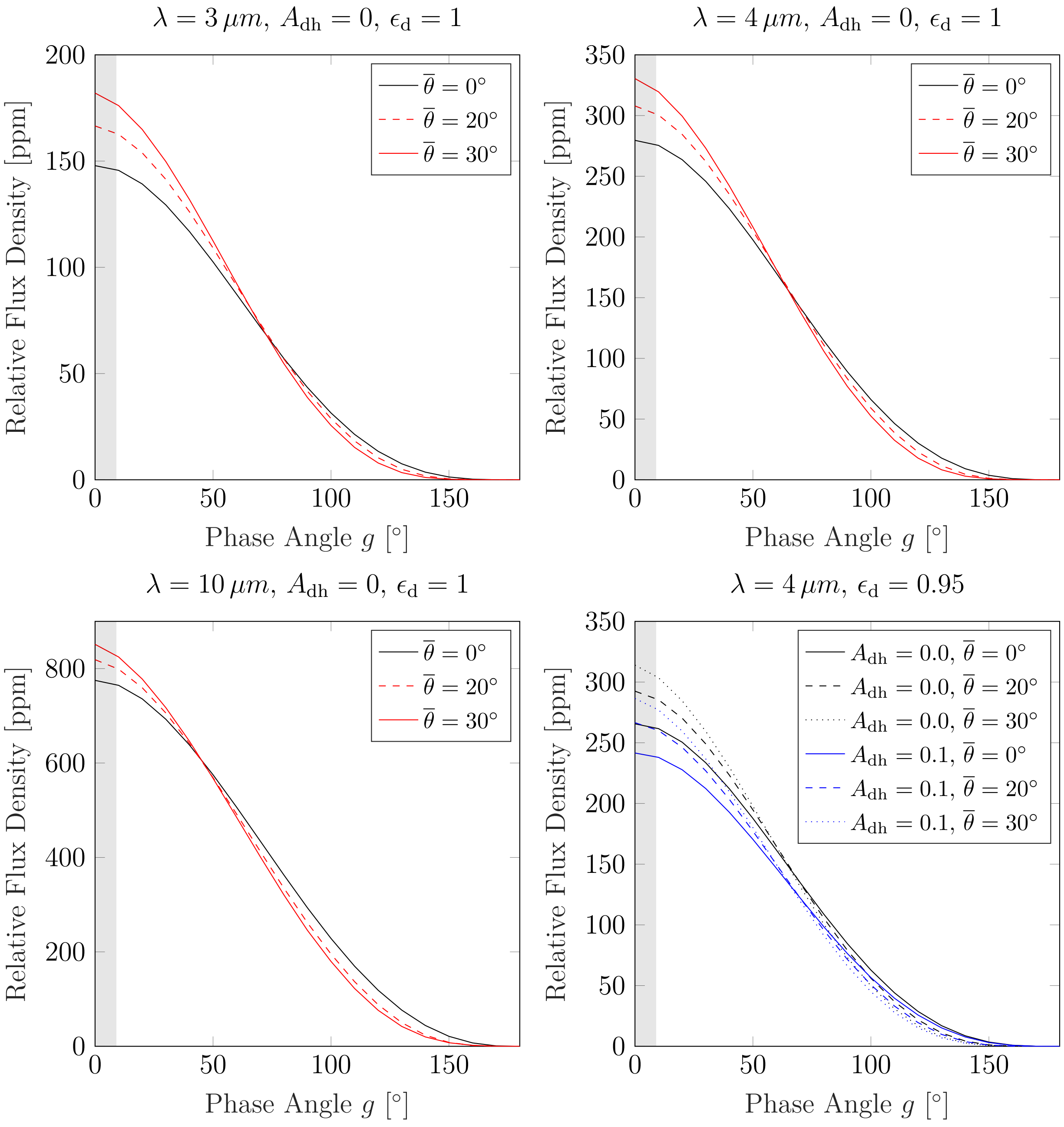

Figure 5.14. Thermal phase curves of exoplanet LHS 3844b for different scenarios. Top left: $\lambda = 3\mu\mathrm{m}$, $A_{\mathrm{dh}} = 0$, $\epsilon_{\mathrm{d}} = 1$. Top right: $\lambda = 4\mu\mathrm{m}$, $A_{\mathrm{dh}} = 0$, $\epsilon_{\mathrm{d}} = 1$. Bottom left: $\lambda = 10\mu\mathrm{m}$, $A_{\mathrm{dh}} = 0$, $\epsilon_{\mathrm{d}} = 1$. Bottom right: various albedo and roughness values for $\epsilon_{\mathrm{d}} = 0.95$ and $\lambda = 4\mu\mathrm{m}$.

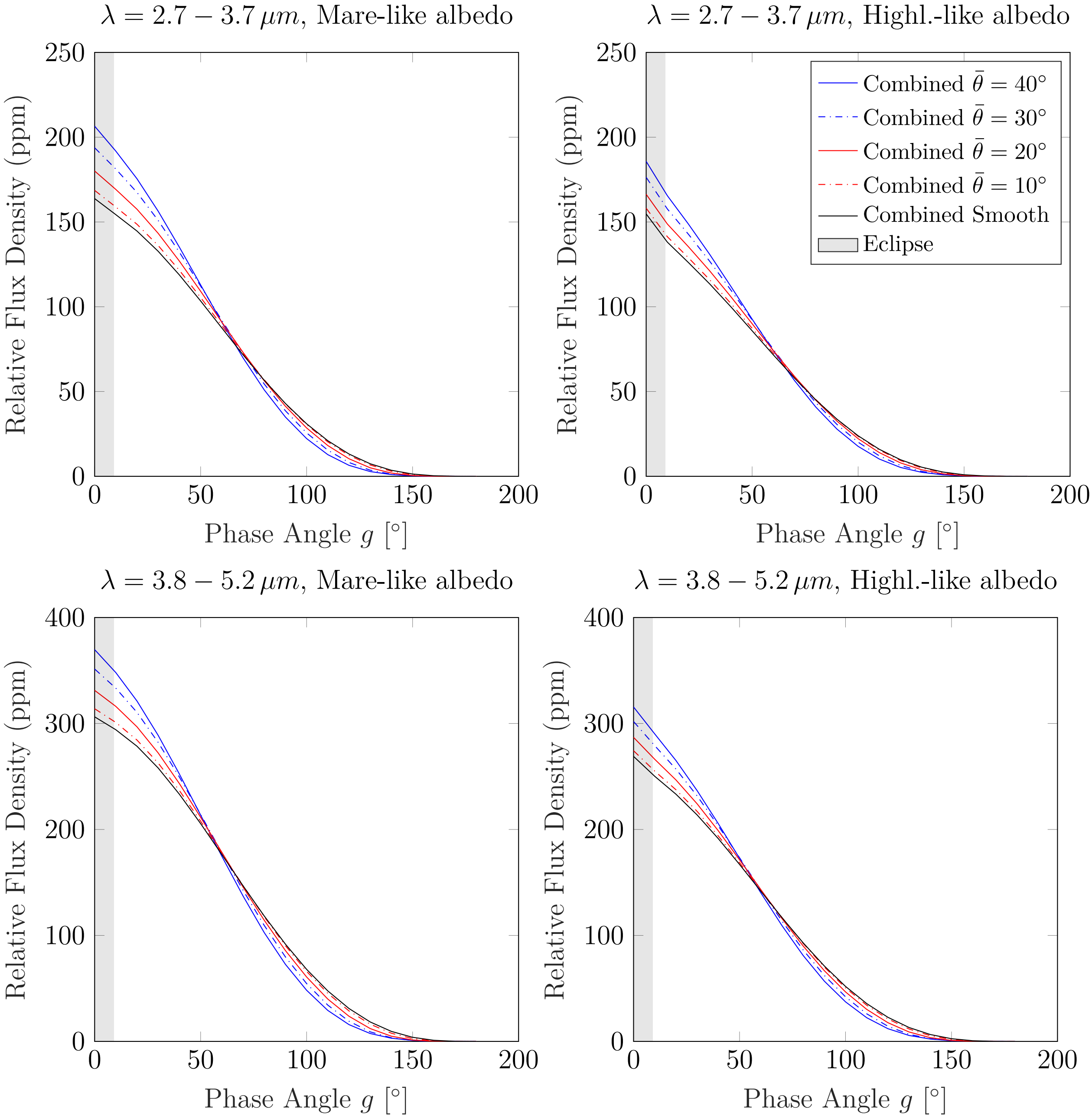

Figure 5.15. Simulated phase curves of LHS 3844b taken from Tenthoff [2023]. The phase curves are either integrated over the spectral regions of NRS1 (2.7–3.7 μm) (top row) or NRS2 (3.8–5.2 μm) (bottom row). The left column assumes a mare-like albedo, and the right column takes a highland-like albedo. The gray bar indicates the secondary eclipse at which the star occludes the planet, and the planetary radiance cannot be measured.

5.5 Discussion and future perspectives

Validation with Gaofen-4 Section 5.4.2 validated the new thermal roughness model with lunar measurements acquired by the GF-4 weather satellite and derived best-fit roughness values. The thermal model generally shows excellent agreement with the GF-4 dataset and accurately describes the spectral radiance at the limb, the dichotomy between maria and highlands, and variations due to topography. Both datasets (July 25 and July 30, 2018) acquired at different phase angles (−30.99° and 26.92°) lead to nearly identical roughness estimates of $\overline{\theta} = 21.6708° \pm 0.007°$ and $\overline{\theta} = 22.8695° \pm 0.007°$, respectively, which equals an RMSL of 22.4098° ± 0.008° and 23.4763° ± 0.007°, respectively. The 1-sigma error range is comparatively small because the number of data points is large, pushing the numerical value down.

The RMSE along the modeled and the measured profiles is $0.1985\,\mathrm{W\,m^{-2}\,\mu m^{-1}\,sr^{-1}}$ for July 25, 2018, and $0.2325\,\mathrm{W\,m^{-2}\,\mu m^{-1}\,sr^{-1}}$ for July 30, 2018. The error between the model and the measurements averaged over the entire disk is $0.1985\,\mathrm{W\,m^{-2}\,\mu m^{-1}\,sr^{-1}}$ for July 25, 2018 and $0.2464\,\mathrm{W\,m^{-2}\,\mu m^{-1}\,sr^{-1}}$ for July 30, 2018. Disk-averaged and the profile-averaged values agree. Relative to a reference value ($8.0\,\mathrm{W\,m^{-2}\,\mu m^{-1}\,sr^{-1}}$) close to the maximum spectral radiance of the disk, the relative disk-integrated RMSE is approximately 2.48% and 3.08%, respectively.

The first question that naturally arises is what causes slight local deviations between modeled and measured spectral radiance in Figure 5.3 and Figure 5.4. Therefore, a subsequent study investigated whether it is possible to force fits by varying the roughness parameter or the single scattering albedo. The roughness values can vary from $\overline{\theta} = 18°$–$30°$, and the single scattering albedo can be altered with a scaling parameter. The integral (Equation 5.9) weights the reflectance with the solar spectrum and thus suppresses spectral effects in the MIR such that albedo variations around $3.77\,\mu\mathrm{m}$ hardly influence the directional-hemispherical albedo, and thus A_{dh} did not need to be reprocessed.

The original model overestimated the spectral radiance around the ejecta blanket of Copernicus (Figure 5.4, profile 30_{R2}, pixel position 240–360 and Figure 5.16 (left) solid black). The smooth equilibrium model with $\overline{\theta} = 0°$ (dashed-dotted red Figure 5.16 (left)) and a rough model with $\overline{\theta} = 30°$ hardly deviated from the initial model (solid red) and could not provide a good fit. Increasing the single scattering albedo by 50 % yielded a good fit. In conclusion, the deviations around Copernicus's ejecta blanket are likely due to an erroneous albedo estimate with the routine (see Appendix E.4) that might be caused by the low maturity of the ejecta material. A similar argument holds for the ejecta blanket of Copernicus in profile 30_{C2} and the highland regions in profiles 30_{R3}, 30_{C3}, 25_{R2}, 25_{C1}, and 25_{C2} (Figures 5.3 and 5.4).

The initial model underestimates the spectral radiance in Oceanus Procellarum that is associated with titanium-rich mare material (Figure 5.4, profile 30_{C1}, pixel position 100–300 and Figure 5.16 (right) solid black line). Even an extremely low single scattering albedo can not provide emissivities that lead to better results (solid blue Figure 5.16 (right)). Increasing the roughness to around $\overline{\theta} = 27.8°$ while keeping the albedo fixed better captures

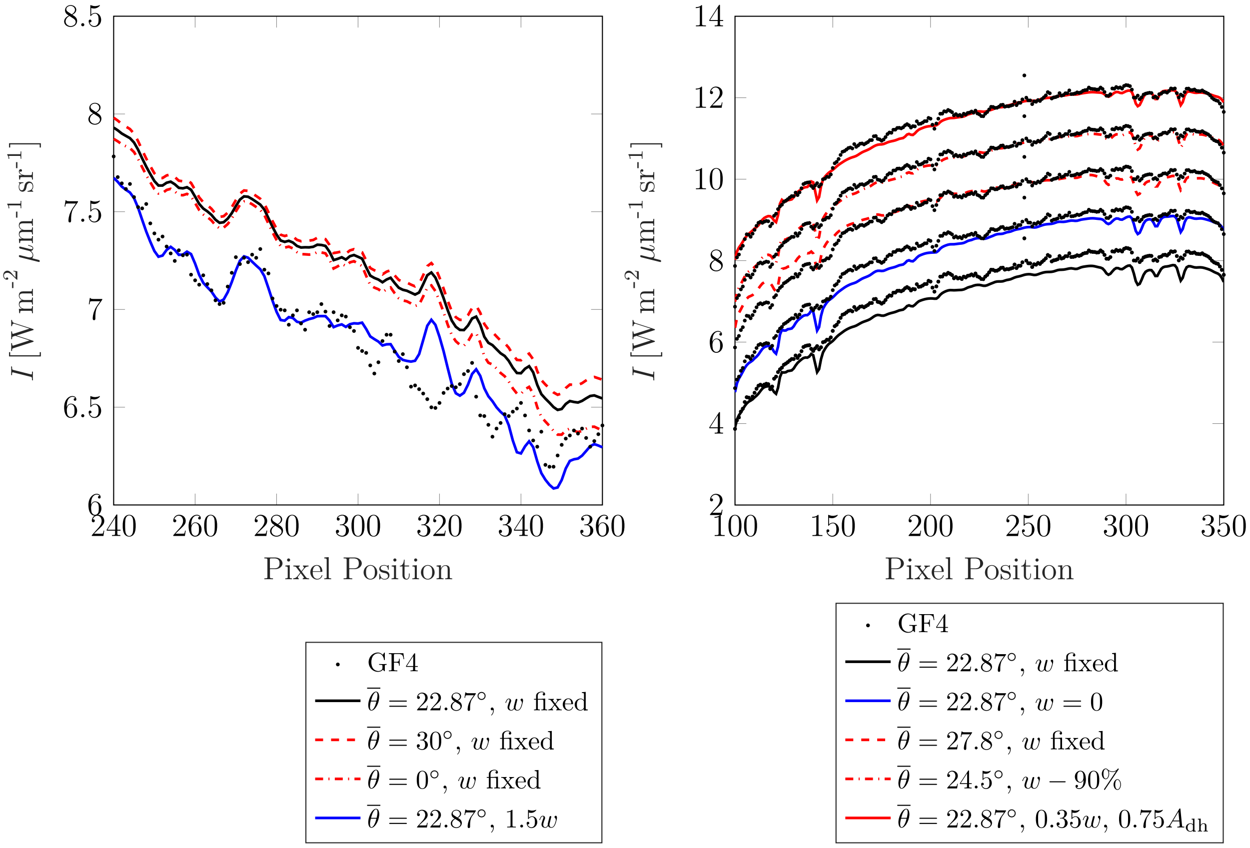

Figure 5.16. Detailed analysis of model deviations around Copernicus and in the Oceanus Procellarum. Left: Measured spectral radiance (points) around crater Copernicus vs. various modeling approaches (solid lines). The data points correspond to a subsample of profile 30_{R2} in Figure 5.4. Adjusting the single scattering albedo w leads to a better agreement. Right: Measured spectral radiance (points) across a titanium-rich region of Oceanus Procellarum vs. various modeling approaches (solid lines). The data points correspond to a subsample of profile 30_{C1} in Figure 5.4. To avoid clutter, the profile groups are offset by $1\,\mathrm{W\,m^{-2}\,\mu m^{-1}\,sr^{-1}}$. Figure from Wohlfarth et al. [2023].

the overall spectral radiance level, but the model still underestimates the spectral radiance in the disk's center and overestimates the spectral radiance at the limb (dashed red). Only combinations of different effects might accurately explain the spectral radiance profiles. A combination of very low albedo (-90 % of the initial value) and slightly increased roughness ($\bar{\theta} = 24.5°$) yields an adequate fit (dashed-dotted red). Furthermore, reducing the directional-hemispherical albedo A_{dh} by 25 % and reducing the single scattering albedo by 65% describes the measurements without the need to change the roughness. For Oceanus Procellarum, the parameter identification is ill-posed, and a conclusive evaluation requires more data under multiple geometric configurations that the GF-4 dataset does not provide. After all, it might be the case that the Apollo extrapolation routine (see Appendix E.4) does not accurately determine the albedo of titanium-rich mare material for the MIR.

All in all, variations of the single scattering albedo can fully explain local deviations around ejecta blankets and bright highland material where the model overestimates the spectral radiance. In Oceanus Procellarum's titanium-rich regions, only combinations of several effects explain the data, but it is also possible to only alter both albedos to achieve good fits. In any case, these results underline that the roughness varies only slightly, if at all. Thus, the results agree with Bandfield et al. [2015] and partly with Rubanenko et al. [2020], though they find highlands slightly rougher than maria.

Validation with Diviner and MERTIS A roughness of $\theta = 20°$ (RMSL = 20.90°) best fits the diviner nadir-observations, which agrees with the RMSL of 20° found by Bandfield et al. [2015]. However, eleven out of twelve off-nadir EPF measurements have roughness values around $\overline{\theta} = 30.25°$ (RMSL = 29.61°) for channel four and $\overline{\theta} = 29.25°$ (RMSL = 28.81°) for channel seven. One particular case (Figure F.6 in Appendix F) only requires $\overline{\theta} = 19°$ (RMSL = 19.98°) for the best fit. Because the neighboring EPF measurement (Figure F.5 in Appendix F) exhibits similar geometric configurations and is well described with $\overline{\theta} = 28°$ (RMSL = 27.88°), the deviation of the odd profile might be due to some localized effect. However, it might also be that the fitting routine could not accurately decouple albedo and roughness effects. These overall results agree with Bandfield et al. [2015], who report RMSL between 20° and 35° to describe EPF measurements. Other studies, such as Rozitis and Green [2011] and references therein and Rubanenko et al. [2020], also point to values around and above RMSL of 30°–35°, which is approximately the same value for $\overline{\theta}$. Due to the challenging observation conditions and underconstrained PSF, a specific roughness value is difficult to obtain from the MERTIS lunar flyby dataset. However, the results tend to be most plausible for values between $\overline{\theta} = 25°–30°$.

Surface roughness is a physical property of a planetary regolith that stays constant on geological timescales. Consequently, one must address why the best-fit roughness values differ between GF-4 and Diviner nadir on the one hand and Diviner EPF data on the other hand, even if they all come from the same body and use the same roughness model. Assuming well-calibrated instruments, this section discusses three hypotheses explaining the deviations: (1) Locally variable roughness, (2) inaccurate model behavior for varying geometric input configurations, and (3) dependence on wavelength.

In principle, the roughness may vary across the lunar surface. However, surface roughness appears to be relatively constant across the lunar surface. In Figure 5.3 and Figure 5.4, one single roughness value leads to model fits that agree with the data in highland and mare regions. There are no systematic deviations toward the limb or the terminator, where roughness effects have the most substantial effect. Only titanium-rich mare regions might exhibit slightly higher values, but the effects can also be due to erroneous albedo extrapolation from Apollo spectra. The new model runs with $\bar{\epsilon}_\mathrm{h} = 0.95$ yield individual roughness estimates for mare and highland that only differ by two degrees (Section 5.6.2). Bandfield et al. [2015] also reported no significant difference, and Rubanenko et al. [2020] only reported a difference of six degrees between maria and highlands. Even if small roughness variations exist, the differences are not large enough to jump from $\overline{\theta} = 20°$ to $\overline{\theta} = 30°$. Consequently, local deviations are considered unlikely to be the main culprit for differing roughness values. However, EPF measurements 5 and 6 point to some local roughness deviation (Table 5.2) that cannot be evaluated further due to the lack of data.

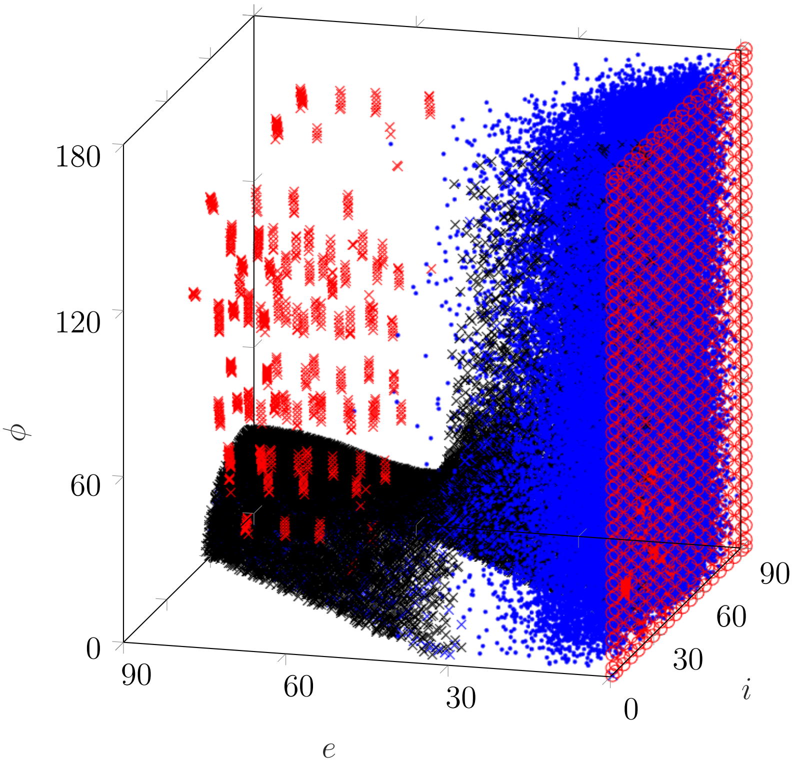

Figure 5.17. The Configuration space is spanned by the incidence angle i, the emission angle e, and the azimuth angle ψ. The data points represent the geometric configurations associated with the measurements used throughout this study. Black crosses: Lunar measurements by GF-4 on July 25, 2018, and July 30, 2018. Red circles: Diviner nadir measurements lie in this plane. Red crosses: Diviner EPF measurements. Blue dots: M^3 global dataset. Blue crosses: MERTIS lunar flyby (almost entirely occluded by GF-4). To avoid clutter, the GF-4, M^3, and MERTIS data points were subsampled. Figure adapted from Wohlfarth et al. [2023].

If a thermal model is accurate, it will yield the same roughness value regardless of the geometric input parameter configuration. However, it appears as if the roughness deviations depend on the model's input geometry. Therefore, the author investigated the configuration space spanned by the incidence, emission, and azimuth angles and traced how all six datasets used here occupy this space (Figure 5.17). The geometric configurations of both GF-4 measurements (black crosses) form a surface that approximately takes the shape of a boot. The emission angles of nadir measurements vanish by definition ($e = 0°$), but the incidence and azimuth angles can take arbitrary values ($i = 0 \ldots 90°$, $\psi = 0 \ldots 180°$). Consequently, nadir measurements occupy a plate in the configuration space (red circles) where the Diviner nadir data form a subset. The EPF measurements (red crosses) observe the Moon under oblique emission angles over a wide range of azimuth angles. The incidence angle remains around $i \approx 60°$. Most geometric configurations of the global M^3 dataset have $e < 30°$, but they span almost the entire azimuth and incidence angle range (blue dots). The geometric configuration of MERTIS measurements is very close to both GF-4 datasets, such that the point clouds are indistinguishable (blue crosses). The point clouds of Diviner nadir measurements ($\overline{\theta} = 20°$) and GF-4 ($\overline{\theta} \approx 22°$) partially overlap. The geometric configurations of the Diviner EPF measurements ($\overline{\theta} = 30°$) lie outside of the other datasets at a different region of the configuration space (see Figure 5.17). Saari et al. [1972] measured parts of the sunlit portion of the Moon over a whole lunation such that the parameter configurations occupy a similar region to the Diviner EPF measurements. Rozitis and Green [2011] used this lunation dataset for roughness model validation, leading to an RMSL of $31.5° \pm 1.5°$ and $33.0° \pm 1.1°$. The same holds for the lunar phase curve observations of Müller et al. [2021], which are best described with a roughness around 32°. This analysis suggests that the roughness fits deviate between datasets taken under different geometric configurations. Nadir-like or frontal disk observations yield roughness values around $\overline{\theta} \approx 20°$, while the EPF measurements and other phase curve observations yield $\overline{\theta} \approx 30°$. Consequently, the observations suggest that the new roughness model, and probably similar approaches, may not be accurate for all geometric input configurations.

Future research should, therefore, identify which model components require improvement. Two candidates may be the roughness type and the emissivity model. Davidsson et al. [2015] discuss that the roughness type partially controls the anisotropic behavior of thermal models. However, the model already used rough fractal surfaces, which is theoretically the most realistic representation of the lunar regolith. The behavior at thermal isolation scales may yield further insights, requiring a small-scale three-dimensional heat-transfer model. Most studies assume a constant isotropic directional emissivity of $\epsilon_{\mathrm{d}} \approx 0.90$–$0.95$ that does not depend on the emission angle. However, the emissivity is anisotropic. Few works provide emissivity models. Hapke's theory predicts that a horizontally stratified medium emits less radiation as the emission angle increases [Hapke, 2012]. The higher the surface albedo, the stronger the effect. Therefore, the anisotropic emission superimposes the anisotropic effects of surface roughness, which changes the overall model behavior. An alternate approach is determining the surface reflectance and inferring the emissivity via Kirchhoff's law. However, lunar reflectance might not be constrained entirely, which adds further uncertainty. The model addressed anisotropic emissivity effects. In retrospect, the author evaluated whether the emissivity model may have caused model variations that are strong enough to explain the differences between GF-4 and Diviner roughness estimates but did not find significant evidence. Diviner channel four is around the Christiansen feature, such that the emissivity is already close to unity, and the single scattering albedo almost vanishes (Table 5.2). In this case, the Hapke emissivity model hardly predicts anisotropic variations (see Hapke [2012]), which further holds for the Kirchhoff approach. In the case of the GF-4 measurements, the single scattering albedo is higher, and the emissivity effect increases. However, the emissivity model yields decreasing emissivity values toward the limb of the disk, while the roughness model counteracts and predicts increasing thermal emission. Removing the emissivity model even leads to slightly smaller roughness values. Consequently, the emissivity model would have to decrease toward higher emission angles for higher roughness values. Further, the emissivity depends on the wavelength and may exhibit different behaviors for spectral regions near the Christiansen feature around $8\,\mu$m compared to the NIR and MIR. Wavelength dependence might explain why the GF-4 data are better matched with $\overline{\theta} \approx 22 - 26°$, while the MERTIS data are better described by higher $\overline{\theta}$, though their geometric configuration is quite similar (Figure 5.17).

A better understanding of the role of the emissivity model requires more theoretical work. The Hapke model is based on radiative transfer for horizontally stratified homogeneous media. The roughness models simulate individual facets of a rough regolith, which might be incompatible on a theoretical level. Warren et al. [2019] present a promising approach in which they numerically compute the emissivity of a rough isothermal surface and validate the results with a goniometer setup. However, the approach has yet to be extended to anisothermal scenarios and must undergo more extensive validation with regolith material. Another idea would be to take up thermal gradients [Millán et al., 2011] and explore how they behave with surface roughness. This approach requires a model that yields the behavior of near-surface thermal gradients for each surface element of the fractals. An exploration of sub-surface thermal gradients was made in Bowkunnyj [2021] under the supervision of the author. Yang and Burgdorf [2022] carried out a comparable study and analyzed how thermal gradients affect the lunar emissivity in the microwave region.

Lunar hydration The author reprocessed the global level 1B spectral radiance of the M^3 instrument with the method of Wöhler et al. [2017] and Grumpe et al. [2019] but with the newly developed thermal model, setting the roughness to the rounded average of the GF-4 results of $\overline{\theta} = 22°$. The following three observations back this choice. First, the GF-4 measurements are in a similar wavelength region compared to the long-wavelength end of M^3 and should exhibit similar behavior. Second, Diviner nadir measurements point to roughness values around $\overline{\theta} = 20°$ and lie in a similar region of the configuration space. Third, GF-4 and M^3 data partially overlap in the configuration space. Consequently, GF-4 and Diviner nadir measurements sufficiently constrain the M^3 data. The value of $\overline{\theta} = 22°$ is similar to the previous roughness estimate of $\overline{\theta} = 20°$ [Wöhler et al., 2017; Grumpe et al., 2019], and the average lunar roughness (RMSL = 20°) used by Bandfield et al. [2015, 2018]. The alternative solution in Wöhler et al. [2017] and Grumpe et al. [2019] of $\overline{\theta} = 9°$, however, appears to be too smooth. For an updated model fit with $\overline{\epsilon}_{\mathrm{h}} = 0.95$, improved A_{dh}, and $\overline{\theta} = 25°$ and subsequent discussion, see Section 5.6.4.

The results from reprocessing the M^3-data align well with other studies, such as Honniball et al. [2020], who reported diurnal and latitudinal variations using an entirely different dataset obtained with the ground-based SpeX instrument. Honniball et al. [2020] also found a dichotomy with higher OH/H_2O abundances in the highland regions, which corresponds to the original findings of Wöhler et al. [2017] and Grumpe et al. [2019] and to the new results for lunar midday. However, Honniball et al. [2020] did not carry out detailed emissivity and albedo modeling. Laferriere et al. [2022] recently reevaluated data from the Deep Impact spacecraft and found that lunar OH/H_2O is widespread but variable across the lunar south pole. Except for the lowest temperatures, highlands have stronger absorption bands than mare regions, which aligns with the new maps at lunar midday. For low temperatures in the morning and evening, maria appear to have a slightly stronger hydration feature than highlands, which does not contradict Laferriere et al. [2022]. Hence, the results largely agree with two independent datasets (SpeX and Deep Impact), which strongly suggest the widespread presence and the diurnal and latitudinal variations of lunar hydration. The observations may be explained by an exospheric process in which solar wind implantation of protons induces an accumulation of lunar OH/H_2O during the morning and afternoon, whereas thermal evaporation and photolysis lead to a depletion during midday [Grumpe et al., 2019; Schörghofer et al., 2021].

Future studies may use the newly calibrated dataset for lunar hydration, such as Bishop et al. [2022]. New datasets from the lunar Trailblazer mission will be highly valuable for conducting more model validation and research on lunar hydration. The thermal model also helps better understand the lunar hydration on rough surfaces. Permanently shadowed regions at the lunar poles and Mercury's poles are believed to host water ice. The thermal model can constrain the thermal environment in these regions and address anisotropy effects because the illumination in the polar regions is so oblique [Wohlfarth et al., 2023a]. Roughness is known to cause small areas, so-called micro cold traps [Rozitis et al., 2020], that are comparatively cold and can host water ice. Wöhler et al. [2022] combined the new thermal model with the dynamic lunar hydration model of Grumpe et al. [2019], generating lunar OH column densities that agree with M^3 observations. OH can persist in the colder regions caused by roughness and thus significantly influence the observed column density.

MERTIS lunar flyby The conditions under which MERTIS observed the Moon were challenging, as it had to acquire the data through the calibration baffle. The distance between the Moon and the instrument was large, so only six pixels scanned the lunar disk. Further, the Moon is much colder than Mercury, and consequently, the MIR emission is approximately ten times smaller than the emission expected for Mercury. Due to the resulting low signal-to-noise ratio, the lunar flyby data were binned into four broad wavelength channels. The analysis generally finds a good match between the modeled spectral radiances and the measured spectral radiance profiles across the disk. However, it is not possible to provide a precise roughness result because of the point spread function.

On December 1, 2024, BepiColombo performed a flyby maneuver around Mercury, and MERTIS acquired the first thermal infrared measurements of Mercury during this mission. The measurements cover a wide stripe from the north pole to the south pole along the 180° longitude meridian. The data is currently compared with the model developed in this chapter. First inspections suggest that the bolometric hemispherical emissivity $\bar{\epsilon}_\mathrm{h}$ is indeed comparatively low, as discussed in Section 5.6.1. Tenthoff et al. [2025] presented the first preliminary results and model comparisons in close cooperation with the author of this thesis.

Combined heat conduction and roughness model This thesis independently modeled the effects of surface roughness and heat conduction for planet Mercury. However, the radiation balance Equation 5.1 states that radiative heat transfer (self-heating and -scattering) and conductive heat transfer are coupled. Some asteroid models have combined both mechanisms but use simplified bowl-shaped craters as roughness models. A step toward a more realistic thermal model would solve the radiation balance equation for a three-dimensional discretized volume bound with a fractal surface on top. This model likely becomes computationally very demanding but bears the chance to explore the behavior near the thermal isolation scale and arrive at a more accurate understanding of near-surface heat conduction. A first simplified step could be a simple iterative scheme that alternately determines the sub-surface heat flow with the 1D heat equation and the thermal emission at the surface with the present roughness model.

Phase curve for the airless exoplanets The simulations show that surface roughness increases the phase curve of LHS 3844b near the secondary eclipse. This effect can be measured with NIRSpec onboard the JWST. However, it is unclear if the phase curve measurements will show an enhancement. If they do, it is a sign that the planet has a surface that can host strong thermal gradients, such as the regolith surface on the Moon or Mercury. Even under the temperatures at LHS 3844b, the thermal isolation of the regolith should be strong enough. If not, the surface cannot host thermal gradients and thus likely has a different structure. Explanations include planetary resurfacing through volcanism or a different environment that prevents regolith from forming. The parameter retrieval proposed by Tenthoff [2023] and Tenthoff et al. [2024] likely helps understand the geophysical makeup.

Coy et al. [2024] recently used the thermal model presented in this thesis to analyze brightness temperature trends observed in the measurements of several airless exoplanets. Further, a Director's Discretionary Time (DDT) program with the JWST has been set up to search for atmospheres of exoplanets around M-dwarfs [Redfield et al., 2024]. Data analysis of the phase curves may benefit from a roughness model.

Applications for Earth science Earth-observation satellites require regular in-flight calibration or performance monitoring, which involves onboard calibration and cross-calibration with other instruments or another target with well-known properties that are regularly measured. The lunar surface only changes on geologic timescales, so it is an ideal calibration object. Consequently, the thermal model predictions discussed in this chapter can be compared to satellite measurements and used for calibration of MIR and TIR instruments in the range of the model accuracy [Wohlfarth and Wöhler, 2024]. More specifically, the company Ororatech is launching its satellite constellation for forest fire detection on Earth. Each satellite carries two infrared cameras, which will be, along with cross-calibration, calibrated with regular lunar acquisitions and the thermal model developed in this chapter [Seifert et al., 2024].

5.6 Addendum: Effect of the bolometric hemispherical emissivity

Between the submission of the thesis and the defense, almost fourteen months passed. During this time, the author further investigated planetary thermal models and conducted more experiments. For simplicity, the original publication [Wohlfarth et al., 2023] and, accordingly, Sections 5.3 and 5.4 assumed a bolometric hemispherical emissivity of $\bar{\epsilon}_\mathrm{h} = 1$. The author now analyzed how the bolometric hemispherical emissivity $\bar{\epsilon}_\mathrm{h}$ behaves for the Moon and Mercury under more detailed assumptions and how it influences the thermal modeling results. For the Moon, a constant value of $\bar{\epsilon}_\mathrm{h} = 0.95$ that is almost independent of the illumination conditions is confirmed to be a viable estimate. Interestingly, the $\bar{\epsilon}_\mathrm{h}$ value of Mercury strongly depends on the illumination conditions and the solar distance and takes values well below unity. Equipped with these insights, the results from Section 5.4 were reprocessed and compared to the previous modeling results. It turns out that the overall influence of $\bar{\epsilon}_\mathrm{h}$ on the modeling results is rather small, but the new parameter fits are considered to be slightly more realistic.

5.6.1 The bolometric hemispherical emissivity for the Moon and Mercury

The bolometric hemispherical emissivity $\bar{\epsilon}_\mathrm{h}$ is rarely discussed in the literature. In theory, $\bar{\epsilon}_\mathrm{h}$ depends on the temperature (see Equation 3.77), but many studies assume $\bar{\epsilon}_\mathrm{h}$ to be a constant. This section explores how the bolometric emissivity $\bar{\epsilon}_\mathrm{h}$ of a planetary surface behaves for various silicate materials and illumination conditions, allowing recommendations for best practice. For the sake of argument, consider an idealized planetary surface at solar distance r illuminated under the solar incidence angle i. The surface is sheeted with a particulate silicate material with an isotropic but spectrally variant directional emissivity $\epsilon_\mathrm{d}(\lambda)$ and a directional-hemispherical albedo A_dh that depends on i. The temperature T and the bolometric emissivity $\bar{\epsilon}_\mathrm{h}$ of the surface have the following mathematical relationship:

$$\bar{\epsilon}_\mathrm{h}(T)\sigma T^4 = (1 - A_\mathrm{dh}(i))\cos(i)\frac{S_\odot}{r^2} \tag{5.25}$$

$$\bar{\epsilon}_\mathrm{h}(T) = \frac{\int_{\lambda=0}^{\infty} \epsilon_\mathrm{d}(\lambda) \int_\Omega \cos(e) U(T,\lambda) d\Omega d\lambda}{\int_{\lambda=0}^{\infty} U(T,\lambda) d\lambda}. \tag{5.26}$$

Both equations are coupled, i.e., T requires $\bar{\epsilon}_\mathrm{h}$ and vice versa. A fixed-point iteration initialized with $\bar{\epsilon}_\mathrm{h} = 1$ converges after several steps and provides the solution for $\bar{\epsilon}_\mathrm{h}$. The equations are solved for several emissivity spectra $\epsilon_\mathrm{d}(\lambda)$, incidence angles from $i = 0 \ldots 85°$, and three different distances (Sun-Moon distance $r = 1\,\mathrm{AU}$, Sun-Mercury perihelion $r = 0.30\,\mathrm{AU}$, and Sun-Mercury aphelion r=0.46 AU). The directional-hemispherical albedo is computed according to Keihm [1984] with $A_\mathrm{dh} = 0.12 + 0.03(i/45°)^3 + 0.14(i/90°)^8$. The computation crucially depends on the directional emissivity of the material. Unfortunately, no in-situ lunar emissivity spectra exist that are both reliable and cover a wavelength region from

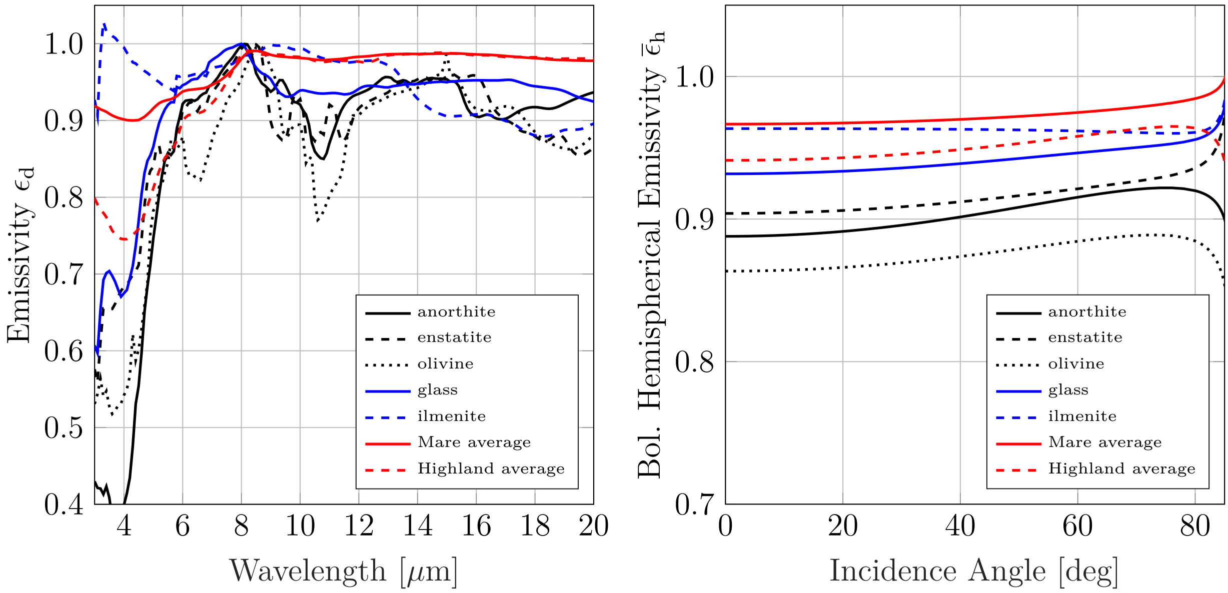

Figure 5.18. Left: Emissivity spectra of various minerals of a mixture of grain sizes taken from Maturilli et al. [2008] and averaged Apollo spectra derived from Salisbury et al. [1987]. Right: Bolometric hemispherical emissivity $\bar{\epsilon}_h$ of a surface covered in regolith of various compositions. The surface is at $r = 1$ AU away from the Sun and illuminated under different incidence angles i. $\bar{\epsilon}_h$ is almost independent of i and usually >0.9.

approximately 3–20 μm that allows computing $\bar{\epsilon}_h$. Therefore, the author considers the best available laboratory spectra. Salisbury et al. [1987] provide reflectance measurements of the Apollo samples that can be converted to emissivity via the Hapke model. Donaldson Hanna et al. [2017] present Apollo measurements under ambient and lunar conditions, but the spectra are not publicly available. Maturilli et al. [2008] measured the emissivity of several analog materials. This analysis considers the average lunar highland and mare spectrum from Salisbury et al. [1987] and several mineral analog spectra from Maturilli et al. [2008].

Figure 5.18 (left) shows the spectral emissivity used for this study. Figure 5.18 (right) shows the bolometric hemispherical emissivity of different minerals as a function of incidence angle at $r = 1$ AU. The values for $\bar{\epsilon}_h$ almost do not depend on the incidence angle for $i < 85°$ at all. The observed emissivity values agree with the literature, which often assumes $\bar{\epsilon}_h = 0.90$ for asteroids and $\bar{\epsilon}_h = 0.95$ for the Moon [Keihm, 1984; Hayne et al., 2017; Müller et al., 2021]. The emissivity spectra derived from Salisbury et al. [1987] exhibit a weak spectral contrast and thus produce a high $\bar{\epsilon}_h$. The lunar analogs and the spectra of Donaldson Hanna et al. [2017], who measured Apollo emissivity spectra under ambient and simulated lunar conditions, have a stronger spectral contrast and yield slightly lower $\bar{\epsilon}_h$-values. The author chooses $\bar{\epsilon}_h = 0.95$ for all upcoming lunar modeling endeavors. Figure 5.19 (left) shows the $\bar{\epsilon}_h$ for $r = 0.30$ AU, which corresponds to Mercury's distance at perihelion. The $\bar{\epsilon}_h$-values are consistently lower compared to the $r = 1$AU-case. Further, the bolometric emissivity strongly depends on the incidence angle. Higher incidence angles cause higher emissivity values. This effect is comparatively strong and must be considered for any future Mercury scenario. To the author's knowledge, a dependency between the incidence angle and the

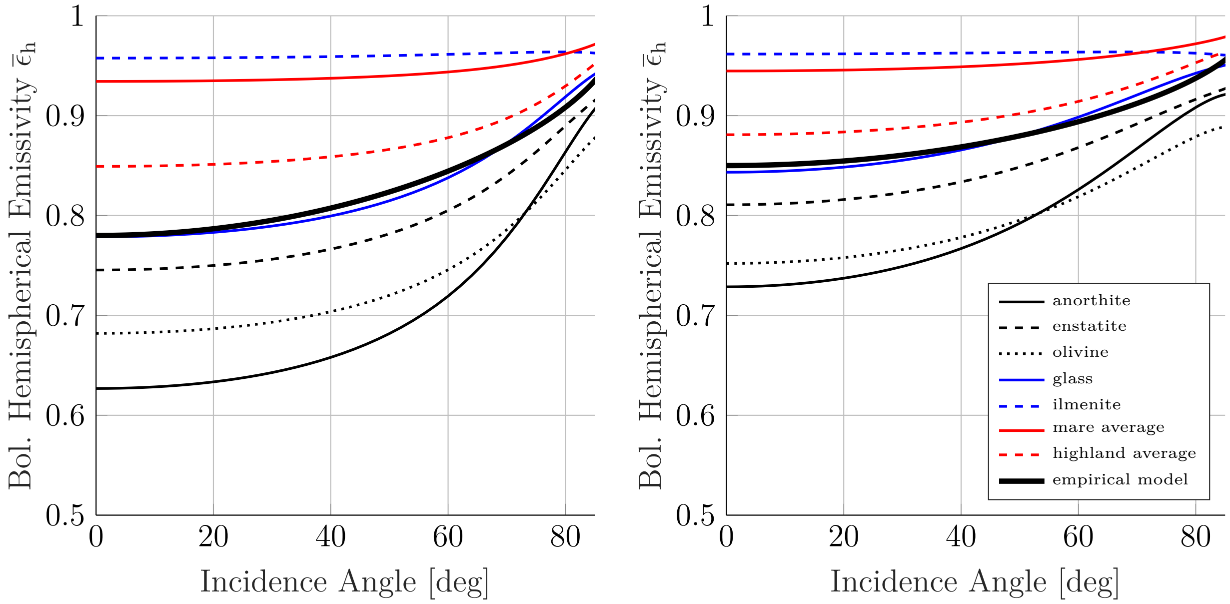

Figure 5.19. Left: Bolometric hemispherical emissivity $\bar{\epsilon}_h$ of a surface covered with regolith of various compositions. At perihelion, the surface is $r = 0.30$ AU away from the Sun and illuminated under different incidence angles i. $\bar{\epsilon}_h$ becomes significantly lower and strongly depends on i. Right: Same as left but for a distance of aphelion with $r = 0.46$ AU.

bolometric hemispherical emissivity has not been discussed in planetary science literature in the recent two decades. Here, a simple empirical relationship is proposed

$$\bar{\epsilon}_h(i, r) = 1 - a(r)\cos^{\frac{1}{2}}(i), \tag{5.27}$$

where $a = 0.22$ for the hermean perihelion and $a = 0.15$ for aphelion. Future studies must generalize these findings. LHS 3844b is comparatively hot. Thus, the thermal emission bulge of the planet is at much lower wavelengths, and $\bar{\epsilon}_h$ is expected to vary less with incidence angle than Mercury but be at a similar level, e.g., $\bar{\epsilon}_h \approx 0.8$. Future studies must investigate the exoplanet's bolometric emissivity in detail.

5.6.2 Reassessing GF-4 lunar measurements with adjusted thermal model

The author refined the approach of Wohlfarth et al. [2023] (Section 5.3.2) and reanalyzed the GF-4 lunar measurements. The thermal model depends on five quantities that are either fixed or variable. The bolometric hemispherical emissivity is set to $\bar{\epsilon}_h = 0.95$ for the entire disk, following Müller et al. [2021], Hayne et al. [2017], and the analysis in Section 5.6.1. Hapke parameters (except w) follow Warell [2004]. Three key variables remain that control the radiance that emerges from a point on the lunar surface: A_{dh}, $\bar{\theta}$, and w. Disk-resolved A_{dh} maps are estimated from M^3 data according to Equation 5.9 and Section 5.2.1. Wu and Hapke [2018] found that the M^3 instrument might underestimate lunar reflectance spectra. Consequently, a factor $a_{A_{dh}}$ is introduced, which scales the A_{dh}-map. Section 5.3.2

Table 5.4. Best fit results for the GF-4 measurements assuming $\bar{\epsilon}_h = 0.95$

	$a_{A_{dh}}$	$\bar{\theta}_{mare}$ [°]	$RMSL_{mare}$ [°]	$\bar{\theta}_{high.}$ [°]	$RMSL_{high.}$ [°]	m_{mare}	$m_{high.}$
July 25,	2.339	22.564	23.207	25.143	25.458	1.776	1.360
2018	±0.001	±0.007	±0.006	±0.010	±0.009	±0.001	±0.001
July 30,	2.432	24.068	24.534	26.196	26.361	1.343	1.224
2018	±0.002	±0.007	±0.006	±0.013	±0.011	±0.002	±0.002
$\bar{x}$	**2.385**	**23.316**	**23.870**	**25.669**	**25.909**	**1.559**	**1.292**

assumes one single global roughness, but other works [Rubanenko et al., 2020, e.g.] point to slightly different roughness values for mare and highland. Therefore, the author introduces two individual roughness factors for mare $\bar{\theta}_{\text{mare}}$ and highland $\bar{\theta}_{\text{highland}}$. Because the single scattering albedo w at the GF-4 channel around 3.77 μm is unknown, it must be estimated. Section 5.3.2 uses a linear relationship inferred from the RELAB database [RELAB, 2014] for the entire Moon (Appendix E.4). However, this assumption might be too strict, and it would be more fruitful to decouple mare and highland. As a best practice, the author introduces two scale factors m_{mare} and m_{highland}, that scale the M^3-derived single scattering albedo at 2.5μm to predict the single scattering albedo at 3.77μm for mare and highland regions. This reasoning leads to five model parameters $a_{A_{dh}}$, m_{mare}, m_{highland}, $\bar{\theta}_{\text{mare}}$, and $\bar{\theta}_{\text{highland}}$ that are determined by minimizing the squared error between the GF-4 measurements and the lunar radiance model. Appendix G.1 describes the details of the optimization task.

Table 5.4 lists the best-fit model parameters. The directional-hemispherical albedo A_{dh} must be scaled by a factor of $a_{A_{dh}} = 2.339 \pm 0.001$ (July 25) or $a_{A_{dh}} = 2.432 \pm 0.002$ (July 30), which yields A_{dh}-values close to the literature, e.g., Keihm [1984], Vasavada et al. [2012], and Feng et al. [2020]. Consider the measurements of July 25 in a region around the subsolar point ($i < 30°$): Scaling the A_{dh}-map with $a_{A_{dh}} = 2.339$ leads to an average of $\overline{A}_{\text{dh,highland}} \cdot a_{A_{dh}} = 0.129$ for highland material and $\overline{A}_{\text{dh,mare}} \cdot a_{A_{dh}} = 0.072$ for mare material. Vasavada et al. [2012], Keihm [1984], and Feng et al. [2020] provide empirical equations to estimate an albedo A that they use for thermal modeling and can be regarded as the equivalent to A_{dh} in this work. Feng et al. [2020] found that their average albedo at zero incidence angle (=subsolar point) is $A_{\text{highland}}(0) = 0.1215$ for highland and $A_{\text{mare}}(0) = 0.07$ for mare regions, which also aligns with the equatorial albedo profile of Vasavada et al. [2012]. Keihm [1984] states an $A(0) = 0.12$ for the entire Moon. It is obvious that $\overline{A}_{\text{dh,mare}} \cdot a_{A_{dh}} \approx A_{\text{mare}}(0)$ and $\overline{A}_{\text{dh,highland}} \cdot a_{A_{dh}} \approx A_{\text{mare}}(0) \approx A(0)$, indicating that the scaled A_{dh} values of the July 25 measurements well align with the literature. The surface roughness ranges between $\bar{\theta} \approx 22.6° - 26.2°$ (RMSL $\approx 23.2° - 26.4°$). Highlands appear to be approximately two degrees rougher than mare, which points in the same direction as Rubanenko et al. [2020], but found a larger difference of around ΔRMSL $= 6°$. The July 25 measurements yield albedo scale factors of $m_{\text{mare}} = 1.776 \pm 0.001$ and $m_{\text{highland}} = 1.360 \pm 0.001$ and the albedo scale factors of the July 30 data are inferred to be $m_{\text{mare}} = 1.343 \pm 0.002$ and $m_{\text{highland}} = 1.224 \pm 0.002$. Different spectral shapes of mare and highland spectra around the center wavelength of GF-4 might explain the different albedo scale factors between highland and mare. On July 30, 2018, the Sun illuminated more Ti-rich mare regions than on July 25, especially in the

Southwest of Oceanus Procellarum. These regions are known to have comparatively low reflectances and high emissivities. Seeing a higher fraction of low-reflectance Ti-rich mare material might explain the lower m_{mare} for July 30 compared to July 25. Both measurements (July 25 and July 30, 2018) produce similar parameter estimates for A_{dh}, $\overline{\theta}_{\mathrm{highland}}$, $\overline{\theta}_{\mathrm{mare}}$, and m_{highland}. The deviations in m_{mare} have a plausible explanation. Thus, the new parameter results support the model's consistency. Overall, the parameter estimates tend to better agree with the literature.

The RMSE along the modeled and the measured profiles is $0.1860\,\mathrm{W\,m^{-2}\,\mu m^{-1}\,sr^{-1}}$ for July 25, 2018, and $0.2270\,\mathrm{W\,m^{-2}\,\mu m^{-1}\,sr^{-1}}$ for July 30, 2018. The error between the model and the measurements averaged over the entire disk is $0.1785\,\mathrm{W\,m^{-2}\,\mu m^{-1}\,sr^{-1}}$ for July 25, 2018 and $0.2346\,\mathrm{W\,m^{-2}\,\mu m^{-1}\,sr^{-1}}$ for July 30, 2018. Disk-averaged and the profile-averaged values agree. Relative to a reference value ($8.0\,\mathrm{W\,m^{-2}\,\mu m^{-1}\,sr^{-1}}$) close to the maximum spectral radiance of the disk, the relative disk-integrated RMSE is approximately 2.23 % and 2.93 %, respectively. The disk-averaged RMSE of the adjusted model variant with $\overline{\epsilon}_{\mathrm{d}} = 0.95$ and regional roughness is thus only marginally better than the RMSE of the variant with $\overline{\epsilon}_{\mathrm{d}} = 1$ and global roughness (see Table 5.1 and text), so both variants can be regarded as performing equally well.

Even though both model variants have similar RMSE values, they produce different parameter fits, which indicates that the parameters internally compensate for each other. As the bolometric emissivity decreases from $\overline{\epsilon}_{\mathrm{h}} = 1.00$ to $\overline{\epsilon}_{\mathrm{h}} = 0.95$, the directional-hemispherical albedo A_{dh} significantly increases, bringing it more in line with the literature. The regional albedos w and the roughness parameters also increase and deviate between mare and highland regions.

Even though the RMSE values of both model variants are almost similar, they differ locally. The adjusted model variant ($\overline{\epsilon}_{\mathrm{h}} = 0.95$) shows better fits in Ti-rich mare regions of Oceanus Procellarum than the first variant (compare, for example, pixel position 100–300 of profile 30_{C1} in Figure 5.4, with the same position of profile 30_{C1} in Figure 5.20 (right)) but induces some deviations and discontinuities at transition zones between mare and highland. Decoupling the parameters for mare and highland likely allowed for improved fits in the Ti-rich mare regions but caused the discontinuities. Still, the second model variant overestimates the spectral radiance for regions around crater Copernicus (pixel position 250–350 of profile 30_{R2}) and exhibits some deviations in Mare Humorum (pixel position 400–450 of profile 30_{C1}). As discussed in Appendix G.2, the unusually bright ejecta material of Copernicus and specific parameter combinations at Mare Humorum explain these deviations.

In summary, the previous and the refined model variants excellently model the data, but the refined variant probably yields more realistic model parameters, especially for the directional-hemispherical albedo aligning with Keihm [1984], Vasavada et al. [2012], and Feng et al. [2020]. Even though the roughness parameters were decoupled for mare and highland regions, highlands are only two degrees rougher than mare, which is less than in Rubanenko et al. [2020] but generally points in the same direction. Again, the single scattering albedo variations can fully explain local deviations around ejecta blankets and bright highland material where the model overestimates the spectral radiance. In Mare Humorum, only

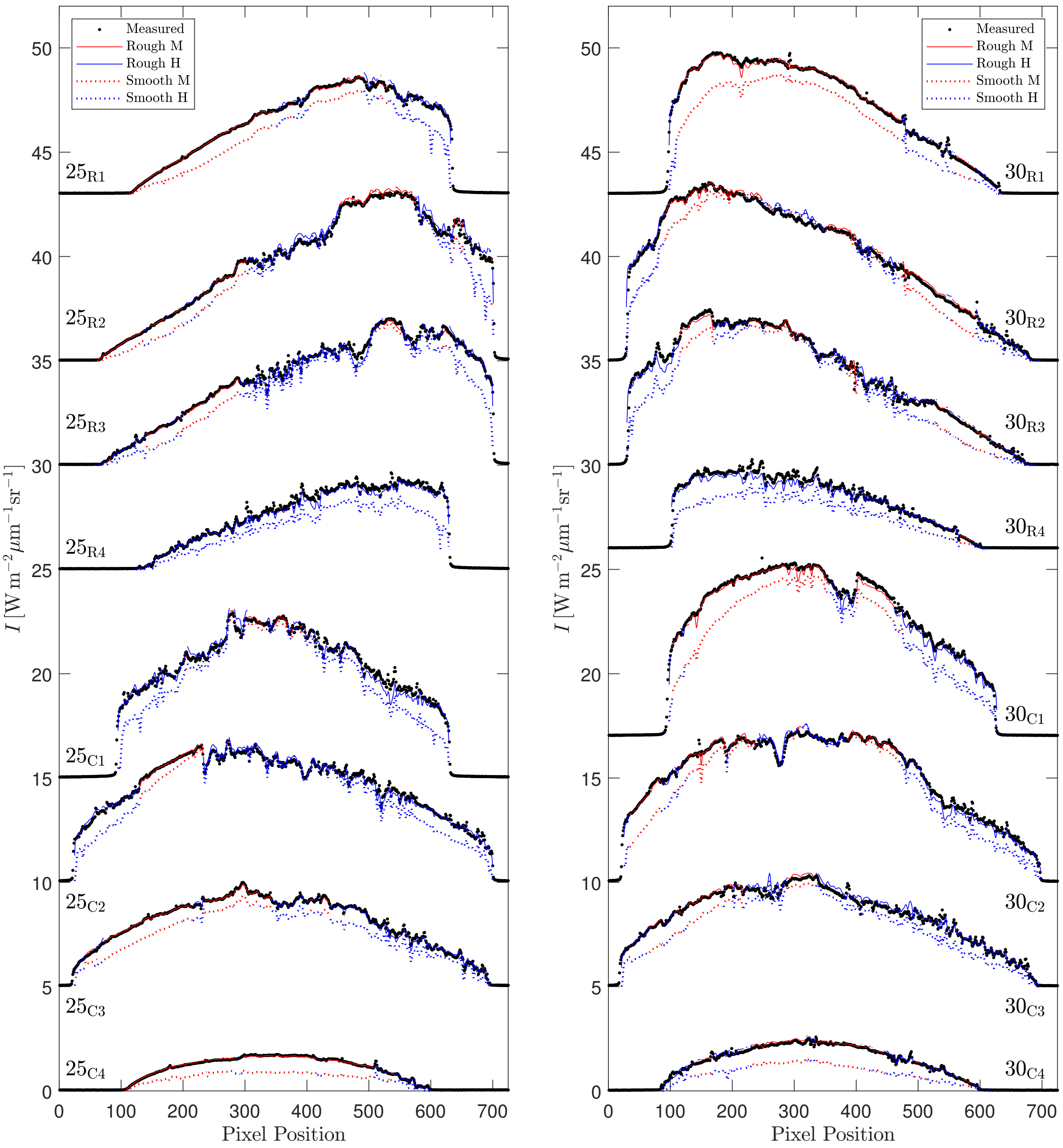

Figure 5.20. Comparison of the measured spectral radiance (black) with the rough model (solid red for mare and solid blue for highland) and the equilibrium model (dashed red for mare and dashed blue for highland) Left: Model comparison with GF-4 measurements of July 25 along the horizontal profiles 25_{R1}–25_{R4} and the vertical profiles 25_{C1}–25_{C4} indicated in Figure 5.3 (bottom). Offsets for clarity. Right: Model comparison with GF-4 measurements of July 30 along the horizontal profiles 30_{R1}–30_{R4} and along the vertical profiles 30_{C1}–30_{C4} indicated in Figure 5.4 (bottom). Offsets for clarity. M denotes mare, and H denotes highland regions.

combinations of several effects may accurately fit the data. Future activities should focus on refining the model further, for example, through better models of w at 3.77 μm, and the transition zones between mare and highlands.

5.6.3 Reassessing Diviner emission phase function measurements

This section discusses reprocessed modeling results of the Diviner EPF measurements. The bolometric hemispherical emissivity is set to $\bar{\epsilon}_{\mathrm{h}} = 0.95$, and the directional-hemispherical albedo A_{dh} is multiplied with the factor $a_{\mathrm{A_{dh}}} = 2.34$ as discussed in Section 5.6.2. Table 5.5 lists the grid search results for the roughness $\overline{\theta}$, the single scattering albedo w, and the RMSE. The RMSE values of the new model variant are nearly identical to the previous model variant (see Table 5.2), which suggests that they perform equally well on the data. Consequently, the plots of the new model variant are virtually indistinguishable from those in Appendix F and are not displayed to avoid duplication. Again, the roughness estimates in Table 5.5 are consistent between the channels (channel 4: $\overline{\theta} = 29.92°$, RMSL=29.36°, channel 7: $\overline{\theta} = 29.50°$, RMSL=29.01°) and are almost similar to the previous modeling attempt (see Table 5.2). The single scattering albedo is consistently lower than the best-fit results of the previous model variant. In many cases (EPF functions 1, 2, 3, 4, 7, 9, 10, and 11), the new model run produces single scattering albedos for channel four ($8.25\,\mu$m) that are close to zero and albedos for channel seven that are slightly larger. This behavior aligns exceptionally well with the spectral shape of silicate minerals with a minimum albedo at the Christiansen feature close to $8\,\mu$m. The remaining cases deviate from this pattern. As discussed in Section 5.4.3, EPF function number six stands out because its roughness is much lower, and its albedo w is much higher than the average. EPF function number nine has an unexplained difference between the roughness estimates of channels 4 and 7. Reprocessing the Diviner nadir measurements leaves no other conclusion than before. All in all, the new modeling attempt yields data fits of similar quality than before. The parameter fits of the roughness $\overline{\theta}$ do not change much, but the parameter estimates of w turn out to be more realistic.

5.6.4 Reassessing time-of-day dependent lunar hydration maps

The author reprocessed the global M^3 dataset according to Section 5.3.4 but with a different parameter choice. As discussed in Sections 5.6.1 and 5.6.2, the bolometric hemispherical emissivity is set to $\bar{\epsilon}_{\mathrm{h}} = 0.95$, and the directional-hemispherical albedo A_{dh} is multiplied with the factor $a_{\mathrm{A_{dh}}} = 2.34$. Section 5.6.2 also revealed a slightly higher roughness for the Moon. Taking the roughness values of mare and highland from Table 5.4, weighting them with their relative coverage of the lunar surface, averaging over the two GF-4 measurements, and rounding to the next whole number yields a global average of $\overline{\theta} = 25°$. The resulting $\mathrm{IBD}_{3\mu\mathrm{m}}$-maps are shown in Appendix G.3 Figure G.3. It turns out that the qualitative trend of the diurnal, compositional, and latitudinal variations of the $\mathrm{IBD}_{3\mu\mathrm{m}}$ parameter (see Section 5.4.4) remains unchanged. Still, the exact values between the maps (Figure 5.7 and Figure G.3) differ numerically. Three differences can be identified: Firstly, the new model run produces $\mathrm{IBD}_{3\mu\mathrm{m}}$ values that are consistently higher in the lunar mare and lower in the lunar highlands compared to the previous results. Consequently, the $\mathrm{IBD}_{3\mu\mathrm{m}}$ dichotomy between mare and highlands becomes even more pronounced for lunar morning and afternoon but less pronounced during lunar midday. Secondly, the differences between the new and

Table 5.5. Best fit parameters for twelve EPF measurements of Diviner channels four and seven. See Table 4.2 for locations and geometries. The bolometric hemispherical emissivity is $\bar{\epsilon}_{\mathrm{h}} = 0.95$, and the directional-hemispherical albedo A_{dh} is derived from M^3 measurements beforehand and multiplied with $a_{\mathrm{A_{dh}}} = 2.34$. The roughness $\overline{\theta}$ and the single scattering albedo w are inferred via a simple grid search. The last row provides the average values. Table adapted from Wohlfarth et al. [2023].

		Channel four (8.25 μm)			Channel seven (25-41 μm)		
No.	A_{dh}	$\overline{\theta}$ [°]	w	RMSE [K]	$\overline{\theta}$ [°]	w	RMSE [K]
01	0.182	32	0.00	28.76	37	0.09	21.46
02	0.180	28	0.00	25.37	29	0.10	22.94
03	0.165	34	0.09	5.77	33	0.14	5.76
04	0.145	36	0.00	5.49	32	0.11	4.37
05	0.167	28	0.00	43.21	28	0.00	42.68
06	0.180	20	0.15	6.58	19	0.07	8.04
07	0.145	29	0.04	5.42	31	0.11	4.50
08	0.105	34	0.17	4.09	36	0.16	3.38
09	0.162	36	0.00	24.48	29	0.12	18.08
10	0.165	27	0.00	26.95	27	0.06	27.13
11	0.139	28	0.05	5.59	26	0.14	6.03
12	0.111	27	0.26	6.38	27	0.21	6.63
$\overline{x}$	0.154	29.917	0.063	15.674	29.500	0.109	14.249

the previous results depend on the time of day and are larger for lunar morning and lunar afternoon compared to lunar midday. Thirdly, the latitudinal dependency of $\mathrm{IBD}_{3\mu\mathrm{m}}$ gets stronger.

5.6.5 Reassessing MERTIS lunar flyby data

The new lunar model for MERTIS lunar flyby data assumes $\bar{\epsilon}_{\mathrm{h}} = 0.95$ and the directional-hemispherical albedo A_{dh} multiplied with the factor $a_{\mathrm{A_{dh}}} = 2.34$. Further, a minor software bug in the interpolation routine was fixed. Most of the resulting model fits turn out to be virtually indistinguishable from the previous attempt (see Figures 5.9–5.11), so they are not displayed for brevity. Comparing Table 5.3 with Table 5.6 indicates that the new parameter estimates for ϵ_{d} are almost similar. Only profile 41 rises slightly above unity. The pointing offsets only marginally change to $\Delta\mathrm{WE} = -0.2276\,\mathrm{mrad}$ and $\Delta\mathrm{NS} = 0.3273\,\mathrm{mrad}$. Furthermore, the author found that the sensitive size of the simulated MERTIS-pixel and the estimated width of the PSF partly compensate for each other. Future studies could investigate this effect further, but the benefit is uncertain given the limited data quality.

Table 5.6. Emissivity values of six profiles that scanned the lunar disk on April 9th, 2020. The values were computed with the refined thermal model assuming $\overline{\epsilon}_{\mathrm{h}} = 0.95$ and $\overline{\theta} = 29°$. See the text for an explanation.

Profile	7.00– 8.62 μm	8.79– 10.41 μm	10.59– 12.21 μm	12.38– 14.00 μm
36	0.91	1.00	0.96	0.95
37	0.94	0.99	0.94	0.93
38	0.91	0.97	0.93	0.93
39	0.98	0.99	0.95	0.96
40	0.95	0.98	0.93	0.93
41	1.01	1.02	0.97	0.95

5.6.6 Reassessing thermal roughness model simulations for Mercury

The theoretical analysis in Section 5.6.1 indicates that Mercury's bolometric hemispherical emissivity $\overline{\epsilon}_{\mathrm{h}}$ might be well below unity, and changes with the solar distance and the incidence angle (Equation 5.27). This section analyzes how varying $\overline{\epsilon}_{\mathrm{h}}$ affects the thermal emission of Mercury for the scenario shown in Figure 5.12. The new model uses Equation 5.27 to simulate $\overline{\epsilon}_{\mathrm{h}}$ across Mercury's disk. Section E.5 describes how to estimate the directional-hemispherical albedo from MDIS data. Following 5.6.2, a correction factor of $a_{\mathrm{A_{dh}}} = 2.34$ for A_{dh} derived from M^3. The directional emissivity ϵ_{d} remains unknown and is set to unity. Comparing the new modeling results to Figure 5.12 shows that all qualitative trends are preserved. For $g = 0°$, the new model consistently predicts a higher thermal emission that increases toward the center of the disc. This observation directly comes from the decrease of $\overline{\epsilon}_{\mathrm{h}}$ toward the disk center that, in turn, increases the thermal emission. For $g = 120°$ at positions 120_0 and 120_1, the new model also predicts higher emissions than the previous model. However, at position 120_3, the new model predicts a lower thermal emission than before. At this point, the incidence angle is high ($i \lesssim 90°$), which causes $\overline{\epsilon}_{\mathrm{h}}$ to approach unity and A_{dh} to grow such that it effectively decreases the thermal emission.

The lunar heat conduction model of Hayne et al. [2017] assumes a constant $\overline{\epsilon}_{\mathrm{h}} = 0.95$ that was also adopted for Mercury, shown in Figure 5.13. Detailed analysis with a variable $\overline{\epsilon}_{\mathrm{h}}$ is beyond the scope of this work. Modeling $\overline{\epsilon}_{\mathrm{h}}$ with Equation 5.27 is expected to increase the thermal emission even further as the planet comes closer to the Sun, compared with previous modeling attempts.

MERTIS measurements were preliminarily analyzed in collaboration with Tenthoff et al. [2025] and empirically support the hypothesis that the bolometric hemispherical emissivity is well below unity. However, the precise quantitative behavior for Mercury's $\overline{\epsilon}_{\mathrm{h}}$ and A_{dh} remains poorly constrained. A more detailed examination with more data is necessary to fully characterize these parameters, which is recommended for further work.

5.6.7 Reassessing exoplanetary phase curves

Investigating the role of $\bar{\epsilon}_{\mathrm{h}}$ for exoplanetary phase curves is recommended for further work, particularly in the context of analyzing the measurements of LHS 3844b.

Chapter 6

Contribution 2: Simulation of space weathering

This chapter and most figures have been adapted from Wohlfarth et al. [2019] but have been partly reworked. Sections contain considerable changes and extensions compared to the original publication. During development, preliminary results of the space weathering model have been published under Grumpe et al. [2018], Wohlfarth et al. [2018], and Wohlfarth et al. [2019b]. This section was extended after submission on January 15, 2024 (see Appendix H).

6.1 Introduction

Space weathering is a complex phenomenon that alters the makeup of the lunar regolith and spawns submicroscopic iron particles that influence the spectral signature. These spectral changes impede compositional interpretation but also help understand the physical mechanisms behind space weathering. Consequently, it is vital to devise simulation models that simulate the spectral effects of space weathering. This chapter introduces such a model combining Mie and Hapke theory, carefully validates and characterizes its behavior, and investigates how space weathering influences the detection of lunar OH/H_2O. Further, the model receives an expansion to work with multiple interacting spheres to explore the effects of closely packed particles. The model is later applied to spectral unmixing and exploration of the lunar swirl Reiner Gamma. Almost the whole lunar surface is exposed to space weathering, which affects the spectral behavior of the regolith. Since the surface material of the lunar surface settled at different times, the exposure time of the regolith to space weathering varies locally. The most prominent example is the Copernicus crater, circumvented by a system of bright ejecta rays. However, many small fresh craters with bright ejecta are scattered across the whole Moon. Because space weathering affects the spectral bands of the regolith (see Section 2.1.2), it has to be considered as a possible reason for local variations found in the 2.8–3 μm absorption band depth, which, in turn, influences the interpretations of lunar surface OH/H_2O. In their study on lunar hydroxyl, Pieters et al. [2009b] state that nanophase iron (npFe^0) "*substantially decreases the measured strength of all absorption* *bands of lunar material*" and the reflectance spectra of the regolith. Li and Milliken [2017] observed that a lower optical maturity parameter (OMAT), which is associated with more intense space weathering [Lucey et al., 2000], is not correlated with OH/H_2O for less than ±30° latitude. For high latitudes (±60°–70°), higher soil maturity was linked to higher levels of OH/H_2O. In this work, the results obtained from Mie modeling are used to understand the influence of space weathering on the 3 μm absorption band and how it affects the detection of lunar OH/H_2O. Further, there is evidence that not all submicroscopic iron particles are well-separated. As TEM measurements suggest [Pieters and Noble, 2016], many particles accumulate in vaporized rims and form closely packed clusters or layers. Light scattering theory predicts particles interact if the particle distance has the same order of magnitude as the particle size. These interactions affect the spectrum of reflected light. All existing space weathering models assume single spheres or comparatively sparse particles. The author issued a thesis to extend the space weathering Mie model with the T-matrix method that considers inter-particle interactions. The author re-ran the model characterization with different types of iron particle clusters and investigated the resulting spectral effects. Hess et al. [2020a] and Hess et al. [2021] subsequently applied the space weathering model in two separate works. The model helps the spectro-photometric characterization of the Reiner Gamma swirl on the Moon and represents a crucial component for spectral unmixing of lunar spectra. The results will be shortly reviewed at the end of the section.

6.2 Space weathering model

6.2.1 Theory

Section 2.1.2 introduced the properties of the space-weathered lunar regolith, and Section 3.4.5 reviewed earlier space weathering models. The space weathering simulation technique developed in this thesis can be formulated as a mixing task utilizing the property of the Hapke model that the albedo of different endmember spectra w_j mix linearly. Hapke [2012] defines the mixing equation for the single scattering albedo w as

$$w_\mathrm{Mix} = \frac{\sum_j \frac{M_j Q_\mathrm{ext,j}}{\rho_j d_j} w_j}{\sum_j \frac{M_j Q_\mathrm{ext,j}}{\rho_j d_j}}, \tag{6.1}$$

where M_j denotes the mass fraction of the j-th endmember, $Q_\mathrm{ext,j}$ denotes the extinction efficiency, ρ_j stands for the material density, and d_j represents the particle diameter of the j-th endmember. The mixing equation of the phase functions $p_\mathrm{j}(g)$ considers the weighting of the phase functions of the individual components with their single scattering albedo

$$p_\mathrm{Mix}(g) = \frac{\sum_j \frac{M_j Q_\mathrm{ext,j}}{\rho_j d_j} w_j p_j(g)}{\sum_j \frac{M_j Q_\mathrm{ext,j}}{\rho_j d_j} w_j}. \tag{6.2}$$

The simulation of smFe^0-induced spectral effects is performed by defining an endmember representing the lunar soil and endmembers representing iron particles of a given size. In the simplest case of a single iron endmember (subscript Fe) with a fixed particle size d_{Fe} and a single soil endmember (subscript Soil), the mixing equations become

$$w_{\mathrm{Soil,SW}} = \frac{\frac{M_{\mathrm{Fe}} Q_{\mathrm{ext,Fe}}}{\rho_{\mathrm{Fe}} d_{\mathrm{Fe}}} w_{\mathrm{Fe}} + \frac{M_{\mathrm{Soil}} Q_{\mathrm{ext,Soil}}}{\rho_{\mathrm{Soil}} d_{\mathrm{Soil}}} w_{\mathrm{Soil}}}{\frac{M_{\mathrm{Fe}} Q_{\mathrm{ext,Fe}}}{\rho_{\mathrm{Fe}} d_{\mathrm{Fe}}} + \frac{Q_{\mathrm{ext,Soil}}}{\rho_{\mathrm{Soil}} d_{\mathrm{Soil}}}(1 - M_{\mathrm{Fe}})}, \tag{6.3}$$

$$p_{\mathrm{Soil,SW}}(g) = \frac{\frac{M_{\mathrm{Fe}} Q_{\mathrm{ext,Fe}}}{\rho_{\mathrm{Fe}} d_{\mathrm{Fe}}} w_{\mathrm{Fe}} p_{\mathrm{Fe}}(g) + \frac{M_{\mathrm{Soil}} Q_{\mathrm{ext,Soil}}}{\rho_{\mathrm{Soil}} d_{\mathrm{Soil}}} w_{\mathrm{Soil}} p_{\mathrm{Soil}}(g)}{\frac{M_{\mathrm{Fe}} Q_{\mathrm{ext,Fe}}}{\rho_{\mathrm{Fe}} d_{\mathrm{Fe}}} w_{\mathrm{Fe}} + \frac{Q_{\mathrm{ext,Soil}}}{\rho_{\mathrm{Soil}} d_{\mathrm{Soil}}}(1 - M_{\mathrm{Fe}}) w_{\mathrm{Soil}}}. \tag{6.4}$$

Increasing the weight percentage M_{Fe} of submicroscopic iron and thus increasing the contribution of the single scattering albedo and the phase function of smFe^0 alters the spectral shape. However, iron particles come in different sizes. Therefore, the author introduces N different iron particle endmembers (subscript Fe,j), each representing particles of a specific size. Consequently, the mixing equations become

$$w_{\mathrm{Soil,SW}} = \frac{\sum_{j=1}^{N} \frac{M_{\mathrm{Fe,j}} Q_{\mathrm{ext,Fe,j}}}{\rho_{\mathrm{Fe}} d_{\mathrm{Fe,j}}} w_{\mathrm{Fe,j}} + \frac{M_{\mathrm{Soil}} Q_{\mathrm{ext,Soil}}}{\rho_{\mathrm{Soil}} d_{\mathrm{Soil}}} w_{\mathrm{Soil}}}{\sum_{j=1}^{N} \frac{M_{\mathrm{Fe,j}} Q_{\mathrm{ext,Fe,j}}}{\rho_{\mathrm{Fe}} d_{\mathrm{Fe,j}}} + \frac{Q_{\mathrm{ext,Soil}}}{\rho_{\mathrm{Soil}} d_{\mathrm{Soil}}}(1 - \sum_{j=1}^{N} M_{\mathrm{Fe,j}})}, \tag{6.5}$$

$$p_{\mathrm{Soil,SW}}(g) = \frac{\sum_{j=1}^{N} \frac{M_{\mathrm{Fe,j}} Q_{\mathrm{ext,Fe,j}}}{\rho_{\mathrm{Fe}} d_{\mathrm{Fe,j}}} w_{\mathrm{Fe,j}} p_{\mathrm{Fe,j}}(g) + \frac{M_{\mathrm{Soil}} Q_{\mathrm{ext,Soil}}}{\rho_{\mathrm{Soil}} d_{\mathrm{Soil}}} w_{\mathrm{Soil}} p_{\mathrm{Soil}}(g)}{\sum_{j=1}^{N} \frac{M_{\mathrm{Fe,j}} Q_{\mathrm{ext,Fe,j}}}{\rho_{\mathrm{Fe}} d_{\mathrm{Fe,j}}} w_{\mathrm{Fe,j}} + \frac{Q_{\mathrm{ext,Soil}}}{\rho_{\mathrm{Soil}} d_{\mathrm{Soil}}}(1 - \sum_{j=1}^{N} M_{\mathrm{Fe,j}}) w_{\mathrm{Soil}}}. \tag{6.6}$$

These equations form the core of the space weathering model. The soil density is set to $\rho_{\mathrm{Soil}} = 1.50\, g/cm^3$ [Carrier et al., 1991], the iron density is $\rho_{\mathrm{Fe}} = 7.87\, g/cm^3$ [NCBI, 2023], and the mineral grains average diameter is assumed to be $60\,\mu$m, which falls right into the range of typical soil sizes 40–100 μm [McKay et al., 1991]. The single scattering albedo w_{Soil} comes from M^3 hyperspectral measurements of immature sites. The extinction efficiency is set to $Q_{\mathrm{ext,Soil}} = 2$, because the size parameter is much larger than the wavelength. The phase function of the soil $p_{\mathrm{Soil}}(g)$ is expressed through the double-lobed Henyey-Greenstein function with the average lunar asymmetry parameter $\xi = 0.21$ and the weight $c = 0.7$, indicating backward-scattering. The space weathering model can simulate non-interacting iron particles of varying sizes with Mie theory or clusters of iron particles that exhibit inter-particle light scattering interactions with the T-matrix method. In any case, the wavelength-dependent single scattering albedo w, the scattering and extinction efficiencies Q_{sca} and Q_{ext}, and the single particle phase function $p_{\mathrm{Fe}}(g)$ are pre-computed and subsequently inserted into the mixing equation.

Assuming non-interacting particles of varying sizes, the only free parameter is the particle radius. The Mie solution then provides w, Q_{sca}, and Q_{ext} (see Section 3.4.2 and Equations 3.16, 3.17, 3.25).

The phase function p_{Fe} entails more effort because the L-functions of the Hapke model (Equation 3.49) requires the Legendre expansion of the phase function of the form

$$p_{\mathrm{Fe}}(\theta) = \sum_{n}^{N} \chi_{\mathrm{n}} P_{\mathrm{n}}(\cos(\theta)). \tag{6.7}$$

It is convenient to use the scattering angle $\theta = 180^\circ - g$ for the derivation and substitute the phase angle g later during application. Computing closed-form expressions of the Legendre coefficients χ_n is intricate. The author uses Equation 3.26, which states that the phase function can, in the case of spherical particles, be expressed through the scattering amplitudes S_{11} and S_{22}. It is possible to introduce the function $\tilde{p}_\mathrm{Fe}$ that does not depend on the scattering cross-section C_sca anymore:

$$p_\mathrm{Fe}(\theta) \sim \tilde{p}_\mathrm{Fe}(\theta) = \frac{1}{2}(|S_{11}(\theta)|^2 + |S_{22}(\theta)|^2) = \sum_n^N \tilde{\chi}_\mathrm{n} P_\mathrm{n}(\cos(\theta)). \tag{6.8}$$

Fowler [1983] derived the Legendre expansions for the elements $|S_j^F|^2$, which directly correspond to the squared absolute values of the amplitude matrix elements $|S_{11}|^2 = |S_2^F|^2$ and $|S_{22}|^2 = |S_1^F|^2$. The expansion is

$$|S_j^F|^2 = \Sigma_{jj} = \frac{1}{k^2} \sum_{n=0}^N (2n+1) h_{njj} P_n(\cos(\theta)), \tag{6.9}$$

where $k = 2\pi/\lambda$ is the wave number and the Legendre coefficients h_{nij} are given by

$$h_{nij} = \sum_{l=0}^N \sum_{k=0}^l \frac{(2k+1)(2l+1)}{(k+l+n'+1)} \beta_{kl,n'} (f_{ki} f_{lj}^* + f_{lj} f_{ki}^*) - \sum_{l=0}^N \frac{(2l+1)}{(2l+n''+1)} \beta_{ll,n''} f_{li} f_{lj}^*. \tag{6.10}$$

For this expression $n' = \frac{k+l-n}{2}$ and $n'' = \frac{2l-n}{2}$ must be integers and it has to be ensured that $k - l \leq n \leq l + k$ and $0 \leq n \leq 2l$. The parameter β is defined as

$$\beta_{kl,m} = \frac{\gamma_{k-m} \gamma_m \gamma_{l-m}}{\gamma_{k+l-m}} \tag{6.11}$$

with

$$\gamma_n = \frac{(2n-1) \cdot (2n-3) \cdot (2n-5) \cdot \ldots \cdot 1}{n!}. \tag{6.12}$$

The parameters f_{k1} and f_{k2} are calculated from a_n and b_n using the method of Fowler [1983]. For more details on calculating f_{ki}, see Fowler [1983]. Subsequently, the Legendre coefficients h_{n11} and h_{n22} can be combined to form the Legendre coefficients $\tilde{\chi_n}$ of the non-normalized phase function $\tilde{p}_\mathrm{Fe}$

$$\tilde{\chi_n} = \frac{(2n+1)}{2} (h_{n11} + h_{n22}). \tag{6.13}$$

Normalizing the coefficients $\tilde{\chi_n}$ with either $4\pi/C_\mathrm{sca}$ or the phase function integral finally yields the desired Legendre coefficients χ_n of the phase function

$$\chi_n = \frac{\tilde{\chi_n}}{2\pi \int_0^\pi Z_{11}(\theta) \sin(\theta) dg}. \tag{6.14}$$

If multiple iron particles are closely packed, light scattering interaction occurs. In this case, simple Mie modeling is insufficient. The T-matrix method becomes necessary, which provides w, Q_{sca}, and Q_{ext} (see Section 3.4.2 and Equations 3.16, 3.17, 3.37). Similar to the previous single-particle case, the space weathering model requires the Legendre expansion of the cluster's phase function p_{Fe}. Because no explicit Legendre development exists, the phase function is first computed according to Equations 3.18, 3.38, and 3.39. Secondly, the resulting phase function is numerically integrated to determine the Legendre coefficients. For a detailed discussion, see Arnaut [2021] (Master's thesis under supervision).

6.2.2 Simulation pipeline

The full space weathering model comprises five steps, summarized in Figure 6.1 and outlined below. The simulation is essentially a mixing task that implements equations 6.5 and 6.6.

(1) First, the simulation computes the efficiencies $Q_{\mathrm{sca,Fe,j}}$ and $Q_{\mathrm{ext,Fe,j}}$, the single scattering albedo $w_{\mathrm{Fe,j}}$, and the phase function's Legendre coefficients for every submicroscopic iron endmember j. The model can either assume non-interacting iron particles of varying sizes (a) or clusters of interacting iron particles (b).

  (a) Non-interacting particles: The model takes the complex refractive index of iron [Trang et al., 2013] and the host medium's refractive index and determines the Mie coefficients for every iron particle endmember j of the desired size d_{j} (see Section 3.4.2). The Mie coefficients then enter the calculations of the efficiencies $Q_{\mathrm{ext,Fe,j}}$ (Equation 3.25) and $Q_{\mathrm{sca,Fe,j}}$ (Equation 3.25) of submicroscopic iron and the single scattering albedo $w_{\mathrm{Fe,j}}$ (Equation 3.17). The Legendre expansion of the phase function $p_{\mathrm{Fe,j}}(g)$ follows Equations 6.7–6.14.

  (b) Particle clusters: Instead of a group of similar-sized non-interacting iron particles, the j-th iron endmember can be a cluster of interacting particles. The multiple-particle model requires the positions and sizes of a set of iron particles. The T-matrix method provides w_{j}, $Q_{\mathrm{sca,Fe,j}}$, and $Q_{\mathrm{ext,Fe,j}}$ (see Section 3.4.2 and Equations 3.16, 3.17, 3.36, 3.37). The phase function is first computed according to Equations 3.18, 3.38, and 3.39 and then numerically integrated to determine the Legendre coefficients with the method of Arnaut [2021].

(2) M^3 spectra of fresh lunar soil are thermally corrected and normalized with the technique described in Section 5.2.1. Subsequently, the Levenberg-Marquardt algorithm [Marsland, 2009] and the Hapke model are employed to retrieve the effective single scattering albedo spectrum of fresh lunar regolith $\mathbf{w}_{\mathrm{Soil,fresh}}$. This task can mathematically be formulated as minimizing the sum of squared errors between the Hapke-modeled radiance spectrum $\mathbf{r}(\mathbf{w}_{\mathrm{Soil,fresh}})$ and M^3 measurements $\mathbf{m}$ for all sampling points. Because a continuous spectrum in the physical world is sampled for technical processing, the resulting spectral data can be summarized in a vector $\mathbf{r} = [r(\lambda_1), r(\lambda_1), ..., r(\lambda_{\mathrm{N}})]$.

$$\mathbf{w}_{\mathrm{Soil,fresh}} = \underset{\mathbf{w}_{\mathrm{Soil,fresh}}}{\operatorname{argmin}} \left[\mathbf{m} - \mathbf{r}(\mathbf{w}_{\mathrm{Soil,fresh}})\right]^T \left[\mathbf{m} - \mathbf{r}(\mathbf{w}_{\mathrm{Soil,fresh}})\right] \tag{6.15}$$

(3) The extinction efficiency Q_{ext} of the lunar soil is inferred from the complex refractive indices of pyroxene and plagioclase (see also Section 6.2.1). The model assumes that the mineral grains are spherical, such that Q_{ext} can be inferred from the Mie-model.

(4) Given the bulk densities M_j, the particle diameter, the particle density and the extinction efficiencies, the albedo spectra $\mathbf{w}_{\text{Soil,fresh}}$ and $\mathbf{w}_{\text{smFe}}$ are mixed linearly to generate the new albedo $\mathbf{w}_{\text{Soil,mature}}$. The same holds for the phase function.

(5) The derived albedo $\mathbf{w}_{\text{Soil,mature}}$ and the $p(g)$ are fed into the Hapke model to generate the reflectance spectra of the weathered soil under normalized illumination conditions $\mathbf{r}(\mathbf{w}_{\text{Soil,mature}})$.

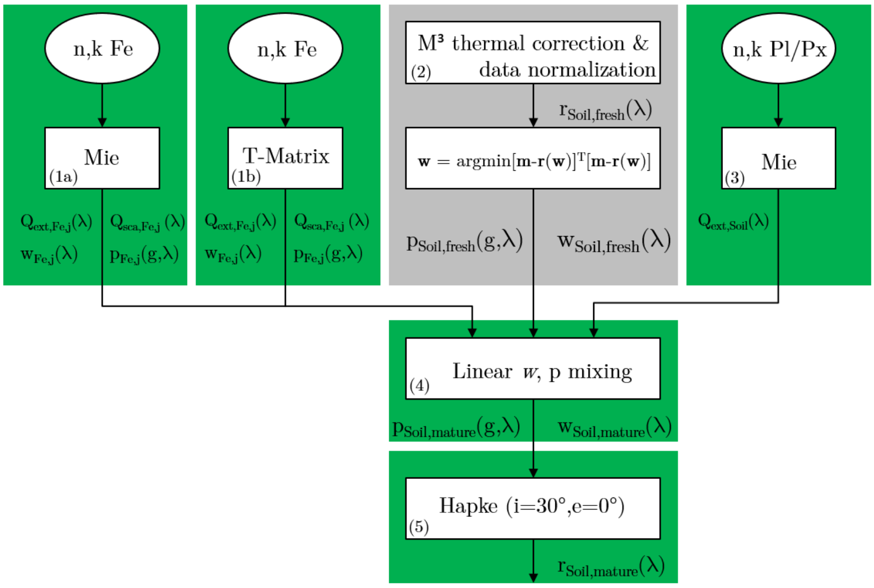

Figure 6.1. Flowchart of the space weathering simulation framework. The contribution of this work is marked in green. Figure extended from [Wohlfarth et al., 2019].

This scheme simulates submicroscopic iron of arbitrary amounts and sizes for a given geometry and a given M^3 spectrum. The routines to compute the Mie coefficients and the efficiencies were adopted from Mätzler [2002] and re-factored to match the data structures of the new framework. The computation of the phase function was newly implemented according to the equations given in Section 6.2.1.

6.3 Simulation results

This section examines how parameter variations influence the simulation results. The author especially investigates (1) the shape of the phase function, which has by date not been systematically described for smFe^0, and how spectral changes depend on (2) the particle size and (3) the amount of smFe^0. (4) Moreover, the simulation study considers the influence smFe^0 has on the depth of the 2.8–3.0 μm absorption band. Previous studies have discussed the particle size and the amount of smFe^0. The spectral maps of Trang and Lucey [2019] find a total smFe^0 abundance of a maximum of 2.0 wt% on the lunar surface. In the study of Lucey and Riner [2011], particles up to 200 nm were assumed. Thus, the study primarily focuses on particle sizes ranging from 1–500 nm, and iron amounts up to a few wt%.

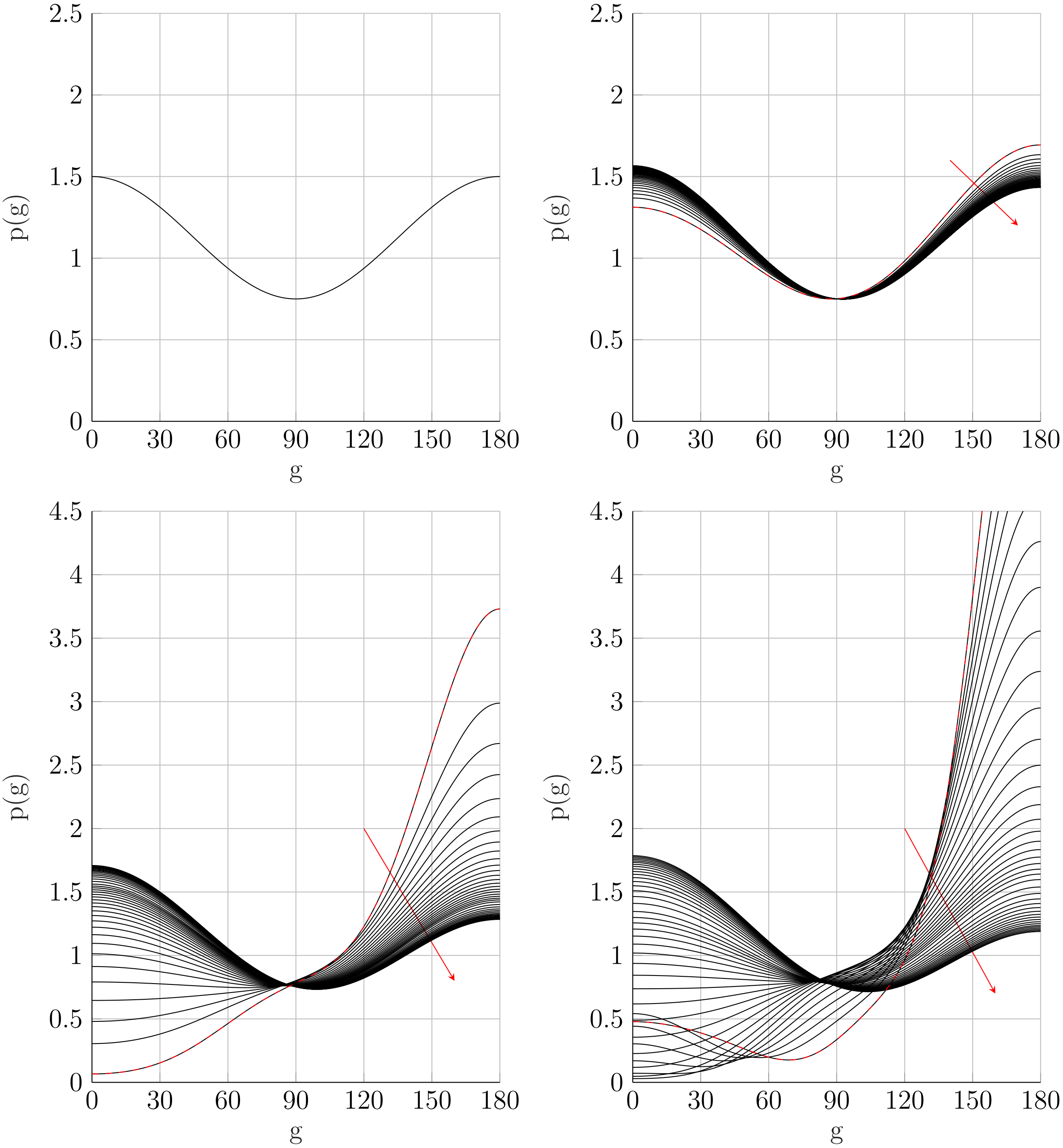

Figure 6.2. Simulated phase functions $p(g)$ of smFe^0 of different particle sizes for 79 channels of the M^3 instrument (660.61 nm to 2936.3 nm). Note that the phase function fans out as the particle size increases. For better orientation, the phase function associated with the smallest M^3 channel is represented by a dashed red line. The particle sizes are from top left to bottom right $d = 1$ nm, $d = 100$ nm, $d = 200$ nm, and $d = 300$ nm. Figure adapted from Wohlfarth et al. [2019].

6.3.1 Shape of the phase function

The single particle phase function $p(g)$ is calculated for several iron particle diameters from 1–500 nm, broadly covering the range of anticipated submicroscopic iron particle sizes. The wavelength-dependent Mie phase functions are evaluated for 79 M^3-bands from 660.61 nm to 2936.3 nm. Figure 6.2 shows the wavelength-dependent family of curves for a particle diameter of 1 nm, 100 nm, 200 nm, and 300 nm. The shape of the phase function of small particles (1 nm) is double-lobed, symmetric, and almost entirely independent of the wavelength in the given range, as seen in Figure 6.2 (top left). For increasing particle sizes, the phase functions fan out: In Figure 6.2 ($d = 100$ nm, top right), the effect is still small, but with increasing wavelength, the forward lobe gradually increases, and the backward lobe decreases, yielding an asymmetric phase function ($d = 200$ nm, bottom left). Figure 6.2 (bottom right) shows phase functions for a diameter of $d = 300$ nm. The forward lobe grew even larger, but the backward lobe now exhibits a more complex pattern. The backward lobe does not simply decrease with decreasing wavelength (as, for example, in Figure 6.2 (bottom left)) but appears to oscillate with wavelength. As the wavelength increases, the phase function of all relevant particle sizes converges to a gently backscattering curve. In conclusion, the phase function shows a complex dependency on the particle size and wavelength that, in turn, influences the spectral behavior of submicroscopic iron inclusions.

6.3.2 Influence of the particle size of submicroscopic iron

The simulation starts with an idealized host medium with a bright and constant albedo of $w = 0.9$ and an isotropic phase function. The optical constants are the same as those used for the lunar soil, and the spectrum is generated with Hapke's model for the standard geometry of $i = 30°$ and $e = 0°$. The space weathering simulation is carried out by mixing the bright and spectrally flat medium with 0.5 wt% of smFe^0 of different particle sizes ranging from $d = 1$–500 nm. This approach is comparable to Lucey and Riner [2011] but covers a broader wavelength range. Figure 6.3 (top) shows the simulation results. The blue line represents the bright and constant spectrum without any iron. Small particles ($d = 1$ nm) significantly affect the spectral shape (solid red). The small iron particles cause significant darkening and a strong red spectral slope up to approximately 2–2.5 μm. As the wavelength increases, both effects weaken and almost vanish at the upper wavelength end ($\lambda = 6\,\mu$m). As the particle diameter increases (up to $d = 500$ nm), the shape of the space-weathered spectra changes. In general, the spectra become flatter but also exhibit oscillations, mainly between 0.5 μm and 1.5 μm. The oscillation pattern moves toward higher wavelengths as the particle size increases but relaxes beyond approximately 3 μm.

Neither laboratory measurements nor remote sensing data show these kinds of oscillations. It is well known from light scattering theory that restricting the scattering target to spherical particles of a fixed size leads to unnatural patterns. Introducing any variation through non-spherical particles or different particle sizes considerably reduces such effects and generally leads to smoother and more natural results. TEM studies referenced in Pieters and Noble [2016] also suggest that smFe^0 indeed does not have one fixed particle size but instead follows a distribution over multiple particle sizes. Unfortunately, the precise particle size distribution remains unknown, and devising an inverse problem to estimate the distribution is out of the scope of this work. For simplicity, the author decides to use two iron endmembers: nanophase iron npFe^0 with $d = 1$ nm and an effective microphase mpFe^0 endmember, which

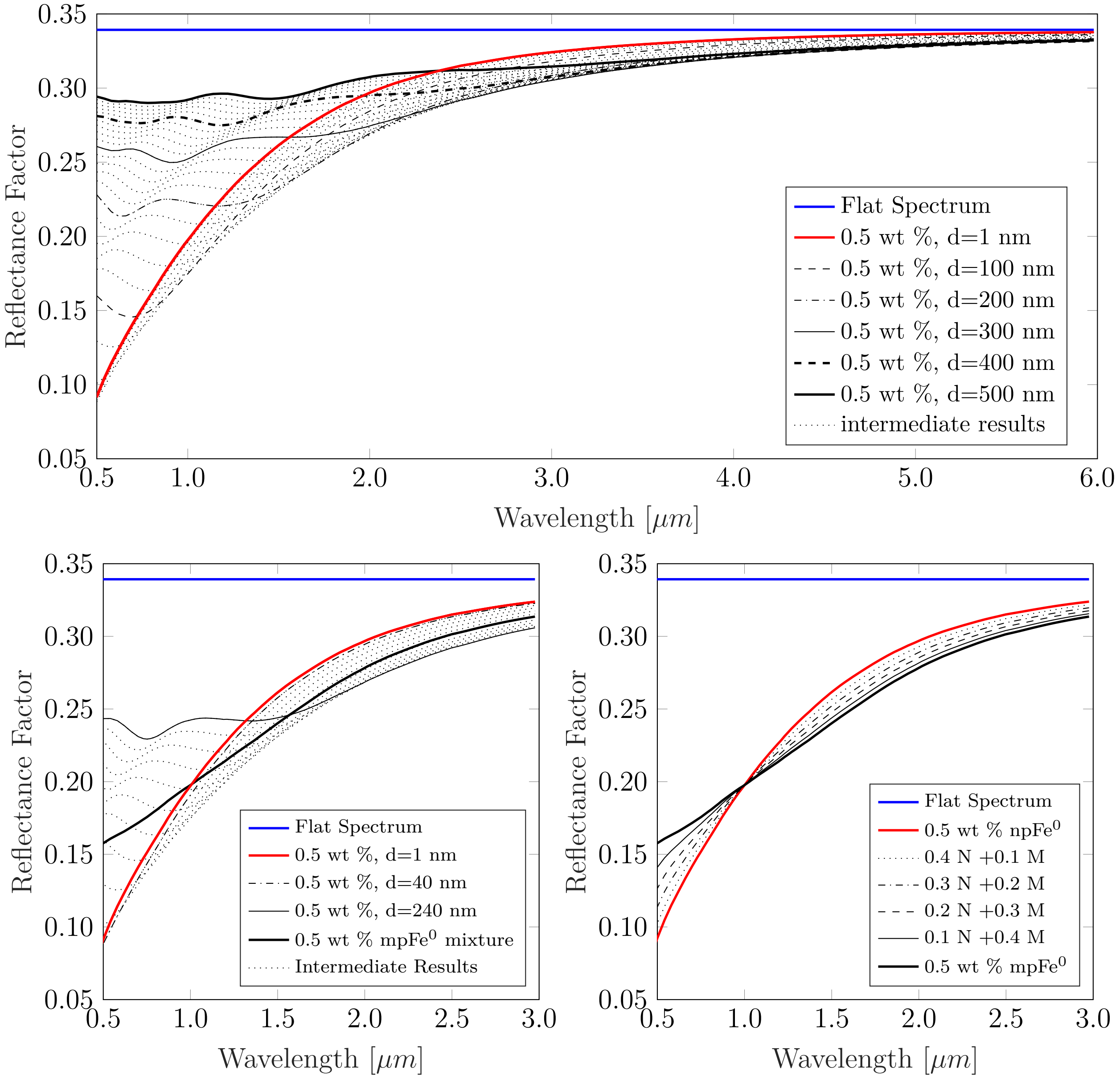

Figure 6.3. Influence of the particle size on submicroscopic iron. Top: Spectral changes of a flat and bright spectrum due to iron of different particle sizes. Small particles ($d = 1\,\mathrm{nm}$, thick solid red) lead to spectral reddening in a wavelength range below approximately $3\,\mu\mathrm{m}$. As the particle size increases, the spectra become flatter but tend to oscillate at the lower wavelength end. Bottom left: Same as top but only for particles of $d = 1\,\mathrm{nm}$ and $d = 40$–$240\,\mathrm{nm}$ in the M^3 wavelength range. The thick, solid black line represents the mixture of all spectra with $d = 40$– $240\,\mathrm{nm}$, which leads to a smooth dark spectrum with a gentle slope. Bottom right: Spectral mixture of small particles ($d = 1\,\mathrm{nm}$, thick solid red) and large particles (mixture $d = 40$–$240\,\mathrm{nm}$, thick solid black). Weighting both components allows the control of the spectral slope. Figures based on Wohlfarth et al. [2019].

is the equally weighted mixture of iron particles in a broad size range $\{d_{\min}, \ldots, d_{\max}\}$, where $d_{\min}$ is the minimal and $d_{\max}$ is the maximal particle size. Appendix H explores the optimal size range and finds that a mpFe^0 mixture of particles from $d = 20$–$200\,\mathrm{nm}$ is optimal for the selected mare sites, and a mpFe^0 mixture of particles from $d = 40$–$240\,\mathrm{nm}$ is optimal for the selected highland sites. Figure 6.3 (bottom left) shows the simulated space weathering spectra for particle sizes of the highland case between $d = 40$–$240\,\mathrm{nm}$ with clear spectral oscillations (dotted black lines). Mixing all the spectra of different particle sizes leads to a smooth spectrum (thick solid black) that has a considerably flatter slope compared to the small ($d = 1\,\mathrm{nm}$) particles (solid red). In Figure 6.3 (bottom right), the spectra of the test medium mixed with various combinations of nanophase and averaged microphase iron are shown. It can be seen that mixtures of different amounts of npFe^0 and mpFe^0 can generate various spectral slopes: More mpFe^0 yields flatter slopes, and more npFe^0 yields redder slopes.

The observed effects largely align with the work of Lucey and Riner [2011] and Trang and Lucey [2019]. These works draw a distinction between nanophase iron, which is typical of several nanometers in size, and microphase iron (or Britt-Pieters particles) of several tens of nanometers size, which *“darken but do not redden”* [Lucey and Riner, 2011]. The author’s simulations confirm that npFe^0 reddens for wavelengths approximately below 2–3 μm, but reveal that the situation is more complex for mpFe^0. The multiform phase functions of smFe^0 lead to oscillations that vanish when superimposing the effect of mpFe^0 particles across a wider size range. The combined spectral effects of particles over a size range, e.g., 40–240 nm, appear to reproduce the darkening effect, which corresponds to Lucey and Riner [2011] with mpFe^0 particles of $d = 200\,\mathrm{nm}$.

6.3.3 Influence of the amount of submicroscopic iron

The same setup as in Section 6.3.2 allows for analyzing how the amount of submicroscopic iron influences the spectral shape. An isotropic and spectrally flat medium with a constant albedo of $w = 0.9$ is interspersed with an increasing amount of nanophase and microphase iron. Figure 6.4 (left) indicates that an increasing amount of nanophase iron from 0.5–2.0 wt% yields stronger darkening while the spectral slope remains largely the same (Figure 6.4, left). In the case of microphase iron (Figure 6.4, right), the darkening effect also becomes stronger, moving the continuum to lower reflectance values. Compared to the previous section, the following view of the behavior of smFe^0 can be formulated: The mixing ratio of npFe^0 and mpFe^0 determines the slope of the space-weathered spectrum (Figure 6.3, right), and the total amount of smFe^0 governs the overall darkening (Figure 6.4, right).

6.3.4 Influence of submicroscopic iron on the 2.8–3.0 μm absorption band

Wohlfarth et al. [2018] previously applied the space-weathering simulation to an Olivine spectrum in the MIR, and Bergmann [2020] conducted a comparable experiment with multiple

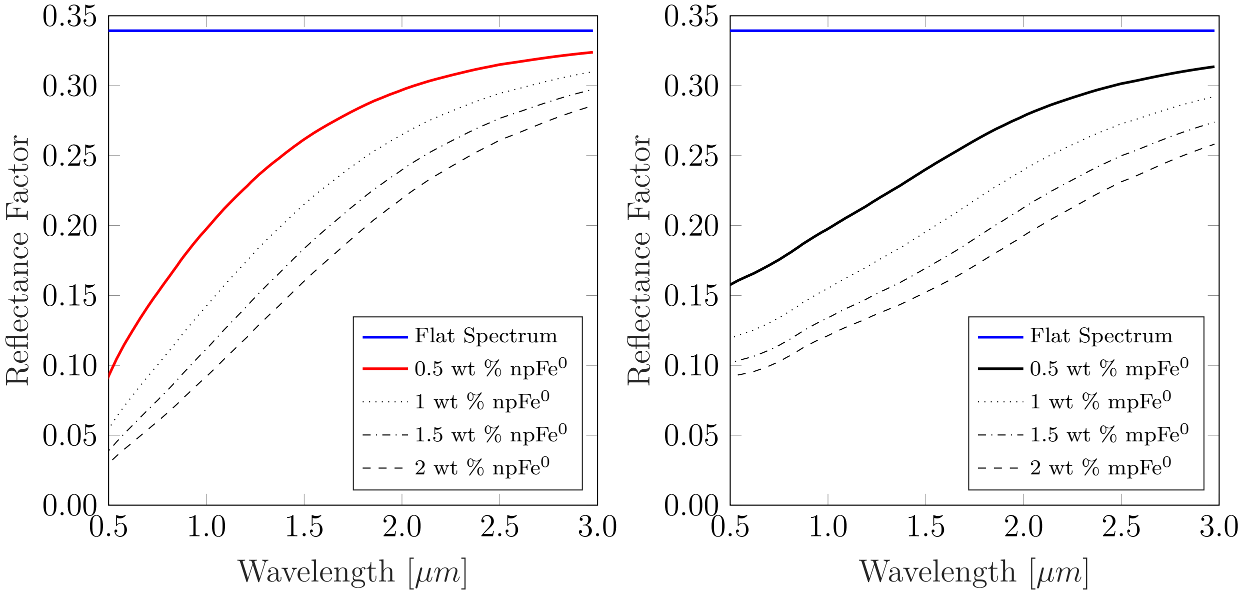

Figure 6.4. Left: Spectral changes of a flat and bright spectrum caused by interspersion of different amounts of npFe^0 ($d = 1\,\text{nm}$). Right: Same setup as left, but for mpFe^0 (mixture $d = 40$–$240\,\text{nm}$). Figures adapted and corrected from Wohlfarth et al. [2019].

mineral samples in the MIR under the author's supervision. Wohlfarth et al. [2019b] investigated the effect of space weathering on M^3 spectra but without a detailed quantification of the effect. For this thesis, the implementations were reworked and extended.

The IBD$_{3\mu\text{m}}$ parameter (Equation 5.24) operationalizes the integrated band-depth of the 2.8–3.0 μm absorption band and thus indicates lunar hydration. This section explores the effect of submicroscopic iron on the IBD$_{3\mu\text{m}}$ parameter for two different cases.

The first case uses a simulated fresh lunar highland soil spectrum from 2–20 μm. It takes several steps to simulate the highland spectrum. Laboratory reflectance spectra of labradorite and enstatite powder samples [Rommel et al., 2014, 2017] serve as input. The laboratory spectra include a strong absorption feature around 3 μm due to hygroscopically bound water comparable to the Moon. The space weathering simulation requires the simulated highland soil's single scattering albedo spectrum $w(\lambda)$. Therefore, the author uses the Hapke model with the lunar average parameters of Warell [2004] and employs a non-linear optimization scheme to extract $w(\lambda)$. A fresh lunar highland spectrum is dominated by plagioclase with a smaller fraction of pyroxene and other components [Heiken et al., 1991]. Therefore, the weighted sum $w_\text{H}(\lambda) = 0.9w_\text{L}(\lambda) + 0.1w_\text{E}(\lambda)$ of the labradorite albedo w_L and the enstatite albedo w_L approximates a fresh highland spectrum w_H. The resulting w_H enters the space-weathering simulation pipeline, which finally outputs reflectance spectra for 0–4 wt% npFe^0 and mpFe^0. Fitting a continuum slope to the spectrum at two intervals between 2500–2600 nm and 3700–3850 nm yields the continuum slope. The enclosed area normalized with the continuum yields the IBD$_{3\mu\text{m}}$ parameter.

The second case explores the effect of submicroscopic iron on M^3 measurements that can only use a mono-lateral continuum slope fit to compute the IBD$_{3\mu\text{m}}$ parameter. Because

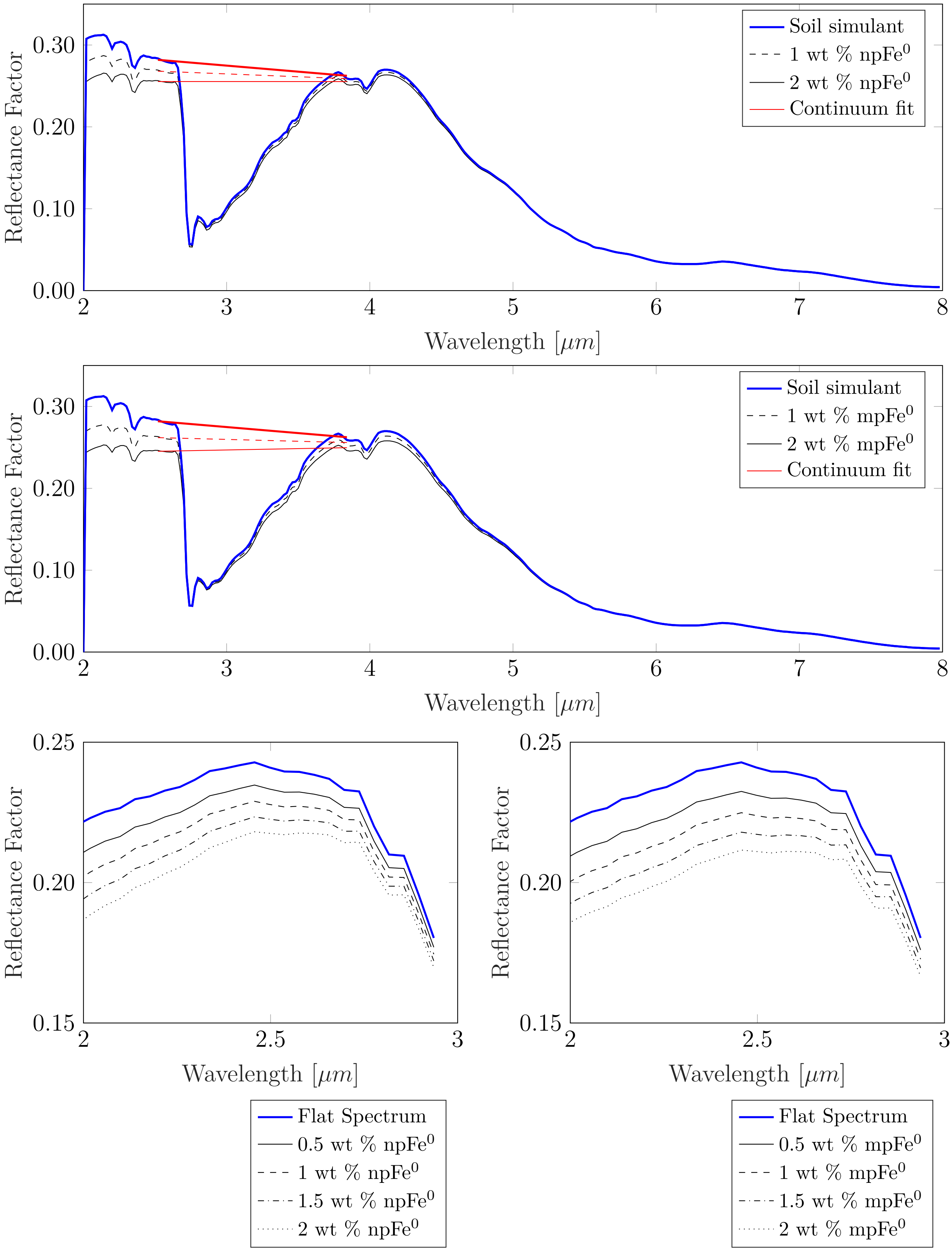

Figure 6.5. Spectral changes of lunar highland soil due to submicroscopic iron. Top: Spectral changes of a lunar highland soil simulant due to nanophase ($d = 1\,\text{nm}$) iron. Center: Same as above but for microphase iron (mixture $d = 40$–$240\,\text{nm}$). Bottom: Spectral changes of an M^3 highland spectrum due to different amounts of nanophase ($d = 1\,\text{nm}$, left) and microphase iron (mixture $d = 40$–$240\,\text{nm}$, right). The fresh soil spectrum was derived from laboratory powder samples, initially characterized and measured by [Rommel et al., 2014, 2017]. Bottom plots based on Wohlfarth et al. [2019].

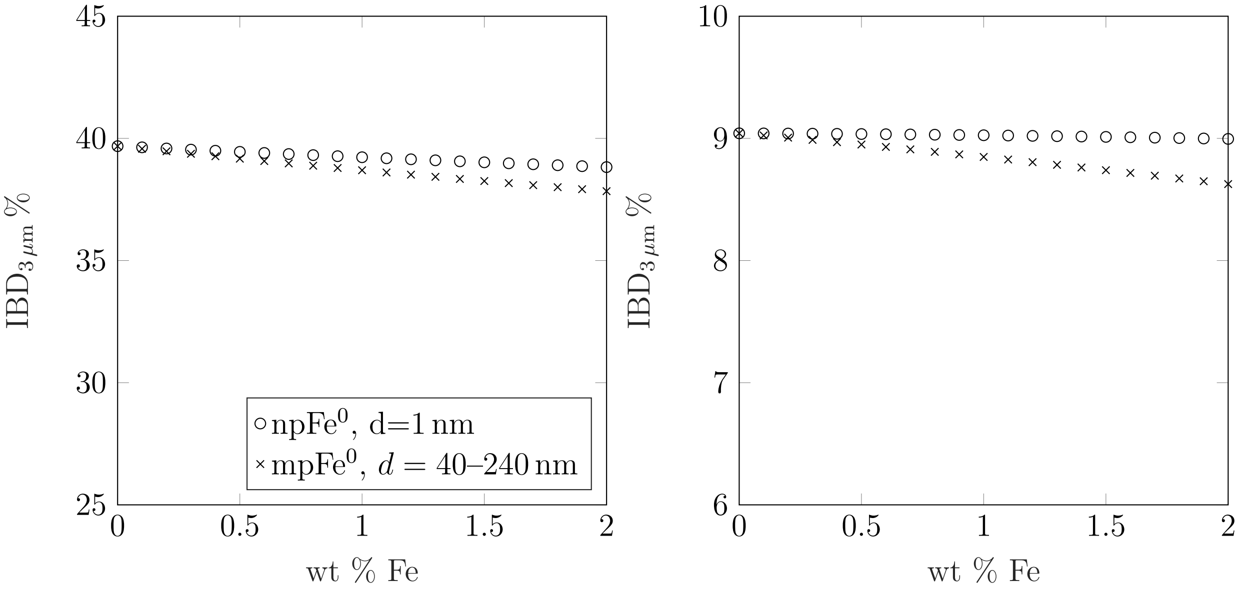

Figure 6.6. Left: Changes in the IBD$_{3\mu m}$ parameter of a lunar soil simulant due to different amounts of nanophase ($d = 1$ nm) and microphase iron (mixture $d = 40$-240 nm). Right: Same as left but for the average fresh M^3 highland soil. Right plot adapted from Wohlfarth et al. [2019].

the wavelength range of M^3 only reaches up to 3 μm, and only approximately half of the band can be measured. Hence, the continuum slope is only fitted to one side of the band, potentially leading to an integrated band depth different from the previous case. The second experiment uses a thermally corrected M^3 spectrum sampled from the ejecta blanket of a small fresh crater near Krasovskiy crater [Wohlfarth et al., 2019]. The location is assumed to bear low concentrations of smFe^0 and serves as a representative fresh spectrum for the simulation framework. Again, the single scattering albedo is retrieved and fed into the space weathering simulation model.

Figure 6.5 (top) shows the spectral behavior of simulated fresh highland soil with varying amounts of nanophase iron. Higher amounts cause reddening, but the effect becomes weaker for longer wavelengths and disappears after approximately 5 μm. Nanophase iron appears to hardly affect the IBD$_{3\mu m}$ parameter at all. The IBD$_{3\mu m}$ parameter declines from 39.7% to 38.8% at 2 wt% (see Figure 6.6 (left)). Microphase iron primarily darkens the spectra around 3 μm, and the IBD$_{3\mu m}$ parameter falls from 39.7% to 37.8% for 2 wt% of iron (see Figure 6.6 (left).

Figure 6.5 (bottom) displays the spectral behavior of a fresh highland soil spectrum measured with M^3 near the Krasovskiy crater. The space weathering simulation of the spectrum is shown in Figure 6.5 (bottom), and Figure 6.6 (right) shows the accompanying IBD$_{3\mu m}$ values. It becomes clear that in both cases, nanophase and microphase iron, the IBD$_{3\mu m}$ parameter decreases with an increasing amount of smFe^0 (Figure 6.6 (right)). However, the values are smaller than in Figure 6.6 (left) because this case only considered part of the 3 μm-band. Again, nanophase iron hardly affects the IBD$_{3\mu m}$ parameter, but with growing abundances of microphase iron, the IBD$_{3\mu m}$ parameter decreases from 9% down to 8.6%.

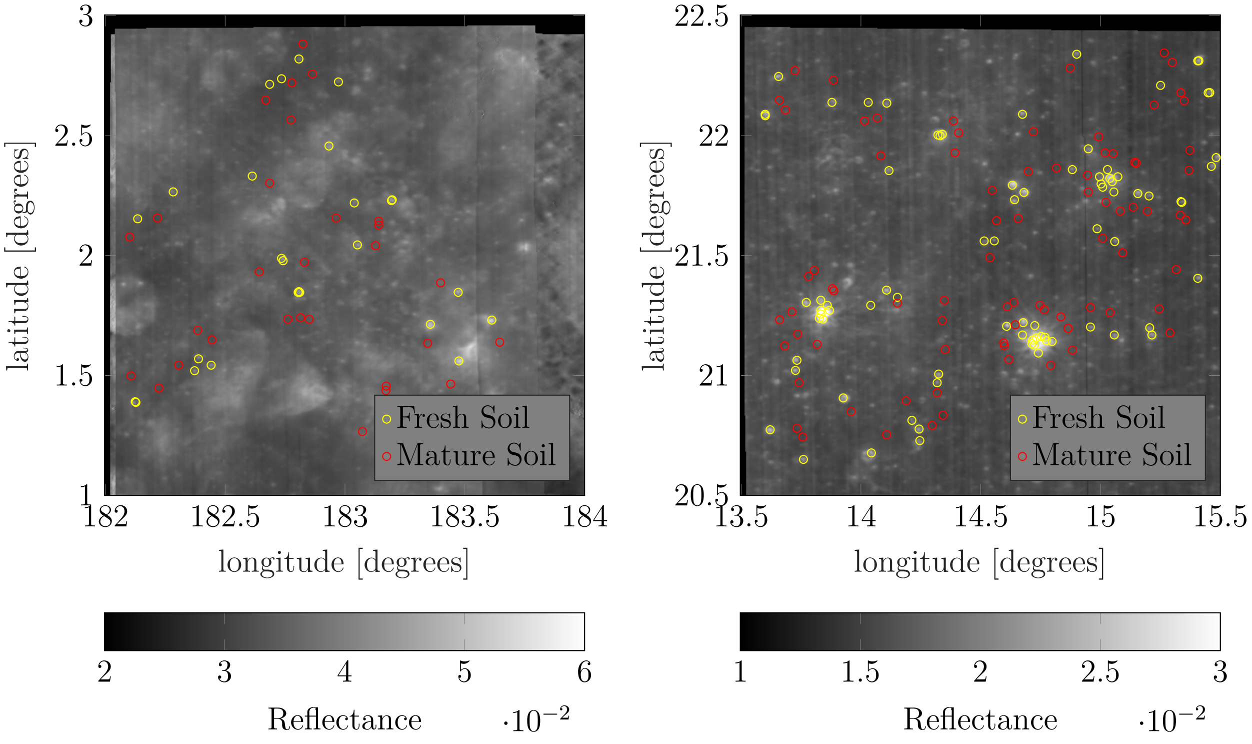

Figure 6.7. Soil spectra sampled in a highland region near Krasovskiy crater (left) and in a mare region around craters Bessel F and G (right). The background image shows the normalized reflectance at 770 nm of the M^3 instrument. Figure from Wohlfarth et al. [2019].

All in all, nanophase iron hardly affects the $\mathrm{IBD}_{3\mu\mathrm{m}}$ parameter, but microphase iron somewhat lowers it. However, realistic lunar cases will often require mixtures of nanophase and microphase iron with comparatively low abundances ($\lesssim$ 1 wt%) to reproduce space weathering effects. Consequently, different space weathering states on the Moon will likely affect the $\mathrm{IBD}_{3\mu\mathrm{m}}$ parameter by less than 10 %.

6.4 Space weathering and hydroxyl mapping

This section validates the previously developed method and assesses the influence of maturity on the continuum-removed integrated band-depth of the 2.8–3.0 μm absorption band by calculating the $\mathrm{IBD}_{3\mu\mathrm{m}}$ parameter. Because the Moon exhibits a compositional and geomorphological dichotomy between maria and highlands [Heiken et al., 1991], typical soil spectra of these regions are investigated separately. Each comparison is based on spectra extracted at a small, fresh crater and from a nearby mature surface area. Of course, besides the nanophase and microphase iron content, the soil properties between these locations may also differ in particle size, compaction/porosity, roughness of the regolith surface, and abundance of boulders. This kind of comparison is commonly used to infer the changes in spectral properties from immature toward mature soil [e.g., Pieters and Noble, 2016].

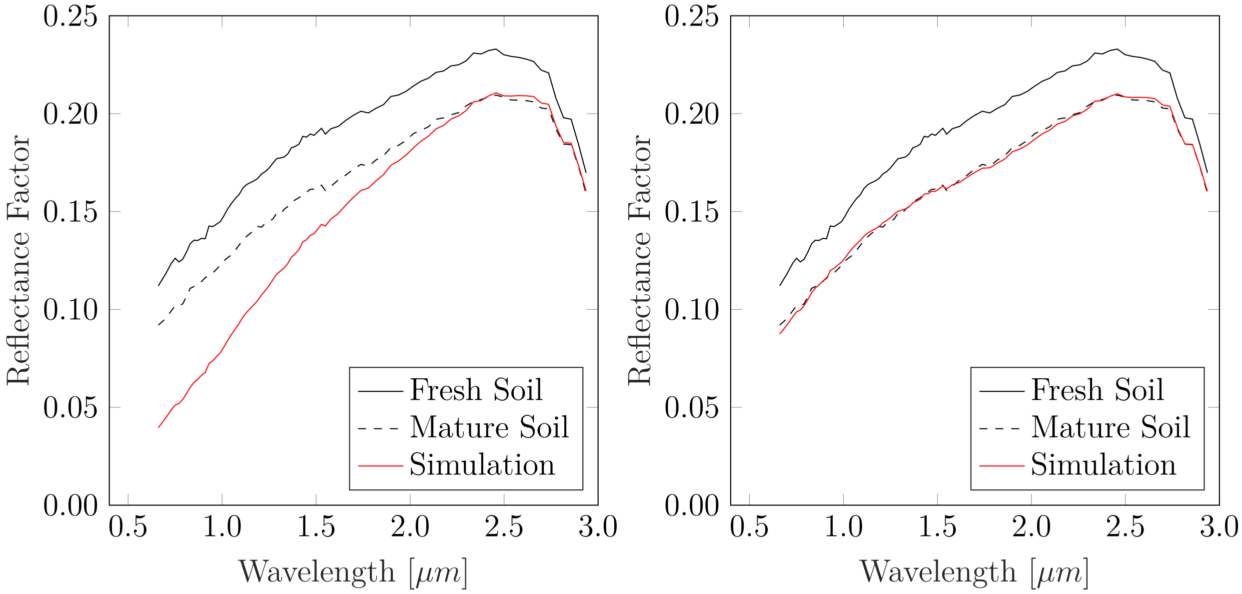

Figure 6.8. Space weathering simulation of highland soil. Left: Simulation with $d = 1\,\mathrm{nm}$ and 1.95 wt%. Reddening is overestimated. Right: Fit obtained with $d = 1\,\mathrm{nm}$, 0.19 wt% and of mixture $d = 40$-$240\,\mathrm{nm}$, 1.37 wt%. Figures adapted from Wohlfarth et al. [2019].

6.4.1 Lunar highlands: space weathering simulation and $3\,\mu$m band depth

Thirty pairs of typical highland soil spectra were sampled from topographically and thermally corrected M^3 data near Krasovskiy crater (3.9°N, 175.5°W) on the lunar far side (Figure 6.7, left). Each of the thirty pairs consists of an example of typical immature soil (yellow circles), which is sampled from fresh ejecta material of small craters, and one example of mature soil (red circles), which is collected in the close vicinity so that each pair is likely to be of comparable soil composition. These spectra are used for two analyses: At first, the shape of the mature spectrum is reproduced from the immature spectrum using the new space weathering simulation method, which essentially serves as model validation and provides an estimate of the smFe^0 abundance. Secondly, the spectra are analyzed in order to infer insights about the change in the IBD$_{3\mu\mathrm{m}}$ parameter.

The fresh and mature spectra of a typical highland soil sample are shown in Figure 6.8, in which the mature spectrum (dashed black) exhibits a darkening effect compared to the fresh spectrum (solid black). The space weathering simulation method is employed to approximate the mature soil spectrum with the results from the space weathering simulation. As can be seen in Figure 6.8 (left), nanophase iron alone ($d = 1\,\mathrm{nm}$) is not sufficient to fit the spectrum. The fit is accurate for larger wavelengths, but the reddening effect is too strong, which causes deviations for smaller wavelengths. Adding larger particles by mixing sizes from $d = 40$–$240\,\mathrm{nm}$ yields a much better fit reproducing the darkening (Figure 6.8 (right)). This behavior aligns with the findings of Lucey and Riner [2011], where larger simulated particles were essential to reproduce the maturity effects even though they overestimated the actual size of the microphase size range. Using nanophase iron alone, Noble et al.

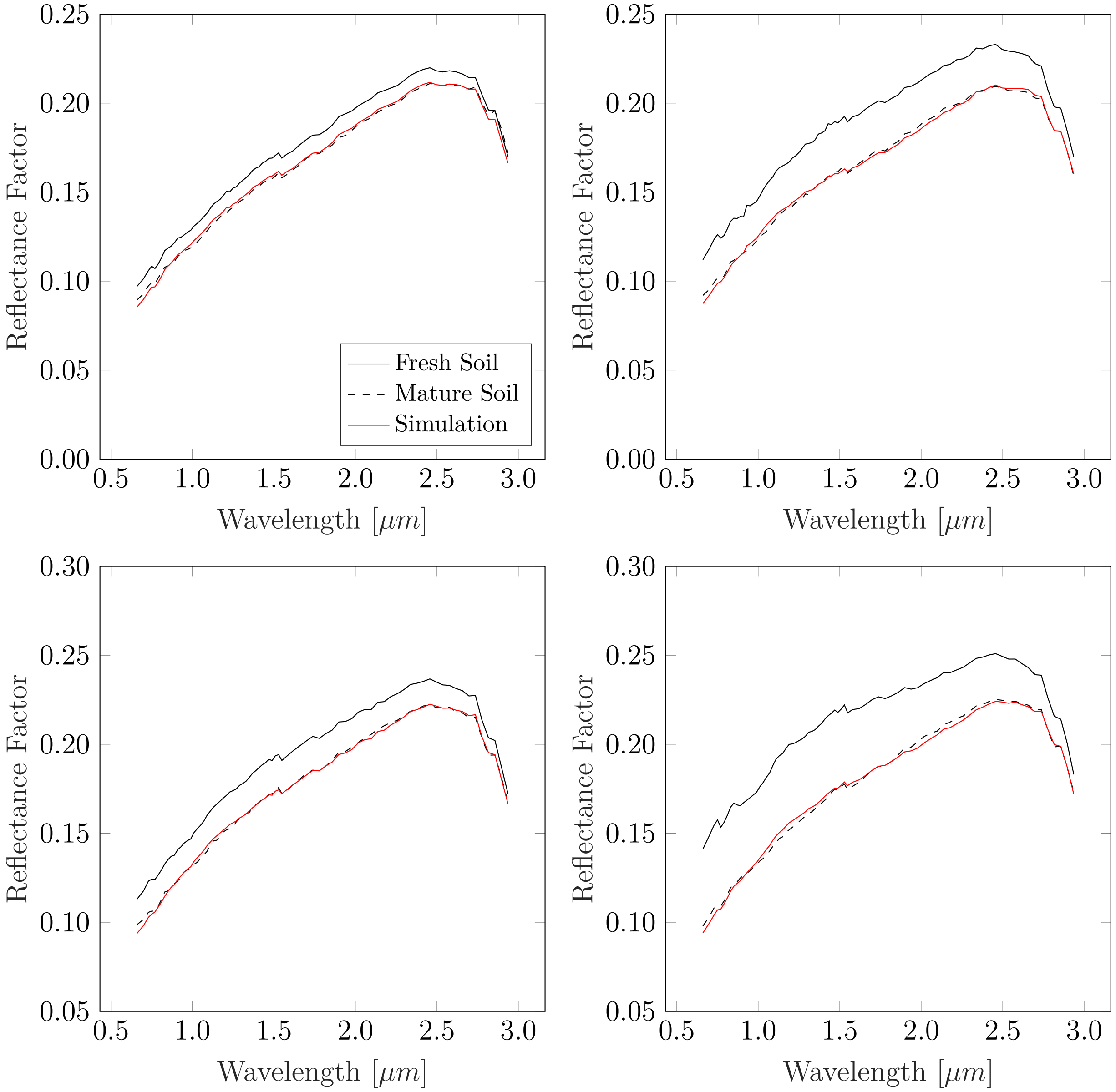

Figure 6.9. Space weathering simulation of typical immature highland spectra. Top left: Sample No. 01. Top right: Sample No. 09. Bottom left: Sample No. 15. Bottom right: Sample No. 24. Note that a variety of different mature spectra (dashed black) can be simulated with the proposed method (red) using the fresh spectra (black). Figure based on Wohlfarth et al. [2019].

[2007] have also overestimated reddening. Moreover, the weight percentages in the range of $\lesssim 1\,\mathrm{wt\%}$ for nanophase and microphase iron are of the same order of magnitude as the nano- and microphase iron levels near Krasovskiy crater sampled from abundance maps of Trang and Lucey [2019] derived from the Kaguya Multiband Imager. An optimization was carried out concerning the RMSE so that the simulated spectra best fit the observed mature soil spectra. In order to emphasize the wavelength range around 2.8–3 μm, the highest eight M^3 channels were given double weight for the fitting procedure. The results are shown in Table 6.1. Overall, there is a small residual RMSE, indicating that all fits resemble the observed mature spectra well. Four representative spectra are plotted in Figure 6.9, showing that the space weathering simulation can reproduce the mature soil spectra. The small RMSE and the excellent agreement between fit and reality serve as a strong indicator that the presented method is well suited to describe the spectral effects of space weathering in lunar highland regions.

No.		smFe^0		No.		smFe^0	
	npFe^0 [wt%]	mpFe^0 [wt%]	RMSE		npFe^0 [wt%]	mpFe^0 [wt%]	RMSE
1	0.1113	0.4239	0.0020	16	0.0812	1.1989	0.0019
2	0.1222	0.5481	0.0018	17	0.3514	0.8011	0.0083
3	0.1924	1.0980	0.0017	18	0.0914	1.3718	0.0026
4	0.1693	1.5079	0.0022	19	0.0519	1.1274	0.0019
5	0.1937	2.8781	0.0034	20	0.0967	2.0230	0.0037
6	0.0548	0.3896	0.0023	21	0.0907	2.3708	0.0047
7	0.2380	2.1023	0.0032	22	0.0046	1.3656	0.0034
8	0.1408	1.0020	0.0015	23	0.0091	1.9107	0.0031
9	0.1939	1.3668	0.0017	24	0.3114	1.3291	0.0022
10	0.0844	0.8950	0.0016	25	0.0001	1.3679	0.0029
11	0.2202	1.4228	0.0021	26	0.3652	1.0432	0.0053
12	0.3528	0.7230	0.0039	27	0.1790	1.4146	0.0016
13	0.3755	0.5750	0.0043	28	0.0019	1.6276	0.0027
14	0.3013	0.3493	0.0049	29	0.1878	1.3525	0.0023
15	0.0951	0.7555	0.0014	30	0.1315	1.1225	0.0019

Table 6.1. Amounts of nanophase ($d = 1\,\mathrm{nm}$) and microphase iron ($d =$ 40-240 nm) in the selected highland region.

To assess the influence of space weathering, the $\mathrm{IBD}_{3\mu\mathrm{m}}$ parameter of the mature soil spectra is plotted against the $\mathrm{IBD}_{3\mu\mathrm{m}}$ parameter of fresh soil sampled nearby (Figure 6.10). Points that are located on the bisecting line (solid black) do not exhibit any change in the $\mathrm{IBD}_{3\mu\mathrm{m}}$ parameter. The mean of the samples is indicated by the red dot and is located 9.92% beneath the bisecting line. This indicates that the $\mathrm{IBD}_{3\mu\mathrm{m}}$ parameter of fresh and mature soil only slightly decreases as the regolith matures. This agrees well with the simulation results in Section 6.3.4, where a small decrease of $\mathrm{IBD}_{3\mu\mathrm{m}}$ was found.

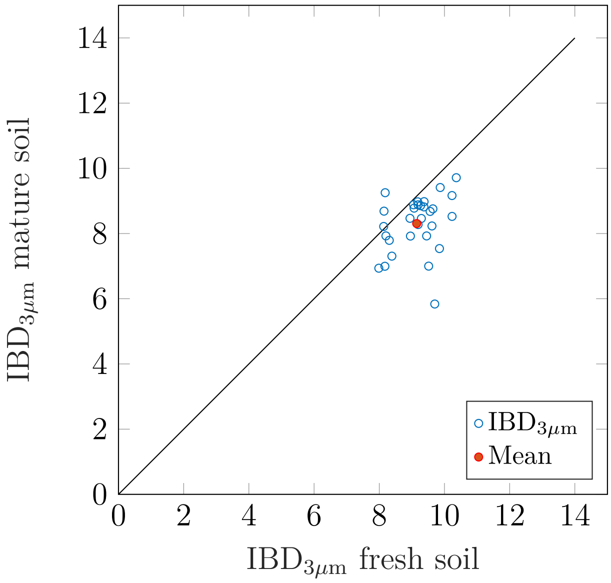

Figure 6.10. $IBD_{3\mu m}$ parameter of fresh soil vs. mature soil of all 30 sample points in the highland region. Note that $IBD_{3\mu m}$ is hardly affected by space weathering. Figure from Wohlfarth et al. [2019].

6.4.2 Lunar mare: space weathering simulation and 3 μm band depth

The area around the small craters Bessel F ($21.2° N, 13.8° E$) and Bessel G ($21.1° N, 14.7° E$) located in southwestern Mare Serenitatis is the primary target of the analysis because both craters exhibit a bright and therefore young ejecta blanket and several young and small craters are scattered across the region. A set of 80 spectra was sampled from the ejecta blankets and served as immature soil samples (yellow circles), and spectra sampled nearby (red circles) are their mature counterparts (Figure 6.7 (right)). The analysis is carried out in the same way as in the previous Section 6.4.1. It is found that the mature soil spectrum is affected by darkening and reddening, and the pyroxene absorption features for 1 μm and 2 μm are obstructed. The 3 μm feature remains intact, but the reflectance is decreased (see Figure 6.11). The space weathering simulation was applied to all 80 fresh soil spectra. Best RMSE fits concerning the amount of nanophase and microphase iron particles were carried out to find approximations of the mature soil spectra. In order to emphasize the wavelength range around 2.8–3 μm, the highest eight M^3 channels were given double weight for the fitting procedure. The results are shown in Table 6.2. Six best-fit results for various spectral shapes are shown in Figure 6.11. It can be seen that the simulated space-weathered soil samples (solid red) match the mature soil spectra (dashed black). The fits are particularly good for the larger and smaller wavelengths. However, around the 2 μm absorption feature, the simulation predicts less flattening compared to the observations (See Figure 6.12).

As in Section 6.4.1, the influence of space weathering is assessed by plotting the $IBD_{3\mu m}$ parameter of the fresh soil spectra against the $IBD_{3\mu m}$ parameter of mature soil (Figure 6.13, left). Similar to the highland soil, the $IBD_{3\mu m}$ value only decreases slightly. Points that are located on the bisecting line (solid black) do not exhibit any change in the $IBD_{3\mu m}$

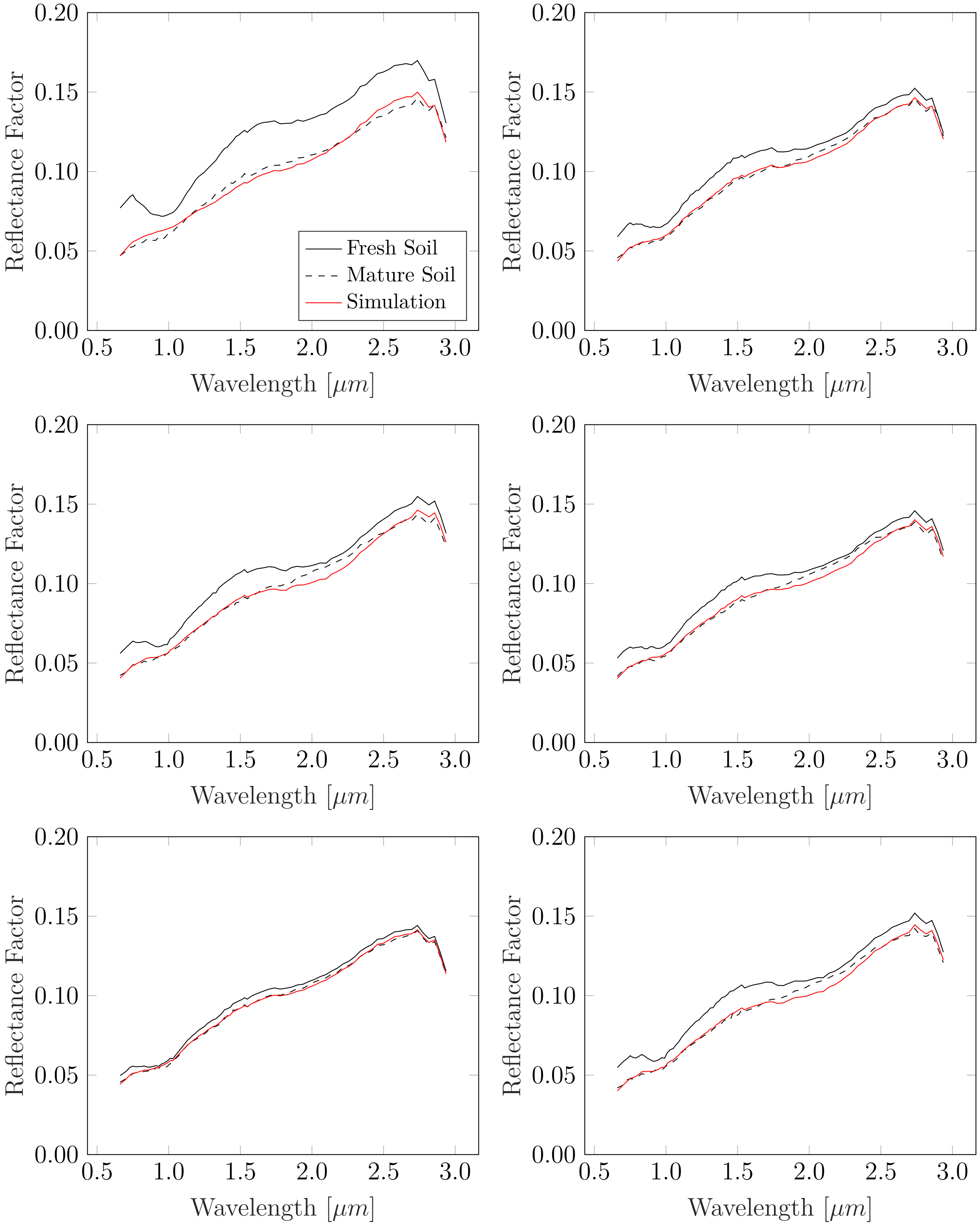

Figure 6.11. Space weathering simulation of typical immature mare spectra. Top left: Sample No. 05. Top right: Sample No. 10. Center left: Sample No. 47. Center right: Sample No. 50. Bottom left: Sample No. 54. Bottom right: Sample No. 66. Note that a variety of different mature spectra (dashed black) can be simulated with the proposed method (solid red). Figure based on Wohlfarth et al. [2019].

No.		smFe^0		No.		smFe^0	
	npFe^0 [wt%]	mpFe^0 [wt%]	RMSE		npFe^0 [wt%]	mpFe^0 [wt%]	RMSE
1	3.1452	2.8951	0.0064	41	0.8977	0.1995	0.0047
2	2.9520	2.6737	0.0063	42	1.0721	0.5146	0.0034
3	3.2686	3.4662	0.0081	43	1.7374	1.2563	0.0066
4	3.9183	3.7909	0.0076	44	0.6827	0.1839	0.0047
5	1.8721	1.4461	0.0034	45	1.0388	0.5490	0.0034
6	1.6068	1.1564	0.0034	46	2.9136	1.9242	0.0080
7	1.8757	1.2351	0.0042	47	1.0086	0.5107	0.0030
8	1.4538	0.9381	0.0047	48	0.6698	0.3623	0.0025
9	1.1635	0.7975	0.0033	49	1.3525	1.0493	0.0065
10	0.7204	0.3346	0.0022	50	0.7404	0.3372	0.0027
11	0.6808	0.4420	0.0024	51	2.1149	1.5510	0.0079
12	1.2742	0.5170	0.0049	52	0.7207	0.0703	0.0058
13	0.6305	0.0869	0.0057	53	0.6755	0.2765	0.0023
14	0.9955	0.6313	0.0035	54	0.3022	0.1816	0.0011
15	0.8500	0.4622	0.0032	55	0.3240	0.2362	0.0017
16	1.2846	0.7619	0.0037	56	0.2677	0.1741	0.0013
17	2.5246	1.9391	0.0086	57	0.5747	0.3822	0.0022
18	1.3351	0.9458	0.0057	58	0.4412	0.2806	0.0015
19	0.7068	0.4014	0.0034	59	1.1769	0.6119	0.0039
20	1.6603	0.9936	0.0052	60	0.5660	0.2352	0.0028
21	0.8476	0.4769	0.0029	61	0.4798	0.1218	0.0033
22	1.4605	1.0944	0.0060	62	0.4893	0.1358	0.0038
23	2.7631	2.7186	0.0107	63	0.6708	0.2915	0.0029
24	1.7351	1.6222	0.0084	64	1.2850	0.9378	0.0051
25	1.2052	0.6396	0.0040	65	2.0148	1.2548	0.0058
26	1.7958	1.0402	0.0056	66	0.9132	0.4308	0.0027
27	1.0061	0.4855	0.0036	67	0.8862	0.4414	0.0037
28	1.2257	0.6783	0.0042	68	2.1818	1.7183	0.0058
29	1.3660	0.4519	0.0042	69	0.7586	0.4358	0.0029
30	1.4717	0.5388	0.0050	70	0.4256	0.1499	0.0025
31	1.2061	0.4122	0.0043	71	0.5883	0.1190	0.0046
32	1.0487	0.4563	0.0039	72	1.8092	2.3803	0.0120
33	1.2173	0.2335	0.0055	73	1.4542	1.5605	0.0096
34	0.6844	0.4151	0.0028	74	2.5626	3.2556	0.0129
35	1.8209	1.2283	0.0057	75	0.6863	0.1627	0.0043
36	1.6345	1.1281	0.0044	76	0.4038	0.0571	0.0042
37	0.6568	0.3628	0.0042	77	0.6557	0.3741	0.0026
38	1.1001	0.7886	0.0031	78	0.2375	0.0405	0.0033
39	0.2128	0.1290	0.0019	79	0.8685	0.5548	0.0039
40	1.4498	1.1491	0.0063	80	1.0534	0.6542	0.0040

Table 6.2. Best-fit abundances of nanophase ($d = 1\,\mathrm{nm}$) and microphase iron ($d =$ 40-240 nm) in the selected mare region of the Moon.

parameter. The mean of the samples is indicated by the red dot and is located 5.08% beneath the bisecting line (9.55 % with outlier removal). This indicates that the $\mathrm{IBD}_{3\mu\mathrm{m}}$

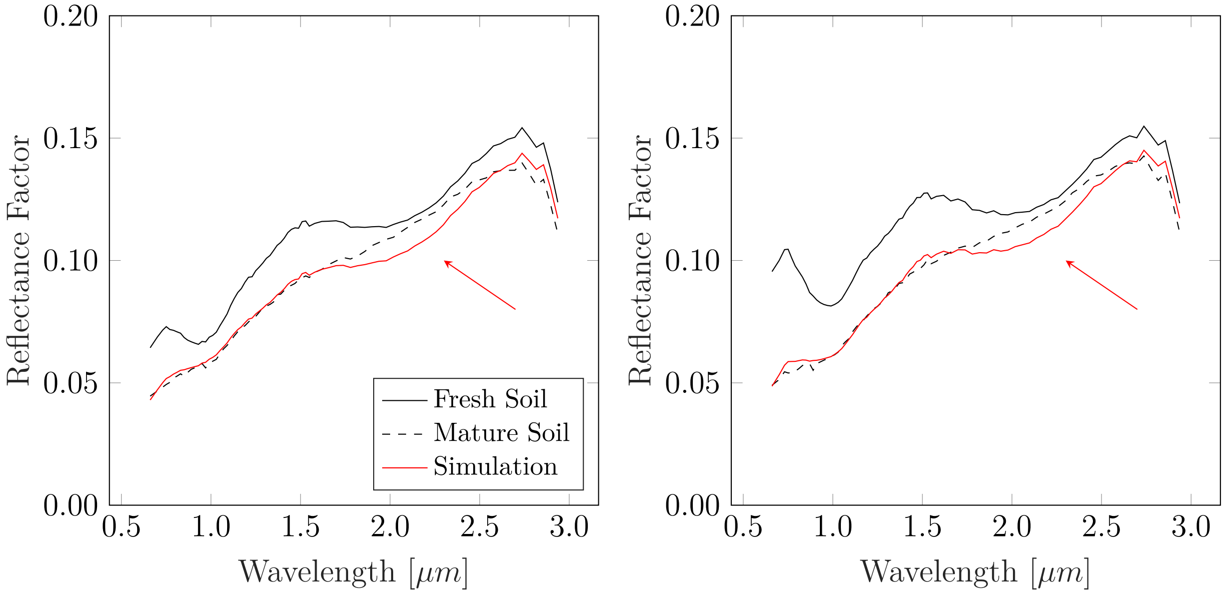

Figure 6.12. Space weathering simulation of mare soil. Left: Sample No. 28, Right: Sample No. 29. Note that the shape of the 1 μm and 3 μm feature is well retrieved, but the simulated 2 μm feature is too strong (red arrows). Figure based on Wohlfarth et al. [2019].

parameter of fresh and mature soil only slightly decreases as the regolith matures. This supports the results in Section 6.3.4, where a comparable decrease of $\text{IBD}_{3\mu\text{m}}$ by 9.92 % was found. However, the point cloud in Figure 6.13 (left) exhibits a large horizontal spread, which is likely due to some sample points with an improper topographic correction (see Section 6.7).

6.4.3 Band depth assessment

The highland material predominantly consists of plagioclase that lacks strong absorption bands except for the OH/H_2O-absorption band, which may be present around 3 μm. In mare regions, the abundance of pyroxenes is considerably higher, and the spectra additionally exhibit iron absorption bands around 1 μm, and 2 μm. To assess and compare the change of the band depth as the regolith matures, the author calculated the Integrated Band-Depth (IBD) parameter for the three absorption bands around 1 μm, 2 μm and 3 μm based on all 80 mare soil sample pairs. Further, the IBD parameter of each mature spectrum was divided by the IBD parameter of the associated fresh spectrum. The resulting quantity is termed the ratioed IBD parameter. The results were grouped in twenty bins with a width of 0.01 each (Figure 6.13, right). The distribution of the ratioed $\text{IBD}_{3\mu\text{m}}$ parameter centers around the 0.9–1.0 interval. As already discussed, this indicates that the $\text{IBD}_{3\mu\text{m}}$ parameter is only slightly affected by space weathering. The large spread and the outliers of the ratioed $\text{IBD}_{3\mu\text{m}}$ distribution are due to the large spread and the outliers in the original data (Figure 6.13, left), which is further discussed in Section 6.7. The ratioed $\text{IBD}_{1\mu\text{m}}$ and $\text{IBD}_{2\mu\text{m}}$ are considerably smaller, which indicates that these bands are more strongly affected by space weathering. The $\text{IBD}_{1\mu\text{m}}$ parameter decreases by roughly 50%, and the $\text{IBD}_{2\mu\text{m}}$ parameter

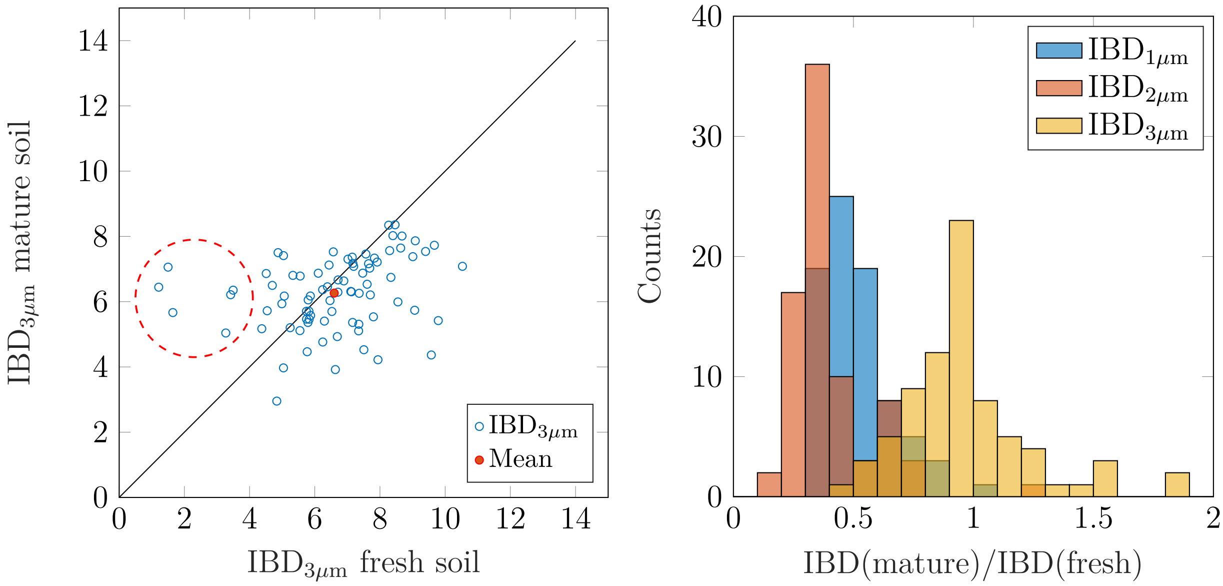

Figure 6.13. Influence of space weathering on the absorption bands. Left: $\mathrm{IBD}_{3\mu\mathrm{m}}$ parameter of mature soil vs. fresh soil of all 80 sample points in the mare region. Note that the $\mathrm{IBD}_{3\mu\mathrm{m}}$ is, on average, hardly affected by space weathering. Outliers are marked by a dashed red circle. Right: The mature vs. immature integrated band depth ratio for 1 μm, 2 μm and 3 μm indicates how strongly the bands are affected by space weathering. Note that the 3 μm band is least affected. Figure from Wohlfarth et al. [2019].

becomes smaller by even about 60%. The analysis indicates that the absorption bands around 1 μm and 2 μm are strongly affected by space weathering, while the 3 μm features remain largely intact.

6.5 Spectral effects of particle clusters

The previous section only considered single spherical particles with varying sizes. To consider clusters of iron particles, the author issued and supervised a master's thesis. Arnaut et al. [2021] and Arnaut [2021] extended the framework of Egel et al. [2017] and computed the light scattering properties of different iron clusters with inter-particle interactions. This section uses the routines of Arnaut [2021] but extends the study to multiple cluster sizes and analyzes the detailed effects on a bright, spectrally flat medium. The simulation takes three steps. The first step generates a random cluster of small particles within a predefined bounding box. The bounding box can be either spherical with a predefined radius or rectangular with a fixed height and varying lateral extent. The tiny particles have varying radii between 10 nm and 30 nm and follow a modified Poisson disc algorithm [Arnaut, 2021], which distributes them randomly. This study takes two types of clusters. Spherical clusters model agglomerations of small particles and take diameters between 100 and 300 nm. Cuboids or plates with a height of 100 nm and a lateral extent of 100 × 100, 150 × 150, ..., 700 × 700 nm simulate particle accumulations in the mineral rims. The second step uses the T-matrix formalism to compute the spherical vector wave expansion coefficients necessary for the efficiencies and

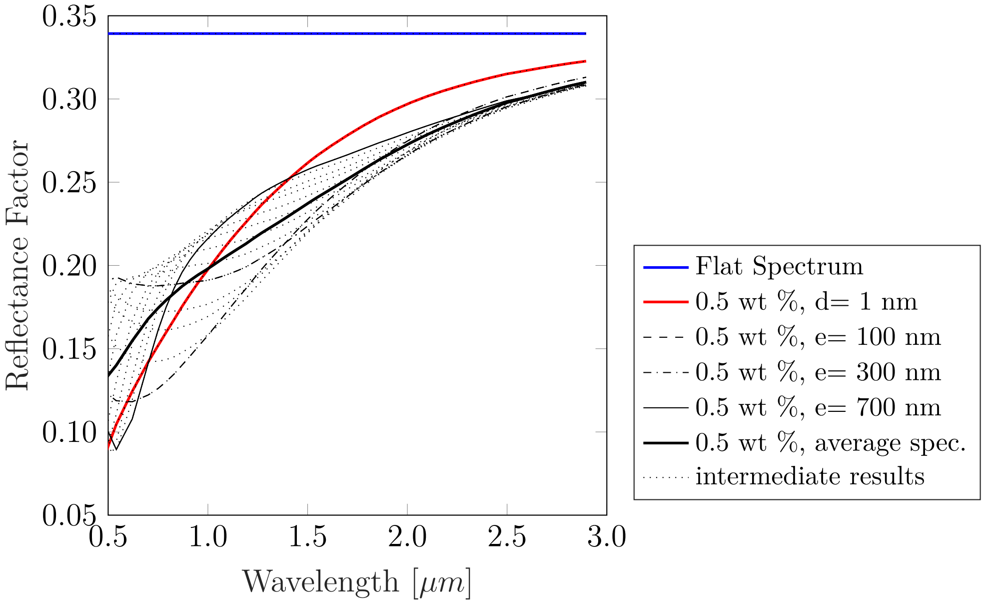

Figure 6.14. Spectral changes of a flat and bright spectrum due to iron clusters of different lateral extents. Small particles ($d = 1\,\text{nm}$, thick solid red) lead to spectral reddening in a wavelength range below approximately $3\,\mu\text{m}$. As the lateral cluster extent e increases, the spectra become flatter but tend to oscillate at the lower wavelength end. A superposition of multiple oscillating spectra leads to a smooth spectrum with a flatter slope (thick black).

the electromagnetic fields for phase function computation. For details, see Arnaut [2021]. The third step takes the results of step two, applies the mixing equation, and simulates the effect of varying cluster sizes on a bright and spectrally flat medium, similar to Figure 6.1. Figure 6.14 shows the spectral effects of iron clusters constrained with bounding boxes. For reference, a small single iron particle causes substantial darkening and reddening (solid red). As the lateral cluster extent increases, the spectral shape changes. At the higher wavelength end ($< 3\,\mu\text{m}$), the simulated spectra of all cluster sizes become slightly darker but remain comparably smooth. However, at shorter wavelengths, between 500 nm and 1500 nm, the simulated spectra strongly oscillate. Again, the oscillation pattern appears to move to longer wavelengths as the lateral cluster extent increases, somewhat resembling a wave that travels along an unilaterally attached rope. The oscillations appear unnatural and have not been reported to occur in any known laboratory study. Following the same argumentation as in Section 6.3.2, the author explores a superposition of multiple clusters with varying extents. The average of differently-sized particle clusters leads to a spectrum with a flatter slope than predicted for the small ($d = 1\,\text{nm}$) particles, similar to Figure 6.3 (bottom left). In principle, iron particle clusters and individual large iron particles have comparable effects on the spectral shape (see Section 6.3.2), where the cluster spectra tend to oscillate more strongly.

6.6 Further applications

The space weathering model played a role in two subsequent studies. Hess et al. [2020a] investigated the spectrophotometric behavior of lunar swirls, and Hess et al. [2021] devised a Bayesian spectral unmixing model for lunar spectra. Lunar swirls are bright vortex structures that occur on the lunar surface. Swirls have no significant topography that distinguishes them from the background [Denevi et al., 2016] and usually appear together with a magnetic anomaly [Hood and Williams, 1989]. However, the Mare Moscoviense Swirl has no magnetic anomaly. Their origin remains elusive, and they are targets of active research, e.g., Blewett et al. [2011]; Denevi et al. [2016]; Hess et al. [2020a]; Blewett et al. [2021]. Hess et al. [2020a] investigated six swirls with NIR spectra of the M^3 instrument, comparing on-swirl and off-swirl spectra. They also used the single-particle space weathering model from Section 6.2.2 and the soil compaction extension of the Hapke model [Hapke, 2008] to simulate the spectral effects at and around the swirls. The authors found that only a combination of reduced space weathering and soil compaction can accurately explain the swirl spectra. Hess et al. [2020a] conclude that their finding is a clue for an external compaction process that may support the hypothesis of swirl formation through comet interaction [Schultz and Srnka, 1980]. The NIR reflectance spectra of an intimate mineral mixture are a nonlinear superposition of the endmember spectra. The Hapke model has the remarkable property that the endmember spectra mix linearly concerning the single scattering albedo [Mustard and Pieters, 1989]. Thus, it is possible to invert the Hapke model of the target reflectance spectrum, extract the albedo, and perform linear spectral unmixing with albedo spectra from an endmember database. The unmixing procedure then yields the abundance of each endmember. However, applying spectral unmixing to lunar reflectance spectra is challenging because the problem is ill-posed, and multiple mechanisms alter the spectra. Most notably, submicroscopic iron, agglutinates, ilmenite, porosity, and grain size all darken the lunar spectrum. Hess et al. [2021] devised a Bayesian unmixing approach with detailed constraints on the darkening agents and performed three unmixing experiments. After demonstrating the approaches' viability with synthetic spectra, the authors perform spectral unmixing with laboratory spectra of lunar analogs characterized by Rommel et al. [2017]. Both cases show that the Bayesian unmixing procedure works robustly. After that, Hess et al. [2021] apply the model to the spectra of lunar return samples of the Lunar Soil Characterisation Consortium (LSCC) and use the space weathering model (as shown in Section 6.2.2) and elemental priors to retrieve the mineral and iron abundances. Unmixing real lunar spectra leads to higher levels of uncertainty, but using the space weathering model and elemental priors can effectively mitigate the problems caused by the darkening components. Hess et al. [2021] found that spectral unmixing on real lunar spectra requires nanophase and microphase iron to have abundances up to approximately 2 wt%, consistent with this study and Lucey and Riner [2011]. Both iron components are strongly correlated to one another and to the magnetic moment I_s [Morris, 1976].

6.7 Discussion

The previous sections show that the space weathering simulation results agree well with the observed data. Nevertheless, five points still need to be discussed: The particle size of smFe^0, the implications of particle clusters, the iron abundance estimates, the deviation around the 2 μm absorption band, and the outliers in Figure 6.13 (left). Previous studies, most notably Lucey and Riner [2011], concluded that small iron particles cause spectral reddening and large iron particles darken but do not redden. This study incorporates the single particle phase function into the simulation pipeline and finds that large spherical particles generate unnatural spectral oscillations and thus cannot fit the shape of space-weathered spectra. Accurate spectral fits with lunar measurements require averaging over a range of different particle sizes from 20–200 nm for lunar maria and 40–240 nm for lunar highlands. TEM images of mineral rims [Noble et al., 2011; Pieters and Noble, 2016] show layers of up to 200 nm in thickness and an unconstrained lateral extent, which consists of nanophase iron particles typically located one or two particle diameters away from each other. This study simulated the spectral effects of clusters and layers of closely packed small iron particles and found that they change the spectral slope and exhibit a behavior similar to single large iron particles. Again, individual clusters lead to spectral oscillations, but averaging over a broad size range can explain spectral darkening. Altogether, these simulations indicate that the spectral effects of submicroscopic iron might be more intricate than previously thought [Lucey and Riner, 2011; Pieters and Noble, 2016]. Above all, the cluster hypothesis challenges the view that darkening is exclusively due to large iron particles. Instead, it could also be due to small iron particles that form close to each other. Yasanayake et al. [2018], Yasanayake et al. [2024] and Denevi et al. [2021] manually separated and measured spectra of agglutinates and minerals from lunar soil samples. They found that the spectral slope of the mineral fraction is surprisingly flat, which contradicts the general view [Lucey and Riner, 2011; Pieters and Noble, 2016] that mineral rims only contain tiny iron particles that primarily lead to reddening. The new simulation presented here and in Arnaut et al. [2021] might explain these findings because vaporized rims contain the described clusters [Yasanayake et al., 2024].

The iron abundance estimates in Table 6.1 agree with Lucey and Riner [2011], who find < 1 wt% of smFe^0. Many iron abundance estimates in Table 6.2 also yield values $\lesssim 1$ wt%, which is also consistent with Lucey and Riner [2011]. However, there are also values with several wt%, which is probably too high. A possible explanation might be that the weight percentage is sensitive to other assumptions on grain size, average density, and more, which makes the parameter uncertain. The retrieved weight percentage is affected if any of these assumptions are inaccurate at a given site. Therefore, it would be instructive to carry out more parameter variations, calibrate the abundance estimates with lunar samples, and compare them to the I_s/FeO parameter.

The fits of the space weathering simulation exhibit a systematic deviation for mare soil around the 2 μm absorption feature. The simulated spectra can reproduce the changes around 1 μm and 3 μm, but the 2 μm band is estimated to be less flat than observed (Figure 6.12). This finding means the space weathering model does not yet comprehensively cover this particular effect, and other explanations must be considered. The simulation is grounded on the assumption that the spectrum of the soil material does not change and smFe^0 is the major contributor to space weathering-induced spectral changes. However, it is commonly known that besides smFe^0 formation, space weathering transforms a considerable amount of the mineral grains into agglutinate glass [e.g., Pieters and Noble, 2016]. These glasses exhibit a different spectral signature, which consequently affects the overall spectral shape of the soil. Tompkins and Pieters [2010] heated mineral powdered samples to generate glass and mixed them with unprocessed powdered samples. They found that an increasing amount of glass yields a flattened 2 μm band while the band depth of the 1 μm band remains unchanged. This finding likely explains the slight deviation of around 2 μm between the model prediction and the observed mature spectra. In other words, the accumulation of smFe^0 changes the overall spectral behavior, i.e., reddening, darkening, obstruction of the 1 μm feature, and partial obstruction of the 2 μm feature. However, to fully explain the observed flattening of the 2 μm band in mare regions, the formation of agglutinate glass has to be taken into account. In Figure 6.13 (left), the point cloud has a large horizontal spread. When analyzing the spectra, it was found that several fresh spectra (No. 17, 23, 49, 72, 73, 74) exhibit an exaggerated “upturn” for wavelengths exceeding 2.5 μm. This signature indicates the presence of a thermal emission component that the temperature correction has not properly removed. A possible explanation might be that localized imperfect surface slope estimation at the small craters’ positions cannot be well resolved in the M^3 images. A residual thermal emission component would fill the 3 μm band, underestimating the $\mathrm{IBD}_{3\mu\mathrm{m}}$ parameter. These effects can explain the outliers in the dashed red circle in Figure 6.13 (left).

Chapter 7

Contribution 3: Reflectance modelling for Mercury telescopic observations

This chapter and all figures have been taken from or adapted from Wohlfarth and Wöhler [2022]. The results have also been presented at the Mercury 2022 conference [Wohlfarth and Wöhler, 2022]. The results for the realistic cases have been reprocessed so that the numerical values differ from the original publication.

7.1 Introduction

Systematic changes in the normalized spectral slope are consistently reported in telescopic measurements and have initially been ascribed to a wavelength-dependent photometric function [Warell, 2002, 2003]. In a subsequent study, Warell and Blewett [2004] concluded that the body's photometric behavior cannot explain the relationship between illumination and observation geometry and the spectral slope. Consequently, the effect remains unexplained. A detailed discussion about the correction of atmospheric absorption bands is given by Erard et al. [2011], but surprisingly, atmospheric seeing has received only moderate attention in all telescopic studies. Warell [2004] and Warell and Blewett [2004] modeled seeing with a Gaussian point spread function (PSF) that is constant over all wavelength regions. However, seeing is well known to depend on the wavelength, as discussed in detail by Boyd [1978]. Kolmogorov turbulence theory suggests that the seeing disk decreases by FWHM $\propto \lambda^{-1/5}$ [Boyd, 1978]. For longer wavelengths, the visible disk may appear smaller. If a spectrum is now sampled near the limb or the terminator, a stronger signal will be present in the shorter wavelengths, effectively changing the spectral slopes. Therefore, wavelength-dependent seeing may explain these systematic spectral slope changes across Mercury. Erard et al. [2011] applied an atmospheric model to correct the atmospheric absorption bands but did not discuss or model wavelength-dependent seeing effects.

The author took two approaches to analyze the influence of wavelength-dependent seeing: In the first step, an idealized observation scenario was simulated. The second step simulated Mercury with known reflectance data from the MESSENGER mission for known scenarios.

This study gives a rare chance for an astronomical analysis to evaluate the hypothesis with the actual ground truth of the celestial target. The reflectance simulation utilized the global photometrically normalized map derived from MDIS data and reproduced the observation scenarios of four different telescopic campaigns (see Table 4.4). The Hapke and Kaasalainen-Shkuratov (KS) models were inverted to extract the albedo (single scattering albedo w for the Hapke model and normal albedo $A_{\vec{n}}$ for the KS model) from the mosaic while keeping the remaining photometric parameters fixed and assuming standard geometry. Then, the Hapke or KS models were applied to simulate any photometric geometry. Subsequently, a simple wavelength-dependent seeing model simulated the atmosphere. This procedure yielded the disk as seen from the Earth for a given observation scenario. Further, the normalized spectral slope was computed. The results were compared to a model with constant seeing across all wavelengths to identify the influence of wavelength-dependent seeing.

7.2 Modeling various observation conditions

This section presents the simulated disk of Mercury for an idealized scenario (section 7.3.1) and for real scenarios (section 7.3.2) as seen during the telescopic observations No. 08, 11, 12, 19, 20 that are listed in Table 4.4. These observations were used in the literature to discuss systematic slope variations. The simulations are based on the global MDIS mosaic from Becker et al. [2009], which contains photometrically normalized reflectance values of the narrow-band channels F, G, and I with center wavelengths of 996.2 nm, 748.7 nm, and 433.2 nm. In the ideal scenario, the author modeled a spherical planet viewed under a phase angle (Sun-object-Earth) of $g = 90°$. Consequently, the observer on Earth observes a disk with an illuminated fraction of 50%. To exclude global spectral variations, the model assumed constant albedo derived from the globally averaged single scattering albedo w from the MDIS mosaic for each wavelength channel. Subsequently, the Hapke model took the remaining model parameters from Table 7.1 and output the reflectance. The results were then orthographically projected to obtain the reflectance of the disk. In the ideal scenario, the author derived the spectral slope between 996.2 nm and 433.2 nm, normalized the spectral slope to 433.2 nm, and applied constant seeing and wavelength-dependent seeing as described in Section 3.6.3. The ratio between the normalized spectral slopes for wavelength-dependent seeing and constant seeing was computed to determine the influence of wavelength-dependent seeing. All steps were repeated with the KS3 model, which required the globally averaged normal albedo $A_{\vec{n}}$ from the MDIS mosaic and utilized the KS3 parameters given in Table 7.2. The reflectance mosaic was downsampled for any realistic observation scenario and projected orthographically. Applying the Hapke model with the parameters from Table 7.1 and the disk-resolved albedo yielded realistic reflectance values. The wavelength-dependent seeing model described in Section 3.6.3 addressed atmospheric effects. Finally, the spectral slopes between the 996.2 nm, and 433.2 nm channels were computed and normalized to 433.2 nm. Again, the simulation of the realistic scenarios was repeated with the KS3 model, using the disk-resolved average albedo and the parameters from Table 7.2.

Table 7.1. Hapke parameters for Mercury [Domingue et al., 2016]

parameter	description	F (430 nm)	G (750 nm)	I (1000 nm)
ξ	DHG-function; asymmetry	0.1551	0.1223	0.1339
c*	DHG-function;	0.7478	0.8542	0.6642
$\overline{\theta}$	roughness	14.6013°	14.2707°	14.0050°

Table 7.2. KS3 model parameters for Mercury [Domingue et al., 2016]

parameter	description	F (430 nm)	G (750 nm)	I (1000 nm)
a	phase function exponent	0.6363	0.5628	0.5200
c_l	disk function weight	0.6293	0.6424	0.6303

7.3 Results

7.3.1 Simulation of ideal scenario

In the first step, the author considered an idealized scenario with a predefined phase angle of $g = 90°$ and an angular diameter of $AD = 7$ arcsec. Therefore, three channels were considered that contain the average albedo of the MDIS channels centered at 996.2 nm, 748.7 nm and 433.2 nm. The photometric parameters of the Hapke model are given in Table 7.1. For this geometry, the author simulated three cases: space view without seeing, terrestrial view with constant seeing (FWHM = 1.5 arcsec), and terrestrial view with wavelength-dependent seeing (FWHM = 1.5 arcsec at the shortest wavelength). For all cases, the reflectance, the spectral slope between 996.2 nm and 433.2 nm, and the spectral slope normalized to 433.2 nm were computed.

Hapke model

Without seeing, the disk's rim is sharp, and the reflectance at 996.2 nm decreases toward the terminator (Figure 7.1 left). The non-normalized spectral slope is correlated with the overall reflectance level and decreases toward the terminator (Figure 7.1 middle). The normalized spectral slope (Figure 7.1 right) exhibits spatial variations with a maximum at point B that is 18 % larger than the smallest value at point A. The color bar was adjusted to visualize this effect. This scenario is not realistic for telescopic observations because the atmosphere is missing.

With constant seeing (FWHM = 1.5 arcsec), the reflectance image exhibits the typical smooth rim of the seeing disk (Figure 7.2 left). The spectral slope decreases toward the terminator and the smooth rim (Figure 7.2 middle). The slope appears to be correlated with the reflectance. However, because of the seeing smear, parts of the signal lie outside the actual boundary of the true disk. The normalized slope in Figure 7.2 (right) exhibits variations that resemble the variations in Figure 7.1 (right) but appear enlarged. The maximum increase inside the true disk is about 11 % from point C to point D (Figure 7.2 (right)) and thus only half as large as between from A to point B (Figure 7.1 (right)). The increase between E and D (Figure 7.2 (right)) is around 15 %. This simulation indicates that constant seeing dampens the spectral slope variations within the disk due to photometry.

In the case of wavelength-dependent seeing, the reflectance at 996.2 nm leads to the same result as in Figure 7.2 (left) and is not displayed separately. For longer wavelengths, the seeing disk grows. Similar to Figure 7.2 (middle), the spectral slope decreases toward the rims of the seeing disk (Figure 7.3 (left)). However, it exhibits small negative values at the outer brink. When normalizing the spectral slopes, systematic effects become evident (Figure 7.2 (middle)). Contrary to Figure 7.2 (right), the normalized spectral slope decreases toward the entire rim of the seeing disk. The larger the FWHM of the seeing parameter becomes, the larger this transition region grows. At the brink of the rim, where the signal is already very low, there is a region with a negative slope (point F). The ratio between the normalized spectral slopes of case 2 and case 3 is given in Figure 7.3 (right). This ratio shows the spectral variations that are entirely due to wavelength dependency. The plot further indicates that the spectral slope is elevated in a C-shaped band in the west of the disk. The spectral slope at point G is 17 % steeper for wavelength-dependent seeing than constant seeing. On the other hand, the slope at point H decreases by 17 %.

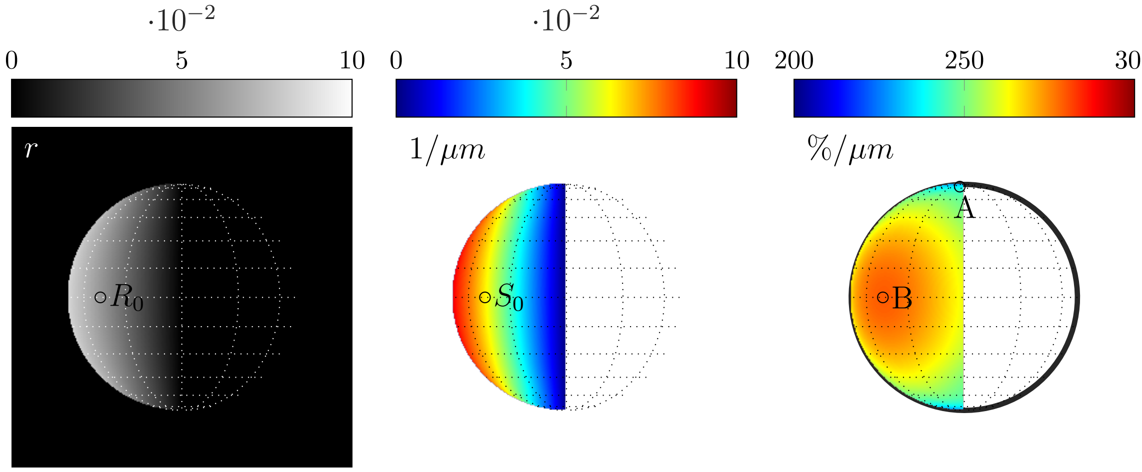

Figure 7.1. Simulated disk of Mercury for idealized case 1 (Hapke model): Space view without seeing at 1000 nm. Left: Reflectance I/J. Middle: Spectral slope (r(1000 nm)-r(430 nm))/(570 nm). Right: Normalized spectral slope (r(1000 nm)-r(430 nm))/(r(430 nm)·570 nm). Note that all plots exhibit a sharp edge between the disk and space. The values at points R_0, S_0, A, and B are compared with each other or with values of other simulation runs sampled at the same positions. For details, see the main text. Figure from Wohlfarth and Wöhler [2022].

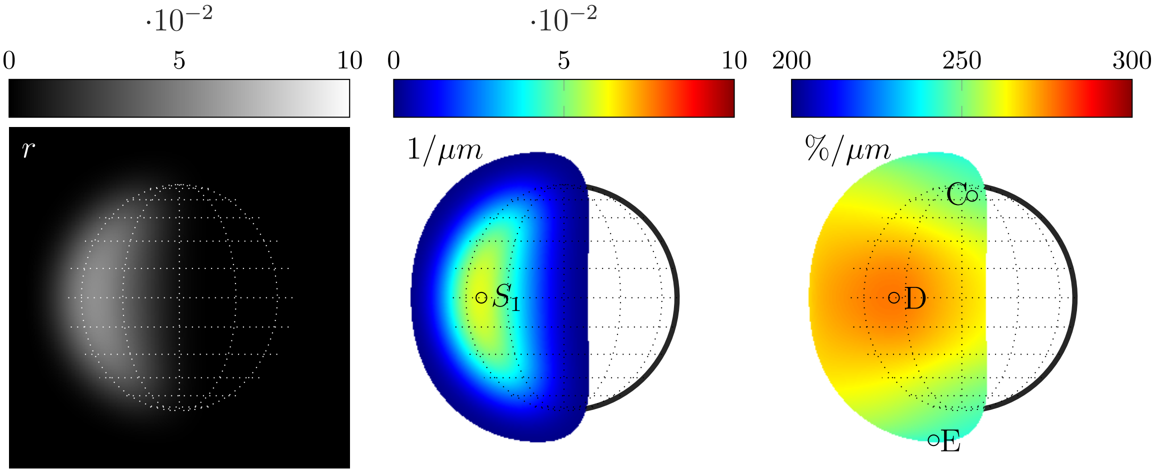

Figure 7.2. Simulated disk of Mercury for idealized case 2 (Hapke model): Terrestrial view with constant seeing at 1000 nm. Left: Reflectance I/J. Middle: Spectral slope (r(1000 nm)-r(430 nm))/(570 nm). Right: Normalized spectral slope (r(1000 nm)-r(430 nm))/(r(430 nm)·570 nm). Note that seeing yields a transition region that outgrows the true size of the disk. Values are only displayed for regions in which the signal of the reflectance map (left) exceeds 1 % of the maximum signal. The values at points S_1, C, D, and E are compared with each other or with values of other simulation runs sampled at the same positions. For details, see the main text. Figure from Wohlfarth and Wöhler [2022].

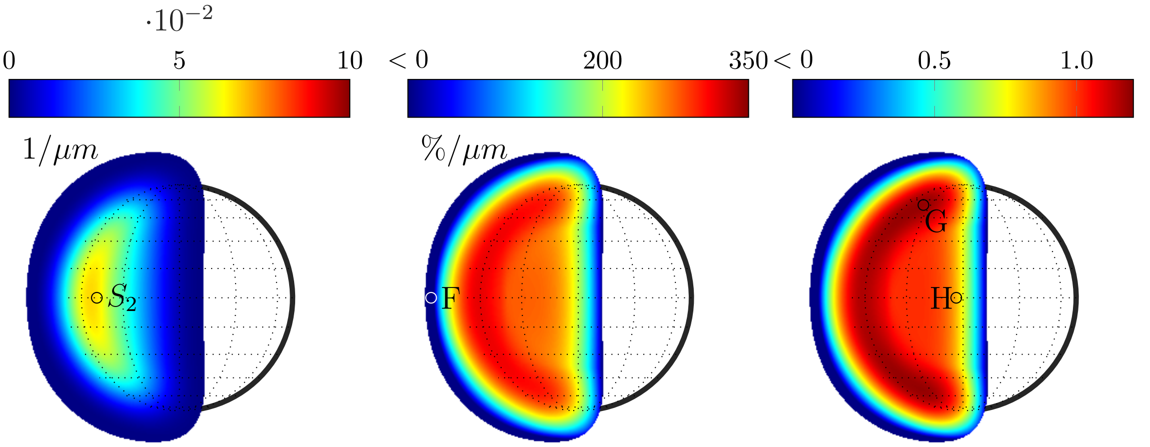

Figure 7.3. Simulated disk of Mercury for idealized case 3 (Hapke model): Terrestrial view with wavelength-dependent seeing at 430 nm. Left: Spectral slope (r(1000 nm)-r(430 nm))/(570 nm). Middle: Normalized spectral slope (r(1000 nm)-r(430 nm))/(r(430 nm)·570 nm). Note that there is a systematic change of the normalized spectral slope and even a region with negative slope values around the seeing disk. Right: Ratio between the normalized spectral slope with wavelength-dependent seeing (Figure 7.3 (middle)) and constant seeing (Figure 7.2 (right)). Values are only displayed for regions in which the signal of the reflectance exceeds 1 % of the maximum signal. The values at points S_2, F, G, and H are compared with each other or with values of other simulation runs sampled at the same positions. For details, see the main text. Figure from Wohlfarth and Wöhler [2022].

KS3 model

The entire analysis was repeated with the KS3 model. Without seeing, the reflectance predicted by the KS3 model (Figure 7.4 (left)) largely resembles the Hapke reflectance (Figure 7.1 (left)). However, the KS3 model predicts increased reflectance values for the largest emission angles near the rim. The reflectance at point R_0 in Figure 7.4 (left) is 7 % larger than at point R_0 in Figure 7.1 (left). Most parts of the disk differ by that value. However, this value increases to more than 20 %, which is very close to the limb. The spectral slope at S_0 appears to be only slightly enhanced by 3 % (compare points S_0 in Figure 7.4 (middle) and 7.1 (middle)). The maximum spectral slope near the limb is more enhanced. Surprisingly, the normalized spectral slope derived from the KS3 model does not exhibit any significant local variations, which aligns with the possibility that the spectral slope effects are not due to photometry. Points A and B differ by less than 1 %. The absence of slope variations is the most significant difference between the KS3 approach and the Hapke-based model (Figure 7.1 (right)), which predicts variations of the normalized slope by up to 18 %. In the case of constant seeing (FWHM = 1.5 arcsec), the reflectance image (Figure 7.5 (left)) and the behavior of the spectral slope (Figure 7.5 (middle)) resemble the results of the Hapke model (Figure 7.2 (left) and Figure 7.2 (middle)). However, the maximum reflectance values and the maximum slope appear enhanced for the KS3 approach (S_1 in Figure 7.2 (middle) is 7 % larger than S_1 in Figure 7.5 (middle)). Again, the normalized spectral slope remains almost constant across the entire seeing disk (Figure 7.5 (right)). In the case of wavelength-dependent seeing, the KS3 model produces results similar to those of the Hapke model. Again, the maximum spectral slope is larger than with the Hapke model, but the overall behavior is similar. The normalized spectral slope is also increased within the C-shaped region (Figure 7.6 (middle)). Finally, the ratio between the wavelength-dependent and constant seeing is displayed in Figure 7.6 (right). At point G, the normalized spectral slope is 19 % steeper for wavelength-dependent seeing than for constant seeing. On the other hand, the slope at point H decreases by 16 %. The overall behavior and the values at points G and H resemble the values from the ratio image in Figure 7.3 (right). This similarity suggests that the effect of wavelength-dependent seeing dominates the photometric variations.

In summary: The simulations based on the Hapke model suggest that the reflectance function of the surface has a systematic effect on the normalized spectral slope, flattening the spectral slope toward the poles. By contrast, the KS3 model predicts no significant variations of the normalized spectral slope caused by photometry. Generally, the KS3 model predicts steeper slopes toward the limb. Wavelength-dependent seeing leads to a systematic decrease of the normalized spectral slope around the entire seeing disk and even negative slopes at the outer brink. It is also responsible for elevated slopes in a C-shaped band near the limb and may compensate for the decrease at the poles due to the reflectance function. The normalized spectral slope for the wavelength-dependent seeing is similar, regardless of the photometric model. Consequently, seeing is the dominant cause of systematic spectral slope changes. For realistic scenarios, global albedo variations must be considered.

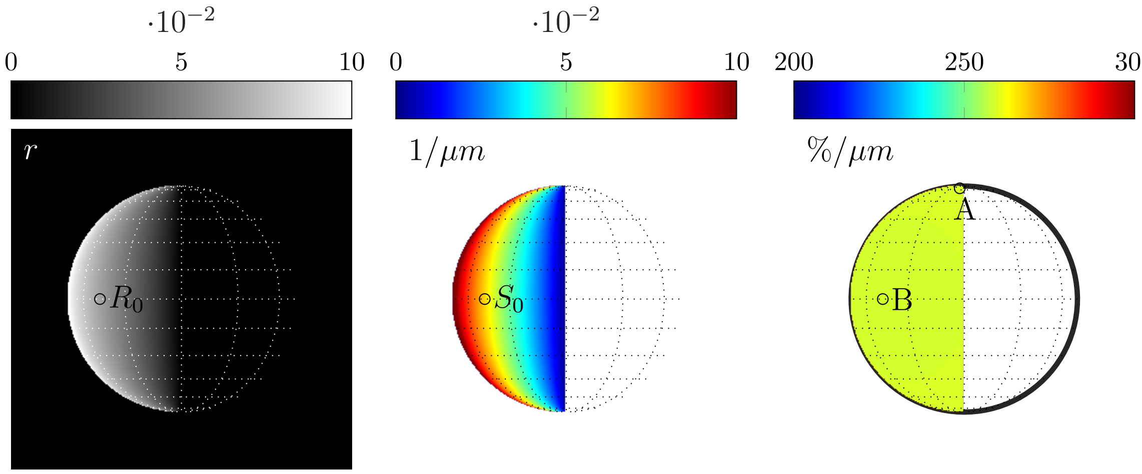

Figure 7.4. Simulated disk of Mercury for idealized case 1 (KS3 model): Space view without seeing at 1000 nm. Left: Reflectance I/J. Middle: Spectral slope (r(1000 nm)-r(430 nm))/(570 nm). Right: Normalized spectral slope (r(1000 nm)-r(430 nm))/(r(430 nm)·570 nm). Note that all plots exhibit a sharp edge between the disk and space. The values at points R_0, S_1, A, and B are compared with each other or with values of other simulation runs sampled at the same positions. For details, see the main text. Figure from Wohlfarth and Wöhler [2022].

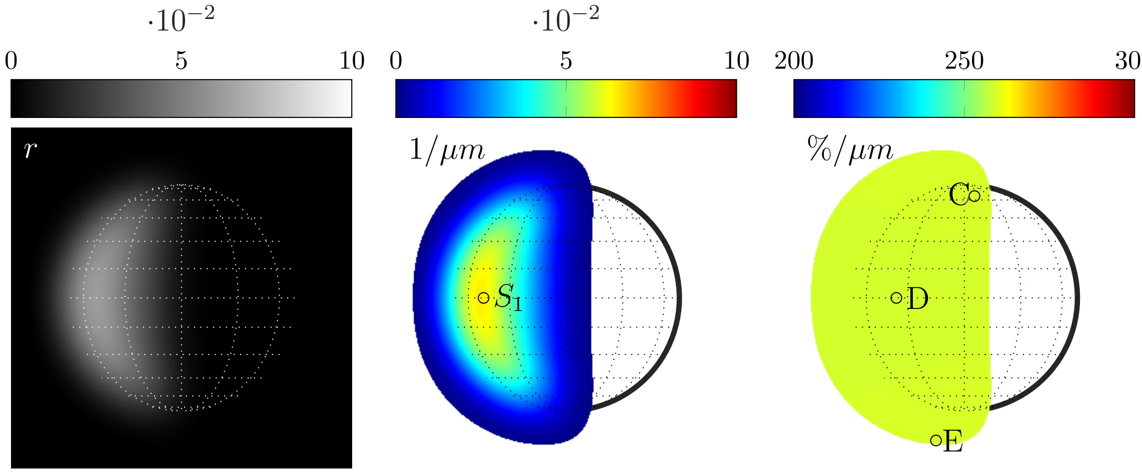

Figure 7.5. Simulated disk of Mercury for idealized case 2 (KS3 model): Terrestrial view with constant seeing at 1000 nm. Left: Reflectance I/J. Middle: Spectral slope (r(1000 nm)-r(430 nm))/(570 nm). Right: Normalized spectral slope (r(1000 nm)-r(430 nm))/(r(430 nm)·570 nm). Note that seeing yields a transition region that outgrows the true size of the disk. Values are only displayed for regions in which the signal of the reflectance map (left) exceeds 1 % of the maximum signal. The values at points S_1, C, D, and E are compared with each other or with values of other simulation runs sampled at the same positions. For details, see the main text. Figure from Wohlfarth and Wöhler [2022].

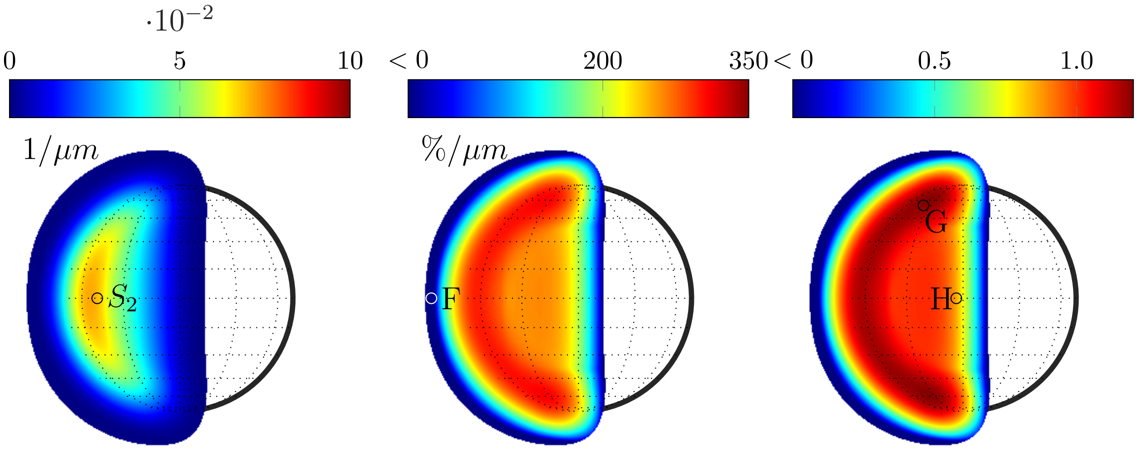

Figure 7.6. Simulated disk of Mercury for idealized case 3 (KS3 model): Terrestrial view with wavelength-dependent seeing at 430 nm. Left: Spectral slope (r(1000 nm)-r(430 nm))/(570 nm). Middle: Normalized spectral slope (r(1000 nm)-r(430 nm))/(r(430 nm)·570 nm). Note that there is a systematic change of the normalized spectral slope and even a region with negative slope values around the seeing disk. Right: Ratio between the normalized spectral slope with wavelength-dependent seeing (Figure 7.6 (middle)) and constant seeing (Figure 7.5 (right)). Values are only displayed for regions in which the signal of the reflectance exceeds 1 % of the maximum signal. The values at points S_2, F, G, and H are compared with each other or with values of other simulation runs sampled at the same positions. For details, see the main text. For details, see the main text. Figure from Wohlfarth and Wöhler [2022].

7.3.2 Simulation of previous measurement campaigns

Observations No. 08, 11, 12, and 19 (Table 4.4) are now discussed in the context of systematic slope variations. For each geometry, the author simulated the visible disk of Mercury under wavelength-dependent seeing conditions and compared the results to the related discussion in the literature. Observations No. 08 and 19 were considered for systematic slope variations, and observations No. 11 and 12 were considered for strong slope variations between different measurements. Again, the first simulation run was carried out with the Hapke model and later repeated with the KS3 model.

Systematic effects of the normalized spectral slopes

Warell [2003] computed the normalized spectral slope for several slit-integrated spectra of the observations from 20th and 22nd June 1999 (Observations No. 08 and 09 in Table 4.4). The normalized slope of the slit-integrated spectra was compared to the emission angle, suggesting a negative correlation. However, careful inspection of the correlation plot in Warell [2003] shows that only the spectral slope of the southernmost and the northernmost slit position appears to be significantly lower than the other slit positions. The author of the present study modeled the spectrum of June 20th and computed the normalized spectral slope for constant seeing (Figure 7.7 (middle)) and wavelength-dependent seeing (Figure 7.7 (right)). However, Warell [2003] provided no accurate information about the slit positions and the actual disk position relative to the seeing disk. It is possible that the actual disk was slightly misaligned, or its size was over-estimated, which induced uncertainty. Therefore, the author assumed two sets of approximate slit positions indicated in Figure 7.7 (middle) and Figure 7.7 (right) with solid black or dashed lines. The seeing disk in Figure 7.7 (middle)

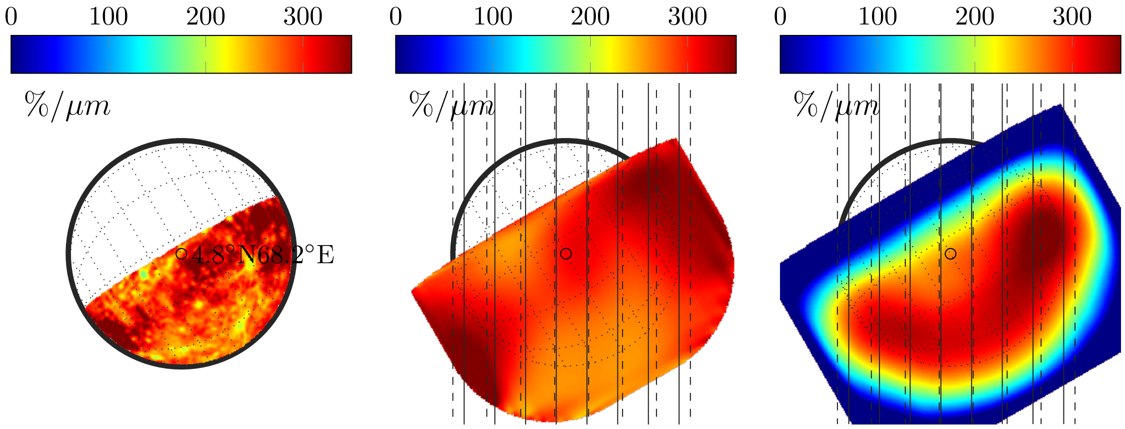

Figure 7.7. Simulated disk of Mercury for observation No. 08 (Hapke model): Left: Normalized slope (r(1000 nm)-r(430 nm))/(r(430 nm)·570 nm) without seeing. Middle: Normalized slope for constant seeing of FWHM = 1.5 arcsec with two approximate sets of slit positions from Warell [2002]. Right: Normalized slopes of slit-integrated spectra with the same slit positions for wavelength-dependent seeing. Solid and dashed black lines in (middle) and (right) indicate the slit positions. Figure adapted from Wohlfarth and Wöhler [2022].

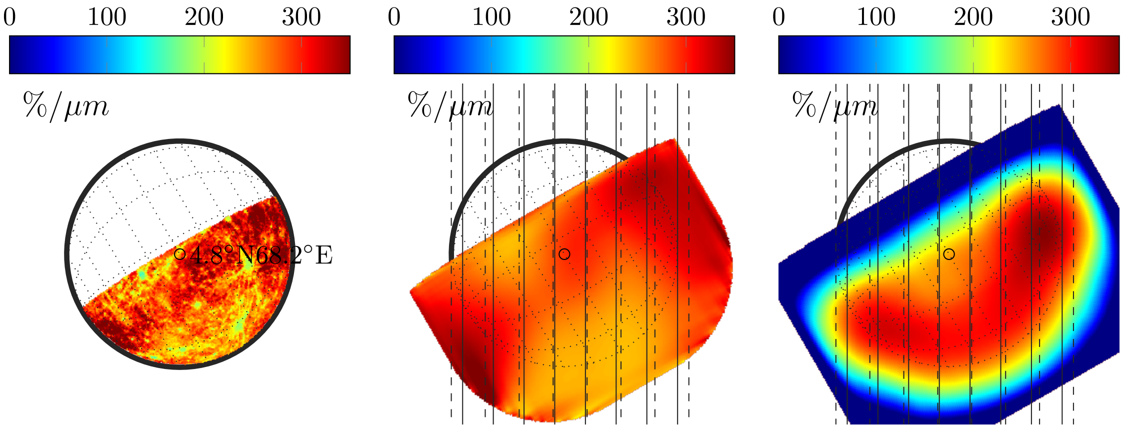

Figure 7.8. Simulated disk of Mercury for observation No. 08 (KS3 model): Left: Normalized slope (r(1000 nm)-r(430 nm))/(r(430 nm)·570 nm) without seeing. Middle: Normalized slope for constant seeing of FWHM = 1.5 arcsec with two approximate sets of slit positions from Warell [2002]. Right: Normalized slopes of slit-integrated spectra with the same slit positions for wavelength-dependent seeing. Solid and dashed black lines in (middle) and (right) indicate the slit positions. Figure adapted from Wohlfarth and Wöhler [2022].

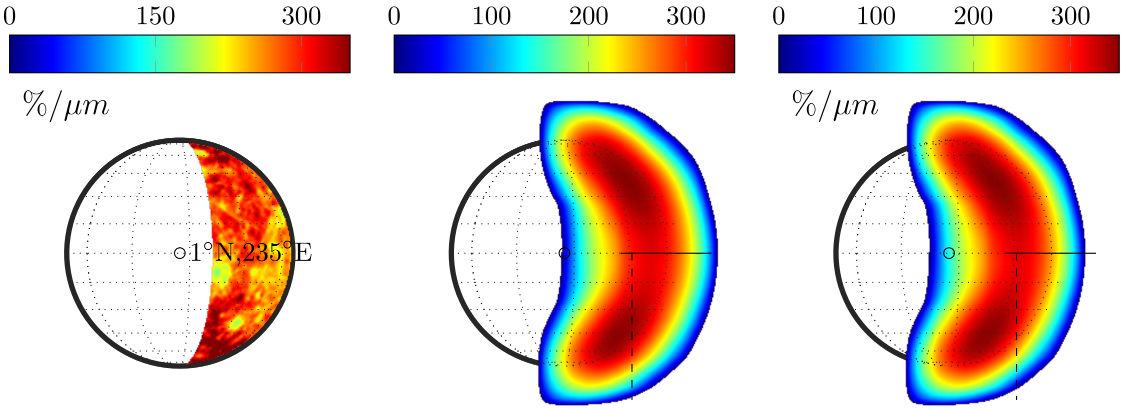

Figure 7.9. Simulated disk of Mercury for observation No. 19 (Hapke model): Left: Normalized slope (r(1000 nm)-r(430 nm))/(r(430 nm)·570 nm) without seeing. Middle: Normalized slopes for wavelength-dependent seeing. Right: Same as middle but translated to the west by 7.5 % of the angular diameter. Solid and dashed black lines in (middle) and (right) indicate the sampling regions. Figure adapted from Wohlfarth and Wöhler [2022].

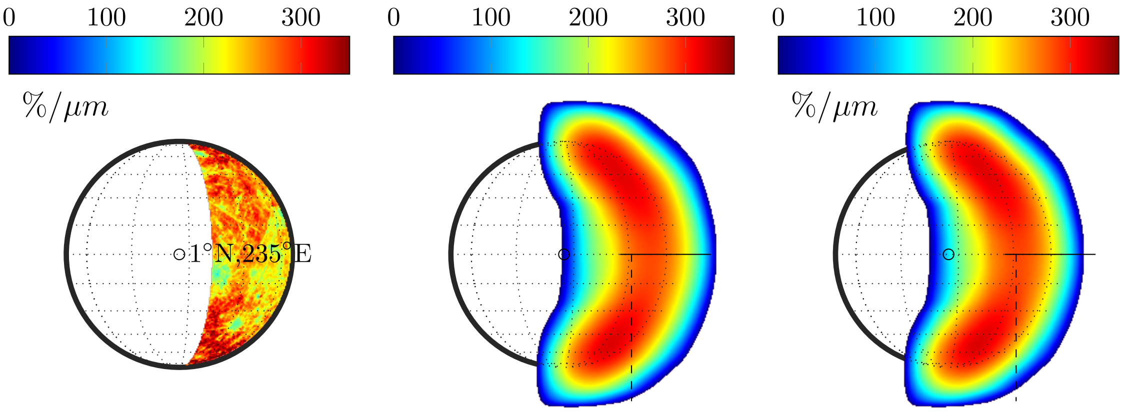

Figure 7.10. Simulated disk of Mercury for observation No. 19 (KS3 model): Left: Normalized slope (r(1000 nm)-r(430 nm))/(r(430 nm)·570 nm) without seeing. Middle: Normalized slopes for wavelength-dependent seeing. Right: Same as middle but translated to the west by 7.5 % of the angular diameter. Solid and dashed black lines in (middle) and (right) indicate the sampling regions. Figure adapted from Wohlfarth and Wöhler [2022].

is dominated by global albedo variations propagating across the actual disk. However, no systematic north-south variations are visible that resemble the photometric effect described in Section 7.3.1 (Figure 7.1 (right) and Figure 7.2 (right)). In the wavelength-dependent case, the seeing disk shows a strong systematic decrease in spectral slope toward the rim and local variations across the disk. Figure 7.11 (left) shows the normalized spectral slope of the slit-integrated profiles, assuming Hapke reflectance. The black markers represent the normalized slopes of slit-integrated spectra along the solid and dashed black line for constant seeing from Figure 7.7 (middle). Contrary to the observed scenario where there is a slope decrease toward the rim, the simulation only shows a small variation of the spectral slope of the model and even a small increase at the rim. The red markers in Figure 7.11 represent the normalized spectral slope of the slit-integrated spectra for wavelength-dependent seeing (Figure 7.7 (right)). They exhibit a significant decline at the rim, consistent with Warell [2003]. At this point, it is impossible to present a correlation plot between the spectral slope and the emission angle because the exact emission angles cannot be reproduced from Warell [2003]. The same simulation is carried out with the KS3 model. The normalized slope for various seeing conditions is shown in Figure 7.8 and resembles the results from Figure 7.7. The normalized slope of the slit-integrated spectra is given in Figure 7.11 (right) and exhibits similar trends as shown in Figure 7.11 (left): Wavelength-dependent seeing leads to a diminished slope toward the rim of the disk. In conclusion, wavelength-dependent seeing generates results consistent with the observations of Warell [2003]. A repeated study with the Hapke and the KS3 model supports that the overall trend is not primarily due to photometric modeling but is dominated by wavelength-dependent seeing.

Vernazza et al. [2010] also reported a strong negative correlation between spectral slope and emission angle. According to the geometries of observation No. 19 in Table 4.4, the author modeled the corresponding seeing disk. The illuminated region (Figure 7.9 (left)) contains the craters Beethoven, Vivaldi, and Sholem Alaichem. Figure 7.9 (middle) shows

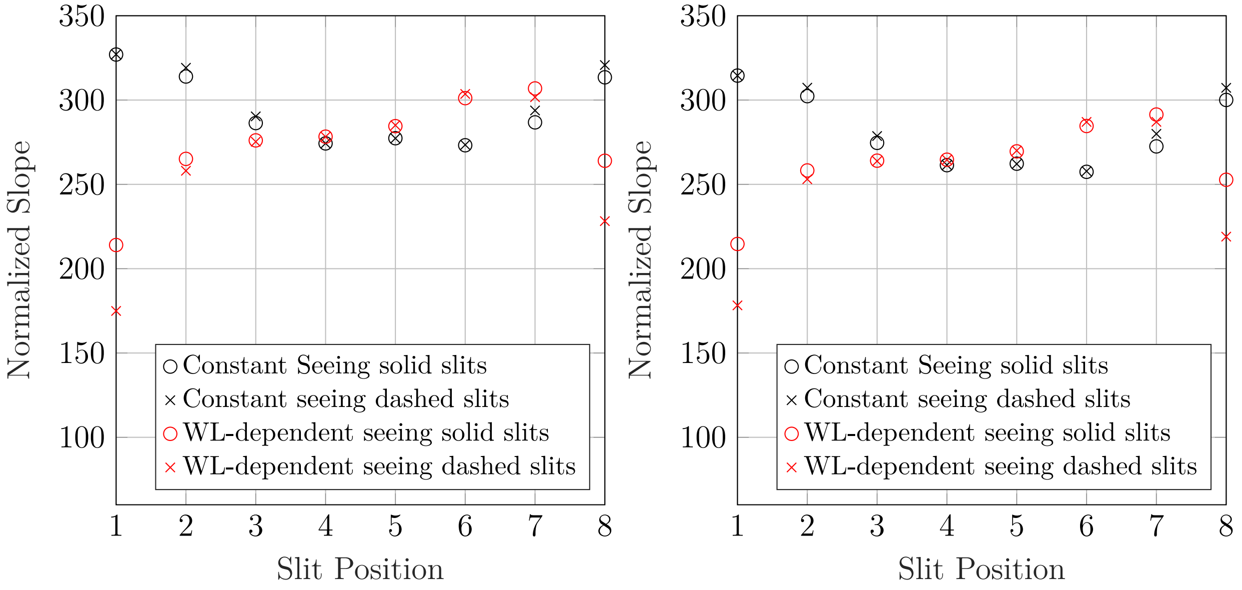

Figure 7.11. Normalized spectral slope at different slit positions of observation No. 08. Left: Normalized slope derived from eight integrated slits of observation No. 08 in Figure 7.7 (left) using the Hapke model. Slit position 1 corresponds to the westernmost slit. Right: Same simulation with the KS3 model. Figure adapted from Wohlfarth and Wöhler [2022].

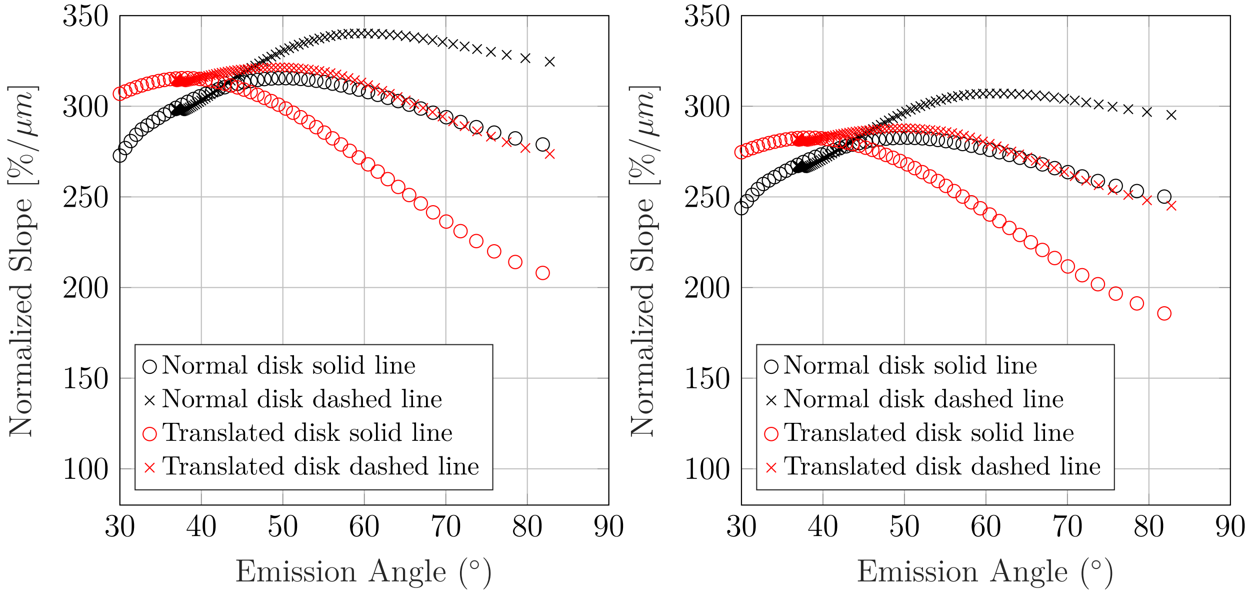

Figure 7.12. Normalized spectral slope at various locations for observation No. 19. Left: Normalized slopes of slit-integrated spectra from observation 19 in Figure 7.9 (right). Right: Same simulation with the KS3 model. Figure adapted from Wohlfarth and Wöhler [2022].

the wavelength-dependent changes of the normalized slope for a FWHM of 1.5 arcsec. A transition region encircles the seeing disk in which the spectral slope decreases. Vernazza et al. [2010] did not provide the exact alignment between the seeing disk and the emission angle. The spectral slope transition region will lie outside the projected disk if the disk is

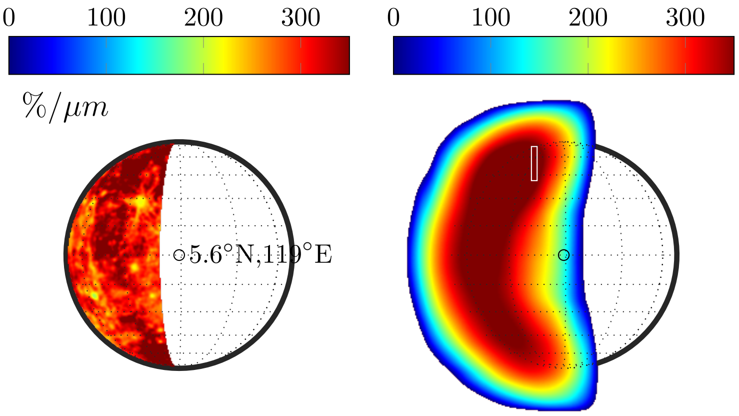

Figure 7.13. Simulated disk of Mercury for observation No. 11 (Hapke model): Left: Normalized slope (r(1000 nm)-r(430 nm))/(r(430 nm)·570 nm) without seeing. Right: Normalized slope for wavelength-dependent seeing with approximate slit position according to Warell et al. [2006]. The box indicates the slit position. Figure adapted from Wohlfarth and Wöhler [2022].

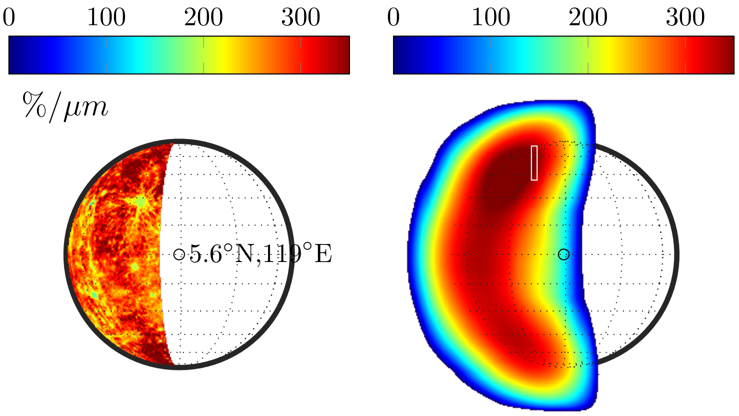

Figure 7.14. Simulated disk of Mercury for observation No. 11 (KS3 model): Left: Normalized slope (r(1000 nm)-r(430 nm))/(r(430 nm)·570 nm) without seeing. Right: Normalized slope for wavelength-dependent seeing with approximate slit position according to Warell et al. [2006]. The box indicates the slit position. Figure adapted from Wohlfarth and Wöhler [2022].

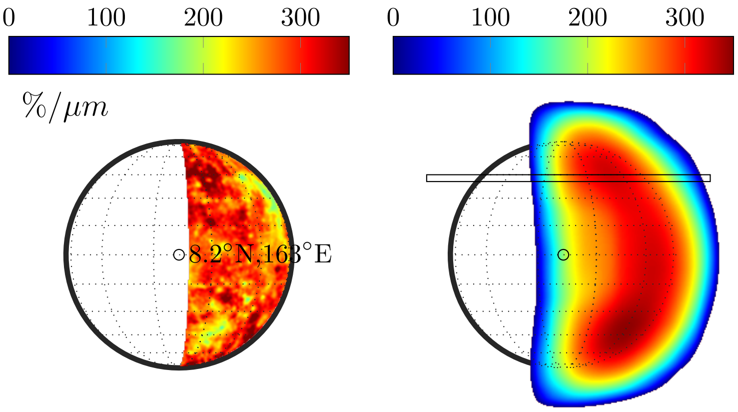

Figure 7.15. Simulated disk of Mercury for observation No. 12 (Hapke model): Left: Normalized slope (r(1000 nm)-r(430 nm))/(r(430 nm)·570 nm) without seeing. Right: Normalized slope for wavelength-dependent seeing with approximate slit position according to Warell et al. [2006]. The box indicates the slit position. Figure adapted from Wohlfarth and Wöhler [2022].

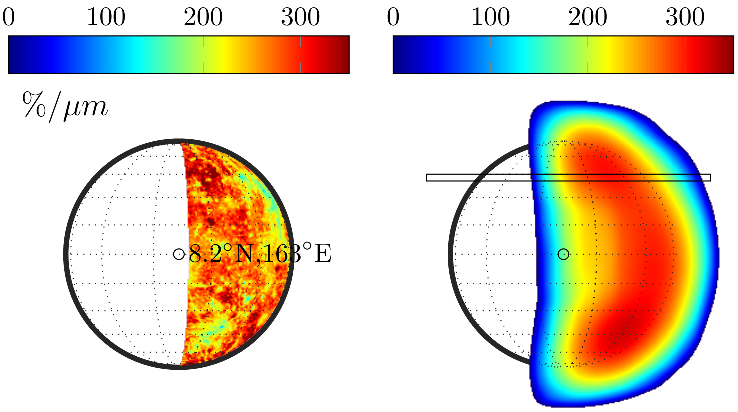

Figure 7.16. Simulated disk of Mercury for observation No. 12 (KS3 model): Left: Normalized slope (r(1000 nm)-r(430 nm))/(r(430 nm)·570 nm) without seeing. Right: Normalized slope for wavelength-dependent seeing approximate slit position according to Warell et al. [2006]. The box indicates the slit position. Figure adapted from Wohlfarth and Wöhler [2022].

perfectly mapped. In this case, the profiles show no meaningful correlation between emission angle and spectral slope. Figure 7.12 (left) displays the relationship (black symbols) between the spectral slope and the emission angle at the indicated profiles in Figure 7.9. However, Vernazza et al. [2010] stated that there is an uncertainty of 10°–20° in the emission angle due to uncertainty of the observation slit's position. The relationship between the emission angle and the spectral slope appears very sensitive to the exact alignment. Uncertainty of the slit position, misalignment, or disk distortion through atmospheric turbulence may cause the disk's rim and the spectral slope transition zone to fall together. Therefore, the author simulated the potential impact of these effects by a small translation. Shifting the disk by just 7.5 % of the angular diameter, which corresponds to roughly 13 ° in emission angle at the center of the disk, already leads to a significant inverse correlation between the emission angle and normalized spectral slope. The shifted disk is seen in Figure 7.9 (right), and the relationship between the emission angle and the slope is plotted in red in Figure 7.12 (left). This observation holds, considering the center of the visible part toward the limb, but the spectral slope also decreases toward the terminator. However, the emission angle remains around 10°–20°, so no relationship between the emission angle and spectral slope can be confirmed in this region. Figure 7.10 shows the disk derived from the KS3 model, and Figure 7.12 (right) presents the slope analysis. The slit-integrated normalized spectral slope behaves similarly to Figure 7.12 (left), but the slope is slightly lower. The study of Vernazza et al. [2010] did not explicitly discuss the spectral slope near the terminator. The work of Warell [2003] only presented slit-integrated spectra that do not resolve the region around the terminator. Therefore, whether the simulation around the terminator is inconsistent with the observations is unclear. The assumption of slit uncertainty, misalignment, or distortion can reproduce the alleged correlation between emission angle and spectral slope for the given profiles. Consequently, the actual cause for a decreasing normalized spectral slope may be rooted in wavelength-dependent seeing and the sampling position on the seeing disk instead of an effect controlled by the emission angle.

Slope differences between observations

Warell et al. [2006] presented SpeX measurements from June 2002 in the north (see Table 4.4 observation No. 11) and August 2003 in the north and the south of Mercury (see Table 4.4 observations No. 12 and 13). The spectra of these measurements exhibited different normalized slopes and were discussed by Vernazza et al. [2010] and Erard et al. [2011]. The spectral slope from the 2002 measurement especially appears to be comparatively steep. The author simulated the normalized spectral slopes of observations No. 11 and 12 from Table 4.4 and analyzed whether the MDIS data combined with the seeing model can explain the different spectral slopes. The parts of Mercury that were visible during the 2002 measurement (Figure 7.13 (left)) and the 2003 measurement (Figure 7.15 (left)) appear patchy and exhibit considerable variations of the spectral slopes. Further, the author simulated the wavelength-dependent seeing of both observation geometries and indicated the approximate sampling slit positions from Warell et al. [2006]. The slit-integrated spectra at the approximate positions from Warell et al. [2006] yield a higher spectral slope (370.58 % μm) in the 2002 measurements

(Figure 7.13 (right)) compared to the spectral slope (226.14 % μm) for the slit in 2003 (Figure 7.15 (right)). The average simulated spectral slope of observation 19 [Vernazza et al., 2010] along the lines indicated in Figure 7.9 (middle) is 260.21 % μm in the west-east-direction and 268.23 % μm in the north-south-direction (for the Hapke model). Hence, the simulated normalized spectral slope of the 2002 measurement appears to be comparatively steep, similar to the observations. Therefore, the model can consistently explain the slope differences between the measurements of 2002 and 2003 that are presented by Warell et al. [2006] and Vernazza et al. [2010]. Given the MDIS data without seeing, there is no clear indication that the side present in 2002 has a steeper spectral slope than the visible side in 2003. Only the combination of local photometric properties, wavelength-dependent seeing, and sampling position leads to the observed variations. However, there is considerable uncertainty in the position of the slit and potential airmass differences [e.g. Marsset et al., 2020] between the campaigns that weaken the commensurability. If the slit is located further to the east, the spectral slope of the 2002 measurement will decrease. Further to the west, it will increase. Repeating the simulation with the KS3 model leads to similar behavior (see Figure 7.14 and Figure 7.16). The normalized spectral slope in the 2002 measurement is 343.31 % μm, and the spectral slope in the 2003 measurement is significantly lower (211.64 % μm).

7.4 Discussion

Hapke modeling in Section 7.3.1 indicates that photometric effects under constant seeing flatten the normalized spectral slope near the poles. This effect mainly occurs in the north-south direction and seems to vanish for realistic albedo distributions, as shown in Figure 7.7 (middle). Wavelength-dependent seeing yields a transition zone that encircles the seeing disk in which the spectral slope decreases and eventually becomes negative. The normalized spectral slope is enhanced near the limb by approximately 15 %. Repeating the simulations with the KS3 model leads to a similar behavior. However, contrary to the Hapke approach, the normalized spectral slope for constant seeing does not change with the KS3 model. From the analysis of Figure 7.3 and Figure 7.6, it can be concluded that wavelength-dependent seeing is the dominant effect on the normalized spectral slope.

The studies of Warell [2002], Warell [2003], Vernazza et al. [2010], and Erard et al. [2011] reported a relationship between emission angle and normalized spectral slope. Section 7.3.2 showed that wavelength-dependent seeing can reproduce systematic slope variations for the geometries of observation No. 08. Wavelength-dependent seeing leads to a decreasing spectral slope near the rims of the seeing disk, which could not be described by photometry for this observation geometry. Most notably, the spectra slope of observation No. 19 appears sensitive to the disk alignment. Uncertainty in the slit position, small misalignment, or distortion due to the atmospheric turbulence was modeled with a small translation that already causes a significant correlation between the assumed emission angle and spectral slope. However, the simulation suggests a decrease in the spectral slope near the terminator that Vernazza et al. [2010] did not report explicitly. The presumed correlation between the emission angle and the normalized spectral slope is possibly a false correlation due to slight misalignment by various causes. Changes in the normalized spectral slope might be caused by sampling a seeing disk that has been affected by wavelength-dependent seeing. Further, Section 7.3.2 found that the combined MDIS mosaic and seeing model can explain a relatively steep spectral slope sampled from observation No. 11 compared to observations No. 12 and 19. However, the spectral slope depends on the exact slit position, and the observations were carried out under possibly different atmospheric conditions, which generally limits the commensurability. In general, a telescopic campaign dedicated to analyzing the spectral slope distribution of Mercury would greatly improve the understanding of the effects.

Spectral slopes result from three intricate physical processes: Actual global spectral slope variations, photometric effects, and wavelength-dependent seeing. Consequently, any telescopic study of Mercury dealing with spectral slopes, such as mineralogic and space weathering analysis, must be carried out carefully. It is essential to separate the photometric and the seeing effects to avoid over-interpretation of the observations. Due to seeing, the normalized slope may be too large near the limb or too flat at the rim of the seeing disk. Therefore, the spectra of the MDIS instrument provide a more reliable source than the telescopic spectra.

This study solely deals with reflectance spectra, but the effects of wavelength-dependent seeing may also affect the shape of thermal emission spectra at longer wavelengths. Among others, the local temperature and surface roughness control the thermal emission of a planetary body. Roughness alters the thermal emission such that it deviates from a single Planck function and may increase or decrease according to the observation geometry. For a Mercury-like observation geometry, the signal will become weaker near the limb and is enhanced near the terminator. In these regions, wavelength-dependent seeing also plays a role. Consequently, thermal emission near the limb would be an intricate function of roughness effects and additional seeing effects. Both effects would result in a distorted spectral emission that reduces the applicability of simple thermal models in the region.

Chapter 8

Conclusion and outlook

This chapter has partly been adopted from Wohlfarth et al. [2023], Wohlfarth et al. [2019], and Wohlfarth and Wöhler [2022] and extended by new findings.

8.1 Thermal model

The first contribution (Chapter 5) characterized, validated, and applied a combined reflectance and thermal emission model for airless planetary bodies. The thermal model comprises rough fractal surfaces, self-heating, self-scattering, and realistic albedos. The matrix-vector formalism and the numerical implementation accelerate the computation time, so that the model can process entire planetary disks with all effects on fractal surfaces.

First, section 5.4.1 characterized the thermal model behavior under various geometries. It becomes clear that surface roughness leads to thermal beaming for small azimuth angles and lower signals for large azimuths. In the nadir view, surface roughness enhances the emitted radiance for large solar incidence angles.

Sections 5.4.2 and 5.4.3 validated the model with lunar measurements acquired by the Gaofen-4 weather satellite and the Diviner lunar radiometer. GF-4 measured the disk-resolved Moon in the MIR around 3.77 μm, providing two lunar disks under phase angles of $-30.99°$ and $26.92°$, respectively. The radiances resulting from the model and the measured radiances agree nearly exactly in most parts of the lunar disk. However, slight deviations occur in regions associated with titanium-rich mare material and brighter regions, such as the ejecta blanket of Copernicus. Both cases might be explained by underconstrained single scattering albedo input for this composition. The best-fit roughness parameters are $\overline{\theta} = 21.671° \pm 0.007°$ (July 25, 2018) and $\overline{\theta} = 22.870° \pm 0.008°$ (July 30, 2018), which equals an RMSL of $22.410° \pm 0.007°$ and $23.476° \pm 0.007°$, respectively. The relative error measured across all sixteen profiles (see Figures 5.3 and 5.3) is approximately 2.7 %, with no profile exceeding 4.40 %. The disk-averaged error is in the same range (2.8 %). A roughness of $\overline{\theta} = 20°$ well approximates Diviner nadir observations. To match the Diviner EPF measurements, roughness values of $\overline{\theta} = 19°$–$37°$ are necessary with an average around $\overline{\theta} \approx 30°$. The roughness derived from the EPF measurements agrees with the work of Bandfield et al.

[2015] and other studies such as Rozitis and Green [2011], Rubanenko et al. [2020], and Müller et al. [2021]. Even though the modeling results are internally consistent, there are systematic deviations between GF-4 and nadir measurements on the one hand and Diviner EPF data on the other hand. This result is also comparable to Bandfield et al. [2015]. Section 5.5 discusses various reasons and concludes that the anisotropic emissivity deviates depending on the geometry and the wavelength.

This finding calls for more theoretical and laboratory work to provide more realistic emissivity models in the future. One direction would be to analyze sub-surface thermal gradients and attempt radiative transfer modeling, comparable to Millán et al. [2011] and Bowkunnyj [2021] in the thermal infrared and Yang and Burgdorf [2022] in the microwave region.

Section 5.4.4 used the new thermal model to reprocess the M^3 radiance measurements of the lunar surface to analyze the 2.8–3.0 μm absorption band that indicates the presence of surficial OH/H_2O. The simulations showed that a roughness value of $\overline{\theta} = 22°$ is realistic for the M^3 wavelengths and configurations. The results clearly show the diurnal variations of the integrated band depth of the 3 μm absorption band. The updated results show more clearly the latitudinal variations with deeper absorption bands toward the lunar poles, which agrees with recent studies (e.g., Honniball et al. [2020] and Laferriere et al. [2022]). The dichotomy between maria and highlands is also visible, where the diurnal amplitude appears stronger for maria than for highlands.

Section 5.4.5 compared the thermal modeling results to lunar measurements at 7–14 μm that MERTIS acquired during a swing-by maneuver. The modeled radiance agrees with how the measured radiance changes across the lunar disk. However, near the resolution limit, the effects of a point spread function had to be considered, which led to an ill-posed problem but provided accurate fits that conform with roughness values between $\overline{\theta} = 25°$–$30°$. Due to observational constraints, the spectral resolution was limited to four broad channels. The emissivity values in these channels are consistent with the emissivity spectra of silicate mineralogy.

In preparation for MERTIS emissivity analysis, section 5.4.5 also simulated the thermal emission for Mercury under phase angles of 0° and 120°. This simulation points out the cases in which the thermal roughness model deviates most strongly from smooth thermal models and a single Planck function. In opposition configuration, the thermal limb brightening becomes evident because the facets tilted toward the Sun are also tilted toward the observer. The limb thus appears hotter than predicted by a smooth model. At large phase angles, the observer sees more shadows, which makes the surface seem colder. In both configurations, the simulated thermal emission does not follow a single Planck function anymore. These effects will be further investigated for Mercury with BepiColombo.

In preparation for MERTIS thermophysical analysis, section 5.4.5 tailored a heat-conduction model to Mercury and simulated the dayside and nightside temperatures, which generally agrees with other studies. Mercury's high eccentricity and its 3:2 spin-orbit coupling cause a complex thermal pattern across the dayside and the nightside. A future step for MERTIS data analysis, as well as better modeling, will be a combination of thermal roughness and heat-conduction models. Such a model can help to derive thermophysical parameters of Mercury, such as the heat conductivity and thermal inertia [Hayne et al., 2017; Bauch et al., 2021], the grain size [Gundlach and Blum, 2013], and the surface roughness. Further model application would be the analysis of the thermal environment of polar craters to assess polar deposits [Paige et al., 2013; Chabot et al., 2018; Wohlfarth et al., 2023a].

Section 5.4.6 simulated the influence of surface roughness on the thermal phase curve of the airless exoplanet LHS 3844b. The thermal model predicts that the phase curve rises by approximately 10 % near the secondary eclipse, which is detectable with the NIRSpec Instrument onboard the JWST [Zieba et al., 2023]. Subsequent studies of Tenthoff [2023] and Tenthoff et al. [2024] added the reflected component and proposed a parameter retrieval technique that likely allows extracting the planet's albedo and surface roughness. The simulations will help constrain the geophysical makeup of the planet. Coy et al. [2024] recently used the thermal model to analyze trends observed in the measurements of several airless exoplanets, and probably, the model aids data analysis within a DDT program [Redfield et al., 2024] for rocky exoplanets.

On December 1, 2024, MERTIS acquired Mercury's first thermal infrared measurements. The data is currently analyzed using the thermal roughness model. Tenthoff et al. [2025] presented the first preliminary results and model comparisons in close cooperation with the author of this thesis.

The newly devised thermal roughness model will also have many applications for future datasets from IIRS, HVM^3, and the LTM instrument. The model will help with calibration and thermal correction for lunar mineralogic analysis, hydration mapping, and accurate roughness estimates. Finally, the thermal model will be used for in-flight calibration of the infrared instruments onboard the fire detection satellites of the company Ororatech [Seifert et al., 2024]. The satellites will occasionally acquire lunar measurements, which will be compared with the modeling results to provide calibration in the model's accuracy range.

Addendum: Further, the author examined how a variable bolometric hemispherical albedo $\overline{\epsilon}_{\mathrm{h}}$ affects the thermal modeling results of the Moon and Mercury. A theoretical investigation (Section 5.6.1) confirms that a constant $\overline{\epsilon}_{\mathrm{h}} = 0.95$ is viable for the Moon. In contrast, Mercury's $\overline{\epsilon}_{\mathrm{h}}$ depends on the solar distance and incidence angle and falls significantly below unity. Equipped with these insights, the author revisited previous experiments from Sections 5.3 and 5.4. The model fits for lunar GF-4 measurements (Section 5.6.2) and Diviner EPF-functions (Section 5.6.3) remain as accurate as before (Sections 5.4.2 and 5.4.3), but the resulting model parameters are considered to be slightly more realistic. The directional-hemispherical albedo A_{dh} for the GF-4 measurements increases, bringing it in line with earlier estimates [Keihm, 1984; Vasavada et al., 2012], while surface roughness for mare and highland stays around the same ($\overline{\theta} \approx 22.6° - 26.2°$, RMSL $\approx 23.2° - 26.4°$) with only a small difference of $\Delta\overline{\theta} \approx 2°$ between mare and highlands. Diviner roughness estimates remain unchanged, but the single scattering albedo is now slightly more consistent with silicate mineral spectra. Reprocessing the M^3 global dataset with $\overline{\theta} = 25°$ and new A_{dh} estimate yields IBD$_{3\mu\mathrm{m}}$-maps

(Section 5.6.4 and Figure G.3) that show the same spatiotemporal trends as before (Figure 5.7). Only the numerical values differ, indicating a stronger dichotomy between mare and highlands in the lunar morning and evening. Fitting the new model to MERTIS lunar flyby data yields similar emissivities (ϵ_d) to the previous simulations (compare Tables 5.3 and 5.6). Forward modeling of Mercury shows that a variable $\bar{\epsilon}_\mathrm{h}$ increases the thermal emission toward the disk's center. Preliminary analyses of the author in collaboration with Tenthoff et al. [2025] empirically support the hypothesis that the bolometric hemispherical emissivity of Mercury is well below unity. In summary, setting $\bar{\epsilon}_\mathrm{h} = 0.95$ preserves fit quality for lunar datasets while getting slightly more realistic estimates for some parameters. Future studies should empirically constrain $\bar{\epsilon}_\mathrm{h}$ for different environments and explore the effects of $\bar{\epsilon}_\mathrm{h}$ at Mercury and in the context of exoplanet modeling.

8.2 Space weathering model

The second contribution (Chapter 6) presented a method based on ab initio Mie modelling and Hapke theory to simulate the spectral effects of submicroscopic iron induced by space weathering. The investigation of parameter variations unveils four phenomena: (1) The phase function $p(g)$ is double-lobed and wavelength-independent for small particles. Larger iron particles yield a complex wavelength-dependent double-lobed function. (2) The particle size causes a difference in how the shape of the spectra is changed, where smaller particles tend to redden the spectra, and large particles darken the spectra but exhibit considerable oscillations. Only the spectral average of large particles with diameters between 20–200 nm for lunar maria and 40–240 nm for lunar highlands reproduces darkening as observed in planetary spectra. The superposition of small and larger particles can describe both darkening and reddening. (3) An increasing amount of smFe^0 intensifies these effects. (4) It is found that the IBD$_{3\mu\mathrm{m}}$ parameter decreases almost linearly with the increase in the content of large iron particles, while small particles hardly change the parameter. Points (2) and (3) align with previous studies [Lucey and Riner, 2011; Trang and Lucey, 2019].

The modeled spectra were compared with thermally corrected M^3 reflectance spectra. The nanophase and microphase iron amounts were adjusted for the best RMSE fit. The results are broadly consistent with the abundance maps of Trang and Lucey [2019]. Typical sites of mare soil samples rich in pyroxene and plagioclase and highland soil samples dominated by plagioclase were sampled at spots of immature ejecta and mature soils nearby. An excellent general agreement exists between the measured spectra of mature soil and the space-weathered spectra generated by simulation. For highland spectra, nearly perfect fits can be generated for all sample locations. For mare spectra, the overall slope and the shape of the 1 μm and 3 μm domains are well reconstructed. However, the 2 μm feature is predicted to be too strong. The deviations may be explained by the additional formation of agglutinitic glass, leading to an additional flattening of the 2 μm band beyond the effect caused by smFe^0.

For mare and highland soils, the 3 μm absorption band depth as quantified by the IBD$_{3\mu\mathrm{m}}$ parameter, is only slightly affected by increasing maturity. Submicroscopic iron generated by space weathering only has a minor effect on the band depth of the 3 μm absorption band.

Hence, the $\mathrm{IBD}_{3\mu\mathrm{m}}$ parameter can be regarded as largely invariant of maturity. This makes the $\mathrm{IBD}_{3\mu\mathrm{m}}$ parameter especially suited for quantifying lunar OH/H_2O. The good agreement between the observations and the present model strongly indicates that the presence of space weathering-induced nanophase and microphase iron can fully explain the observed spectral behavior around the $3\,\mu$m absorption band.

Similar to Lucey and Riner [2011], the study finds that the iron particle size of so-called microphase iron needed to generate good fits is, on average, 200 nm. However, TEM measurements suggest that nanophase iron accumulates in vaporized rims, and the particles are closely packed. Simulations with the T-matrix method showed that clusters of nanophase can also lead to spectral darkening, which challenges the current view that only large particles darken. The new simulation might even explain the findings of Yasanayake et al. [2018], Denevi et al. [2021], and Yasanayake et al. [2024] that spectra of lunar grains with nanophase inclusions in vaporized rims are surprisingly flat.

8.3 Telescopic observations of Mercury

The third contribution (Chapter 7) revisited telescopic observations of Mercury in the near-infrared. Applying the Hapke and KS3 models to an idealized geometry indicates that wavelength-dependent seeing significantly affects the normalized slope of near-infrared reflectance spectra, regardless of the reflectance model in use. The normalized spectral slope appears to be enhanced near the limb and decreases at the edges of the blurred planetary disk. Zones appear to exist in which the spectral slope becomes negative. Re-analyzing previous telescopic campaigns shows that the observations are consistent with the wavelength-dependent seeing model allowing for some uncertainty of the slit position. The observed correlation between emission angle and normalized spectral slope described in previous studies is misleading because it can be explained by the effect of wavelength-dependent seeing. In the future, a telescopic campaign of Mercury that analyzes the normalized spectral slope will significantly enhance the understanding of this effect.

This thesis employed computational models to calibrate and understand the infrared spectra of airless planetary bodies. Thereby, it made a small contribution to the field, hopefully stimulating further research.

Bibliography

M. A. Abramson. Pattern Search Filter Algorithms for Mixed Variable General Constrained Optimization Problems. *Ph.D. thesis, Rice University*, 2002.

C. H. Acton. Ancillary data services of NASA's Navigation and Ancillary Information Facility. *Planetary and Space Science*, 44(1):65–70, 1996. doi: 10.1016/0032-0633(95)00107-7.

S. Anderl. Astronomy and Astrophysics. In P. Humphreys, editor, *The Oxford Handbook of Philosophy of Science*, chapter 31, pages 652–670. Oxford University Press, Oxford, 2016.

S. Anderl. *Dunkle Materie.* C. H. Beck, München, 2022. doi: 10.17104/9783406783623.

M. Arnaut. Unmixing of CRISM Hyperspectral Data. *Bachelor's thesis, TU Dortmund University*, 2018.

M. Arnaut. Light Scattering of Small Particles on Planetary Surfaces. *Master's thesis, TU Dortmund University*, 2021.

M. Arnaut, K. Wohlfarth, A. Grumpe, and C. Wöhler. Mineralogical Maps of Mars from Hapke Modeling and Spectral Unmixing. *50th Annual Lunar and Planetary Science Conference*, 50:2661, 2019.

M. Arnaut, K. Wohlfarth, and W. Wöhler. A Study of Hyperspectral Clustering - How to Speed Up Spectral Unmixing of Moon Mineralogy Mapper Data. *51st Annual Lunar and Planetary Science Conference*, 51:3008, 2020.

M. Arnaut, K. Wohlfarth, and C. Wöhler. The interaction between multiple nanophase iron particles changes the slope of lunar reflectance spectra. *European Planetary Science Congress 2021 , Abstract No. 770*, 2021. doi: 10.5194/epsc2021-770.

M. Arnaut, K. Wohlfarth, and C. Wöhler. Space Weathering Simulation of Interacting Nanophase Iron Particles in the Thermal Infrared Region. *53rd Lunar and Planetary Science Conference*, 53:2184, 2022.

M. Arnaut, K. Wohlfarth, and C. Wöhler. Yet Another Scattering Framework: Simulation of Light Scattering Interaction Between Spherical Particles Using the T-Matrix. *54th Lunar and Planetary Science Conference*, 54:2997, 2023.

J. L. Bandfield and A. D. Rogers. Thermal Infrared Spectral Modeling. In J. L. Bishop, J. F. Bell III, and J. E. Moersch, editors, *Remote Compositional Analysis: Techniques for Understanding Spectroscopy, Mineralogy, and Geochemistry of Planetary Surfaces*, Cambridge Planetary Science, pages 324–336. Cambridge University Press, Cambridge, 2019. doi: 10.1017/9781316888872.017.

J. L. Bandfield, P. R. Christensen, and M. D. Smith. Spectral data set factor analysis and end-member recovery: Application to analysis of Martian atmospheric particulates. *Journal of Geophysical Research: Planets*, 105(E4):9573–9587, 2000. doi: 10.1029/1999JE001094.

J. L. Bandfield, P. O. Hayne, J-P. Williams, B. T. Greenhagen, and D. A. Paige. Lunar surface roughness derived from LRO Diviner Radiometer observations. *Icarus*, 248:357–372, 2015. doi: 10.1016/j.icarus.2014.11.009.

J. L. Bandfield, M. J. Poston, R. L. Klima, and C. S. Edwards. Widespread distribution of OH/H2O on the lunar surface inferred from spectral data. *Nature Geoscience*, 11(3): 173–177, 2018. doi: 10.1038/s41561-018-0065-0.

M. Bartelmann, B. Feuerbacher, T. Krüger, D. Lüst, A. Rebhan, and A. Wipf. *Theoretische Physik 2 | Elektrodynamik*. Springer Spektrum, Berlin, Heidelberg, 2018a.

M. Bartelmann, B. Feuerbacher, T. Krüger, D. Lüst, A. Rebhan, and A. Wipf. *Theoretische Physik 4 | Thermodynamik und Statistische Physik*. Springer Spektrum, Berlin, Heidelberg, 2018b.

A. Bartsch. Lokale Analyse von lunaren Hydroxylvorkommen bezogen auf topografische und geologische Effekte. *Bachelor's thesis, TU Dortmund University*, 2020.

Basaltic Volcanism Study Project. *Basaltic Volcanism on the Terrestrial Planets*. Pergamon Press, New York, 1981. doi: 10.1007/978-3-642-54618-1.

R. W. Batterman. The Tyranny of Scales. In R. W. Batterman, editor, *The Oxford Handbook of Philosophy of Physics*, chapter 7, pages 255–286. Oxford University Press, Oxford, 2013.

K. E. Bauch, H. Hiesinger, J. Helbert, M. S. Robinson, and F. Scholten. Estimation of lunar surface temperatures and thermophysical properties: test of a thermal model in preparation of the MERTIS experiment onboard BepiColombo. *Planetary and Space Science*, 101:27–36, 2014. doi: 10.1016/j.pss.2014.06.004.

K. E. Bauch, H. Hiesinger, B. T. Greenhagen, and J. Helbert. Estimation of surface temperatures on Mercury in preparation of the MERTIS experiment onboard BepiColombo. *Icarus*, 354:114083, 2021. doi: 10.1016/j.icarus.2020.114083.

K. E. Bauch, A. Morlok, H. Hiesinger, M. P. Reitze, N. Schmedemann, A. N. Stojic, I. Weber, M. D'Amore, J. Helbert, A. Maturilli, I. Varatharajan, K. Wohlfarth, and C. Wöhler. Unmixing of Laboratory IR Spectral Reflectance Measurements of Labradorite-Enstatite-Glass Mineral Mixtures. *52nd Lunar and Planetary Science Conference*, page 1567, 2021.

K. E. Bauch, A. Morlok, H. Hiesinger, M. P. Reitze, N. Schmedemann, A. N. Stojic, I. Weber, J. H. Pasckert, M. D'Amore, J. Helbert, A. Maturilli, K. Wohlfarth, and C. Wöhler. Unmixing of Laboratory IR Spectral Reflectance Measurements of Smooth Plains Analogs. *53rd Lunar and Planetary Science Conference*, 53:1989, 2022.

K. E. Bauch, A. Morlok, H. Hiesinger, M. P. Reitze, N. Schmedemann, A. N. Stojic, I. Weber, J. H. Pasckert, M. D'Amore, J. Helbert, A. Maturilli, K. Wohlfarth, and C. Wöhler. Unmixinig of Laboratory IR Spectral Reflectance Measurements of Low-Mg Northern Volcanic Plains Analogs. *54th Lunar and Planetary Science Conference*, 54:2247, 2023.

J. Beck. Implementierung eines Verfahrens zur Erkennung von Spielkarten. *Bachelor's thesis, TU Dortmund University*, 2020.

K. J. Becker, M. S. Robinson, T. L. Becker, L. A. Weller, S. Turner, L. Nguyen, C. Selby, B. W. Denevi, S. L. Murchie, R. L. McNutt, and S. C. Solomon. Near Global Mosaic of Mercury. *AGU Fall Meeting Abstracts*, 2009:P21A–1189, 2009.

N. Bergmann. Spektrales Reddening und Darkening von planetaren Oberflächen. *Bachelor's thesis, TU Dortmund University*, 2020.

J. L. Bishop, J. F. Bell III, and J. E. Moersch, editors. *Remote Compositional Analysis: Techniques for Understanding Spectroscopy, Mineralogy, and Geochemistry of Planetary Surfaces*. Cambridge Planetary Science. Cambridge University Press, Cambridge, 2019. doi: 10.1017/9781316888872.

J. L. Bishop, C. Wöhler, K. Wohlfarth, R. L. Klima, A. Dapremont, J. Flahaut, and M. Parente. Characterizing Variations in the Hydrous Components of the Moon. *AGU Fall Meeting Abstracts*, 2022:P41A–05, 2022.

D. T. Blewett, E. I. Coman, B. R Hawke, J. J. Gillis-Davis, M. E. Purucker, and C. G. Hughes. Lunar swirls: Examining crustal magnetic anomalies and space weathering trends. *Journal of Geophysical Research: Planets*, 116(E2), 2011. doi: 10.1029/2010JE003656.

D. T. Blewett, C. M. Ernst, S. L. Murchie, and F. Vilas. Mercury's Hollows. In S. C. Solomon, L. R. Nittler, and B. J. Anderson, editors, *Mercury: The View after MESSENGER*, Cambridge Planetary Science, pages 324–345. Cambridge University Press, Cambridge, 2018. doi: 10.1017/9781316650684.013.

D. T. Blewett, B. W. Denevi, J. T. S. Cahill, and R. L. Klima. Near-UV and near-IR reflectance studies of lunar swirls: Implications for nanosize iron content and the nature of anomalous space weathering. *Icarus*, 364:114472, 2021. doi: 10.1016/j.icarus.2021.114472.

C. F. Bohren and D. R. Huffman. Absorption and Scattering by a Sphere. In *Absorption and Scattering of Light by Small Particles*, chapter 4, pages 82–129. John Wiley and Sons, Ltd, 1998. doi: 10.1002/9783527618156.ch4.

A. Bowkunnyj. Simulation der elektromagnetischen Streuung im oberen Mondregolith. *Master's thesis, TU Dortmund University*, 2021.

N. E. Bowles, B. L. Ehlmann, R. L. Klima, D. Blaney, S. Calcutt, J. Dickson, K. L. Donaldson Hanna, C. S. Edwards, R. Evans, R. Green, W. Frazier, R. Greenberger, M. A. House, C. Howe, J. Miura, C. Pieters, M. Sampson, R. Schindhelm, E. Scheller, C. Seybold, D. R. Thompson, J. Troeltzsch, T. J. Warren, K. Shirley, and J. Weinberg. The Lunar Thermal Mapper Instrument for the Lunar Trailblazer Mission. *Lunar and Planetary Science Conference*, 51:1350, 2020.

N. M. Boyd. Are Astrophysical Models Permanently Underdetermined?, 2014. URL `http://jamesowenweatherall.com/wp-content/uploads/2014/10/Boyd_SoCal_060615.pdf`. Online; accessed December 4, 2023.

R. W. Boyd. The wavelength dependence of seeing. *Journal of the Optical Society of America*, 68(7):877–883, 1978. doi: 10.1364/JOSA.68.000877.

V. Bozza, L. Mancini, and A. Sozzetti, editors. *Methods of Detecting Exoplanets: 1st Advanced School on Exoplanetary Science.* Springer International Publishing, Cham, 2016. doi: 10.1007/978-3-319-27458-4.

J. E. Bresenham. Algorithm for computer control of a digital plotter. *IBM Systems Journal*, 4(1):25–30, 1965. doi: 10.1147/sj.41.0025.

D. Buhl, W. J. Welch, and D. G. Rea. Reradiation and Thermal Emission from Illuminated Craters on the Lunar Surface. *Journal of Geophysical Research*, 73:5281, 1968. doi: 10.1029/JB073i016p05281.

Adam D. Bull. Convergence Rates of Efficient Global Optimization Algorithms. *J. Mach. Learn. Res.*, 12(null):2879–2904, November 2011.

B. J. Buratti and J. Veverka. Photometry of rough planetary surfaces: The role of multiple scattering. *Icarus*, 64(2):320–328, 1985. doi: 10.1016/0019-1035(85)90094-6.

P. K. Byrne, C. Klimczak, and A. M. C Şengör. The Tectonic Character of Mercury. In S. C. Solomon, L. R. Nittler, and B. J. Anderson, editors, *Mercury: The View after MESSENGER*, Cambridge Planetary Science, page 249–286. Cambridge University Press, Cambridge, 2018. doi: 10.1017/9781316650684.011.

F. Cakoni and D. Colton. *A Qualitative Approach to Inverse Scattering Theory.* Springer, New York, 2013. doi: 10.1007/978-1-4614-8827-9.

K. M. Cannon, A. N. Deutsch, J. W. Head, and D. T. Britt. Stratigraphy of Ice and Ejecta Deposits at the Lunar Poles. *Geophysical Research Letters*, 47(21):e2020GL088920, 2020. doi: 10.1029/2020GL088920.

M. T. Capria, F. Tosi, M. C. De Sanctis, F. Capaccioni, E. Ammannito, A. Frigeri, F. Zambon, S. Fonte, E. Palomba, D. Turrini, T. N. Titus, S. E. Schröder, M. Toplis, J.-Y. Li, J.-P. Combe, C. A. Raymond, and C. T. Russell. Vesta surface thermal properties map. *Geophysical Research Letters*, 41(5):1438–1443, 2014. doi: 10.1002/2013GL059026.

W. D. Carrier, G. R. Olhoeft, and W. Mendell. Physical Properties of the Lunar Surface. In G. H. Heiken, D. T. Vaniman, and B. M. French, editors, *Lunar Sourcebook, A User's Guide to the Moon*, pages 475–594. Cambridge University Press, Cambridge, 1991.

W. Cassidy and B. Hapke. Effects of darkening processes on surfaces of airless bodies. *Icarus*, 25(3):371–383, 1975. doi: 10.1016/0019-1035(75)90002-0.

N. L. Chabot, D. J. Lawrence, G. A. Neumann, W. C. Feldman, and D. A. Paige. Mercury's Polar Deposits. In S. C. Solomon, L. R. Nittler, and B. J. Anderson, editors, *Mercury: The View after MESSENGER*, Cambridge Planetary Science, pages 346–370. Cambridge University Press, Cambridge, 2018. doi: 10.1017/9781316650684.014.

A. R. Chowdhury, A. Banerjee, S. R. Joshi, M. Dutta, A. Kumar, S. Bhattacharya, Amitabh, S U. Rehman, S. Bhati, J. Karelia, A. Biswas, A. R. Saxena, S. Sharma, S. R. Somani, H. V. Bhagat, J. Sharma, D. N. Ghonia, B. B. Bokarwadia, and A. Parasar. Imaging Infrared Spectrometer onboard Chandrayaan-2 Orbiter. *Current Science*, 118(3):368–375, 2020. doi: 10.18520/cs/v118/i3/368-375.

P. R. Christensen, V. E. Hamilton, G. L. Mehall, D. Pelham, W. O'Donnell, S. Anwar, H. Bowles, S. Chase, J. Fahlgren, Z. Farkas, T. Fisher, O. James, I. Kubik, I. Lazbin, M. Miner, M. Rassas, L. Schulze, K. Shamordola, T. Tourville, G. West, R. Woodward, and D. Lauretta. The OSIRIS-REx Thermal Emission Spectrometer (OTES) Instrument. *Space Science Reviews*, 214(article 87), 2018. doi: 10.1007/s11214-018-0513-6.

M. Ciarniello, F. Capaccioni, and G. Filacchione. A test of Hapke's model by means of Monte Carlo ray-tracing. *Icarus*, 237:293–305, 2014. doi: 10.1016/j.icarus.2014.04.045.

R. N. Clark. Planetary Reflectance Measurements in the Region of Planetary Thermal Emission. *Icarus*, 40(1):94–103, 1979. doi: 10.1016/0019-1035(79)90056-3.

R. N. Clark. Detection of Adsorbed Water and Hydroxyl on the Moon. *Science*, 326(5952): 562–564, 2009. doi: 10.1126/science.1178105.

A. Coradini, F. Capaccioni, P. Drossart, G. Arnold, E. Ammannito, F. Angrilli, A. Barucci, G. Bellucci, J. Benkhoff, G. Bianchini, J. P. Bibring, M. Blecka, D. Bockelee-Morvan, M. T. Capria, R. Carlson, U. Carsenty, P. Cerroni, L. Colangeli, M. Combes, M. Combi, J. Crovisier, M. C. Desanctis, E. T. Encrenaz, S. Erard, C. Federico, G. Filacchione, U. Fink, S. Fonti, V. Formisano, W. H. Ip, R. Jaumann, E. Kuehrt, Y. Langevin, G. Magni, T. Mccord, V. Mennella, S. Mottola, G. Neukum, P. Palumbo, G. Piccioni, H. Rauer, B. Saggin, B. Schmitt, D. Tiphene, and G. Tozzi. Virtis: An Imaging Spectrometer for the Rosetta Mission. *Space Science Review*, 128:529–559, 2007. doi: 10.1007/s11214-006-9127-5.

B. P. Coy, J. Ih, E. S. Kite, D. D. B. Koll, M. Tenthoff, J. L. Bean, M. Weiner Mansfield, M. Zhang, Qiao Xue, E. M. R. Kempton, K. Wolhfarth, R. Hu, X. Lyu, and Wöhler. Population-level hypothesis testing with rocky planet emission data: A tentative trend in the brightness temperatures of m-earths. *arXiv*, 2024. doi: 10.48550/arXiv.2412.06573.

H. D. Curtis. *Orbital Mechanics: For Engineering Students*. Aerospace Engineering. Elsevier Science, 2015.

A. M. Dapremont, J. L. Bishop, C. Wöhler, K. S. Wohlfarth, M. Parente, R. Klima, and J. Flahaut. Comparing Thermally Corrected Spectra from the Moon Mineralogy Mapper (M3). *56th Lunar and Planetary Science Conference*, 56:2337, 2024.

B. J. R. Davidsson, H. Rickman, J. L. Bandfield, O. Groussin, P. J. Gutiérrez, M. Wilska, M. T. Capria, J. P. Emery, J. Helbert, L. Jorda, A. Maturilli, and T. G. Mueller. Interpretation of thermal emission. I. The effect of roughness for spatially resolved atmosphereless bodies. *Icarus*, 252:1–21, 2015. doi: 0.1016/j.icarus.2014.12.029.

M. C. De Sanctis, A. Coradini, E. Ammannito, G. Filacchione, M. T. Capria, S. Fonte, G. Magni, A. Barbis, A. Bini, M. Dami, I. Ficai-Veltroni, and G. Preti. The VIR Spectrometer. In C. Russell and C. Raymond, editors, *The Dawn Mission to Minor Planets 4 Vesta and 1 Ceres*, chapter 12, pages 329–369. Springer, New York, 2012. doi: 10.1007/978-1-4614-4903-4_13.

P. Debye. Der Lichtdruck auf Kugeln von beliebigem Material. *Annalen der Physik*, 335 (11):57–136, 1909. doi: 10.1002/andp.19093351103.

M. Delbo, M. Mueller, J. P. Emery, B. Rozitis, and M. T. Capria. Asteroid thermophysical modeling. In P. Michel, F. E. Demeo, and W. F. Bottke, editors, *Asteroids IV*, pages 107–128. The University of Arizona Press, Tucson, 2015. doi: 10.1353/book.43354.

B. W. Denevi, M. S. Robinson, S. C. Solomon, S. L. Murchie, D. T. Blewett, D. L. Domingue, T. J. McCoy, C. M. Ernst, J. W. Head, T. R. Watters, and N. L. Chabot. The evolution of mercury's crust: A global perspective from messenger. *Science*, 324(5927):613–618, 2009. doi: 10.1126/science.1172226.

B. W. Denevi, M. S. Robinson, A. K. Boyd, D. T. Blewett, and R. L. Klima. The distribution and extent of lunar swirls. *Icarus*, 273:53–67, 2016. doi: 10.1016/j.icarus.2016.01.017.

B. W. Denevi, N. L. Chabot, S. L. Murchie, K. J. Becker, D. T. Blewett, D. L. Domingue, C. M. Ernst, C. D. Hash, S. E. Hawkins, M. R. Keller, N. R. Laslo, H. Nair, M. S. Robinson, F. P. Seelos, G. K. Stephens, F. S. Turner, and S. C. Solomon. Calibration, Projection, and Final Image Products of MESSENGER's Mercury Dual Imaging System. *Space Science Research*, 214(article number 2), 2017. doi: 10.1007/s11214-017-0440-y.

B. W. Denevi, C. M. Ernst, L. M. Prockter, and M. S. Robinson. The Geologic History of Mercury. In S. C. Solomon, L. R. Nittler, and B. J. Anderson, editors, *Mercury: The View after MESSENGER*, Cambridge Planetary Science, chapter 6, pages 144–175. Cambridge University Press, Cambridge, 2018. doi: 10.1017/9781316650684.007.

B. W. Denevi, C. N. Yasanayake, B. L. Jolliff, S. J. Lawrence, T. Hiroi, and A. C. Martin. The Spectral Characteristics of Lunar Agglutinates. *Lunar and Planetary Science Conference*, 52:2368, 2021.

H. Diamond-Lowe, D. Charbonneau, M. Malik, E. M.-R. Kempton, and Y. Beletsky. Optical Transmission Spectroscopy of the Terrestrial Exoplanet LHS 3844b from 13 Ground-based Transit Observations. *The Astronomical Journal*, 160(4):188, 2020. doi: 10.3847/1538-3881/abaf4f.

D. L. Domingue, C. R. Chapman, R. M. Killen, T. H. Zurbuchen, J. A. Gilbert, M. Sarantos, M. Benna, J. A. Slavin, D. Schriver, P. M. Trávníček, T. M. Orlando, A. L. Sprague, D. T. Blewett, J. J. Gillis-Davis, W. C. Feldman, D. J. Lawrence, G. C. Ho, D. S. Ebel, L. R. Nittler, F. Vilas, C. M. Pieters, S. C. Solomon, C. L. Johnson, R. M. Winslow, J. Helbert, P. N. Peplowski, S. Z. Weider, N. Mouawad, N. R. Izenberg, and W. E. McClintock. Mercury's Weather-Beaten Surface: Understanding Mercury in the Context of Lunar and Asteroidal Space Weathering Studies. *Space Science Reviews*, 181(1):121–214, 2014. doi: 10.1007/s11214-014-0039-5.

D. L. Domingue, B. W. Denevi, S. L. Murchie, and C. D. Hash. Application of multiple photometric models to disk-resolved measurements of Mercury's surface: Insights into Mercury's regolith characteristics. *Icarus*, 268:172–203, 2016. doi: 10.1016/j.icarus.2015.11.040.

K. L. Donaldson Hanna, B. T. Greenhagen, W. R. Patterson, C. M. Pieters, J. F. Mustard, N. E. Bowles, D. A. Paige, T. D. Glotch, and C. Thompson. Effects of varying environmental conditions on emissivity spectra of bulk lunar soils: Application to Diviner thermal infrared observations of the Moon. *Icarus*, 283:326–342, 2017. doi: 10.1016/j.icarus.2016.05.034.

D. S. Ebel and S. T. Stewart. The Elusive Origin of Mercury. In S. C. Solomon, L. R. Nittler, and B. J. Anderson, editors, *Mercury: The View after MESSENGER*, Cambridge Planetary Science, pages 497–515. Cambridge University Press, Cambridge, 2018. doi: 10.1017/9781316650684.019.

A. Egel, L. Pattelli, G. Mazzamuto, D. S. Wiersma, and U. Lemmer. CELES: CUDA-accelerated simulation of electromagnetic scattering by large ensembles of spheres. *Journal of Quantitative Spectroscopy and Radiative Transfer*, 199:103–110, 2017. doi: 10.1016/j.jqsrt.2017.05.010.

B. L. Ehlmann, R. L. Klima, C. C. Seybold, A. T. Klesh, M. H. Au, H. A. Bender, C. L. Bennett, D. L. Blaney, N. Bowles, S. Calcutt, D. Copley-Woods, J. L. Dickson, K. Djotni, K. Donaldson Hanna, C. S. Edwards, R. Evans, E. Felder, R. Fogg, R. O. Green, G. Hawkins, M. House, S. Islas, G. Lantoine, S. Linch, T. McCaa, I. McKinley, T. F. Merkley, J. K. Miura, C. M. Pieters, W. Santiago, E. Scire, R. Sherwood, K. Shirley, C. Smith, M. Sondheim, P. Sullivan, J. Temples, D. R. Thompson, K. I. Waldorff, W. R. Williamson, T. J. Warren, J. L. Wood, and S. Zareh. Nasa's lunar trailblazer mission: A pioneering small satellite for lunar water and lunar geology. In *2022 IEEE Aerospace Conference (AERO)*, pages 1–14, 2022. doi: 10.1109/AERO53065.2022.9843663.

N. Elkhouly. Tailoring a Thermal Model to Planet Mercury. *Master's thesis, TU Dortmund University*, 2023.

J. P. Emery, A. L. Sprague, F. C. Witteborn, J. E. Colwell, R .W. H. Kozlowski, and D. H. Wooden. Mercury: Thermal Modeling and Mid-infrared (5–12 μm) Observations. *Icarus*, 136(1):104–123, 1998. doi: 10.1006/icar.1998.6012.

S. Erard, B. Bézard, A. Doressoundiram, and D. Despan. Mercury resolved spectroscopy from NTT. *Planetary and Space Science*, 59(15):1842–1852, 2011. doi: 10.1016/j.pss.2011.07.004.

W. H. Farrand, E. Merényi, and M. C. Parente. Hyper- and Multispectral Visible and Near-Infrared Imaging Analysis. In J. L. Bishop, J. F. Bell III, and J. E. Moersch, editors, *Remote Compositional Analysis: Techniques for Understanding Spectroscopy, Mineralogy, and Geochemistry of Planetary Surfaces*, Cambridge Planetary Science, pages 307–323. Cambridge University Press, Cambridge, 2019. doi: 10.1017/9781316888872.016.

W. M. Farrell, D. M. Hurley, and M. I. Zimmerman. Solar wind implantation into lunar regolith: Hydrogen retention in a surface with defects. *Icarus*, 255:116–126, 2015. doi: 10.1016/j.icarus.2014.09.014.

W. C. Feldman, S. Maurice, A. B. Binder, B. L. Barraclough, R. C. Elphic, and D. J. Lawrence. Fluxes of Fast and Epithermal Neutrons from Lunar Prospector: Evidence for Water Ice at the Lunar Poles. *Science*, 281:1496, 1998. doi: 10.1126/science.281.5382.1496.

J. Feng, M. A. Siegler, and P. O. Hayne. New Constraints on Thermal and Dielectric Properties of Lunar Regolith from LRO Diviner and CE-2 Microwave Radiometer. *Journal of Geophysical Research: Planets*, 125(1):e2019JE006130, 2020. doi: 10.1029/2019JE006130.

Jean Baptiste Joseph Fourier. *Théorie Analytique de la Chaleur*. Cambridge Library Collection - Mathematics. Cambridge University Press, Cambridge, 2009. doi: 10.1017/CBO9780511693229.

B. W. Fowler. Expansion of Mie-theory phase functions in series of Legendre polynomials. *Journal of the Optical Society of America*, 73(1):19–22, 1983. doi: 10.1364/JOSA.73.000019.

P. I. Frazier. A Tutorial on Bayesian Optimization. *arXiv e-prints*, page arXiv:1807.02811, 2018.

M. A. Gelbart, J. Snoek, and R. P. Adams. Bayesian optimization with unknown constraints. In *30th Conference on Uncertainty in Artificial Intelligence*, UAI'14, page 250–259, Arlington, Virginia, USA, 2014. AUAI Press.

T. Gold. The lunar surface. *MNRAS*, 115:585, 1955. doi: 10.1093/mnras/115.6.585.

T. Gold. Lunar surface closeup stereoscopic photography. In *Apollo 11 –Preliminary Science Report*. NSA, 1969.

R. O. Green, C. Pieters, P. Mouroulis, M. Eastwood, J. Boardman, T. Glavich, P. Isaacson, M. Annadurai, S. Besse, D. Barr, B. Buratti, D. Cate, A. Chatterjee, R. Clark, L. Cheek,

J. Combe, D. Dhingra, V. Essandoh, S. Geier, J. N. Goswami, R. Green, V. Haemmerle, J. Head, L. Hovland, S. Hyman, R. Klima, T. Koch, G. Kramer, A. S. K. Kumar, K. Lee, S. Lundeen, E. Malaret, T. McCord, S. McLaughlin, J. Mustard, J. Nettles, N. Petro, K. Plourde, C. Racho, J. Rodriquez, C. Runyon, G. Sellar, C. Smith, H. Sobel, M. Staid, J. Sunshine, L. Taylor, K. Thaisen, S. Tompkins, H. Tseng, G. Vane, P. Varanasi, M. White, and D. Wilson. The Moon Mineralogy Mapper (M3) imaging spectrometer for lunar science: Instrument description, calibration, on-orbit measurements, science data calibration and on-orbit validation. *Journal of Geophysical Research: Planets*, 116(E10), 2011. doi: 10.1029/2011JE003797.

T. P. Greene, T. J. Bell, E. Ducrot, A. Dyrek, P.-O. Lagage, and J. J. Fortney. Thermal emission from the Earth-sized exoplanet TRAPPIST-1 b using JWST. *Nature*, 618(7963): 39–42, 2023. doi: 10.1038/s41586-023-05951-7.

B. T. Greenhagen, P. G. Lucey, M. B. Wyatt, T. D. Glotch, C. C. Allen, J. A. Arnold, J. L. Bandfield, N. E. Bowles, K. L. Donaldson Hanna, P. O. Hayne, E. Song, I. R. Thomas, and D. A. Paige. Global Silicate Mineralogy of the Moon from the Diviner Lunar Radiometer. *Science*, 329(5998):1507–1509, 2010. doi: 10.1126/science.1192196.

M. Grott, J. Knollenberg, and C. Krause. Apollo lunar heat flow experiment revisited: A critical reassessment of the in situ thermal conductivity determination. *Journal of Geophysical Research: Planets*, 115(E11), 2010. doi: 10.1029/2010JE003612.

O. Groussin, M. F. A'Hearn, J.-Y. Li, P. C. Thomas, J. M. Sunshine, C. M. Lisse, K. J. Meech, T. L. Farnham, L. M. Feaga, and W. A. Delamere. Surface temperature of the nucleus of Comet 9P/Tempel 1. *Icarus*, 191(2, Supplement):63–72, 2007. doi: 10.1016/j.icarus.2006.08.031.

O. Groussin, K. Wohlfarth, P. Vernazza, H. Hiesinger, and J. Helbert. Thermal modelling of Mercury's surface for the MERTIS instrument. *European Planetary Science Congress*, pages EPSC2022–202, 2022. doi: 10.5194/epsc2022-202.

A. Grumpe and C. Wöhler. Recovery of elevation from estimated gradient fields constrained by digital elevation maps of lower lateral resolution. *ISPRS Journal of Photogrammetry and Remote Sensing*, 94:37–54, 2014. doi: 10.1016/j.isprsjprs.2014.04.011.

A. Grumpe, K. S. Wohlfarth, and C. Wöhler. Simulation of Space Weathering based on Mie Theory. *Lunar and Planetary Science Conference*, 49:2533, 2018.

A. Grumpe, C. Wöhler, A. A. Berezhnoy, and V. V. Shevchenko. Time-of-day-dependent behavior of surficial lunar hydroxyl/water: Observations and modeling. *Icarus*, 321:486–507, 2019. doi: 10.1016/j.icarus.2018.11.025.

Y. Grynko, Y. Shkuratov, and J. Förstner. Light backscattering from large clusters of densely packed irregular particles. *Journal of Quantitative Spectroscopy and Radiative Transfer*, 255:107234, 2020. doi: 10.1016/j.jqsrt.2020.107234.

Y. Grynko, Y. Shkuratov, S. Alhaddad, and J. Förstner. Negative polarization of light at backscattering from a numerical analog of planetary regoliths. *Icarus*, 384:115099, 2022. doi: 10.1016/j.icarus.2022.115099.

B. Gundlach and J. Blum. A new method to determine the grain size of planetary regolith. *Icarus*, 223(1):479–492, 2013. ISSN 0019-1035. doi: 10.1016/j.icarus.2012.11.039.

J. Hadamard. Sur les problèmes aux dérivés partielles et leur signification physique. *Princeton University Bulletin*, 13:49–52, 1902.

D. L. Hampton, J. W. Baer, M. A. Huisjen, C. C. Varner, A. Delamere, D. D. Wellnitz, M. F. A'Hearn, and K. P. Klaasen. An Overview of the Instrument Suite for the Deep Impact Mission. *Space Science Reviews*, 117(1):43–93, 2005. doi: 10.1007/s11214-005-3390-8.

B. Hapke. Bidirectional reflectance spectroscopy: 1. Theory. *Journal of Geophysical Research: Solid Earth*, 86(B4):3039–3054, 1981. doi: 10.1029/JB086iB04p03039.

B. Hapke. Bidirectional reflectance spectroscopy: 3. Correction for macroscopic roughness. *Icarus*, 59(1):41–59, 1984. doi: 10.1016/0019-1035(84)90054-X.

B. Hapke. Bidirectional reflectance spectroscopy: 4. The extinction coefficient and the opposition effect. *Icarus*, 67(2):264–280, 1986. doi: 10.1016/0019-1035(86)90108-9.

B. Hapke. A model of radiative and conductive energy transfer in planetary regoliths. *Journal of Geophysical Research: Planets*, 101(E7):16817–16831, 1996. doi: 10.1029/96JE00917.

B. Hapke. Space weathering from Mercury to the asteroid belt. *Journal of Geophysical Research: Planets*, 106(E5):10039–10073, 2001. doi: 10.1029/2000JE001338.

B. Hapke. Bidirectional Reflectance Spectroscopy: 5. The Coherent Backscatter Opposition Effect and Anisotropic Scattering. *Icarus*, 157(2):523–534, 2002. doi: 10.1006/icar.2002.6853.

B. Hapke. Bidirectional reflectance spectroscopy: 6. Effects of porosity. *Icarus*, 195(2): 918–926, 2008. doi: 10.1016/j.icarus.2008.01.003.

B. Hapke. *Theory of Reflectance and Emittance Spectroscopy.* Cambridge University Press, Cambridge, 2012.

B. Hapke. Bidirectional reflectance spectroscopy 7. The single particle phase function hockey stick relation. *Icarus*, 221(2):1079–1083, 2012. doi: 10.1016/j.icarus.2012.10.022.

B. Hapke. Comment on "A critical assessment of the Hapke photometric model" by Y. Shkuratov et al. *Journal of Quantitative Spectroscopy and Radiative Transfer*, 116:184–190, 2013. doi: 10.1016/j.jqsrt.2012.11.002.

T. Harnisch. Entwurf eines mikrocontrollerbasierten Systems zur Anwendung moderner Bilderkennungsalgorithmen. *Bachelor's thesis, TU Dortmund University*, 2019.

A. W. Harris. A Thermal Model for Near-Earth Asteroids. *Icarus*, 131(2):291–301, 1998. doi: 10.1006/icar.1997.5865.

S. M. Hauck II, M. Grott, P. K. Byrne, B. W. Denevi, S. Stanley, and T. J. McCoy. Mercury's Global Evolution. In S. C. Solomon, L. R. Nittler, and B. J. Anderson, editors, *Mercury: The View after MESSENGER*, Cambridge Planetary Science, pages 516–543. Cambridge University Press, 2018. doi: 10.1017/9781316650684.020.

S. E. Hawkins, J. D. Boldt, E. H. Darlington, R. Espiritu, R. E. Gold, B. Gotwols, M. P. Grey, C. D. Hash, J. R. Hayes, S. E. Jaskulek, C. J. Kardian, M. R. Keller, E. R. Malaret, S. L. Murchie, P. K. Murphy, K. Peacock, L. M. Prockter, R. A. Reiter, M. Robinson, E. D. Schaefer, R. G. Shelton, R. E. Sterner, H. W. Taylor, T. R. Watters, and B. D. Williams. The mercury dual imaging system on the MESSENGER spacecraft. *Space Science Reviews*, 131(1-4):247–338, 2007. doi: 10.1007/s11214-007-9266-3.

P. O. Hayne, J. L. Bandfield, M. A. Siegler, A. R. Vasavada, R. R. Ghent, J.-P. Williams, B. T. Greenhagen, O. Aharonson, C. M. Elder, P. G. Lucey, and D. A. Paige. Global Regolith Thermophysical Properties of the Moon From the Diviner Lunar Radiometer Experiment. *Journal of Geophysical Research: Planets*, 122(12):2371–2400, 2017. doi: 10.1002/2017JE005387.

J. Heidt. *Astronomy in the Near-Infrared - Observing Strategies and Data Reduction Techniques*, volume 467 of *Book Series: Astrophysics and Space Science Library*. Springer, Cham, 2022. doi: 10.1007/978-3-030-98441-0.

G. Heiken, D. Vaniman, and B. M French, editors. *Lunar Sourcebook: A User's Guide to the Moon*. LPI contribution. Cambridge University Press, Cambridge, 1991.

P. Helfenstein and M. K. Shepard. Submillimeter-Scale Topography of the Lunar Regolith. *Icarus*, 141(1):107–131, 1999. doi: 10.1006/icar.1999.6160.

M. Hess. Shape from Shading Applied to the Martian Surface: Compensation of Atmospheric Effects. *Master's thesis, TU Dortmund University*, 2019.

M. Hess, K. Wohlfarth, A. Grumpe, C. Wöhler, O. Ruesch, and B. Wu. Overcoming Troublesome Stereo Artifacts: Towards the Perfect Digital Terrain Model of Mars. *50th Annual Lunar and Planetary Science Conference*, 50:2565, 2019a.

M. Hess, K. Wohlfarth, A. Grumpe, C. Wöhler, O. Ruesch, and B. Wu. Atmospherically Compensated Shape from Shading on the Martian Surface: Towards the Perfect Digital Terrain Model of Mars. *ISPRS - International Archives of the Photogrammetry, Remote Sensing and Spatial Information Sciences*, 4213:1405–1411, 2019b. doi: 10.5194/isprs-archives-XLII-2-W13-1405-2019.

M. Hess, K. Wohlfarth, O. Ruesch, C. Wöhler, and A. Grumpe. High Resolution Digital Terrain Model for the Landing Site of the Rosalind Franklin (ExoMars) Rover. *EPSC-DPS Joint Meeting 2019*, 2019:EPSC–DPS2019–1533, 2019c.

M. Hess, C. Wöhler, M. Bhatt, A. A. Berezhnoy, A. Grumpe, K. Wohlfarth, A. Bhardwaj, and V. V. Shevchenko. Processes governing the VIS/NIR spectral reflectance behavior of lunar swirls. *Astronomy and Astrophysics*, 639:A12, 2020a. doi: 10.1051/0004-6361/201937299.

M. Hess, K. Wohlfarth, and C. Wöhler. Quantifying Lunar Spinel-Rich Lithologies with Nonlinear Spectral Unmixing Considering Space-Weathering Effects. *51st Annual Lunar and Planetary Science Conference*, 51:1863, 2020b.

M. Hess, K. Wohlfarth, C. Wöhler, A. A. Berezhnoy, M. Bhatt, and A. Bhardwaj. Space Weathering Trends at the Mare Moscoviense Swirl. *European Planetary Science Congress*, pages EPSC2020–716, 2020c. doi: 10.5194/epsc2020-716.

M. Hess, T. Wilhelm, C. Wöhler, and K. Wohlfarth. Uncertainty Introduced by Darkening Agents in the Lunar Regolith: An Unmixing Perspective. *Remote Sensing*, 13(22):4702, 2021. doi: 10.3390/rs13224702.

M. Hess, M. Tenthoff, K. Wohlfarth, and C. Wöhler. Atmospheric Correction for High-Resolution Shape from Shading on Mars. *Journal of Imaging*, 8(6), 2022. doi: 10.3390/jimaging8060158.

M. Hess, C. Wöhler, L. Qiao, and M. Bhatt. Comparative photometric analysis of the Reiner Gamma swirl and Chang'e 5 landing site. *Astronomy & Astrophysics*, 674:A226, 2023. doi: 10.1051/0004-6361/202346098.

P. J. Hickson. Lunar Surface Temperatures from Apollo 11 Data. Technical report, Bellcomm, 1970.

H. Hiesinger and J. Helbert. The Mercury Radiometer and Thermal Infrared Spectrometer (MERTIS) for the BepiColombo mission. *Planetary and Space Science*, 58(1):144–165, 2010. doi: 10.1016/j.pss.2008.09.019.

H. Hiesinger, J. W. Head III, U. Wolf, R. Jaumann, and G. Neukum. Ages and stratigraphy of mare basalts in Oceanus Procellarum, Mare Nubium, Mare Cognitum, and Mare Insularum. *Journal of Geophysical Research: Planets*, 108(E7), 2003. doi: 10.1029/2002JE001985.

H. Hiesinger, J. Helbert, G. Alemanno, K. E. Bauch, M. D'Amore, A. Maturilli, A. Morlok, M. P. Reitze, C. Stangarone, A. N. Stojic, I. Varatharajan, I. Weber, and the MERTIS Co-I Team. Studying the Composition and Mineralogy of the Hermean Surface with the Mercury Radiometer and Thermal Infrared Spectrometer (MERTIS) for the BepiColombo Mission: An Update. *Space Science Reviews*, 216(6), 2020. doi: 10.1007/s11214-020-00732-4.

H. Hiesinger, J. Helbert, K. Bauch, M. D'Amore, M. Maturilli, A. Morlok, M. Reitze, A. N. Stojic, I. Varatharajan, I. Weber, K. Wohlfarth, and C. Wöhler. The Mercury Radiometer and Thermal Infrared Spectrometer (MERTIS) at the Moon — First Results and Status Report. *Lunar and Planetary Science Conference*, page 1494, 2021.

C. I. Honniball, P. G. Lucey, C. M. Ferrari-Wong, A. Flom, S. Li, H. M. Kaluna, and D. Takir. Telescopic Observations of Lunar Hydration: Variations and Abundance. *Journal of Geophysical Research: Planets*, 125(9):e2020JE006484, 2020. doi: 10.1029/2020JE006484.

C. I. Honniball, P. G. Lucey, S. Li, S. Shenoy, T. M. Orlando, C. A. Hibbitts, D. M. Hurley, and W. M. Farrell. Molecular water detected on the sunlit Moon by SOFIA. *Nature Astronomy*, 5:121–127, 2021. doi: 10.1038/s41550-020-01222-x.

L. L. Hood and C. R. Williams. The lunar swirls: distribution and possible origins. *Lunar and Planetary Science Conference*, 19:99–113, 1989.

P. K. Hopke. Target transformation factor analysis. *Chemometrics and Intelligent Laboratory Systems*, 6(1):7–19, 1989. doi: 10.1016/0169-7439(89)80061-9.

J. R. Howell, M. P. Mengüc, K. Daun, and R. Siegel. *Thermal Radiation Heat Transfer*. CRC Press, Boca Raton, 2020. doi: 10.1201/9780429327308.

ISO 20473:2007. Optics and photonics – Spectral bands. Standard, International Organization for Standardization, Geneva, CH, 2007.

G. Ito, M. I. Mishchenko, and T. D. Glotch. Radiative-transfer modeling of spectra of planetary regoliths using cluster-based dense packing modifications. *Journal of Geophysical Research: Planets*, 123(5):1203–1220, 2018. doi: 10.1029/2018JE005532.

N. R. Izenberg, R. L. Klima, S. L. Murchie, D. T. Blewett, G. M. Holsclaw, W. E. McClintock, E. Malaret, C. Mauceri, F. Vilas, A. L. Sprague, J. Helbert, D. L. Domingue, J. W. Head, T. A. Goudge, S. C. Solomon, C. A. Hibbitts, and M. Darby Dyar. The low-iron, reduced surface of Mercury as seen in spectral reflectance by MESSENGER. *Icarus*, 228:364–374, 2014. doi: 10.1016/j.icarus.2013.10.023.

J. D. Jackson. *Classical electrodynamics*. Wiley, New York, 1998.

P. Jakobsen, P. Ferruit, C. Alves de Oliveira, S. Arribas, G. Bagnasco, R. Barho, T. L. Beck, S. Birkmann, T. Böker, A. J. Bunker, S. Charlot, P. de Jong, G. de Marchi, R. Ehrenwinkler, M. Falcolini, R. Fels, M. Franx, D. Franz, M. Funke, G. Giardino, X. Gnata, W. Holota, K. Honnen, P. L. Jensen, M. Jentsch, T. Johnson, D. Jollet, H. Karl, G. Kling, J. Köhler, M. G. Kolm, N. Kumari, M. E. Lander, R. Lemke, M. López-Caniego, N. Lützgendorf, R. Maiolino, E. Manjavacas, A. Marston, M. Maschmann, R. Maurer, B. Messerschmidt, S. H. Moseley, P. Mosner, D. B. Mott, J. Muzerolle, N. Pirzkal, J. F. Pittet, A. Plitzke, W. Posselt, B. Rapp, B. J. Rauscher, T. Rawle, H. W. Rix, A. Rödel, P. Rumler, E. Sabbi, J. C. Salvignol, T. Schmid, M. Sirianni, C. Smith, P. Strada, M. te Plate, J. Valenti, T. Wettemann, T. Wiehe, M. Wiesmayer, C. J. Willott, R. Wright, P. Zeidler, and C. Zincke. The Near-Infrared Spectrograph (NIRSpec) on the James Webb Space Telescope. I. Overview of the instrument and its capabilities. *Astronomy & Astrophysics*, 661:A80, 2022. doi: 10.1051/0004-6361/202142663.

B. L. Jolliff, M. A. Wieczorek, C. K. Shearer, and C. R. Neal, editors. *New Views of the Moon*. De Gruyter, Berlin, Boston, 2006. doi: 10.1515/9781501509537.

M. Kaasalainen, J. Torppa, and K. Muinonen. Optimization Methods for Asteroid Lightcurve Inversion: II. The Complete Inverse Problem. *Icarus*, 153(1):37–51, 2001. doi: 10.1006/icar.2001.6674.

S. J. Keihm. Interpretation of the lunar microwave brightness temperature spectrum: Feasibility of orbital heat flow mapping. *Icarus*, 60(3):568–589, 1984. ISSN 0019-1035. doi: doi.org/10.1016/0019-1035(84)90165-9.

S. J. Keihm and M. G. Langseth Jr. Surface brightness temperatures at the Apollo 17 heat flow site: Thermal conductivity of the upper 15 cm of regolith. *Lunar and Planetary Science Conference*, 4:2503, 1973.

L. P. Keller and D. S. McKay. Discovery of Vapor Deposits in the Lunar Regolith. *Science*, 261(article number 5126):1305–1307, 1993. doi: 10.1126/science.261.5126.1305.

L. P. Keller and D. S. McKay. The nature and origin of rims on lunar soil grains. *Geochimica et Cosmochimica Acta*, 61(11):2331–2341, 1997. doi: 10.1016/S0016-7037(97)00085-9.

M. G. Kleinhans, C. J. J. Buskes, and H. W. de Regt. Philosophy of Earth Science. In F. Allhoff, editor, *Philosophies of the Sciences*, chapter 9, pages 213–236. John Wiley and Sons, Ltd, 2010. doi: 10.1002/9781444315578.ch9.

R. L. Klima, B. W. Denevi, C. M. Ernst, S. L. Murchie, and P. N. Peplowski. Global Distribution and Spectral Properties of Low-Reflectance Material on Mercury. *Geophysical Research Letters*, 45(7):2945–2953, 2018. doi: 10.1002/2018GL077544.

T. G Kolda, R. M. Lewis, and V. Torczon. Optimization by direct search: New perspectives on some classical and modern methods. *SIAM review*, 45(3):385–482, 2003.

L. Kolokolova, G. Ito, K. M. Pitman, K. McMichael, and N. Reui. Spectral Modeling Using Radiative Transfer Theory with Packing Density Correction: Demonstration for Saturnian Icy Satellites. *The Planetary Science Journal*, 1(3):74, 2020. doi: 10.3847/PSJ/abb5b3.

A. Kosak, M. Arnaut, S. Beck, H. Schippers, K. Wohlfarth, T. Wilhelm, and C. Wöhler. Geomorphologic Feature Extraction and Clustering of Martian DTM Data. *51st Annual Lunar and Planetary Science Conference*, 51:3044, 2020.

L. Kreidberg. Exoplanet Atmosphere Measurements from Transmission Spectroscopy and Other Planet Star Combined Light Observations. In H. J. Deeg and J. A. Belmonte, editors, *Handbook of Exoplanets*, pages 1–23. Springer International Publishing, Cham, 2017. doi: 10.1007/978-3-319-30648-3_100-1.

L. Kreidberg, D. D. B. Koll, C. Morley, R. Hu, L. Schaefer, D. Deming, K. B. Stevenson, J. Dittmann, A. Vanderburg, D. Berardo, X. Guo, K. Stassun, I. Crossfield, D. Charbonneau, D. W. Latham, A. Loeb, G. Ricker, S. Seager, and R. Vanderspek. Absence of a thick atmosphere on the terrestrial exoplanet LHS 3844b. *Nature*, 573(7772):87–90, 2019. doi: 10.1038/s41586-019-1497-4.

G. Kristensson. Spherical Vector Waves, 2014. URL `https://www.eit.lth.se/fileadmin/eit/courses/eit080f/Literature/book.pdf`. Online; accessed December 4, 2023.

I. Krüll, K. Wohlfarth, M. Tenthoff, C. Wöhler, V. Galluzzi, J. Wright, J. Benkhoff, and J. Zender. Shape and Albedo from Shading with Planetary Flyby Images of Mercury and the Moon. *European Planetary Science Congress*, pages EPSC2024–247, 2024. doi: 10.5194/epsc2024-247.

I. Krüll. Shape from Shading with Planetary Fly-By Images. *Bachelor's thesis, TU Dortmund University*, 2023.

C. Künzer and S. Dech. *Thermal Infrared Remote Sensing: Sensors, Methods, Applications*, volume 17 of *Remote Sensing and Digital Image Processing*. Springer, Dordrecht, 2013. doi: 10.1007/978-94-007-6639-6.

K. L. Laferriere, J. M. Sunshine, and L. M. Feaga. Variability of Hydration Across the Southern Hemisphere of the Moon as Observed by Deep Impact. *Journal of Geophysical Research: Planets*, 127(8):e2022JE007361, 2022. doi: 10.1029/2022JE007361.

J. S. V. Lagerros. Thermal physics of asteroids. I. Effects of shape, heat conduction and beaming. *Astronomy & Astrophysics*, 310:1011–1020, 1996.

M. G. Langseth, S. J. Keihm, and K. Peters. Revised lunar heat-flow values. *Lunar and Planetary Science Conference*, 3:3143–3171, 1976.

L. A. Lebofsky, G. J. Veeder, M. J. Lebofsky, and D. L. Matson. Visual and radiometric photometry of 1580 Betulia. *Icarus*, 35(3):336–343, 1978. doi: 10.1016/0019-1035(78)90086-6.

L. A. Lebofsky, M. V. Sykes, E. F. Tedesco, G. J. Veeder, D. L. Matson, R. H. Brown, J. C. Gradie, M. A. Feierberg, and R. J. Rudy. A refined "standard" thermal model for asteroids based on observations of 1 Ceres and 2 Pallas. *Icarus*, 68(2):239–251, 1986. doi: 10.1016/0019-1035(86)90021-7.

D. R. Li. China's High-Resolution Earth Observation System (cheos): Advances and Perspectives. *ISPRS Annals of Photogrammetry, Remote Sensing and Spatial Information Sciences*, 53:583–590, May 2022. doi: 10.5194/isprs-annals-V-3-2022-583-2022.

S. Li and R. E. Milliken. An empirical thermal correction model for Moon Mineralogy Mapper data constrained by laboratory spectra and Diviner temperatures. *Journal of Geophysical Research: Planets*, 121(10):2081–2107, 2016. doi: 10.1002/2016JE005035.

S. Li and R. E. Milliken. Water on the surface of the Moon as seen by the Moon Mineralogy Mapper: Distribution, abundance, and origins. *Science Advances*, 3(9):e1701471, 2017. doi: 10.1126/sciadv.1701471.

Y. Liu, T. D. Glotch, N. A. Scudder, M. L. Kraner, T. Condus, R. E. Arvidson, E. A. Guinness, M. J. Wolff, and M. D. Smith. End-member identification and spectral mixture analysis of CRISM hyperspectral data: A case study on southwest Melas Chasma, Mars. *Journal of Geophysical Research: Planets*, 121(10):2004–2036, 2016. doi: 10.1002/2016JE005028.

T. A. Livengood, G. Chin, R. Z. Sagdeev, I. G. Mitrofanov, W. V. Boynton, L. G. Evans, M. L. Litvak, T. P. McClanahan, A. B. Sanin, R. D. Starr, and J. J. Su. Moonshine: Diurnally varying hydration through natural distillation on the Moon, detected by the Lunar Exploration Neutron Detector (LEND). *Icarus*, 255:100–115, 2015. doi: 0.1016/j.icarus.2015.04.004.

H. A. Lorentz. Ueber die Beziehung zwischen der Fortpflanzungsgeschwindigkeit des Lichtes und der Körperdichte. *Annalen der Physik*, 245(4):641–665, 1880. doi: 10.1002/andp.18802450406.

P. G. Lucey and M. A. Riner. The optical effects of small iron particles that darken but do not redden: Evidence of intense space weathering on Mercury. *Icarus*, 212(2):451–462, 2011. doi: 10.1016/j.icarus.2011.01.022.

P. G. Lucey, D. T. Blewett, and B. L. Jolliff. Lunar iron and titanium abundance algorithms based on final processing of Clementine ultraviolet-visible images. *Journal of Geophysical Research: Planets*, 105(E8):20297–20305, 2000. doi: 10.1029/1999JE001117.

P. G. Lucey, B. Greenhagen, K. Donaldson Hanna, N. Bowles, A. Flom, and D. A. Paige. Christiansen Feature Map From the Lunar Reconnaissance Orbiter Diviner Lunar Radiometer Experiment: Improved Corrections and Derived Mineralogy. *Journal of Geophysical Research: Planets*, 126(6):e2020JE006777, 2021. doi: 10.1029/2020JE006777.

K. Lumme and E. Bowell. Radiative transfer in the surfaces of atmosphereless bodies. I. Theory. *Astronomical Journal*, 86:1694–1721, 1981. doi: 10.1086/113054.

D. W. Mackowski and M. I. Mishchenko. A multiple sphere T-matrix FORTRAN code for use on parallel computer clusters. *Journal of Quantitative Spectroscopy and Radiative Transfer*, 112:2182–2192, 2011. doi: 10.1016/j.jqsrt.2011.02.019.

E. M. MacLennan and J. P. Emery. Thermophysical Modeling of Asteroid Surfaces Using Ellipsoid Shape Models. *Astronomical Journal*, 157(1):2, 2018. doi: 10.3847/1538-3881/aaed47.

B. Man, D. A. Rothery, and M. R. Balme. Widespread small grabens consistent with recent tectonism on Mercury. *Nature Geoscience*, 16(10):856–862, 2023. doi: 10.1038/s41561-023-01281-5.

L. Mandel and E. Wolf. *Optical Coherence and Quantum Optics*. Cambridge University Press, Cambridge, 1995. doi: 10.1017/CBO9781139644105.

R. Marshal, K. Wohlfarth, and O. Ruesch. Insights on Pixel and Sub-Pixel Scale Rock Abundance on the Moon with LROC/NAC. *52nd Lunar and Planetary Science Conference*, 52: 1457, 2021.

R. M. Marshal, O. Rüsch, C. Wöhler, and K. Wohlfarth. Estimating Lunar Rock Abrasion Stage Using Photometric Studies. *53rd Lunar and Planetary Science Conference*, 53:1108, 2022a.

R. M. Marshal, O. Rüsch, C. Wöhler, and K. Wohlfarth. Estimating Lunar Rock Abrasion Stage using Photometric Studies. *EGU General Assembly Conference*, pages EGU22–12217, 2022b. doi: 10.5194/egusphere-egu22-12217.

R. M. Marshal, O. Rüsch, C. Wöhler, K. Wohlfarth, and S. Velichko. Photometry of rock-rich surfaces on the Moon. *European Planetary Science Congress*, pages EPSC2022–871, 2022c. doi: 10.5194/epsc2022-871.

R. M. Marshal, O. Rüsch, C. Wöhler, K. Wohlfarth, and S. Velichko. Photometry of LROC NAC resolved rock-rich regions on the Moon. *Icarus*, 394:115419, 2023a. doi: 10.1016/j.icarus.2022.115419.

R. M. Marshal, O. Rüsch, C. Wöhler, K. Wohlfarth, S. Velichko, and M. Patzek. Photometry of Rock-Rich Surfaces on Airless Bodies. *54th Lunar and Planetary Science Conference*, 54:1650, 2023b.

R. M. Marshal, O. Rüsch, C. Wöhler, K. Wohlfarth, S. Velichko, and M. Patzek. Photometry of rock-rich surfaces on airless bodies. *EGU General Assembly Conference*, pages EGU–14255, 2023c. doi: 10.5194/egusphere-egu23-14255.

D. Marshall, O. Groussin, J. B. Vincent, Y. Brouet, D. Kappel, G. Arnold, M. T. Capria, G. Filacchione, P. Hartogh, M. Hofstadter, W. H. Ip, L. Jorda, E. Kührt, E. Lellouch, S. Mottola, L. Rezac, R. Rodrigo, S. Rodionov, P. Schloerb, and N. Thomas. Thermal inertia and roughness of the nucleus of comet 67P/Churyumov-Gerasimenko from MIRO and VIRTIS observations. *Astronomy & Astrophysics*, 616:A122, 2018. doi: 10.1051/0004-6361/201833104.

S. Marsland. *Machine Learning, An Algorithmic Perspective.* CRC Press, New York, 2009.

M. Marsset, F. E. DeMeo, R. P. Binzel, S. J. Bus, T. H. Burbine, B. Burt, N. Moskovitz, D. Polishook, A. S. Rivkin, S. M. Slivan, and C. Thomas. Twenty Years of SpeX: Accuracy Limits of Spectral Slope Measurements in Asteroid Spectroscopy. *The Astrophysical Journal Supplement Series*, 247(2):73, 2020. doi: 10.3847/1538-4365/ab7b5f.

M. Massimi. Three Problems About Multi-Scale Modelling in Cosmology. *Studies in History and Philosophy of Science Part B: Studies in History and Philosophy of Modern Physics*, 64:26–38, 2018. doi: 10.1016/j.shpsb.2018.04.002.

A. Maturilli, J. Helbert, and L. Moroz. The Berlin emissivity database. *Planetary and Space Science*, 56(3-4):420–425, 2008.

A. Maturilli, J. Helbert, S. Ferrari, and M. D'Amore. On the effect of emergence angle on emissivity spectra: application to small bodies. *Earth, Planets and Space*, 68(article number 84), 2016. doi: 10.1186/s40623-016-0464-7.

A. Maturilli, K. Wohlfarth, G. Alemanno, C. Woehler, M. D'Amore, J. Helbert, and H. Hiesinger. Spectral Signatures of Glass on Lunar Analogue Rocks. *52nd Lunar and Planetary Science Conference*, 52:2085, 2021.

C. Mätzler. MATLAB Functions for Mie Scattering and Absorption. Technical report, University of Bern, 2002. URL `http://www.atmo.arizona.edu/students/courselinks/spring09/atmo656b/maetzler_mie_v2.pdf`. Online; accessed December 08, 2023.

A. S. Maurin, F. Selsis, F. Hersant, and A. Belu. Thermal phase curves of nontransiting terrestrial exoplanets. II. Characterizing airless planets. *Astronomy and & Astrophysics*, 538:A95, 2012. doi: 10.1051/0004-6361/201117054.

S. Mayhew. *A Dictionary of Geography.* Oxford University Press, Oxford, 2009.

R. Mbakop. Methode zur Bestimmung von Endgliedern in Mineralmischungen. *Bachelor's thesis, TU Dortmund University*, 2019.

D. J. McCleese, J. T. Schofield, F. W. Taylor, S. B. Calcutt, M. C. Foote, D. M. Kass, C. B. Leovy, D. A. Paige, P. L. Read, and R. W. Zurek. Mars Climate Sounder: An investigation of thermal and water vapor structure, dust and condensate distributions in the atmosphere, and energy balance of the polar regions. *Journal of Geophysical Research: Planets*, 112(E5), 2007. doi: 10.1029/2006JE002790.

T. J. McCoy, P. N. Peplowski, F. M. McCubbin, and S. Z. Weider. The Geochemical and Mineralogical Diversity of Mercury. In S. C. Solomon, L. R. Nittler, and B. J. Anderson, editors, *Mercury: The View after MESSENGER*, Cambridge Planetary Science, pages 176–190. Cambridge University Press, Cambridge, 2018. doi: 10.1017/9781316650684.008.

A. S. McEwen. A Precise Lunar Photometric Function . *Lunar and Planetary Science Conference*, 27:841, 1996.

D. S. McKay, G. Heiken, A. Basu, G. Blanford, S. Simon, R. Reedy, B. M. French, and J. Papike. The Lunar Regolith. In G. H. Heiken, D. T. Vaniman, and B. M. French, editors, *Lunar Sourcebook, A User's Guide to the Moon*, pages 285–356. Cambridge University Press, Cambridge, 1991.

A. Meister. *Numerik linearer Gleichungssysteme.* Springer Spektrum, Wiesbaden, 2015. doi: 10.1007/978-3-658-07200-1.

G. Meister, E. J. Kwiatkowska, B. A. Franz, F. S. Patt, G. C. Feldman, and C. R. McClain. Moderate-Resolution Imaging Spectroradiometer ocean color polarization correction. *Appl. Opt.*, 44(26):5524–5535, 2005. doi: 10.1364/AO.44.005524.

G. Mie. Beiträge zur Optik trüber Medien, speziell kolloidaler Metallösungen. *Annalen der Physik*, 330(3):377–445, 1908. doi: 10.1002/andp.19083300302.

L. Millán, I. Thomas, and N. Bowles. Lunar regolith thermal gradients and emission spectra: Modeling and validation. *Journal of Geophysical Research: Planets*, 116(E12), 2011. doi: 10.1029/2011JE003874.

W. J. Minkowycz, E. M. Sparrow, and J. Y. Murthy. *Handbook of Numerical Heat Transfer*. Wiley, Hoboken, 2006.

M. I. Mishchenko. Asymmetry parameters of the phase function for densely packed scattering grains. *Journal of Quantitative Spectroscopy and Radiative Transfer*, 52:95–110, 1994. doi: 10.1016/0022-4073(94)90142-2.

M. I. Mishchenko. Radiative transfer theory: From Maxwell's equations to practical applications. In B. A. van Tiggelen and S. E. Skipetrov, editors, *Wave Scattering in Complex Media: From Theory to Applications*, pages 367–414. Kluwer Academic, Dordrecht, 2003.

M. I. Mishchenko. Directional radiometry and radiative transfer: The convoluted path from centuries-old phenomenology to physical optics. *Journal of Quantitative Spectroscopy and Radiative Transfer*, 146:4–33, 2014a. doi: 10.1016/j.jqsrt.2014.02.033.

M. I. Mishchenko. *Electromagnetic Scattering by Particles and Particle Groups: An Introduction.* Cambridge University Press, Cambridge, 2014b.

M. I. Mishchenko, L. D. Travis, and A. A. Lacis. *Scattering, Absorption, and Emission of Light by Small Particles.* Cambridge University Press, Cambridge, 2002.

M. I. Mishchenko, L. D. Travis, and A. A. Lacis. *Multiple Scattering of Light by Particles: Radiative Transfer and Coherent Backscattering.* Cambridge University Press, Cambridge, 2006.

A. F. J. Moffat. A Theoretical Investigation of Focal Stellar Images in the Photographic Emulsion and Application to Photographic Photometry. *Astronomy & Astrophysics*, 3: 455, 1969.

A. Morlok, B. Charlier, M. P. Reitze, C. J. Renggli, S. Klemme, O. Namur, M. Sohn, D. Martin, I. Weber, A. N. Stojic, K. E. Bauch, K. Wohlfarth, C. Wöhler, K. H. Joy, R. Wogelius, C. Carli, H. Hiesinger, and J. Helbert. BepiColombo and MERTIS @Moon: A Very First Comparison of Mid-Infrared (7-14 µm) Spectra. *52nd Lunar and Planetary Science Conference*, 52:1964, 2021a.

A. Morlok, M. P. Reitze, I. Weber, A. N. Stojic, K. E. Bauch, K. Wohlfarth, C. Wöhler, H. Hiesinger, and J. Helbert. FTIR Studies of Planetary Materials: The Impact of Temperature and Vacuum on Spectral Features. *84th Annual Meeting of the Meteoritical Society*, 84:6184, 2021b.

R. V. Morris. Surface exposure indices of lunar soils: a comparative FMR study. *Lunar and Planetary Science Conference*, 1:315–335, 1976.

T. G. Müller, M. Burgdorf, V. Alí-Lagoa, S. A. Buehler, and M. Prange. The Moon at thermal infrared wavelengths: a benchmark for asteroid thermal models. *Astronomy & Astrophysics*, 650:A38, 2021. doi: 10.1051/0004-6361/202039946.

S. L. Murchie, R. L. Klima, B. W. Denevi, C. M. Ernst, M. R. Keller, D. L. Domingue, D. T. Blewett, N. L. Chabot, C. D. Hash, E. Malaret, N. R. Izenberg, F. Vilas, L. R. Nittler, J. J. Gillis-Davis, J. W. Head, and S. C. Solomon. Orbital multispectral mapping of Mercury with the MESSENGER Mercury Dual Imaging System: Evidence for the origins of plains units and low-reflectance material. *Icarus*, 254:287–305, 2015. doi: 10.1016/j.icarus.2015.03.027.

S. L. Murchie, R. L. Klima, N. R. Izenberg, D. L. Domingue, D. T. Blewett, and J. Helbert. Spectral Reflectance Constraints on the Composition and Evolution of Mercury's Surface. In S. C. Solomon, L. R. Nittler, and B. J. Anderson, editors, *Mercury: The View after MESSENGER*, Cambridge Planetary Science, pages 191–216. Cambridge University Press, Cambridge, 2018.

J. F. Mustard and C. M. Pieters. Photometric phase functions of common geologic minerals and applications to quantitative analysis of mineral mixture reflectance spectra. *Journal of Geophysical Research: Solid Earth*, 94(B10):13619–13634, 1989. doi: 10.1029/JB094iB10p13619.

N. Myhrvold. Asteroid thermal modeling in the presence of reflected sunlight. *Icarus*, 303: 91–113, 2018. doi: 10.1016/j.icarus.2017.12.024.

S. Nagihara, W. S. Kiefer, P. T. Taylor, D. R. Williams, and Y. Nakamura. Examination of the Long-Term Subsurface Warming Observed at the Apollo 15 and 17 Sites Utilizing the Newly Restored Heat Flow Experiment Data From 1975 to 1977. *Journal of Geophysical Research: Planets*, 123(5):1125–1139, 2018. doi: 10.1029/2018JE005579.

NCBI. Density in the Periodic Table of Elements. Technical report, National Center for Biotechnology Information, 2023. URL `https://pubchem.ncbi.nlm.nih.gov/periodic-table/density`. Online; accessed December 09, 2023.

G. Neukum. Meteorite Bombardement and Dating of Planetary Surfaces. *Technical University Munich*, 1983.

G. A. Neumann. Lunar Orbiter Laser Altimeter Raw Data Set, 2009. URL `https://pds.nasa.gov/ds-view/pds/viewProfile.jsp?dsid=LRO-L-LOLA-4-GDR-V1.0`. Online; accessed January 27, 2022.

S. K. Noble, C. M. Pieters, and L. P. Keller. An experimental approach to understanding the optical effects of space weathering. *Icarus*, 192(2):629–642, 2007. doi: 10.1016/j.icarus.2007.07.021.

S. K. Noble, T. Hiroi, L. P. Keller, Z. Rahman, S. Sasaki, and C. M. Pieters. Experimental Space Weathering of Ordinary Chondrites by Nanopulse Laser: TEM Results. *Lunar and Planetary Science Conference*, 42:1382, 2011.

T. Okada, T. Fukuhara, S. Tanaka, M. Taguchi, T. Arai, H. Senshu, H. Demura, Y. Ogawa, T. Kouyama, N. Sakatani, J. Takita, T. Sekiguchi, J. Helbert, T. G. Mueller, and A. Hagermann. Earth and moon observations by thermal infrared imager on Hayabusa2 and the application to detectability of asteroid 162173 Ryugu. *Planetary and Space Science*, 158: 46–52, 2018. doi: 10.1016/j.pss.2018.05.007.

D. A. Paige and M. A. Siegler. New Constraints on Lunar Heat Flow rates from LRO Diviner Lunar Radiometer Experiment Polar Observations. *Lunar and Planetary Science Conference*, 47:2753, 2016.

D. A. Paige, M. C. Foote, B. T. Greenhagen, J. T. Schofield, S. Calcutt, A. R. Vasavada, D. J. Preston, F. W. Taylor, C. C. Allen, K. J. Snook, B. M. Jakosky, B. C. Murray, L. A. Soderblom, B. Jau, S. Loring, J. Bulharowski, N. E. Bowles, I. R. Thomas, M. T. Sullivan, C. Avis, E. M. De Jong, W. Hartford, and D. J. and. McCleese. The Lunar Reconnaissance Orbiter Diviner Lunar Radiometer Experiment. *Space Science Reviews*, 150(1):125–160, 2010a. doi: 10.1007/s11214-009-9529-2.

D. A. Paige, M. A. Siegler, J. A. Zhang, P. O. Hayne, E. J. Foote, K. A. Bennett, A. R. Vasavada, B. T. Greenhagen, J. T. Schofield, D. J. McCleese, M. C. Foote, E. DeJong, B. G. Bills, W. Hartford, B. C. Murray, C. C. Allen, K. Snook, L. A. Soderblom, S. Calcutt, F. W. Taylor, N. E. Bowles, J. L. Bandfield, R. Elphic, R. Ghent, T. D. Glotch, M. B. Wyatt, and P. G. Lucey. Diviner Lunar Radiometer Observations of Cold Traps in the Moon's South Polar Region. *Science*, 330(6003):479–482, 2010b. doi: 10.1126/science.1187726.

D. A. Paige, M. A. Siegler, J. K. Harmon, G. A. Neumann, E. M. Mazarico, D. E. Smith, M. T. Zuber, E. Harju, M. L. Delitsky, and S. C. Solomon. Thermal Stability of Volatiles in the North Polar Region of Mercury. *Science*, 339(6117):300–303, 2013. doi: 10.1126/science.1231106.

T. Panambur, T. Sander, K. Wohlfarth, M. Martinot, S. Zorzan, M. Arnaut, J. L. Bishop, M. Parente, and C. Wöhler. Using machine learning to find relationships between different lunar maps: A case study of lunar hydration. *AGU24*, 2024:IN51B–06, 2024.

V. Parmentier and I. J. M. Crossfield. Exoplanet Phase Curves: Observations and Theory. In H. J. Deeg and J. A. Belmonte, editors, *Handbook of Exoplanets*, pages 1419–1440. Springer International Publishing, Cham, 2018. doi: 10.1007/978-3-319-55333-7_116.

A. Penttilä, T. Väisänen, J. Markkanen, J. Martikainen, T. Kohout, G. Videen, and K. Muinonen. Rigorous light-scattering simulations of nanophase iron space-weathering effects on reflectance spectra of olivine grains. *Icarus*, 345:113727, 2020. doi: 10.1016/j.icarus.2020.113727.

E. Pettit and S. B. Nicholson. Lunar radiation and temperatures. *The Astrophysical Journal*, 71:102–135, 1930. doi: 10.1086/143236.

C. M. Pieters and S. K. Noble. Space weathering on airless bodies. *Journal of Geophysical Research: Planets*, 121(10):1865–1884, 2016. doi: 10.1002/2016JE005128.

C. M. Pieters, J. Boardman, B. Buratti, A. Chatterjee, R. Clark, T. Glavich, R. Green, J. Head, P. Isaacson, E. Malaret, T. Mccord, J. Mustard, N. Petro, C. Runyon, M. Staid, J. Sunshine, L. Taylor, S. Tompkins, P. Varanasi, and M. White. The Moon Mineralogy Mapper (M3) on Chandrayaan-1. *Current Science*, 96:500–505, 2009a.

C. M. Pieters, J. N. Goswami, R. N. Clark, M. Annadurai, J. Boardman, B. Buratti, J.-P. Combe, M. D. Dyar, R. Green, J. W. Head, C. Hibbitts, M. Hicks, P. Isaacson, R. Klima, G. Kramer, S. Kumar, E. Livo, S. Lundeen, E. Malaret, T. McCord, J. Mustard, J. Nettles, N. Petro, C. Runyon, M. Staid, J. Sunshine, L. A. Taylor, S. Tompkins, and P. Varanasi. Character and Spatial Distribution of OH/H2O on the Surface of the Moon Seen by M3 on Chandrayaan-1. *Science*, 326(5952):568–572, 2009b. doi: 10.1126/science.1178658.

C. M. Pieters, R. L. Klima, and R. O. Green. Compositional Analysis of the Moon in the Visible and Near-Infrared Regions. In J. L. Bishop, J. F. Bell III, and J. E. Moersch, editors, *Remote Compositional Analysis: Techniques for Understanding Spectroscopy, Mineralogy, and Geochemistry of Planetary Surfaces*, Cambridge Planetary Science, pages 368–392. Cambridge University Press, Cambridge, 2019. doi: 10.1017/9781316888872.020.

M. Planck. Ueber das Gesetz der Energieverteilung im Normalspectrum. *Annalen der Physik*, 309(3):553–563, 1900. doi: 10.1002/andp.19013090310.

R. W. Preisendorfer. *Radiative Transfer on Discrete Spaces.* International series of monographs in pure and applied mathematics. Pergamon Press, Oxford, 1965.

T. H. Prettyman, P. A. J. Englert, and N. Yamashita. Neutron, Gamma-Ray, and X-Ray Spectroscopy: Theory and Applications. In J. L. Bishop, J. F. Bell III, and J. E. Moersch, editors, *Remote Compositional Analysis: Techniques for Understanding Spectroscopy, Mineralogy, and Geochemistry of Planetary Surfaces*, Cambridge Planetary Science, pages 191–238. Cambridge University Press, Cambridge, 2019.

M. S. Ramsey and P. R. Christensen. Mineral abundance determination: Quantitative deconvolution of thermal emission spectra. *Journal of Geophysical Research: Solid Earth*, 103(B1):577–596, 1998. doi: 10.1029/97JB02784.

J. T. Rayner, D. W. Toomey, P. M. Onaka, A. J. Denault, W. E. Stahlberger, W. D. Vacca, M. C. Cushing, and S. Wang. SpeX. *Publications of the Astronomical Society of the Pacific*, 115(805):362–382, 2003. doi: 10.1086/367745.

V. Reddy, J. P. Emery, M. J. Gaffey, W. F. Bottke, A. Cramer, and M. S. Kelley. Composition of 298 Baptistina: Implications for the K/T impactor link. *Meteoritics & Planetary Science*, 44(12):1917–1927, 2009. doi: 10.1111/j.1945-5100.2009.tb02001.x.

S. Redfield, N. Batalha, B. Benneke, B. Biller, N. Espinoza, K. France, Q. Konopacky, L. Kreidberg, E. Rauscher, and D. Sing. Report of the Working Group on Strategic

Exoplanet Initiatives with HST and JWST. *arXiv e-prints*, art. arXiv:2404.02932, April 2024. doi: 10.48550/arXiv.2404.02932.

RELAB. RELAB Spectral Database. Technical report, Brown University, 2014. URL `https://sites.brown.edu/relab/`. Online; accessed December 08, 2023.

A. S. Rivkin, R. P. Binzel, and S. J. Bus. Constraining near-Earth object albedos using near-infrared spectroscopy. *Icarus*, 175(1):175–180, 2005. doi: 10.1016/j.icarus.2004.11.005.

M. S. Robinson, S. L. Murchie, D. T. Blewett, D. L. Domingue, S. E. Hawkins, J. W. Head, G. M. Holsclaw, W. E. McClintock, T. J. McCoy, R. L. McNutt, L. M. Prockter, S. C. Solomon, and T. R. Watters. Reflectance and Color Variations on Mercury: Regolith Processes and Compositional Heterogeneity. *Science*, 321(5885):66–69, 2008. doi: 10.1126/science.1160080.

E. Rognini, M. T. Capria, F. Tosi, M. C. De Sanctis, M. Ciarniello, A. Longobardo, F. G. Carrozzo, A. Raponi, A. Frigeri, E. Palomba, S. Fonte, M. Giardino, E. Ammannito, C. A. Raymond, and C. T. Russell. High Thermal Inertia Zones on Ceres From Dawn Data. *Journal of Geophysical Research: Planets*, 125(3):e2018JE005733, 2020. doi: 10.1029/2018JE005733.

D. Rommel, A. Grumpe, C. Wöhler, A. Morlok, H. Hiesinger, and U. Mall. Nonlinear Spectral Unmixing of Lunar Analog Materials in the Thermal Infrared Range. *European Planetary Science Congress*, 9:606, 2014.

D. Rommel, A. Grumpe, M. P. Felder, C. Wöhler, U. Mall, and A. Kronz. Automatic endmember selection and nonlinear spectral unmixing of Lunar analog minerals. *Icarus*, 284:126–149, 2017. doi: 10.1016/j.icarus.2016.10.029.

A. P. Rossi and S. van Gasselt, editors. *Planetary Geology.* Springer Praxis Books. Springer International Publishing, Cham, 2018. doi: 10.1007/978-3-319-65179-8.

A. P. Rossi, S. van Gasselt, and H. Hiesinger. The Terrestrial Planets. In A.P. Rossi and S. van Gasselt, editors, *Planetary Geology*, pages 249–283. Springer International Publishing, Cham, 2018. doi: 10.1007/978-3-319-65179-8_11.

B. Rozitis and S. F. Green. Directional characteristics of thermal–infrared beaming from atmosphereless planetary surfaces – a new thermophysical model. *MNRAS*, 415(3):2042–2062, 2011. doi: 10.1111/j.1365-2966.2011.18718.x.

B. Rozitis and S. F. Green. The influence of rough surface thermal-infrared beaming on the Yarkovsky and YORP effects. *MNRAS*, 423(1):367–388, 2012. doi: 10.1111/j.1365-2966.2012.20882.x.

B. Rozitis and S. F. Green. The influence of global self-heating on the Yarkovsky and YORP effects. *MNRAS*, 433(1):603–621, 2013. doi: 10.1093/mnras/stt750.

B. Rozitis, J. P. Emery, M. A. Siegler, H. C. M. Susorney, J. L. Molaro, C. W. Hergenrother, and D. S. Lauretta. Implications for Ice Stability and Particle Ejection From High-Resolution Temperature Modeling of Asteroid (101955) Bennu. *Journal of Geophysical Research: Planets*, 125(8):e2019JE006323, 2020. doi: 10.1029/2019JE006323.

L. Rubanenko, N. Schorghofer, B. T. Greenhagen, and D. A. Paige. Equilibrium Temperatures and Directional Emissivity of Sunlit Airless Surfaces With Applications to the Moon. *Journal Geophysical Research: Planets*, 125(6):e2020JE006377, 2020. doi: 10.1029/2020JE006377.

O. Ruesch, M. Hess, K. Wohlfarth, T. Heyer, C. Wöhler, T. R. R. Bontognali, C. Orgel, E. Sefton-Nash, J. L. Josset, and J. L. Vago. Synthetic topography from the decameter to the centimeter scale on Mars for scientific and rover operations of the ESA-Roscosmos ExoMars mission. *Planetary and Space Science*, 205:105301, 2021. doi: 10.1016/j.pss.2021.105301.

S. Ruphy. Limits to Modeling: Balancing Ambition and Outcome in Astrophysics and Cosmology. *Simulation & Gaming*, 42(2):177–194, 2011. doi: 10.1177/1046878108319640.

J. M. Saari, R. W. Shorthill, and D. F. Winter. The sunlit lunar surface. *The moon*, 5(1): 179–199, 1972. doi: 10.1007/BF00562112.

J. W. Salisbury, L. S. Walter, and N. Vergo. Mid-infrared (2.1-25 um) spectra of minerals; first edition. Technical report, U.S. Geological Survey,, 01 1987.

A. B. Sanin, I. G. Mitrofanov, M. L. Litvak, B. N. Bakhtin, J. G. Bodnarik, W. V. Boynton, G. Chin, L. G. Evans, K. Harshman, F. Fedosov, D. V. Golovin, A. S. Kozyrev, T. A. Livengood, A. V. Malakhov, T. P. McClanahan, M. I. Mokrousov, R. D. Starr, R. Z. Sagdeev, V. I. Tret'yakov, and A. A. Vostrukhin. Hydrogen distribution in the lunar polar regions. *Icarus*, 283:20–30, 2017. doi: 10.1016/j.icarus.2016.06.002.

H. Sato, M. S. Robinson, B. Hapke, B. W. Denevi, and A. K. Boyd. Resolved Hapke parameter maps of the Moon. *Journal of Geophysical Research: Planets*, 119(8):1775–1805, 2014. doi: 10.1002/2013JE004580.

D. Saupe. Random Fractals in Image Synthesis. In A. J. Crilly, R. A. Earnshow, and H. Jones, editors, *Fractals and Chaos*, pages 89–118. Springer, New York, 1991. doi: 10.1007/978-1-4612-3034-2_6.

D. Schauten. Thermische Modellierung von planetaren Oberflächen: Modellierung und Analyse verschiedener Rauigkeitsskalen. *Bachelor's thesis, TU Dortmund University*, 2021.

N. Schmedemann, H. Hiesinger, K. Wohlfarth, C. Wöhler, K. Bauch, M. D'Amore, J. Helbert, A. Maturilli, A. Morlok, M. Reitze, A. Stojic, I. Weber, I. Varatharajan, and the MERTIS Team. BepiColombo - Correction of MERTIS Geometry. *Lunar and Planetary Science Conference*, 52:1290, 2021.

F. Schmidt and J. Fernando. Realistic uncertainties on Hapke model parameters from photometric measurements. *European Planetary Science Congress*, page 331, 2015.

F. Scholten, J. Oberst, K.-D. Matz, T. Roatsch, M. Wählisch, E. J. Speyerer, and M. S. Robinson. GLD100: The near-global lunar 100 m raster DTM from LROC WAC stereo image data. *Journal of Geophysical Research: Planets*, 117(E12):2011JE003926, 2012. doi: 10.1029/2011JE003926.

N. Schörghofer, M. Benna, A. A. Berezhnoy, B. Greenhagen, B. M. Jones, S. Li, T. M. Orlando, P. Prem, O. J. Tucker, and C. Wöhler. Water Group Exospheres and Surface Interactions on the Moon, Mercury, and Ceres. *Space Science Reviews*, 217(74), 2021. doi: 10.1007/s11214-021-00846-3.

D. J. Schroeder. *Astronomical Optics*. Academic Press, San Diego, 2000. doi: 10.1016/B978-0-12-629810-9.X5000-2.

P. H. Schultz and L. J. Srnka. Cometary collisions on the Moon and Mercury. *Nature*, 284 (5751):22–26, 1980. doi: 10.1038/284022a0.

M. Seifert, K. Wohlfarth, T. Müller, S. Adriaensen, D. Nuyts, J. Léon-Tavares, J. Blommaert, F. Kahil, J. Mollière C1, Gottfriedsen, M. Langer, and D. Rio Fernandes. Lunar calibration of Earth observation thermal infrared imagers using cross-calibration and thermo-physical models. *VH-RODA*, 2024.

R. U. Sexl, H. Sexl, H. Stremnitzer, and D. G. Burkhard. The Directional Characteristics of Lunar Infrared Radiation. *Moon*, 3(2):189–213, 1971. doi: 10.1007/BF00561908.

M. K. Shepard. *Introduction to Planetary Photometry*. Cambridge University Press, 2017.

M. K. Shepard and P. Helfenstein. A test of the Hapke photometric model. *Journal of Geophysical Research: Planets*, 112(E3), 2007. doi: 10.1029/2005JE002625.

Y. Shkuratov, V. Kaydash, V. Korokhin, Y. Velikodsky, N. Opanasenko, and G. Videen. Optical measurements of the Moon as a tool to study its surface. *Planetary and Space Science*, 59(13):1326–1371, 2011. doi: 10.1016/j.pss.2011.06.011.

Y. Shkuratov, V. Kaydash, V. Korokhin, Y. Velikodsky, D. Petrov, E. Zubko, D. Stankevich, and G. Videen. A critical assessment of the Hapke photometric model. *Journal of Quantitative Spectroscopy and Radiative Transfer*, 113(18):2431–2456, 2012. doi: 10.1016/j.jqsrt.2012.04.010.

Y. Shkuratov, V. Kaydash, V. Korokhin, Y. Velikodsky, D. Petrov, E. Zubko, D. Stankevich, and G. Videen. Response to the comment by B. Hapke on “A critical assessment of the Hapke photometric model”. *Journal of Quantitative Spectroscopy and Radiative Transfer*, 116:191–195, 2013. doi: 10.1016/j.jqsrt.2012.11.004.

W. M. Sinton. Temperatures on the Lunar Surface. In Z. Kopal, editor, *Physics and Astronomy of the Moon*, pages 407–428. Academic Press, New York, 1961.

B. G. Smith. Lunar surface roughness: Shadowing and thermal emission. *Journal of Geophysical Research*, 72(16):4059–4067, 1967. doi: 10.1029/JZ072i016p04059.

W. J. Smith. *Modern Optical Engineering: The Design of Optical Systems.* McGraw-Hill series on optical and electro-optical engineering. McGraw-Hill, New York, 2000.

J. Snoek, H. Larochelle, and R. P Adams. Practical Bayesian Optimization of Machine Learning Algorithms. In F. Pereira, C.J. Burges, L. Bottou, and K.Q. Weinberger, editors, *Advances in Neural Information Processing Systems*, volume 25. Curran Associates, Inc., 2012.

J. R. Spencer. A rough-surface thermophysical model for airless planets. *Icarus*, 83:27–38, 1990. doi: 10.1016/0019-1035(90)90004-S.

J. R. Spencer, L. A. Lebofsky, and M. V. Sykes. Systematic biases in radiometric diameter determinations. *Icarus*, 78(2):337–354, 1989. doi: 10.1016/0019-1035(89)90182-6.

A. Sprague, J. Warell, G. Cremonese, Y. Langevin, J. Helbert, P. Wurz, I. Veselovsky, S. Orsini, and A. Milillo. Mercury's Surface Composition and Character as Measured by Ground-Based Observations. *Space Science Reviews*, 132(2-4):399–431, 2007. doi: 10.1007/s11214-007-9221-3.

K. Stamnes, G. E. Thomas, and J. J. Stamnes. *Radiative Transfer in the Atmosphere and Ocean.* Cambridge University Press, Cambridge, 2017. doi: 10.1017/9781316148549.

L. V. Starukhina and Y. G. Shkuratov. The Lunar Poles: Water Ice or Chemically Trapped Hydrogen? *Icarus*, 147(2):585–587, 2000. doi: 10.1006/icar.2000.6476.

B. Sun, L. Bi, P. Yang, M. Kahnert, and G. Kattawar. Fundamentals. In *Invariant Imbedding T-Matrix Method for Light Scattering by Nonspherical and Inhomogeneous Particles*, pages 7–56. Elsevier, 2020a. doi: 10.1016/B978-0-12-818090-7.00002-4.

B. Sun, L. Bi, P. Yang, M. Kahnert, and G. Kattawar. T-matrix concept. In *Invariant Imbedding T-Matrix Method for Light Scattering by Nonspherical and Inhomogeneous Particles*, pages 57–144. Elsevier, 2020b. doi: 10.1016/B978-0-12-818090-7.00003-6.

J. M. Sunshine, T. L. Farnham, L. M. Feaga, O. Groussin, F. Merlin, R. E. Milliken, and M. F. A'Hearn. Temporal and Spatial Variability of Lunar Hydration As Observed by the Deep Impact Spacecraft. *Science*, 326(5952):565–568, 2009. doi: 10.1126/science.1179788.

D. Takir and J. P. Emery. Outer Main Belt asteroids: Identification and distribution of four 3-μm spectral groups. *Icarus*, 219(2):641–654, 2012. doi: 10.1016/j.icarus.2012.02.022.

L. A. Taylor, C. M. Pieters, L. P. Keller, R. V. Morris, and D. S. McKay. Lunar mare soils: Space weathering and the major effects of surface-correlated nanophase Fe. *Journal of Geophysical Research: Planets*, 106(E11):27985–28000, 2001. doi: 10.1029/2000JE001402.

L. A. Taylor, C. Pieters, A. Patchen, D.-H. S. Taylor, R. V. Morris, L. P. Keller, and D. S. McKay. Mineralogical and chemical characterization of lunar highland soils: Insights into the space weathering of soils on airless bodies. *Journal of Geophysical Research: Planets*, 115(E2), 2010. doi: 10.1029/2009JE003427.

S. R. Taylor. *Planetary Science: A Lunar Perspective.* Lunar and Planetary Institute, Houston, 1982.

J. Tennyson. *Astronomical Spectroscopy: An Introduction To The Atomic And Molecular Physics Of Astronomical Spectroscopy.* Advanced Textbooks In Physics. World Scientific Publishing Company, London, 2019.

M. Tenthoff. 3D-Rekonstruktion der Merkuroberfläche mit Shape from Shading. *Bachelor's thesis, TU Dortmund University*, 2019.

M. Tenthoff. Reflectance and Emission Models for Airless Planetary Bodies: Application to Solar System Objects and Exoplanets. *Master's thesis, TU Dortmund University*, 2023.

M. Tenthoff, K. Wohlfarth, and C. Wöhler. High Resolution Digital Terrain Models of Mercury. *Remote Sensing*, 12(23):3989, 2020. doi: 10.3390/rs12233989.

M. Tenthoff, C. Wöhler, and K. Wohlfarth. Accurate 3D Reconstruction of Mercury with Shape from Shading. *Mercury 2022*, pages 98–98, 2022.

M. Tenthoff, M. Arnaut, T. Barot, N. Elkhouly, M. Faizan, A. Gulati, D. Hallmann, M. Karam, A. Nedungadi, J. Ravikumar, M. Hess, K. Wohlfarth, and C. Wöhler. 3D Models of the Martian Surface in Virtual Reality. *AAS/Division for Planetary Sciences Meeting*, 55:212.04, 2023a.

M. Tenthoff, K. Wohlfarth, S. Zieba, L. Kreidberg, and C. Wöhler. How does Surface Roughness affect the Phase Curve of Airless Exoplanets? *Thermal Modeling for Planetary Science IV (TherMoPS IV)*, 4:71, 2023b.

M. Tenthoff, K. Wohlfarth, C. Wöhler, S. Zieba, and L. Kreidberg. Reflectance and Emission Modelling of Airless Exoplanets. *European Planetary Science Congress*, pages EPSC2024–649, 2024. doi: 10.5194/epsc2024-649.

M. Tenthoff, K. Wohlfarth, C. Wöhler, N. Schmedemann, K. E. Bauch, N. Verma, T. M. Powell, B. Greenhagen, M. Knollenberg, M. D'Amore, S. Adeli, H. Hiesinger, J. Helbert, and MERTIS Team. Thermal modeling of Mercury's surface: Parameter estimation from MERTIS flyby data. *Lunar and Planetary Science Conference*, 56:2272, 2025.

The MathWorks Inc. Global Optimization Toolbox, 2022a. URL `https://www.mathworks.com/help/gads/index.html`. Online; accessed February 18, 2025.

The MathWorks Inc. Statistics and Machine Learning Toolbox, 2022b. URL `https://www.mathworks.com/help/stats/index.html`. Online; accessed February 18, 2025.

S. Tompkins and C. M. Pieters. Spectral characteristics of lunar impact melts and inferred mineralogy. *Meteoritics & Planetary Science*, 45(7):1152–1169, 2010. doi: 10.1111/j.1945-5100.2010.01074.x.

D. Trang and P. G. Lucey. Improved space weathering maps of the lunar surface through radiative transfer modeling of Kaguya multiband imager data. *Icarus*, 321:307–323, 2019. doi: 10.1016/j.icarus.2018.11.014.

D. Trang, P. G. Lucey, J. J. Gillis-Davis, J. T. S. Cahill, R. L. Klima, and P. J. Isaacson. Near-infrared optical constants of naturally occurring olivine and synthetic pyroxene as a function of mineral composition. *Journal of Geophysical Research: Planets*, 118(4): 708–732, 2013. doi: 10.1002/jgre.20072.

K. E. Vander Kaaden and F. M. McCubbin. Exotic crust formation on Mercury: Consequences of a shallow, FeO-poor mantle. *Journal of Geophysical Research: Planets*, 120(2): 195–209, 2015. doi: 10.1002/2014JE004733.

R. Vanderspek, C. X. Huang, A. Vanderburg, G. R. Ricker, D. W. Latham, S. Seager, J. N. Winn, J. M. Jenkins, J. Burt, J. Dittmann, E. Newton, S. N. Quinn, A. Shporer, D. Charbonneau, J. Irwin, K. Ment, J. G. Winters, K. A. Collins, P. Evans, T. Gan, R. Hart, E. L. N. Jensen, J. Kielkopf, S. Mao, W. Waalkes, F. Bouchy, M. Marmier, L. D. Nielsen, G. Ottoni, F. Pepe, D. Ségransan, S. Udry, T. Henry, L. A. Paredes, H.-S. James, R. H. Hinojosa, M. L. Silverstein, E. Palle, Z. Berta-Thompson, I. Crossfield, M. D. Davies, D. Dragomir, M. Fausnaugh, A. Glidden, J. Pepper, E. H. Morgan, M. Rose, J. D. Twicken, J. N. S. Villaseñor, L. Yu, G. Bakos, J. Bean, L. A. Buchhave, J. Christensen-Dalsgaard, J. L. Christiansen, D. R. Ciardi, M. Clampin, N. D. Lee, D. Deming, J. Doty, J. G. Jernigan, L. Kaltenegger, J. J. Lissauer, P. R. McCullough, N. Narita, M. Paegert, A. Pal, S. Rinehart, D. Sasselov, B. Sato, A. Sozzetti, K. G. Stassun, and G. Torres. TESS Discovery of an Ultra-short-period Planet around the Nearby M Dwarf LHS 3844. *The Astrophysical Journal Letters*, 871(2):L24, 2019. doi: 10.3847/2041-8213/aafb7a.

I. Varatharajan, C. Tsang, K. Wohlfarth, C. Wöhler, N. Izenberg, and J. Hebert. Surface Composition of Mercury from NIR (0.7-4.2 μm) Ground-Based IRTF/SpeX Spectroscopy. *EPSC-DPS Joint Meeting 2019*, 2019:EPSC–DPS2019–1331, 2019.

I. Varatharajan, C. Tsang, K. Wohlfarth, C. Wöhler, N. Izenberg, and J. Helbert. Simulation of combined reflectance and emittance spectra in the thermal infrared band on mercury. *European Planetay Science Congress 2019, Abstract No. 1331*, 2019.

I. Varatharajan, C. Tsang, K. Wohlfarth, C. Wöhler, N. Izemberg, and J. Helbert. Surface Mineralogy of Major Geochemical Terranes of Mercury: Results from NIR (0.7-4.2 microns) Ground Based IRTF/SpeX Spectroscopy. *Lunar and Planetary Science Conference*, 52:1359, 2021.

A. R. Vasavada, D. A. Paige, and S. E. Wood. Near-Surface Temperatures on Mercury and the Moon and the Stability of Polar Ice Deposits. *Icarus*, 141(2):179–193, 1999. doi: 10.1006/icar.1999.6175.

A. R. Vasavada, J. L. Bandfield, B. T. Greenhagen, P. O. Hayne M. A., Siegler, and J.-P. Williams D. A. Paige. Lunar equatorial surface temperatures and regolith properties from the Diviner Lunar Radiometer Experiment. *Journal of Geophysical Research: Planets*, 117(E12), 2012. doi: 10.1029/2011JE003987.

P. Vernazza, F. DeMeo, D. A. Nedelcu, M. Birlan, A. Doressoundiram, S. Erard, and E. Volquardsen. Resolved spectroscopy of Mercury in the near-IR with SpeX/IRTF. *Icarus*, 209(1):125–137, 2010. doi: 10.1016/j.icarus.2009.12.010.

J. Warell. Properties of the Hermean Regolith: II. Disk-Resolved Multicolor Photometry and Color Variations of the "Unknown" Hemisphere. *Icarus*, 156(2):303–317, 2002. doi: 10.1006/icar.2002.6814.

J. Warell. Properties of the hermean regolith: iii. disk-resolved vis–NIR reflectance spectra and implications for the abundance of iron - Based on observations made with the Nordic Optical Telescope, operated on the island of La Palma jointly by Denmark, Finland, Iceland, Norway, and Sweden, in the Spanish Observatorio del Roque de los Muchachos of the Instituto de Astrofisica de Canarias. *Icarus*, 161(2):199–222, 2003. doi: 10.1016/S0019-1035(02)00055-6.

J. Warell. Properties of the Hermean regolith: IV. Photometric parameters of Mercury and the Moon contrasted with Hapke modelling. *Icarus*, 167(2):271–286, 2004. doi: 10.1016/j.icarus.2003.10.010.

J. Warell and D. T. Blewett. Properties of the Hermean regolith: V. New optical reflectance spectra, comparison with lunar anorthosites, and mineralogical modelling. *Icarus*, 168(2): 257–276, 2004. doi: 10.1016/j.icarus.2003.10.020.

J. Warell and S. S. Limaye. Properties of the Hermean regolith: I. Global regolith albedo variation at 200km scale from multicolor CCD imaging. *Planetary and Space Science*, 49 (14):1531–1552, 2001. doi: 10.1016/S0032-0633(01)00091-5.

J. Warell, A. L. Sprague, J. P. Emery, R. W. H. Kozlowski, and A. Long. The 0.7–5.3 μm IR spectra of Mercury and the Moon: Evidence for high-Ca clinopyroxene on Mercury. *Icarus*, 180(2):281–291, 2006. doi: 10.1016/j.icarus.2005.09.007.

T. J. Warren, N. E. Bowles, K. Donaldson Hanna, and J. L. Bandfield. Modeling the Angular Dependence of Emissivity of Randomly Rough Surfaces. *Journal of Geophysical Research: Planets*, 124(2):585–601, 2019. doi: doi.org/10.1029/2018JE005840.

P. C. Waterman. Matrix formulation of electromagnetic scattering. *Proceedings of the IEEE*, 53(8):805–812, 1965. doi: 10.1109/PROC.1965.4058.

I. Weber, M. P. Reitze, A. Morlok, A. N. Stojic, H. Hiesinger, N. Schmedemann, K. E. Bauch, J. H. Pasckert, and J. Helbert. Mid-IR spectral properties of different surfaces of silicate mixtures before and after excimer laser irradiation. *Icarus*, 404:115683, 2023. doi: 10.1016/j.icarus.2023.115683.

S. Z. Weider, L. R. Nittler, R. D. Starr, E. J. Crapster-Pregont, P. N. Peplowski, B. W. Denevi, J. W. Head, P. K. Byrne, S. A. Hauck, D. S. Ebel, and S. C. Solomon. Evidence for geochemical terranes on Mercury: Global mapping of major elements with MESSENGER's X-Ray Spectrometer. *Earth and Planetary Science Letters*, 416:109–120, 2015. doi: 10.1016/j.epsl.2015.01.023.

T. Wilhelm, M. Geis, J. Püttschneider, T. Sievernich, T. Weber, K. Wohlfarth, and C. Wöhler. DoMars16k: A Diverse Dataset for Weakly Supervised Geomorphologic Analysis on Mars. *Remote Sensing*, 12(23):3981, 2020. doi: 10.3390/rs12233981.

D. R. Williams. Mercury factsheet. Technical report, NASA Goddard Space Flight Center, 2023. URL `https://nssdc.gsfc.nasa.gov/planetary/factsheet/mercuryfact.html`. Online; accessed December 08, 2023.

W. Windelband. Rede zum Antritt des Rektorats der Kaiser-Wilhelm-Universität Straßburg, 1904.

W. Windelband, J. Bohr, and S. Luft. *Präludien: Aufsätze und Reden zur Philosophie und ihrer Geschichte*. Philosophische Bibliothek. Felix Meiner Verlag, Hamburg, 2021.

C. Wöhler, A. Grumpe, A. A. Berezhnoy, and V. V. Shevchenko. Time-of-day–dependent global distribution of lunar surficial water/hydroxyl. *Science Advances*, 3(9):e1701286, 2017. doi: 10.1126/sciadv.1701286.

C. Wöhler, K. Wohlfarth, and A. A. Berezhnoy. Time-of-Day-Dependent Behavior of Lunar Surficial Hydroxyl on a Rough Regolith Surface. *Lunar and Planetary Science Conference*, 53:1492, 2022.

K. Wohlfarth and C. Wöhler. Wavelength-Dependent Seeing Systematically Changes the Normalized Slope of Telescopic Reflectance Spectra of Mercury. *Remote Sensing*, 14(2): 405, 2022. doi: 10.3390/rs14020405.

K. Wohlfarth and C. Wöhler. A Mystery solved: Wavelength-dependent Seeing changes the normalized spectral slope of Mercury. *Mercury 2022*, pages 100–101, 2022.

K. Wohlfarth and C. Wöhler. A new roughness model for the Moon and other airless bodies. In M. Bali, editor, *GSICS Quaterly*, volume 2024, pages 5–7, 2024. doi: 10.25923/6c4m-y998.

K. Wohlfarth, A. Grumpe, C. Wöhler, A. Stojic, A. Morlok, and H. Hiesinger. Simulation of Space-Weathered TIR Spectra on Mercury. *European Planetary Science Congress*, pages EPSC2018–649, 2018.

K. Wohlfarth, C. Schröer, M. Klaß, S. Hakenes, M. Venhaus, S. Kauffmann, T. Wilhelm, and C. Wöhler. Dense Cloud Classification on Multispectral Satellite Imagery. *2018 10th IAPR Workshop on Pattern Recognition in Remote Sensing (PRRS)*, pages 1–6, 2018. doi: 10.1109/PRRS.2018.8486379.

K. Wohlfarth, A Grumpe, C. Wöhler, J. Maturilli, A. andHelbert, A. Morlok, and H. Hiesinger. Combined Reflectance and Emittance Model for Spectral Unmixing. *Thermal Modeling for Planetary Science III (TherMoPS III)*, 3, 2019a.

K. Wohlfarth, C. Wöhler, and A. Grumpe. How Does Space Weathering Affect the Detection of Lunar OH/H2O? Insights from Ab-Initio Mie Modeling of Submicroscopic Iron. *Lunar and Planetary Science Conference*, 50:2584, 2019b.

K. Wohlfarth, C. Wöhler, K. Bauch, M. D'Amore, H. Hiesinger, J. Helbert, A. Maturilli, A. Morlok, M. P. Reitze, N. Schmedemann, A. Stojic, I. Varaharajan, and I. Weber. The Lunar EPI-Regolith — A Hypothesis to Explain the Lunar Flyby Data of MERTIS. *52nd Lunar and Planetary Science Conference*, 52:1236, 2021a.

K. Wohlfarth, C. Wöhler, K. Bauch, M. D'Amore, H. Hiesinger, J. Helbert, A. Maturilli, A. Morlok, M. P. Reitze, N. Schmedemann, A. Stojic, I. Varaharajan, and I. Weber. A Fractal Rough Thermal Model for Emissivity Retrieval of MERTIS Lunar Flyby Spectra. *Lunar and Planetary Science Conference*, 52:1241, 2021b.

K. Wohlfarth, C. Wöhler, K. E. Bauch, M. D'Amore, H. Hiesinger, J. Helbert, A. Maturilli, A. Morlok, M. P. Reitze, N. Schmedemann, A. N. Stojic, I. Varatharajan, and I. Weber. Mercury is hot: A fractal thermal roughness Model for MERTIS spectral calibration. *Mercury 2022*, pages 102–103, 2022a.

K. Wohlfarth, M. Tenthoff, J. Wright, V. Galluzzi, C. A. Wöhler, H. Hiesinger, J. Helbert, J. Zender, and J. Benkhoff. Computational Models for Mercury Surface Analysis. *Mercury Exploration Assessment Group (MExAG) Annual Meeting 2023*, 2023.

K. Wohlfarth, C. Wöhler, H. Hiesinger, and J. Helbert. An advanced thermal roughness model for airless planetary bodies. Implications for global variations of lunar hydration and mineralogical mapping of Mercury with the MERTIS spectrometer. *Astronomy & Astrophysics*, 674:A69, 2023. doi: 10.1051/0004-6361/202245343.

K. Wohlfarth, M. Martinot, T. Panambur, T. Sander, S. Zorzan, M. Arnaut, J. L. Bishop, M. Parente, and C. Wöhler. Seeking Relationships Between Lunar Hydration and Surface Composition. *AGU24*, 2024:P41C–02, 2024.

K. S. Wohlfarth. Reflectance and Emittance Spectroscopy based Unmixing of Planetary Spectra. *Master's thesis, TU Dortmund University*, 2018.

K. S. Wohlfarth and C. Wöhler. Computational Techniques for Fractal Rough Thermal Models. *Thermal Modeling for Planetary Science IV (TherMoPS IV)*, 4:15, 2023.

K. S. Wohlfarth, A. Grumpe, C. Wöhler, A. Morlok, and H. Hiesinger. Combined Reflectance and Emittance Spectroscopy in the Thermal Infrared Band: Implications for Mercury. *49th Annual Lunar and Planetary Science Conference*, 49:2519, 2018a.

K. S. Wohlfarth, W. C. Liu, B. Wu, A. Grumpe, and C. Wöhler. High Resolution Digital Terrain Models of the Martian Surface: Compensation of the Atmosphere on CTX Imagery. *49th Annual Lunar and Planetary Science Conference*, 49:2498, 2018b.

K. S. Wohlfarth, C. Wöhler, and A. Grumpe. Space Weathering and Lunar OH/H2O - Insights from Ab Initio Mie Modeling of Submicroscopic Iron. *The Astronomical Journal*, 158(2):80, 2019. doi: 10.3847/1538-3881/ab26af.

K. S. Wohlfarth, C. Wöhler, J. Helbert, H. Hiesinger, and Mertis-Team. Disk-Resolved Validation of a Fractal Rough Thermal Model for the Moon. *Lunar and Planetary Science Conference*, 53:2431, 2022b.

K. S. Wohlfarth, M. Tenthoff, and C. Wöhler. How does small-scale roughness influence thermal infrared spectra around Mercury's north pole? *Thermal Modeling for Planetary Science IV (TherMoPS IV)*, 4:57, 2023a.

K. S. Wohlfarth, C. Wöhler, J. Helbert, and H. Hiesinger. A New Thermal Roughness Model for the Moon and Mercury: implications for the diurnal lunar hydroxyl cycle and mineralogical mapping with MERTIS onboard Bepicolombo. *Thermal Modeling for Planetary Science IV (TherMoPS IV)*, 4:47, 2023b.

Y. Wu. The 'super blood wolf Moon' from space. *Nature Astronomy*, 3(3):204–204, 2019. doi: 10.1038/s41550-019-0719-x.

Y. Wu and B. Hapke. Spectroscopic observations of the Moon at the lunar surface. *Earth and Planetary Science Letters*, 484:145–153, 2018. ISSN 0012-821X. doi: doi.org/10.1016/j.epsl.2017.12.003.

Y. Wu, Q. Jin, C. Li, T. Xu, W. Qi, W. Tan, X. Li, Z. Shi, H. He, S. Dai, G. Li, F. Liu, J. Wang, X. Wang, Y. Lu, W. Cai, Q. Wang, L. Meng, and D. Guo. Unveiling the Secrets of the Midinfrared (3–5 μm) Moon. *Geophysical Research Letters*, 48(4):e2020GL088393, 2021. doi: 10.1029/2020GL088393.

H. Yang and M. Burgdorf. A Calibrated Lunar Microwave Radiative Transfer Model Based on Satellite Observations. *Remote Sensing*, 14(21), 2022. doi: 10.3390/rs14215501.

C. N. Yasanayake, B. W. Denevi, B. L. Jolliff, S. J. Lawrence, and R. R. Ghent. The Spectral Characteristics of Lunar Agglutinates. *Lunar and Planetary Science Conference*, 49:2159, 2018.

C. N. Yasanayake, B. W. Denevi, T. Hiroi, B. L. Jolliff, A. C. Martin, A. L. Gao, M. L. Zhang, L. M. Bloom, and S. J. Lawrence. The Spectral Characteristics of Lunar Agglutinates: Visible–Near-Infrared Spectroscopy of Apollo Soil Separates. *Journal of Geophysical Research: Planets*, 129(2):e2023JE008115, 2024. doi: 10.1029/2023JE008115.

S. Zieba, L. Kreidberg, E. Ducrot, M. Gillon, C. Morley, L. Schaefer, P. Tamburo, D. D. B. Koll, X. Lyu, L. Acuña, E: Agol, A. R. Iyer, R. Hu, A. P. Lincowski, V. S. Meadows, F. Selsis, E. Bolmont, A. M. Mandell, and G. Suissa. No thick carbon dioxide atmosphere on the rocky exoplanet TRAPPIST-1 c. *Nature*, 620(7975):746–749, 2023. doi: 10.1038/s41586-023-06232-z.

S. Zieba, L. Kreidberg, R. Hu, C. Morley, K. Wohlfarth, M. Tenthoff, and C Wöhler. The search for regolith on the airless exoplanet LHS3844b. *James Webb Space Telescope Proposal*, Cycle 2(4008), 2023. URL `https://www.stsci.edu/jwst/phase2-public/4008.pdf`. Online; accessed December 4, 2023.

List of Figures

List of Tables

List of Abbreviations

ALFOCS	Alhambra Faint Object Spectrograph and Camera. 63, 64
AMSA	anisotropic multiple scattering approximation. 31
BOTS	bright object time series. 65
CBOE	coherent backscatter opposition effect. 31, 41
CCD	charge-coupled device. 54
CIPW	Cross Iddings, Pirsson, Washington. 19
CMS	Compact Modular Sounder. 61
DDT	Director's Discretionary Time. 112, 169
DEM	digital elevation model. 29
DHG	double-lobed Henyey-Greenstein. xi, xii, 40, 41, 151
EPF	emission phase function. xxxiii–xl, 7, 15, 52, 60, 61, 68, 77, 78, 87–90, 107–109, 119, 169
ESA	European Space Agency. 18, 20
FATT	Factor Analysis Target Transform. 57
FWHM	full-width half maximum. 55, 56, 93, 149, 151, 152, 154, 157, 158, 160
GF-4	Gaofen-4. xxx, xxxi, xli, xlii, 7, 28, 59, 63, 65–69, 76–78, 82, 84, 86, 91, 105–110, 115, 116, 118, 119, 167–169
GLD100	Global Lunar DTM. 66

GO	General Observer Program. 8, 65, 70
GSI	ground sampling interval. 62, 65, 66
HRP	high reflectance material. 20
HVM^3	High-Resolution Volatiles Mineral Moon Mapper. 9, 17, 61, 62, 169
IBD	Integrated Band-Depth. 143
IBD$_{3\mu\mathrm{m}}$	Integrated Band-Depth at $3\,\mu$m. xlv, 75, 76, 91, 92, 119, 120, 133, 135–137, 139, 140, 142–144, 148, 169–171
IIRS	Imaging Infrared Spectrometer. 9, 17, 61, 62, 169
IP	intermediate plains. 20
IRTF	Infrared Telescope Facility. 17, 63, 64
JAXA	Japan Aerospace Exploration Agency. 18, 20
JWST	James Webb Space Telescope. 8, 21, 53, 65, 70, 80, 102, 112, 169
KS	Kaasalainen-Shkuratov. 42, 43, 150, 151, 154–164, 171
LBP	low reflectance blue plains. 20
LHS	Luyten Half-Second. 1, 8, 21, 53, 57, 65, 68, 70, 76, 80, 82, 102–104, 112, 115, 122, 169
LOLA	Lunar Orbiter Laser Altimeter. 65
LRM	Low-reflectance material. 18, 20
LRO	Lunar Reconnaissance Orbiter. 7, 14, 52, 60
LTM	Lunar Thermal Mapper. 61, 62, 169
M^3	Moon Mineralogy Mapper. xxxi, xlvii, xlviii, 8, 9, 16, 17, 28, 52, 61, 66–69, 73, 75–78, 85, 87, 88, 91, 102, 108, 110, 111, 115, 116, 119–121, 125, 127–131, 133–137, 139, 140, 146, 148, 168–170
MASCS	Mercury Atmospheric and Surface Composition Spectrometer. 19

MATLAB	MATrix LABoratory. xli, xlii, 79
MDIS	Mercury Dual Imaging System. xxxii, 18, 19, 43, 63, 69, 70, 79, 121, 150, 151, 163–165
MERTIS	MErcury Radiometer and Thermal Infrared Spectrometer. 3, 8, 9, 20, 28, 52, 53, 57, 62, 63, 66–70, 76, 78–80, 82, 93, 98, 107–109, 111, 120, 121, 168–170, III
MESSENGER	Mercury Surface, Space Environment, Geochemistry and Ranging. 10, 17–20, 63, 69, 79, 149
MGNS	Mercury Gamma-ray and Neutron Spectrometer. 20
MIO	Mercury Magnetospheric Orbiter. 20
MIR	mid-infrared. 26, 54, 56, 57, 59, 61, 63, 77, 78, 82, 87–89, 105, 106, 109, 111, 112, 132, 133, 167
MIXS	Mercury Imaging X-ray spectrometer. 20
mpFe^0	microphase iron. xlvii, xlviii, 13, 44, 130, 132, 133, 139, 142
MPO	Mercury Planetary Orbiter. 20
MSA	micro shutter array. 65
MTF	modulation transfer function. 55
NAC	narrow-angle camera. 63
NASA	National Aeronautics and Space Administration. 17, 29, 61, 79
NEATM	near earth asteroid thermal model. 51
NIR	near-infrared. 9, 10, 26, 56, 59–61, 63, 77, 78, 82, 109, 146
NIRSpec	Near-Infrared Spectrograph. 8, 65, 68, 80, 102, 112, 169
NOT	Nordic Optical Telescope. 63, 64
npFe^0	nanophase iron. xlvii, 13, 44, 123, 130, 132, 133, 139, 142
NTT	New Technology Telescope. 63, 64
PDS	Planetary Data System. 61, 75
PSF	point spread function. 55, 56, 76–79, 93, 107, 120, 149

RMSE	root mean square error. xlvii, xlviii, 86–88, 105, 117, 119, 120, 139, 140, 142, 170
RMSL	root mean square slope. xxix, 15, 42, 51, 52, 83, 85, 87, 89, 90, 105, 107, 109, 110, 116, 119, 167, 169
RTE	radiative transfer equation. 31
RTT	radiative transfer theory. 31
SHOE	shadow-hiding opposition effect. 31, 41
smFe^0	submicroscopic iron. 13, 43, 44, 124, 125, 128–130, 132, 135, 137, 139, 142, 147, 148, 170
Sofi	Son of ISAAC. 63, 64
SOFIA	Stratospheric Observatory for Infrared Astronomy. 17
SpeX	Spectrograph at the IRTF facility. 17, 64, 110, 163
STM	standard thermal model. 51
SVST	Swedish Vacuum Solar Telescope. 63, 64
SVWF	spherical vector wave function. xxi, 35, 37, 38
TEM	Tunneling Electron Microscope. xlvii, 9, 13, 124, 130, 147, 171
TESS	Transiting Exoplanet Survey Satellite. 70
TIR	thermal infrared. 26, 112
TPM	thermophysical model. 51, 78
TRAPPIST	Transiting Planets and Plenetesimals Small Telescope. 8, 21
VNIR	visible and near-infrared. 19, 54, 59, 63
WAC	wide-angle camera. 63

List of Symbols

Symbol	**Unit**	**Description**
A	[m^2]	Area
a_0, a_1, a_2	–	Phase function parameters for the KS model
$a_{\mathrm{A_{dh}}}$	–	Scale factor for the directional-hemispherical albedo
dA	[m^2]	Differential surface element
A_{dh}	–	Directional-hemispherical bolometric albedo
$A_{\mathrm{dh,th}}$	–	Directional-hemispherical bolometric albedo in the thermal regime
A_{eq}	–	Equigonal albedo
$a_{\mathrm{l}}^{\mathrm{i}}$	–	Expansion coefficients of the field at the i$^{\mathrm{th}}$ particle
$a_{\mathrm{inc,l}}^{\mathrm{i}}$	–	Expansion coefficients of the incidence field at the i$^{\mathrm{th}}$ particle
$a_{\mathrm{n}}^{\mathrm{Mie}}$	–	Mie coefficients
a_{mn}	–	Expansion coefficients of the incidence field
A_{n}	–	Hapke expansion coefficients
$A_{\vec{n}}$	–	Normal albedo
B_{C0}	–	Coherent backscattering opposition effect amplitude
B_{CB}	–	Coherent backscattering opposition effect
β_{klm}	–	Legendre expansion coefficients for scattering amplitudes helper function
β_{p}	[°]	Photometric latitude
b_{j}	[m^2]	Area of the j$^{\mathrm{th}}$surface element
$b_{\mathrm{n}}^{\mathrm{Mie}}$	–	Mie coefficients
b_{mn}	–	Expansion coefficients of the incidence field
b_{n}	–	Legendre-coefficient for DHG phase function

Symbol	Unit	Description
B_{S0}	–	Shadow-hiding opposition effect amplitude
B_{SH}	–	Shadow-hiding opposition effect
c	–	Relative strength of scattering lobes in the DHG phase fucntion
c_0	$[\mathrm{m} \cdot \mathrm{s}^{-2}]$	Speed of light
C_{ext}	$[\mathrm{m}^2]$	Extinction cross section
χ_{n}	–	Legendre expansion coefficients for arbitrary phase function
c_{l}	–	Disk function weight (KS3 model)
c_{p}	$[\mathrm{J} \cdot \mathrm{kg}^{-1} \cdot \mathrm{K}^{-1}]$	Specific heat capacity
C_{sca}	$[\mathrm{m}^2]$	Scattering cross section
ct	–	Linear continuum fit
$\mathbf{D}$	$[\mathrm{W} \cdot \mathrm{m}^{-2}]$	Incident flux matrix
D	–	Disk function
d_{j}	$[\mathrm{m}]$	Diameter of particle j
$\mathbf{d}$	$[\mathrm{W} \cdot \mathrm{m}^{-2}]$	Incident flux vector
δ_{ij}	–	Kronecker symbol
$d_{\mathrm{i,j}}$	$[\mathrm{m}]$	Distance between areas that illuminate each other
DN_{nm}	–	Digital number
e	$[^\circ]$	Emission angle
$\mathbf{E}$	$[\mathrm{V} \cdot \mathrm{m}^{-2}]$	Electric field
$\mathbf{E}_1$	$[\mathrm{V} \cdot \mathrm{m}^{-2}]$	Radial free electric field
$\mathbf{E}_{\mathrm{m}}$	–	Emission matrix
ϵ	$[\mathrm{C} \cdot \mathrm{V}^{-1} \cdot \mathrm{m}^{-1}]$	Electric permittivity
ϵ_{d}	–	Directional emissivity
ϵ_{h}	–	Hemispherical emissivity
$\bar{\epsilon}_{\mathrm{h}}$	–	Bolometric hemispherical emissivity
η	–	Parameter for KS-model
$\mathbf{F}$	$[\mathrm{W} \cdot \mathrm{m}^{-2}]$	Flux matrix
F	$[\mathrm{W} \cdot \mathrm{m}^{-2}]$	Flux
$\mathbf{f}$	$[\mathrm{W} \cdot \mathrm{m}^{-2}]$	Flux vector

Symbol	**Unit**	**Description**
$f_{\mathrm{i,j}}$	–	Configuration factor for radiative heat transfer
G	$[\mathrm{m}^2]$	Geometric cross section
g	$[^\circ]$	Phase angle
γ	–	Auxiliary function for H-function
γ_{n}	–	Legendre expansion coefficients for scattering amplitudes helper function
γ_{p}	$[^\circ]$	Photometric longitude
g_{nm}	–	Gain factor for a pixel (n,m)
$H(x)$	–	Ambratsumian Chandrasekhar H-function
h	$[\mathrm{J} \cdot \mathrm{s}]$	Planck constant
h_{nji}	–	Legendre expansion coefficients for scattering amplitudes
h_{c}	–	Angular width of the coherent backscatter opposition effect
$\mathrm{H_2O}$	–	Water
h_{s}	–	Angular width of the shadow-hiding opposition effect
$\mathbf{I}$	$[\mathrm{W} \cdot \mathrm{m}^{-2} \cdot \mathrm{m}^{-1} \cdot \mathrm{sr}^{-1}]$	Stokes vector of the spectral radiance/diffuse specific intensity
I	$[\mathrm{W} \cdot \mathrm{m}^{-2} \cdot \mathrm{m}^{-1} \cdot \mathrm{sr}^{-1}]$	Spectral radiance, diffuse specific intensity, first Stokes parameter
i	$[^\circ]$	Incidence angle
i	–	Imaginary unit, use context to distinguish it from the incidence angle i
I_{b}	$[\mathrm{W} \cdot \mathrm{m}^{-2} \cdot \mathrm{m}^{-1} \cdot \mathrm{sr}^{-1}]$	Spectral radiance/diffuse specific intensity of a blackbody
I_{nm}	$[\mathrm{W} \cdot \mathrm{m}^{-2} \cdot \mathrm{m}^{-1} \cdot \mathrm{sr}^{-1}]$	Calibrated specteral radiance/diffuse specific intensity for a single pixel (n,m)
$\mathbf{I}_{\mathrm{t}}$	$[\mathrm{W} \cdot \mathrm{m}^{-2} \cdot \mathrm{m}^{-1} \cdot \mathrm{sr}^{-1}]$	Stokes vector of the spectral radiance/diffuse specific intensity through thermal radiation
J	$[\mathrm{W} \cdot \mathrm{m}^{-2} \cdot \mathrm{m}^{-1}]$	Spectral irradiance, coherent specific intensity

Symbol	Unit	Description
$\mathbf{J}_0$	$[\mathrm{W} \cdot \mathrm{m}^{-2} \cdot \mathrm{m}^{-1}]$	Stokes vector of the solar spectral irradiance/specific intensity
J_0	$[\mathrm{W} \cdot \mathrm{m}^{-2} \cdot \mathrm{m}^{-1}]$	Solar spectral irradiance/specific intensity
$\mathbf{k}$	$[\mathrm{m}^{-1}]$	Wave vector of electromagnetic wave
k	$[\mathrm{m}^{-1}]$	Wave number of electromagnetic wave
k_1	$[\mathrm{m}^{-1}]$	Wave number of electromagnetic wave inside a particle
k_b	$[\mathrm{J} \cdot \mathrm{K}^{-1}]$	Boltzmann constant
k_h	$[\mathrm{W} \cdot \mathrm{m}^{-1} \cdot \mathrm{K}^{-1}]$	Heat conductivity
k_m	–	Minnaert exponent
L_1	–	Auxiliary function for Hapke model
L_2	–	Auxiliary function for Hapke model
Λ	[m]	Average photon travel distance in regolith
λ	[m]	Wavelength
$\lambda/\Delta\lambda$	–	Spectral resolution
$\mathbf{M}$	–	Self heating/self scattering matrix
$\mathbf{M}_\mathrm{mn}$	–	Spherical vector wave
m	–	Phase function parameter for KS model
m_highland	–	Scale factor for the single scattering albedo in highland regions
M_j	[kg]	Mass of particle j
$M_{\mathrm{ll}'}^{ii'}$	–	Auxilliary component for deriving the T matrix
m_mare	–	Scale factor for the single scattering albedo in mare regions
$\mathrm{Rg}\mathbf{M}_\mathrm{mn}$	–	Spherical vector wave
μ	–	Cosine of the emission angle e
μ_0	–	Cosine of the incidence angle i
$\mu_{0,\mathrm{e}}$	–	Modified cosine of the incidence angle i
μ_e	–	Modified cosine of the emission angle e
μ_mag	$[\mathrm{H} \cdot \mathrm{m}^{-1}]$	Magnetic permeability
$\mathbf{N}_\mathrm{mn}$	–	Spherical vector wave

Symbol	Unit	Description
$\mathbf{n}$	–	Normal vector
N	–	Refractive index medium
N_1	–	Refractive index of a particle
$\mathrm{Rg}\mathbf{N}_{\mathrm{mn}}$	–	Spherical vector wave
$\nu_{\mathrm{m,j}}$	–	Visibility switch
OH	–	Hydroxyl
ω	$[\mathrm{s}^{-1}]$	Angular frequency
Ω	[sr]	Solid angle
Ω_{n}	–	Phase space of the n^{th} thermodynamical system
P_{n}^{l}	–	Associated Legendre function
P	[W]	Power
$p(g)$	–	Phase function
ϕ	[°]	Azimuthal angle in spherical coordinate system
ϕ_{Δ}	[°]	Angle between surface element normal and connection vector
π_{n}	–	Expansion function for Mie scattering
$p_{\mathrm{l}}^{\mathrm{i}}$	–	Expansion coefficients of the field scattered at the i^{th} particle in the T matrix formalism
$p_{\mathrm{m,j}}$	[m]	Distance between surface elements
p_{mn}	–	Expansion coefficients of the scatterd field
PSF	–	Point spread function
ψ	[°]	Azimuth angle
p_{n}	–	Expansion coefficients of the scattered field in the T matrix formalism
Q	$[\mathrm{W} \cdot \mathrm{m}^{-2} \cdot \mathrm{m}^{-1} \cdot \mathrm{sr}^{-1}]$	Second Stokes parameter
d^2Q	[W]	Heat flux
Q_{ext}	–	Extinction efficiency
q_{mn}	–	Expansion coefficients of the scatterd field
Q_{sca}	–	Scattering efficiency
q_{n}	–	Expansion coefficients of the scattered field in the T matrix formalism

Symbol	Unit	Description
R	[AU]	Solar distance
r	[m]	Particle radius
r_0	–	Auxiliary function for H-function
r_d	–	Bi-directional reflectance
r_dh	–	Directional-hemispherical reflectance
r_hd	–	Hemispherical-directional reflectance
ρ	$[\mathrm{kg} \cdot \mathrm{m}^{-3}]$	Material density
ρ_j	$[\mathrm{kg} \cdot \mathrm{m}^{-3}]$	Material density of particle j
$\mathbf{R}_\mathrm{m}$	–	Reflectance matrix
$\mathcal{R}_{u\leftarrow v}$	–	Translation operator for scattering expansions
$\mathbf{r}$	[m]	Position in space
S	–	Shadowing function
$\mathbf{S}$	–	Amplitude scattering matrix
$\mathbf{s}$	–	Solar illumination vector
$S_\odot$	$[\mathrm{W} \cdot \mathrm{m}^{-2}]$	Solar constant at 1 AU
Σ	$[\mathrm{m}^2]$	Area in which to consider self-heating and self-scattering
σ	$[\mathrm{W} \cdot \mathrm{m}^{-2} \cdot \mathrm{K}^{-4}]$	Stefan-Boltzmann constant
$\sigma(\lambda)$	–	Wavelength-dependent standard deviation
S_{ij}	–	Amplitude scattering matrix elements
s	–	Relative refractive index
T	[K]	Temperature
τ_n	–	Expansion function for Mie scattering
θ	$[^\circ]$	Polar angle in spherical coordinate system
ϑ	$[^\circ]$	Zenith angle
$\overline{\theta}$	$[^\circ]$	Hapke roughness
$\mathbf{T}$	–	T matrix
U	$[\mathrm{W} \cdot \mathrm{m}^{-2} \cdot \mathrm{m}^{-1} \cdot \mathrm{sr}^{-1}]$	Third Stokes parameter, use context to distinguish from Planck function
U_0	[J]	Inner energy
U	$[\mathrm{W} \cdot \mathrm{m}^{-2} \cdot \mathrm{m}^{-1} \cdot \mathrm{sr}^{-1}]$	Blackbody emission

Symbol	**Unit**	**Description**
U_{n}	[J]	Internal energy of the n$^{\mathrm{th}}$ thermodynamical system
V	$[\mathrm{W} \cdot \mathrm{m}^{-2} \cdot \mathrm{m}^{-1} \cdot \mathrm{sr}^{-1}]$	Fourth Stokes parameter
v	–	Visibility switch
$\mathbf{v}$	–	View vector
v_1, v_2	–	Stretching vibrations of hydroxyl
W	–	Point spread function
w	–	Single-scattering albedo
W^{ext}	[W]	Power removed from beam through scattering
W^{sca}	[W]	Scattered power
$W_{\mathrm{ll'}}^{ii'}$	–	Translation operator for T matrix
$\mathbf{X}$	–	Modified **M** matrix for fixed-point iteration
X	$[\mathrm{W} \cdot \mathrm{m}^{-2} \cdot \mathrm{m}^{-1} \cdot \mathrm{sr}^{-1}]$	Anisotropic thermal emission
ξ	–	Asymmetry factor of the Henyey-Greenstein phase function
Z	[m]	Arbitrary planetary surface height
$\mathbf{Z}$	–	Stokes phase matrix

Appendix A

Normal vector computation for planetary shape models

Assume that the planetary height map in equirectangular projection is a function $D(\lambda, \phi)$ that depends on the longitude $\lambda \in [-\pi ... \pi]$ and the latitude $\phi \in [-\pi/2 ... + \pi/2]$. A planet can then be modeled as a sphere, where the height map acts as a bump map. For each latitude and longitude, the height map D offsets the planetary radius R such that the planetary surface $\mathbf{r}(\lambda, \phi)$ becomes

$$\mathbf{r}(\lambda, \phi) = (R + D(\lambda, \phi)) \begin{pmatrix} \cos(\lambda)\cos(\phi) \\ \sin(\lambda)\cos(\phi) \\ \sin(\phi) \end{pmatrix}. \tag{A.1}$$

It is convenient to define

$$D_\lambda(\lambda, \phi) = \frac{\partial D(\lambda, \phi)}{\partial \lambda},\ D_\phi(\lambda, \phi) = \frac{\partial D(\lambda, \phi)}{\partial \phi}. \tag{A.2}$$

Deriving the planet model with respect to λ and ϕ yields

$$\frac{\partial \mathbf{r}(\lambda, \phi)}{\partial \lambda} = \begin{pmatrix} D_\lambda(\lambda, \phi)\cos(\lambda)\cos(\phi) - (R + D(\lambda, \phi))\sin(\lambda)\cos(\phi) \\ D_\lambda(\lambda, \phi)\sin(\lambda)\cos(\phi) + (R + D(\lambda, \phi))\cos(\lambda)\cos(\phi) \\ D_\lambda(\lambda, \phi)\sin(\phi) \end{pmatrix} \tag{A.3}$$

$$\frac{\partial \mathbf{r}(\lambda, \phi)}{\partial \phi} = \begin{pmatrix} D_\phi(\lambda, \phi)\cos(\lambda)\cos(\phi) - (R + D(\lambda, \phi))\cos(\lambda)\sin(\phi) \\ D_\phi(\lambda, \phi)\sin(\lambda)\cos(\phi) - (R + D(\lambda, \phi))\sin(\lambda)\sin(\phi) \\ D_\phi(\lambda, \phi)\sin(\phi) + (R + D(\lambda, \phi))\cos(\phi) \end{pmatrix}. \tag{A.4}$$

The normalized cross-product then defines a vector field $\mathbf{N}(\lambda, \phi)$ that is normal to the planetary surface

$$\mathbf{N}(\lambda, \phi) = \frac{\frac{\partial \mathbf{r}(\lambda, \phi)}{\partial \lambda} \times \frac{\partial \mathbf{r}(\lambda, \phi)}{\partial \phi}}{\left\| \frac{\partial \mathbf{r}(\lambda, \phi)}{\partial \lambda} \times \frac{\partial \mathbf{r}(\lambda, \phi)}{\partial \phi} \right\|}. \tag{A.5}$$

With a suitable discretization, this formalism can be used to compute the orientation of any surface element n toward the sun and the observer (see Figure 3.1 right).

Appendix B

Mathematical tools for light scattering

The macroscopic Maxwell equations fully determine classic electrodynamics and, thus, any light scattering problem commonly encountered on planetary surfaces or elsewhere. Combining the last two Maxwell equations leads to the wave equation that describes how electromagnetic waves travel through space. Omitting the temporal oscillations and considering only the spatial component gives the vector-valued Helmholtz equation. Because the electromagnetic waves propagate concentrically after scattering, it is useful to consider spherical coordinates. The fundamental solutions of the vector-valued Helmholtz equation in spherical coordinates are termed vector spherical wave functions and turn out to be useful building blocks for the theoretical treatment of light scattering problems. Closely following Sun et al. [2020b] and the summary in Arnaut [2021], this section presents the definition of spherical vector wave function (SVWF). The Helmholtz-equation for a vector-valued function $\mathbf{F}$ is given by

$$\nabla^2\mathbf{F} + k^2\mathbf{F} = 0. \tag{B.1}$$

Bohren and Huffman [1998] show with vector identities that a scalar function ψ exists that solves the scalar Helmholtz equation

$$\nabla^2\mathbf{F} + k^2\mathbf{F} = \nabla \times [\mathbf{c}(\nabla^2\psi + k^2\psi)] \tag{B.2}$$

and generates the fundamental solutions for the vector-valued case. For light scattering theory, spherical coordinates (r, θ, ϕ) are convenient. Replacing the radial component r with $\zeta = kr$ is useful, where k is the wave number. The scalar Helmholtz equation in spherical coordinates with a modified radial component (ζ, θ, ϕ) now has the solution

$$\psi_{\mathrm{ml}}(\zeta, \theta, \phi) = z_l(\zeta) P_l^m(\cos(\theta)) \exp(im\phi), \tag{B.3}$$

where $z_l(\zeta)$ is either the spherical Bessel function $j_l(\zeta)$ or the spherical Hankel function $h_l^{(1)}(\zeta)$, and P_l^m denotes the associated Legendre polynomials. The indices l and m run from $l = 0, 1, ...$ and $m = -l, ..., -1, 0, 1, ..., +l$. Depending on the choice of z_l, two functions can be defined:

$$\psi_{\mathrm{ml}}(\zeta,\theta,\phi) = h_l^{(1)}(\zeta)P_l^m(\cos(\theta))\exp(im\phi) \tag{B.4}$$

$$\mathrm{Rg}\psi_{\mathrm{ml}}(\zeta,\theta,\phi) = j_l(\zeta)P_l^m(\cos(\theta))\exp(im\phi). \tag{B.5}$$

Following Sun et al. [2020b] and references therein, the field $\mathbf{F}$ can be decomposed into two longitudinal ($\mathbf{L}_{\mathrm{ml}}$, $\mathrm{Rg}\mathbf{L}_{\mathrm{ml}}$) and four transverse vector spherical wave functions with the help of the scalar solution ψ ($\mathbf{M}_{\mathrm{ml}}$, $\mathrm{Rg}\mathbf{M}_{\mathrm{ml}}$, $\mathbf{N}_{\mathrm{ml}}$, $\mathrm{Rg}\mathbf{N}_{\mathrm{ml}}$)

$$\mathbf{L}_{\mathrm{ml}}(\zeta,\theta,\phi) = \gamma'_{\mathrm{ml}}\nabla_\zeta\psi_{\mathrm{ml}}(\zeta,\theta,\phi) \tag{B.6}$$

$$= \gamma'_{\mathrm{ml}}\left\{\frac{d}{d\zeta}h_l^{(1)}(\zeta)\mathbf{P}_{\mathrm{ml}}(\theta,\phi) + \frac{1}{\zeta}h_l^{(1)}(\zeta)\mathbf{B}_{\mathrm{ml}}(\theta,\phi)\right\} \tag{B.7}$$

$$\mathrm{Rg}\mathbf{L}_{\mathrm{ml}}(\zeta,\theta,\phi) = \gamma'_{\mathrm{ml}}\nabla_\zeta\mathrm{Rg}\psi_{\mathrm{ml}}(\zeta,\theta,\phi) \tag{B.8}$$

$$= \gamma'_{\mathrm{ml}}\left\{\frac{d}{d\zeta}j_l(\zeta)\mathbf{P}_{\mathrm{ml}}(\theta,\phi) + \frac{1}{\zeta}j_l(\zeta)\mathbf{B}_{\mathrm{ml}}(\theta,\phi)\right\}, \tag{B.9}$$

where $\nabla_\zeta = \nabla/k$. Applying the rotation to the scalar wave functions multiplied with the radius vector ζ yields the first set of vector spherical wave functions

$$\mathbf{M}_{\mathrm{ml}}(\zeta,\theta,\phi) = \gamma_{\mathrm{ml}}\nabla_\zeta\times\boldsymbol{\zeta}\psi(\zeta,\theta,\phi) = \gamma_{\mathrm{ml}}h_l^{(1)}(\zeta)\mathbf{C}_{\mathrm{ml}}(\theta,\phi) \tag{B.10}$$

$$\mathrm{Rg}\mathbf{M}_{\mathrm{ml}}(\zeta,\theta,\phi) = \gamma_{\mathrm{ml}}\nabla_\zeta\times\boldsymbol{\zeta}\mathrm{Rg}\psi(\zeta,\theta,\phi) = \gamma_{\mathrm{ml}}j_l(\zeta)\mathbf{C}_{\mathrm{ml}}(\theta,\phi), \tag{B.11}$$

where $\boldsymbol{\zeta} = k\mathbf{r}$. Applying the rotation a second time, yields another set of transverse vector spherical wave functions

$$\mathbf{N}_{\mathrm{ml}}(\zeta,\theta,\phi) = \nabla_\zeta\times\mathbf{M}_{\mathrm{ml}}(\zeta,\theta,\phi) \tag{B.12}$$

$$= \gamma_{\mathrm{ml}}\left\{\frac{l(l+1)}{\zeta}h_l^{(1)}(\zeta)\mathbf{P}_{\mathrm{ml}}(\theta,\phi) + \frac{1}{\zeta}\frac{1}{d\zeta}\zeta h_l^{(1)}(\zeta)\mathbf{B}_{\mathrm{ml}}(\theta,\phi)\right\} \tag{B.13}$$

$$\mathrm{Rg}\mathbf{N}_{\mathrm{ml}}(\zeta,\theta,\phi) = \gamma_{\mathrm{ml}}\nabla_\zeta\times\mathrm{Rg}\mathbf{M}_{\mathrm{ml}}(\zeta,\theta,\phi) \tag{B.14}$$

$$= \gamma_{\mathrm{ml}}\left\{\frac{l(l+1)}{\zeta}j_l(\zeta)\mathbf{P}_{\mathrm{ml}}(\theta,\phi) + \frac{1}{\zeta}\frac{1}{d\zeta}\zeta j_l(\zeta)\mathbf{B}_{\mathrm{ml}}(\theta,\phi)\right\}. \tag{B.15}$$

Mishchenko et al. [2002] defines

$$\gamma'_{\mathrm{ml}} = \sqrt{\frac{(2l+1)(l-m)!}{4\pi(l+m)!}} \tag{B.16}$$

$$\gamma_{\mathrm{ml}} = \sqrt{\frac{(2l+1)(l-m)!}{4\pi l(l+1)(l+m)!}} = \gamma'_{\mathrm{ml}}\frac{1}{\sqrt{l(l+1)}}. \tag{B.17}$$

The remaining functinos are vector spherical harmonics defined as:

$$\begin{aligned}
\mathbb{Y}_{\mathrm{lm}}(\theta,\phi) &= P_l^m(\cos(\theta))\exp(im\phi) && \text{(B.18)}\\
\mathbf{V}^{(1)}_{\mathrm{ml}}(\theta,\phi) &= \mathbf{P}_{\mathrm{ml}}(\theta,\phi)(\theta,\phi) = \mathbf{n}_{\mathrm{r}}\mathbb{Y}_{\mathrm{lm}}(\theta,\phi) && \text{(B.19)}\\
\mathbf{V}^{(2)}_{\mathrm{ml}}(\theta,\phi) &= \mathbf{B}_{\mathrm{ml}}(\theta,\phi) = \zeta\nabla_\zeta\mathbb{Y}_{\mathrm{ml}}(\theta,\phi) && \text{(B.20)}\\
&= \left[\frac{dP_l^m(\cos(\theta))}{d\theta}\boldsymbol{\theta} + \frac{im}{\sin(\theta)}P_l^m(\cos(\theta))\boldsymbol{\phi}\right]\exp(im\phi) && \text{(B.21)}\\
&= \mathbf{n}_{\mathrm{r}}\times\mathbf{C}_{\mathrm{ml}}(\theta,\phi) && \text{(B.22)}\\
\mathbf{V}^{(3)}_{\mathrm{ml}}(\theta,\phi) &= \mathbf{C}_{\mathrm{ml}}(\theta,\phi) = \nabla_\zeta\times[\mathbf{r}\mathbb{Y}_{lm}(\theta,\phi)] && \text{(B.23)}\\
&= \left[\frac{im}{\sin(\theta)}P_l^m(\cos(\theta))\boldsymbol{\theta} - \frac{dP_l^m(\cos(\theta))}{d\theta}\boldsymbol{\phi}\right]\exp(im\phi) && \text{(B.24)}\\
&= \mathbf{B}_{\mathrm{ml}}(\theta,\phi)\times\mathbf{n}_{\mathrm{r}}. && \text{(B.25)}
\end{aligned}$$

The spherical Bessel functions $j_{\mathrm{n}}(\zeta)$ and $y_{\mathrm{n}}(\zeta)$ are the solutions of the differential equation

$$\left(\zeta^2\frac{d^2}{d\zeta^2} + \zeta\frac{d}{d\zeta} + \zeta^2 - \left[l+\frac{1}{2}\right]\right)z_{\mathrm{l}}(\zeta) = 0, \tag{B.26}$$

and can be expressed with either the Bessel functions J and Y

$$\begin{aligned}
j_{\mathrm{l}}(\zeta) &= \sqrt{\frac{\pi}{2\zeta}}J_{\mathrm{l}+1/2}(\zeta) && \text{(B.27)}\\
y_{\mathrm{l}}(\zeta) &= \sqrt{\frac{\pi}{2\zeta}}Y_{\mathrm{l}+1/2}(\zeta) && \text{(B.28)}
\end{aligned}$$

or with the Rayleigh equations [Sun et al., 2020b]

$$\begin{aligned}
j_{\mathrm{l}}(\zeta) &= (-\zeta)^l\left(\frac{1}{\zeta}\frac{d}{d\zeta}\right)^l\frac{\sin(\zeta)}{\zeta} && \text{(B.29)}\\
y_{\mathrm{l}}(\zeta) &= -(-\zeta)^l\left(\frac{1}{\zeta}\frac{d}{d\zeta}\right)^l\frac{\cos(\zeta)}{\zeta}. && \text{(B.30)}
\end{aligned}$$

The spherical Hankel functions of the first $h^{(1)}_{\mathrm{n}}(x)$ and second kind $h^{(2)}_{\mathrm{n}}(x)$ are defined as:

$$\begin{aligned}
h^{(1)}_{\mathrm{l}}(\zeta) &= j_{\mathrm{l}}(\zeta) + iy_{\mathrm{l}}(\zeta) && \text{(B.31)}\\
h^{(2)}_{\mathrm{l}}(\zeta) &= j_{\mathrm{l}}(\zeta) - iy_{\mathrm{l}}(\zeta). && \text{(B.32)}
\end{aligned}$$

The associated Legendre polynomials $P_{\mathrm{l}}^{\mathrm{m}}$ solve the differntial equation [Bartelmann et al., 2018a]

$$\left((1-\zeta^2)\frac{d^2}{d\zeta^2} - 2\zeta\frac{d}{d\zeta} - \frac{m^2}{1-\zeta^2} + l(l+1)\right)P_{\mathrm{l}}^{\mathrm{m}}(\zeta) = 0 \tag{B.33}$$

and have the solution [Bartelmann et al., 2018a]

$$P_{\mathrm{l}}^{\mathrm{m}}(\zeta) = (-1)^m (1-\zeta^2)^{m/2} \frac{d^m}{dx^m} P_l(\zeta). \tag{B.34}$$

Appendix C

Macroscopic roughness and roughness correction for the the Hapke model

The roughness of planetary surfaces can be defined via equations 3.57 and 3.58. The first planetary reflectance models [e.g. Hapke, 1981] modeled planetary regolith as a flat and horizontally stratified medium. However, the planetary regolith is rough below the millimeter scale. Complex shadowing effects of the rough surface affect the directional reflectance. Consequently, Hapke [1984] introduced a correction for his model that addresses macroscopic roughness. The correction introduces the cosines of the modified cosines of the incidence and emission angles $\mu_{0\mathrm{e}}$ and μ_{e}, respectively, that replace μ_0 and μ in the original model. Further, the shadowing function $S(i, e, g)$ is multiplied by the entire bi-directional reflectance. Depending on i, e, and $\overline{\theta}$, the roughness correction is defined the following for two cases $(i \leq e)$ and $(e \leq i)$.

Case $i \leq e$:

$$\mu_{0\mathrm{e}}(i,e,\psi) \simeq \chi(\overline{\theta}) \left[\cos(i) + \sin(i)\tan(\overline{\theta}) \frac{-\cos(\psi)E_2(e) + \sin^2(\psi/2)E_2(i)}{2 - E_1(e) - (\psi/\pi)E_1(i)}\right] \tag{C.1}$$

$$\mu_{\mathrm{e}}(i,e,\psi) \simeq \chi(\overline{\theta}) \left[\cos(e) + \sin(e)\tan(\overline{\theta}) \frac{E_2(e) - \sin^2(\psi/2)E_2(i)}{2 - E_1(e) - (\psi/\pi)E_1(i)}\right] \tag{C.2}$$

$$S(i,e,\psi) \simeq \frac{\mu_e}{\eta_e(e)} \frac{\mu_0}{\eta_{0e}(i)} \frac{\chi(\overline{\theta})}{1 - f(\psi) + f(\psi)\chi(\theta)\left[\mu_0/\eta_{0e}(i)\right]} \tag{C.3}$$

Case $e \leq i$:

$$\mu_{0\mathrm{e}}(i,e,\psi) \simeq \chi(\overline{\theta}) \left[\cos(i) + \sin(i)\tan(\overline{\theta}) \frac{E_2(i) - \sin^2(\psi/2)E_2(e)}{2 - E_1(i) - (\psi/\pi)E_1(e)}\right] \tag{C.4}$$

$$\mu_{\mathrm{e}}(i,e,\psi) \simeq \chi(\overline{\theta}) \left[\cos(e) + \sin(e)\tan(\overline{\theta}) \frac{-\cos(\psi)E_2(i) + \sin^2(\psi/2)E_2(e)}{2 - E_1(i) - (\psi/\pi)E_1(e)}\right] \tag{C.5}$$

$$S(i,e,\psi) \simeq \frac{\mu_e}{\eta_e(e)} \frac{\mu_0}{\eta_{0e}(i)} \frac{\chi(\overline{\theta})}{1 - f(\psi) + f(\psi)\chi(\theta)\left[\mu/\eta_e(e)\right]} \tag{C.6}$$

With the following helper functions:

$$\psi = \arccos\left(\frac{\cos(g) - \cos(e)\cos(i)}{\sin(e)\sin(i)}\right) \tag{C.7}$$

$$\chi(\overline{\theta}) = \left\langle \cos(\overline{\theta}) \right\rangle = \frac{1}{\sqrt{(1 + \pi\tan^2(\overline{\theta}))}} \tag{C.8}$$

$$E_1(x) = \exp\left(-\frac{2}{\pi}\cot(\overline{\theta})\cot(x)\right) \tag{C.9}$$

$$E_2(x) = \exp\left(-\frac{1}{\pi}\cot^2(\overline{\theta})\cot^2(x)\right) \tag{C.10}$$

$$\eta_e(e) \simeq \chi(\overline{\theta}) \left[\cos(e) + \sin(e)\tan(\overline{\theta}) \frac{E_2(e)}{2 - E_1(e)}\right] \tag{C.11}$$

$$\eta_{0e}(i) \simeq \chi(\overline{\theta}) \left[\cos(i) + \sin(i)\tan(\overline{\theta}) \frac{E_2(i)}{2 - E_1(i)}\right] \tag{C.12}$$

$$f(\psi) = \exp\left(-2\tan(\psi/2)\right) \tag{C.13}$$

Appendix D

Directional-hemispherical reflectance of the Hapke model

The master's thesis of Wohlfarth [2018] presents a closed-form solution of the directional-hemispherical reflectance r_{dh} derived from Hapke's anisotropic multiple scattering approximation [Hapke, 2012] without macroscopic roughness and opposition effects. The equation derived in Wohlfarth [2018] reads

$$\begin{aligned}
r_{\mathrm{dh}}(i,w) =& 1-\gamma H(\mu_0)+\sum_{n=1}^{\infty} b_n\{P_n(\mu_0)+A_n\left[H(\mu_0)-1\right]\} \\
&\times\left\{\frac{w}{2}\sum_{k=0}^{\lfloor n/2\rfloor}(-1)^k\frac{(2n-2k)!}{(n-k)!(n-2k)!k!2^n}\right. \\
&\cdot\left[\mu_0^{n-2k+1}((ln(\mu_0)-ln(\mu_0+1))\cdot(-1)^{n-2k})+\sum_{j=0}^{n-2k}\frac{(-\mu_0)^j}{n-2k+1-j}\right] \\
&\left.+A_n\left[\frac{1}{H(\mu_0)}-\gamma\right]-A_n\frac{w}{2}\left[1-\mu_0 ln\left(\frac{1+\mu_0}{\mu_0}\right)\right]\right\},
\end{aligned} \tag{D.1}$$

where $\mu_0=\cos(i)$, and equations 3.52, 3.44, and 3.47 define A_{n}, b_{n}, and γ, respectively. The r_{dh}-value helps determine the emissivity ϵ of a planetary surface via Kirchhoff's law (equation 3.78).

Appendix E

Tools for thermal modeling

This chapter with the associated figures has been taken from Wohlfarth et al. [2023].

E.1 Fractal surface generation

We used a spectral synthesis method that generates fractional Brownian motion representing the rough lunar regolith. Saupe [1991] outlines the theoretical approach of Fourier-based algorithms, and the authors of Grumpe et al. [2019] wrote the initial implementation for this study. They averaged over the RMSL angle statistics shown in Figure 9 of Helfenstein and Shepard [1999]. The resulting RMSL statistic set our reference. We then scaled the RMSL of the reference fractal statistics up and down to generate smoother or rougher surfaces. The observation that the RMSL statistic of smoother and rougher planetary regolith can be converted by simple multiplication supports our approach. We realized ten different fractals drawn from the scaled RMSL input statistics for each roughness level and computed the corresponding thermal models. Finally, we average over the resulting thermal emission to even out directional effects that stem from individual realizations of the fractal surface.

E.2 Geometric relations for the thermal model

Figure E.1 sketches the geometric relations for self-heating and self-scattering between two thermally isolated facets m and j of one fractal surface. The Sun has a distance of r_h to the entire scene and illuminates the surface with irradiance S_0. The self-heating (and self-scattering) coefficients $f_\mathrm{m,j}$ indicate how much radiation facet m receives from facet j and vice versa

$$f_\mathrm{m,j} = \frac{\nu_\mathrm{m,j} b_\mathrm{j} \cos\phi_\mathrm{\Delta,j} \cos\phi_\mathrm{\Delta,m}}{\pi p_\mathrm{m,j}^2}. \tag{E.1}$$

The angle $\phi_\mathrm{\Delta,m}$ is measured between the normal vector Z_m of facet m and the vector that connects the center of facet m with facet j. The angle $\phi_\mathrm{\Delta,j}$ is measured between the normal vector Z_j of facet j and the vector that connects the center of facet j with facet m. $p_\mathrm{m,j}$ is the distance between both facets.

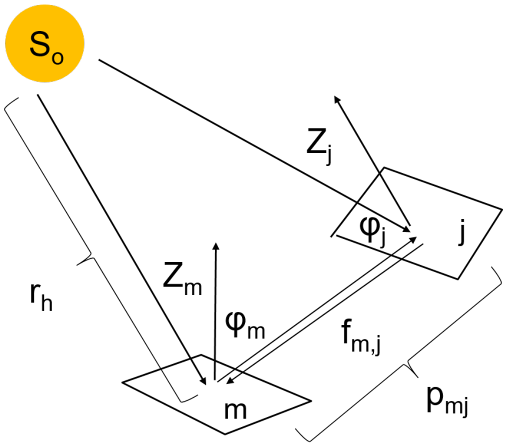

Figure E.1. Geometric relations for self-heating and self-scattering.

E.3 Implementation details

Subsampling of parameter space Even for a moderate discretization of the lunar surface, the number of geometric configurations N becomes very large. The GF-4 measurement of July 25, 2018, contains about 360,000 pixels. Running the model for ten fractals with a size of 200×200 pixels for each surface element results in 144 billion operations. Each operation encompasses self-heating and visibility analysis, making the total problem impractical. However, analyzing the mathematical structure of the geometries yields a way to decouple the computational effort of the thermal model from the initial problem size. This step dramatically reduces the total computational burden. For illumination and viewing vectors, we found that all geometric configurations lie on a continuous manifold within a space spanned by the geometry parameters i, e, and ψ. We found that it suffices to sample the manifold and compute the thermal model via equation 5.20 for only several thousand points in this parameter space. We further exploited equation 5.18 and precomputed the model for $A_{\mathrm{dh}} = 0$ and later scaled it to the desired values. Simple linear interpolation between sample points suffices to reconstruct a scene of arbitrary size. This approach drastically reduced the computational effort, such that the model now finishes within several hours on an AMD EPYC 7742 CPU. This approach is illustrated in Figure E.2 (top).

Periodicity for efficient self-heating Self-heating and self-scattering consider the power the current surface facet receives from its neighbors. We must collect all contributions from the neighborhood to fulfill energy conservation. Ideally, this neighborhood would be infinite, but the contributions rapidly get smaller with increasing distance. Because the computational complexity grows quadratically with the size of the neighborhood, it is helpful to limit the neighborhood by introducing a self-heating radius. We found that at a self-heating radius of 100 pixels, the fractal surface collects 95% of self-heating and self-scattering radiation while keeping the computational complexity reasonable. However, facets near the edge or in the corners of a rectangular fractal receive less radiation via self-heating, which leads to an underestimation of their temperature. Enlarging the fractal surface and neglecting the edges would alleviate the issue but is computationally expensive. A more

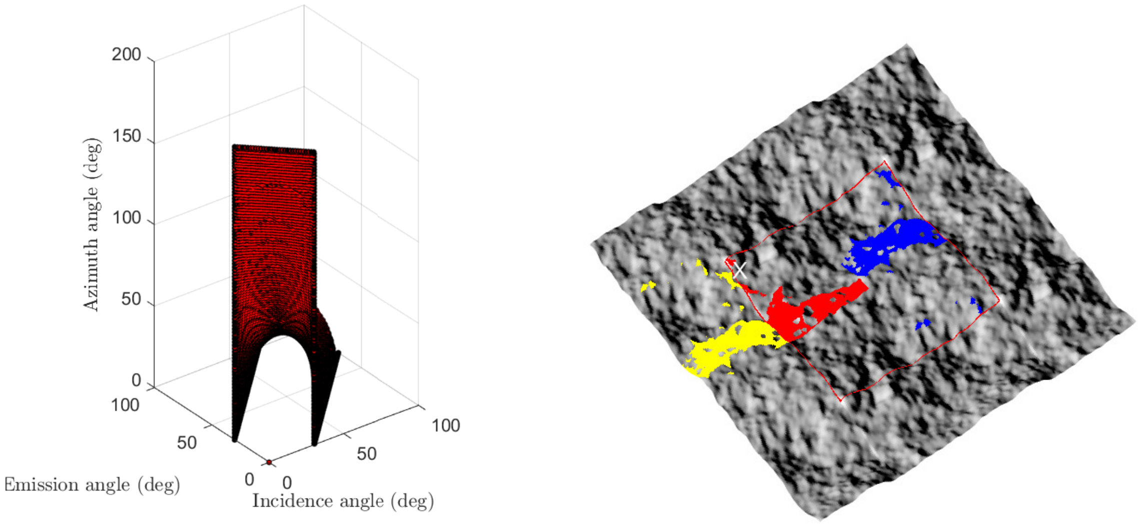

Figure E.2. Geometric conventions for computational techniques that speed up the thermal model computation. Top: The red surface represents all geometric configurations of the angles i, e, and ψ that describe the lunar surface seen by GF-4 on July 25, 2018. The black dots indicate the sampling points at which we evaluate the thermal model. Bottom: Example for self-heating on periodic fractal surfaces. A red square encircles the original fractal surface of 200×200 pixels. Outside the red square, it is repeated periodically. A white X marks the pixel of interest. The red pixels within the red square directly illuminate X for a given self-heating radius of 100 pixels. When assuming periodicity, the blue pixels within the original fractal are transported to the yellow pixel positions. Now, X receives a realistic amount of self-heating radiation, even though it is located at the edge of the original fractal surface.

efficient way is to exploit the properties of the fractal generation algorithm, which is based on the Fourier transform. The fractal landscape is periodically continuous, which means that opposite edges of the fractal surface are identical (gluing the left and the right edges together would result in a cylinder with a seamless transition). This property allows us to compute the self-heating *over the edges* and collect an adequate amount of self-heating radiation even for pixels near the edge. We set the fractal surface to 200×200 pixels and define a self-heating area of 100×100 pixels. An example is given in Figure E.2 (bottom).

E.4 Albedo estimation from RELAB data

Figure E.3 shows the correlation between the single scattering albedo of the Apollo samples measured at 2500 nm and 3770 nm. The reflectance spectra are taken from the RELAB database. The albedos are inferred via the Hapke model. The highland samples (blue) are brighter compared to the mare samples. We found a linear correlation between the albedo at both wavelength channels, which helped to extrapolate the albedo in the GF-4 wavelength range, given the M^3 global mosaic.

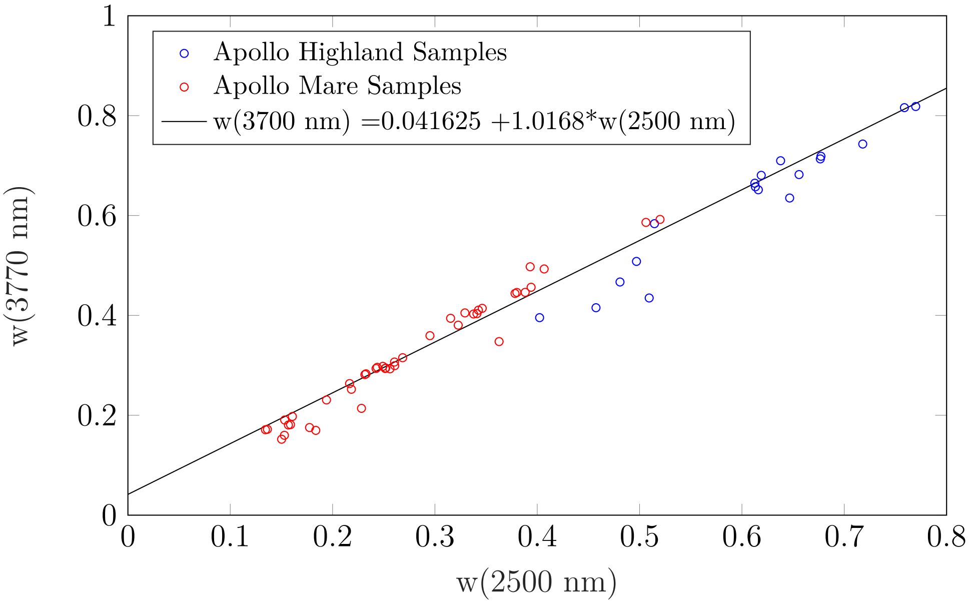

Figure E.3. Correlation between the single scattering albedo at 2500 nm and 3770 nm for Apollo samples.

E.5 Directional-hemispherical albedo for Mercury

According to equation 3.80, the directional-hemispherical albedo is the bolometric integral over the directional-hemispherical reflectance weighted with the solar spectrum. Consequently, the value for A_{dh} is primarily controlled by the reflectance from the ultraviolet to the mid-infrared. Currently, no reflectance spectra that cover a spectral region that is broad enough to directly compute the directional-hemispherical albedo of Mercury are available. However, it is possible to establish an empirical relationship that robustly predicts the directional-hemispherical albedo A_{dh} given the incidence angle i and the single scattering albedo w at 750 nm. Therefore, the author assumes a two-dimensional polynomial of the form

$$A_{\mathrm{dh}}(i, w) = a_0 + a_1 i + a_2 w + a_3 i w + a_4 i^2 + a_5 w^2. \tag{E.2}$$

We insert i, w, and A_{dh} as computed for the lunar observation on July 25, 2018, and estimate the coefficients a_0–a_5 with Least-squares. The author chooses a wavelength of 750 nm for the albedo because it is not affected by spectral absorption bands. The Moon and Mercury have silicate mineralogies, so the overall spectral shapes are roughly comparable. Direct comparison shows that the reflectance spectra of Mercury are featureless in the near-infrared and approximately as dark as the lunar maria. Because the bolometric integral mainly depends on the overall spectral shape, we assume that the empirical relationship inferred for the lunar surface also holds for Mercury. Consequently, we derive the single scattering albedo from the MDIS global mosaic at 750 nm and then estimate A_{dh} for Mercury.

Appendix F

Diviner emission phase function results

This chapter with the associated figures has been adapted from Wohlfarth et al. [2023]. This section displays the results of our thermal model compared with the EPF measurements for all 12 EPF measurements. Table 4.2 provides the observation conditions, and Table 5.2 lists the fitting results for the single scattering albedo w and the roughness $\overline{\theta}$. All figures are adapted from Wohlfarth et al. [2023].

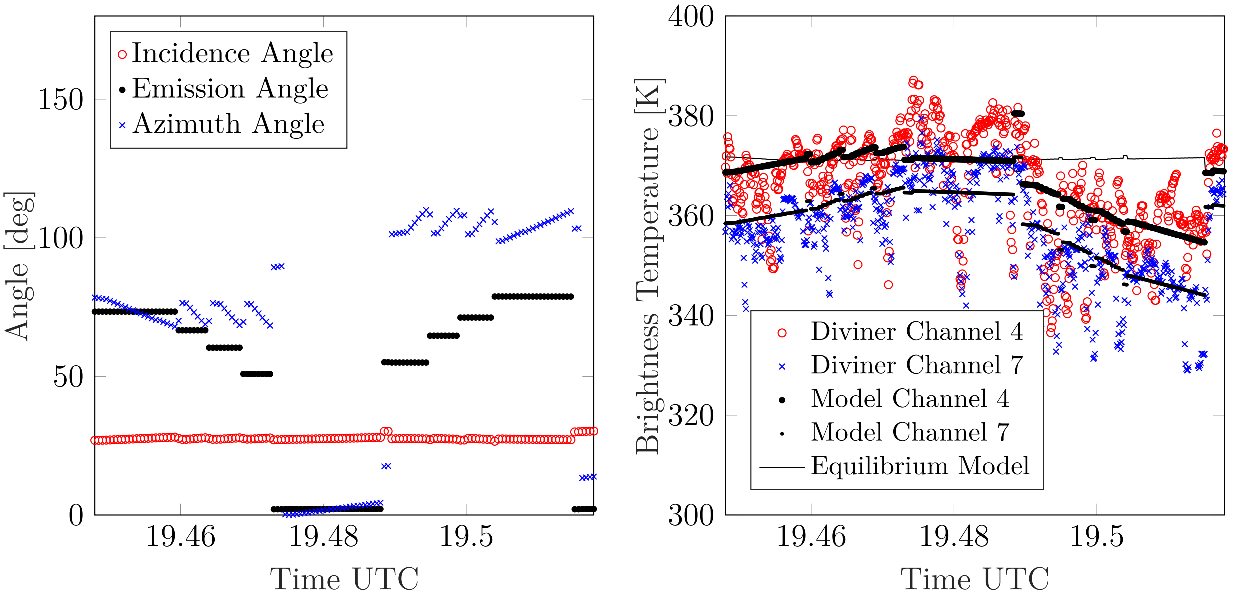

Figure F.1. EPF maneuver 1. Left: Geometry. Right: Modeled vs. measured brightness temperatures.

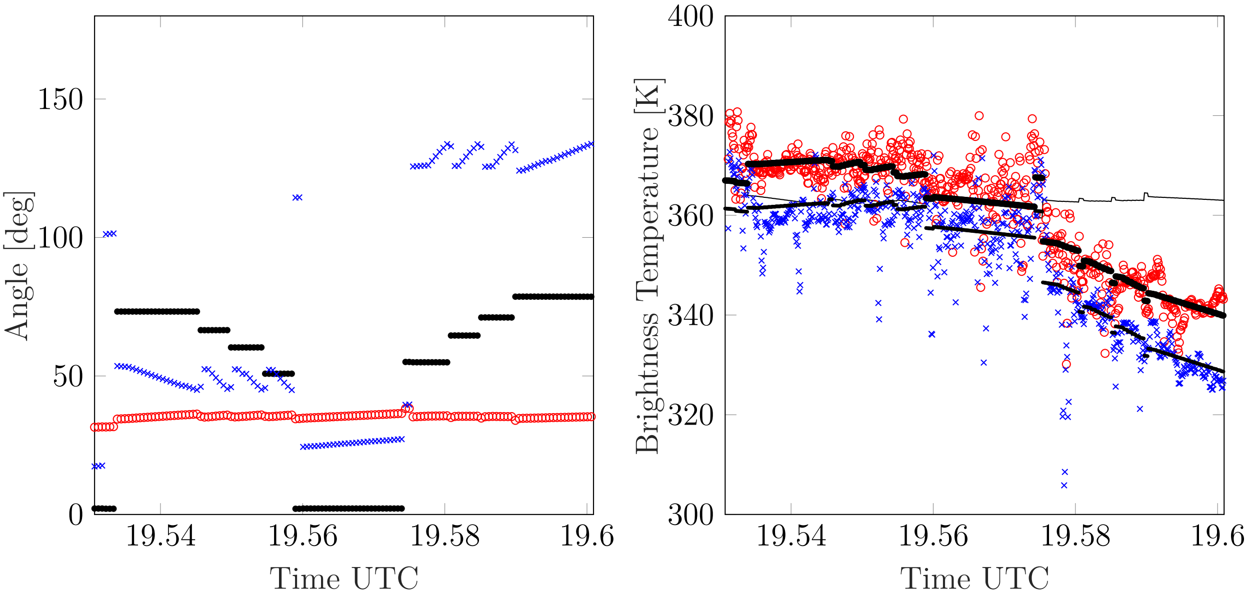

Figure F.2. EPF maneuver 2. Left: Geometry. Right: Modeled vs. measured brightness temperatures. For legend, see Figure F.1.

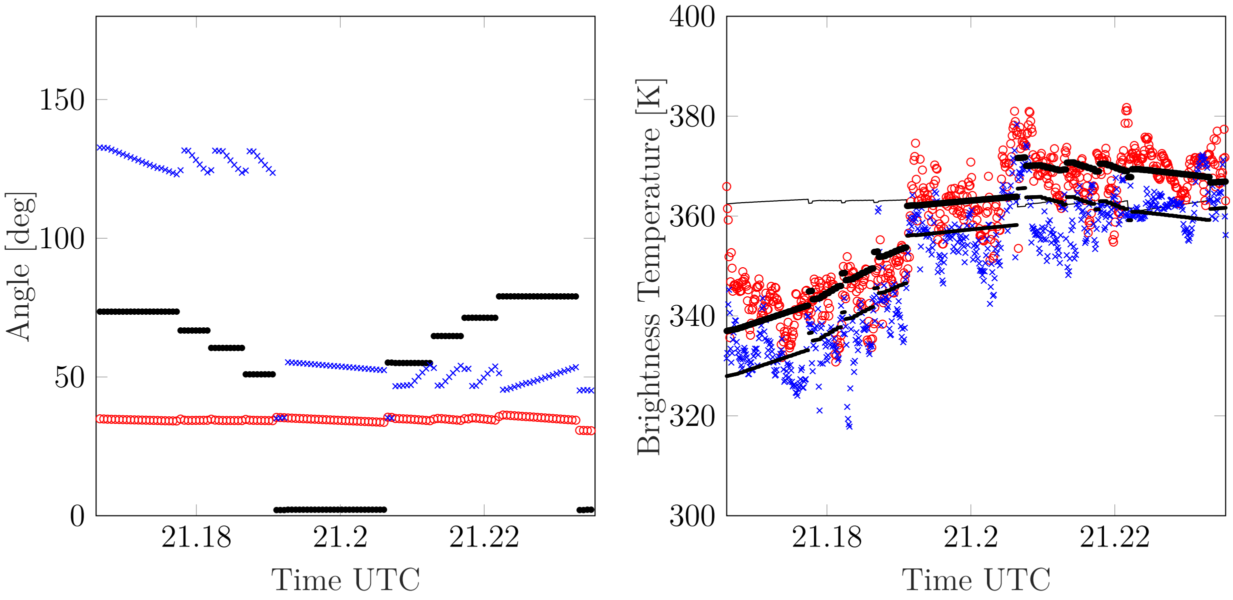

Figure F.3. EPF maneuver 3. Left: Geometry. Right: Modeled vs. measured brightness temperatures. For legend, see Figure F.1.

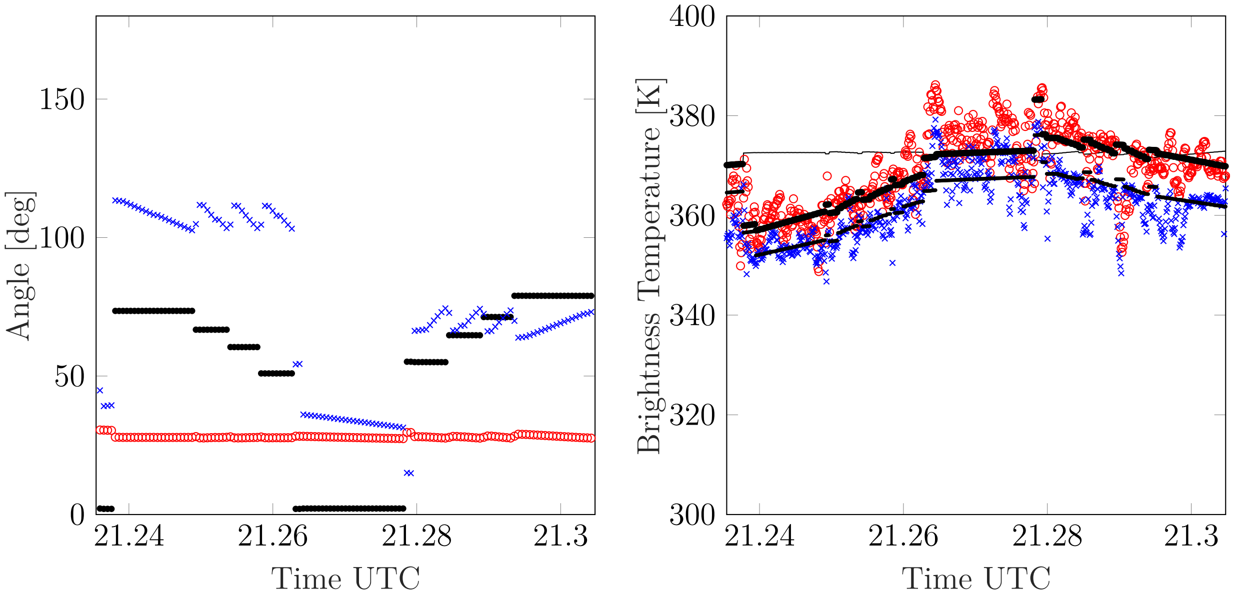

Figure F.4. EPF maneuver 4. Left: Geometry. Right: Modeled vs. measured brightness temperatures. For legend, see Figure F.1.

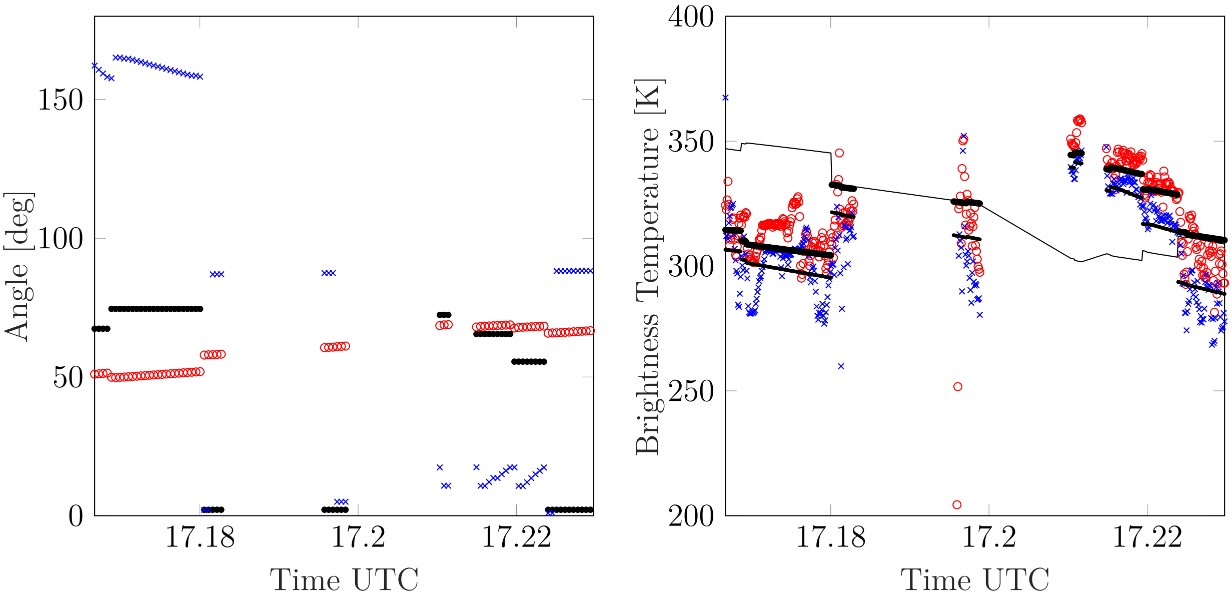

Figure F.5. EPF maneuver 5. Left: Geometry. Right: Modeled vs. measured brightness temperatures. For legend, see Figure F.1.

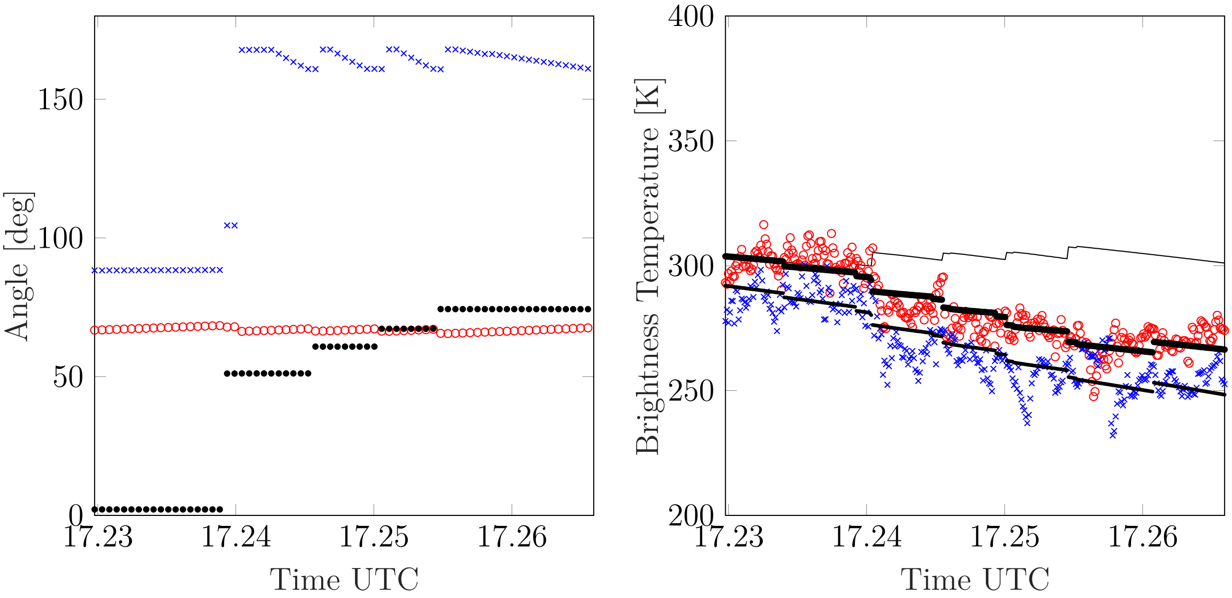

Figure F.6. EPF maneuver 6. Left: Geometry. Right: Modeled vs. measured brightness temperatures. For legend, see Figure F.1.

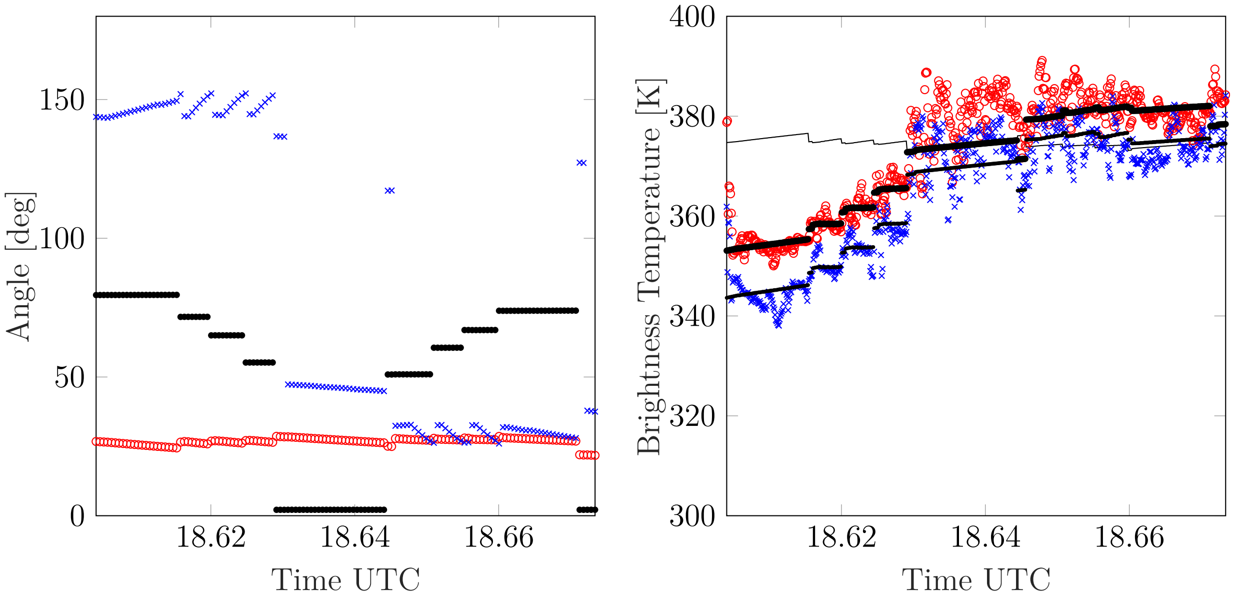

Figure F.7. EPF maneuver 7. Left: Geometry. Right: Modeled vs. measured brightness temperatures. For legend, see Figure F.1.

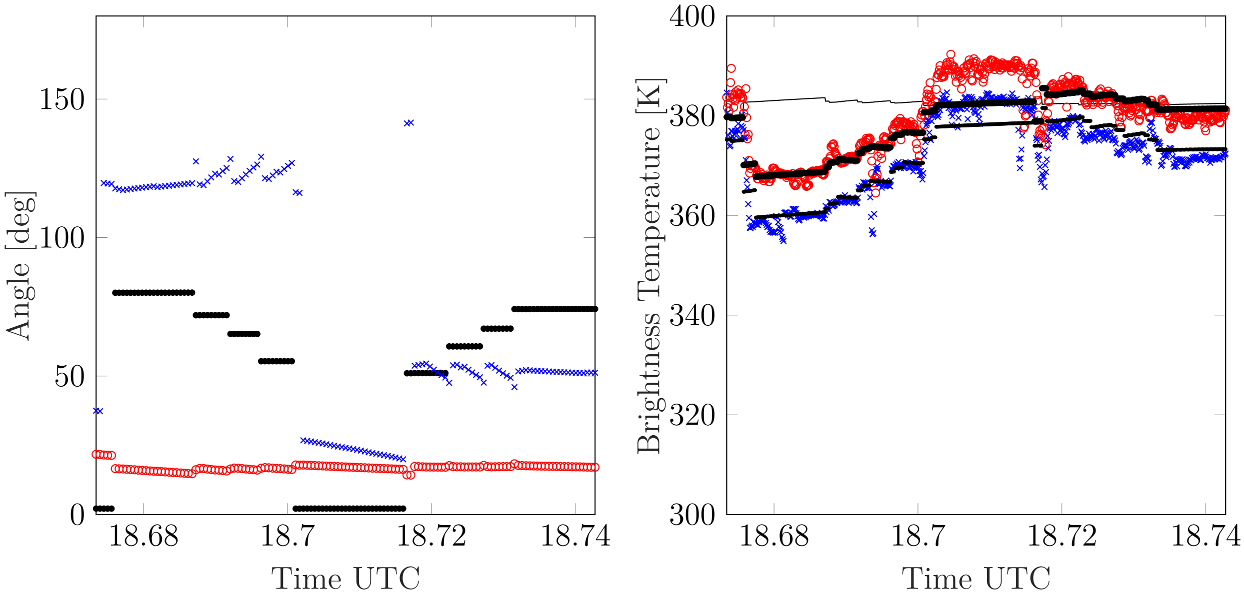

Figure F.8. EPF maneuver 8. Left: Geometry. Right: Modeled vs. measured brightness temperatures. For legend, see Figure F.1.

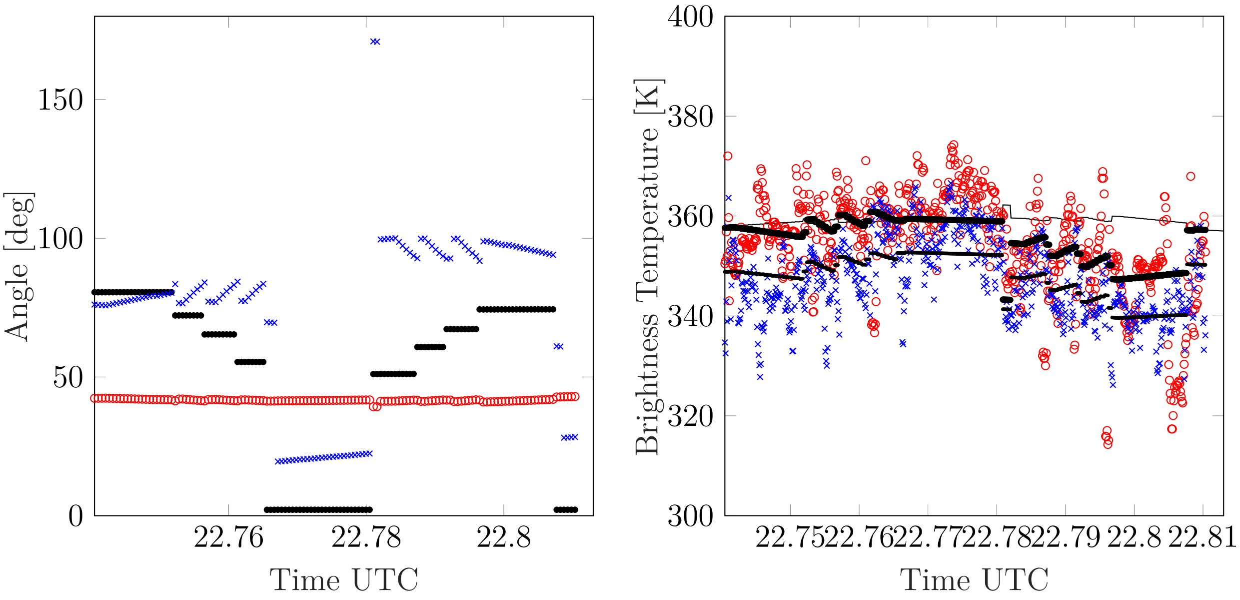

Figure F.9. EPF maneuver 9. Left: Geometry. Right: Modeled vs. measured brightness temperatures. For legend, see Figure F.1.

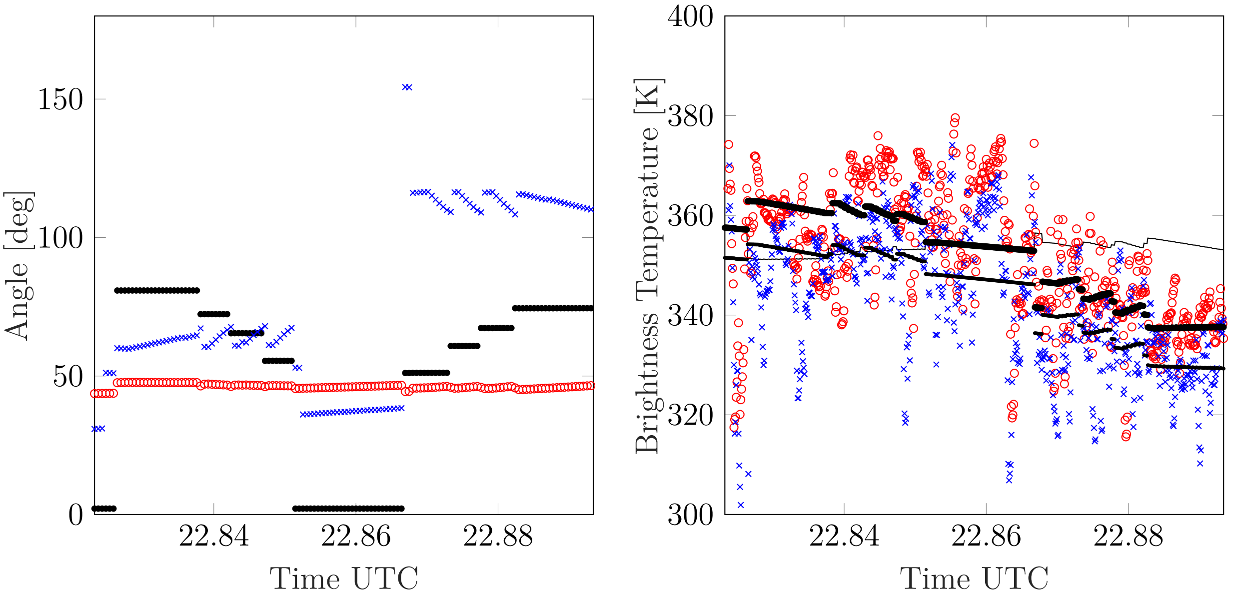

Figure F.10. EPF maneuver 10. Left: Geometry. Right: Modeled vs. measured brightness temperatures. For legend, see Figure F.1.

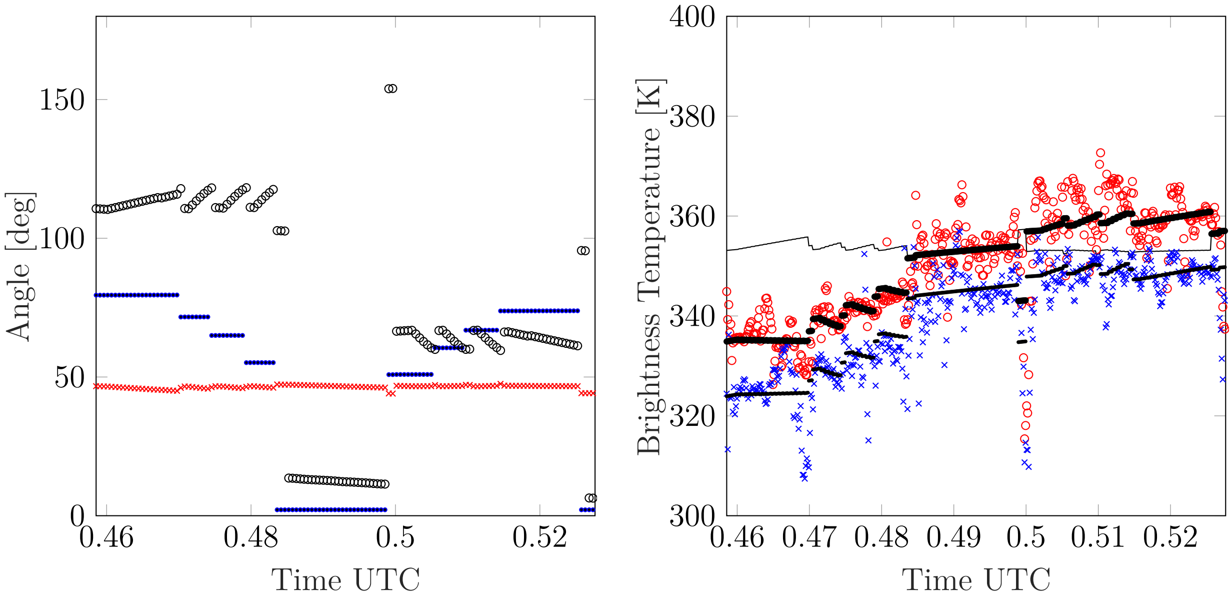

Figure F.11. EPF maneuver 11. Left: Geometry. Right: Modeled vs. measured brightness temperatures. For legend, see Figure F.1.

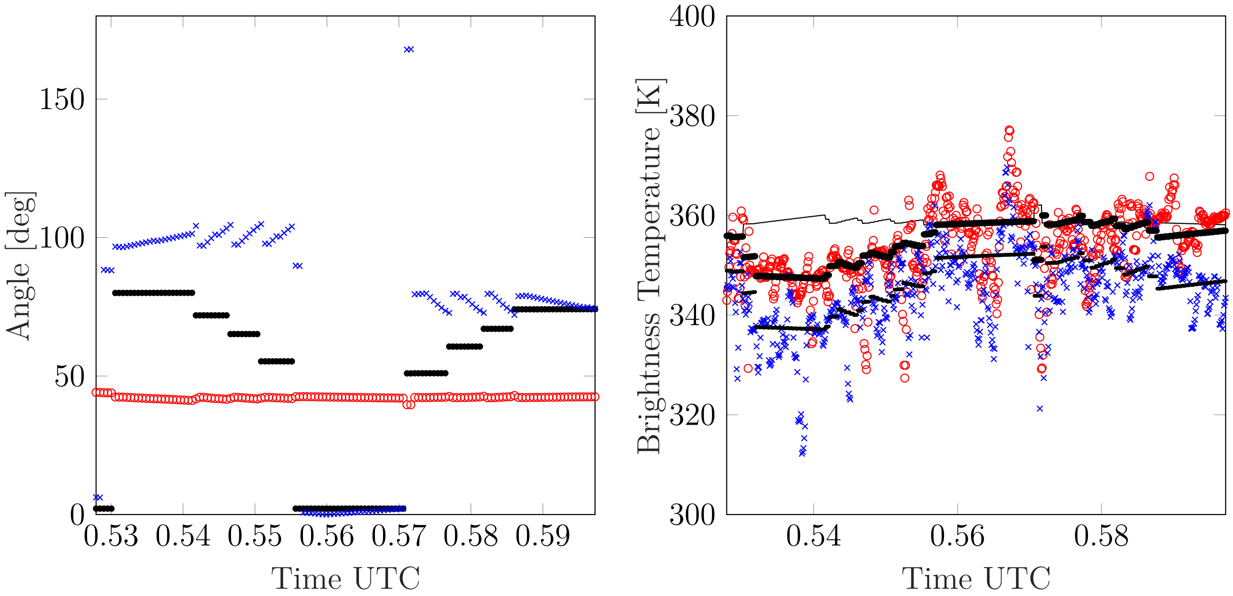

Figure F.12. EPF maneuver 12. Left: Geometry. Right: Modeled vs. measured brightness temperatures. For legend, see Figure F.1.

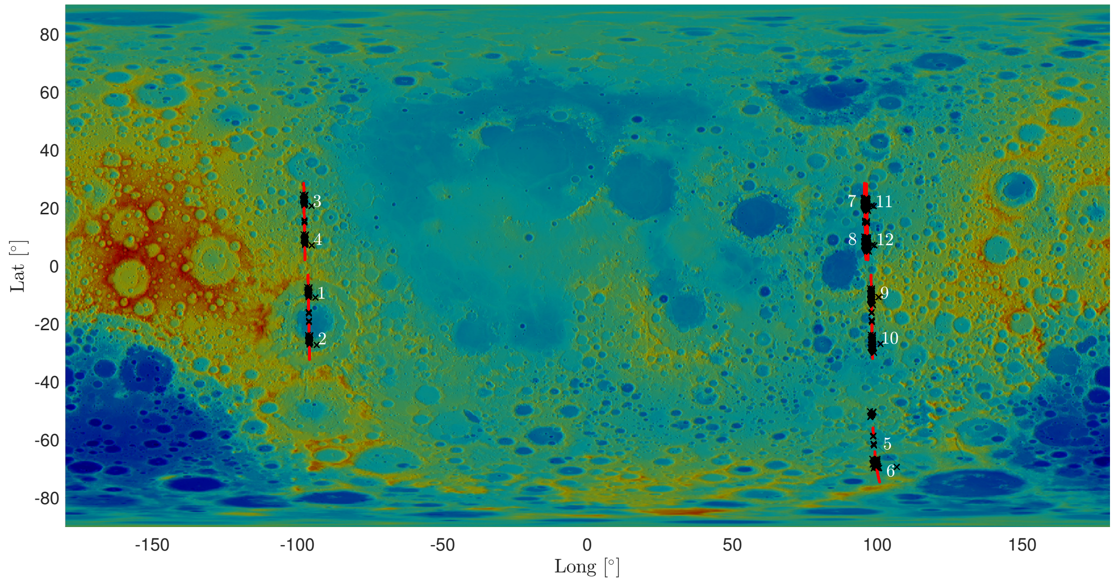

Figure F.13. Lunar topographic map with all 12 EPF measurements listed in Table 4.2. White numbers indicate the EPF measurement counted from first to last. Red lines indicate the subspacecraft point. Black stars show the locations of the measurements.

Appendix G

Addendum: Effects of the bolometric hemispherical albedo

G.1 Refined fitting routine for GF-4 lunar measurements

Minimizing the error between the lunar radiance model and the GF-4 measurements comes with two challenges: First, constructing an objective function that is cheap to evaluate, and second, finding a robust minimum. Evaluating the lunar radiance model (Section 5.6.2) for a given set of parameters is computationally costly, which prevents the model from being directly used in the objective function. Instead, the objective function is constructed through interpolating between pre-computed model results. The mare and highland regions of the lunar thermal model are independently evaluated for a three-dimensional grid of 1309 input parameter combinations. The grid consists of all possible combinations of eleven scaling values for A_{dh} denoted as $a_{\mathrm{A_{dh}}} \in \{1.0, 1.2, \dots, 2.8, 3.0\}$, seven roughness values $\overline{\theta}_{\mathrm{mare/highland}} \in \{18°, 20°, \dots, 28°, 30°\}$, and seventeen albedo-scaling values $m_{\mathrm{mare/highland}} \in \{1.0, 1.05, \dots, 1.75, 1.80\}$. If different ranges are required, the grid must be adapted accordingly. Sometimes, intermediate points are necessary for adequate sampling. Subsequently, a five-dimensional multilinear interpolation is devised, which interpolates between the grid points for any given real-valued input parameter set of ($a_{\mathrm{A_{dh}}}$, $\overline{\theta}_{\mathrm{mare}}$, $\overline{\theta}_{\mathrm{highland}}$, m_{mare}, and m_{highland}). Subtracting the interpolated model from the measured data finally yields the objective function. The author found a gradient-free approach with two steps that yield a robust minimum likely global: First, the Bayesian optimization performs 20 optimization runs with 100 iterations each to explore the parameter space. The Bayesian optimization comes from the MATLAB Statistics and Machine Learning Toolbox [The MathWorks Inc., 2022b], which implements Bull [2011], Snoek et al. [2012], and Gelbart et al. [2014]. For reference, see also Frazier [2018]. The results of the different optimization runs do not agree on the optimal parameter set but cluster in a small region inside the parameter space. This behavior indicates multiple local minima in a specific region of the parameter space or an extremely flat objective function. Varying the exploration parameter of the Bayesian optimization did not qualitatively change the behavior but only altered the cluster extents.

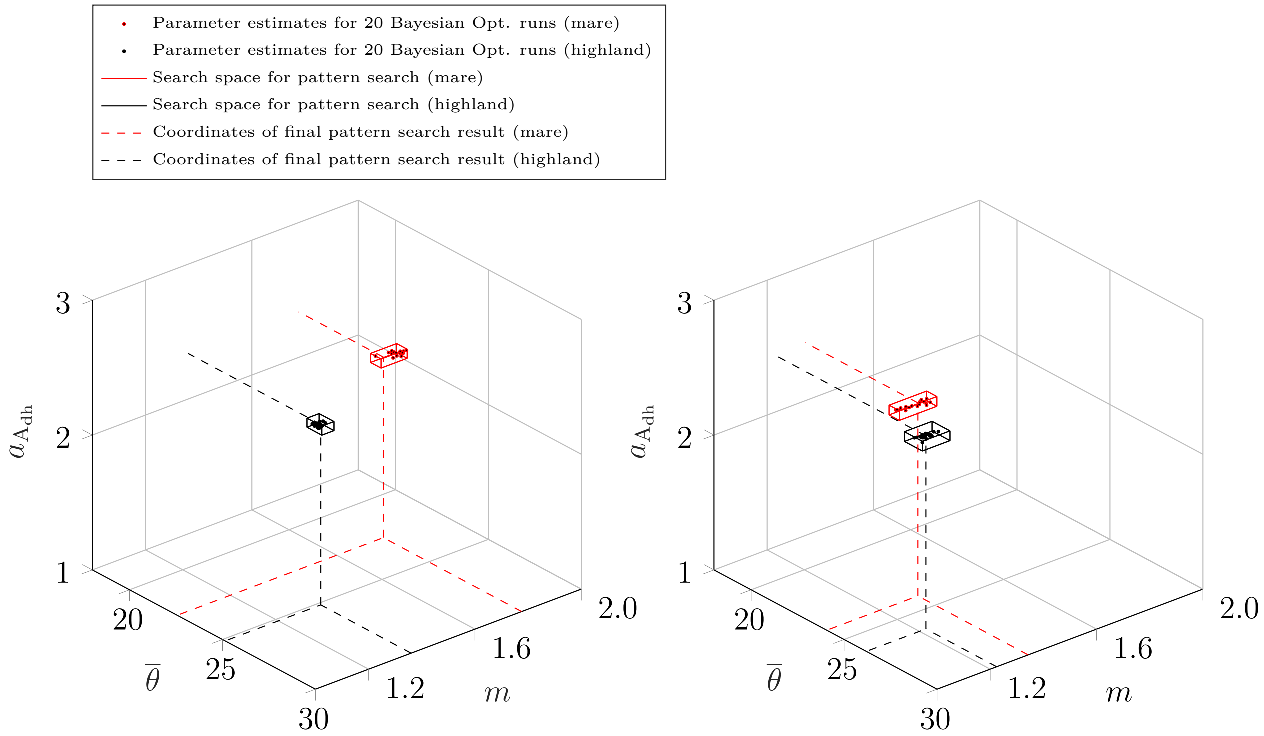

Figure G.1. Parameter space and parameter estimates that minimize the error between the radiance model and the GF-4 measurements (see also Table 5.4). The scaling factor $a_{\mathrm{A_{dh}}}$ for the directional-hemispherical albedo, the roughness $\overline{\theta}$, and the scale factor m for the single scattering albedo at $3.77\,\mu$m span the parameter space. Left: Results for the GF-4 measurements from July 25, 2018. The red dots indicate the parameter estimates of each of the 20 optimization runs of the Bayesian optimization for the mare region; the black dots indicate the Bayesian parameter estimates for the highland region. The bounding boxes tightly enclose the Bayesian parameter estimates and define the new search space for the pattern search routine. The dashed lines indicate the coordinates of the final result from the pattern search, which is considered the best fit. Right: Results for the GF-4 measurements from July 30, 2018.

The author found that applying a pattern search to the region where the Bayesian optimization results cluster yields a robust minimum against input variations. The pattern search comes from the MATLAB Global Optimization Toolbox The MathWorks Inc. [2022a] that implements, among others, Abramson [2002] and Kolda et al. [2003]. Tracing the objective function around this minimum along the axes of each parameter dimension indicates that the objective function is indeed extremely flat along some dimensions but convex, such that the result is likely an actual minimum. Though not an exhaustive search, the result is expected to be the global optimum of the entire parameter space. For illustration, Figure G.1 shows the parameter space and the results of the optimization routine for the GF-4 measurements from July 25 and July 30, 2018.

G.2 Detailed analysis of refined GF-4 model

The refined thermal model variant exhibits local deviations (Figure 5.20). Similar to Section 5.5, the author tested whether varying the parameters ($\overline{\theta}$, m_{mare} or m_{highland}, and $a_{\mathrm{A_{dh}}}$) can further improve the model fits. The thermal model overestimates the spectral radiance around the ejecta blanket of Copernicus (Figure 5.20 (right), profile 30_{R2}, pixel position 250–350 and Figure G.2 (left, black dots)). Highland parameters (solid blue) and mare parameters (solid red) failed to fit the measurements (black dots). Varying the roughness from smooth ($\overline{\theta} = 0°$, dotted red) to rough ($\overline{\theta} = 30°$, dashed red) has hardly any effect. Scaling w with a factor of $m = 1.85$ improves the fit (dashed black). Scaling the albedo only with $m = 1.60$ and compensating with $a_{\mathrm{A_{dh}}} = 2.60$ produces similar results (solid black). Even though m and $a_{\mathrm{A_{dh}}}$ can be exchanged, the values must both be increased. These results are consistent with a surface with exceptionally high reflectance and low emissivity, precisely like the immature ejecta blanket of Copernicus. The results align well with Section 5.5 and Figure 5.16 (left).

The adjusted model variant now accurately fits Titanium-rich mare regions of Oceanus Procellarum (compare Figure 5.4, profile 30_{C1}, pixel position 100–300 and the same position in Figure 5.20 (left)) but still underestimates the spectral radiance in Mare Humorum (Figure 5.20, profile 30_{C1}, pixel position 400–450 and Figure 5.16 (right, black dots for data and red line for model)). A smooth model (dotted red) strongly underestimates the measured radiance while increasing the roughness to $\overline{\theta} = 28.5°$ (dashed red) matches the data. Reducing the albedo factor to $m = 1.25$ and the directional-hemispherical albedo factor to $a_{\mathrm{A_{dh}}} = 2.10$ (dashed black) or gently changing the parameters to $\overline{\theta} = 26°$, $m = 1.30$, and $a_{\mathrm{A_{dh}}} = 2.25$ (solid black) also produces plausible results. A conclusive evaluation requires more data under multiple geometric configurations.

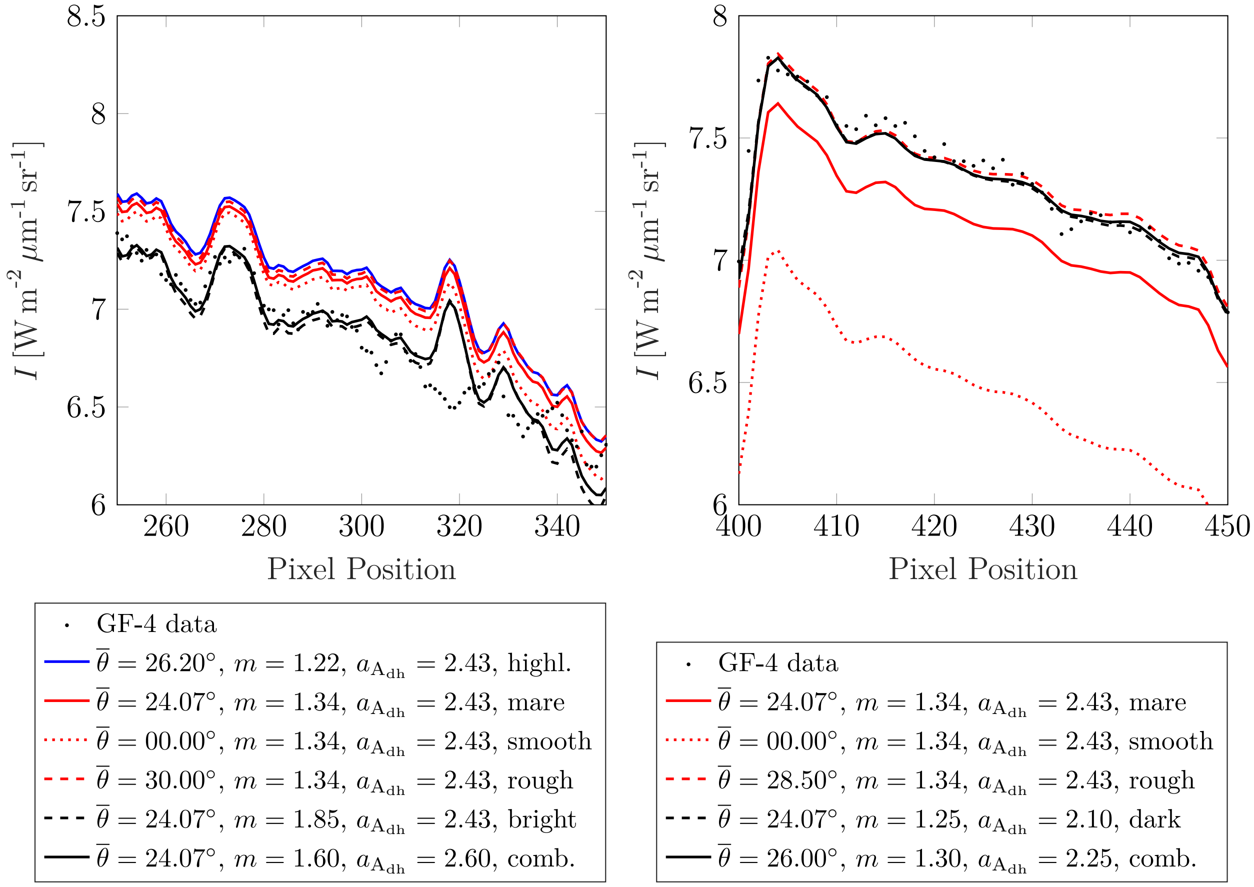

Figure G.2. Detailed analysis of model deviations around Copernicus and in the Mare Humorum. Left: Measured spectral radiance (black dots) around crater Copernicus vs. various modeling approaches (different lines). The data points correspond to a subsample of profile 30_{R2} in Figure 5.20 from pixel position 250–350. Adjusting the single scattering albedo w leads to a better agreement. Right: Measured spectral radiance (black dots) across Mare Humorum vs. various modeling approaches (different lines). The data points correspond to a subsample of profile 30_{C1} in Figure 5.20 from pixel position 400–450. Figure inspired by Wohlfarth et al. [2023].

G.3 Reassessing time-of-day dependent lunar hydration maps

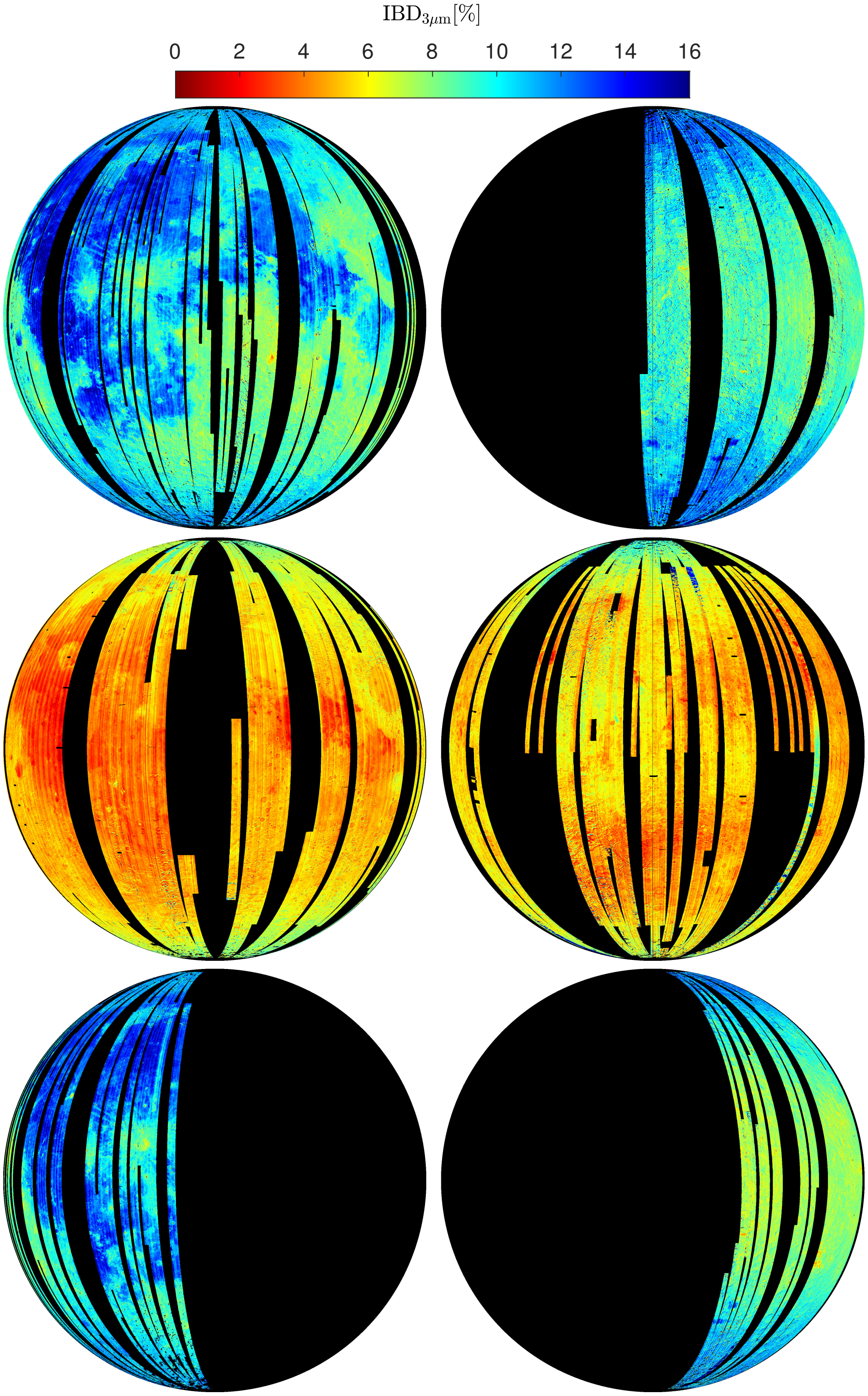

Figure G.3. Global $IBD_{3\mu m}$ map in an orthogonal projection of the lunar nearside (left column) and the lunar farside (right column). Top row: $IBD_{3\mu m}$ maps in the morning (7:00–8:00). Central row: $IBD_{3\mu m}$ maps at noon (12:00–14:00 at the nearside and 10:00–12:00 at the farside). Bottom row: $IBD_{3\mu m}$ maps in the lunar evening (16:00–17:00). Black indicates missing data. New parameters: $\bar{\epsilon}_h = 0.95$, $\bar{\theta} = 25°$, $a_{A_{dh}} = 2.34$. Modified version of Figure 5.7 based on Wohlfarth et al. [2023].

G.4 Reassessing thermal roughness model simulations for Mercury

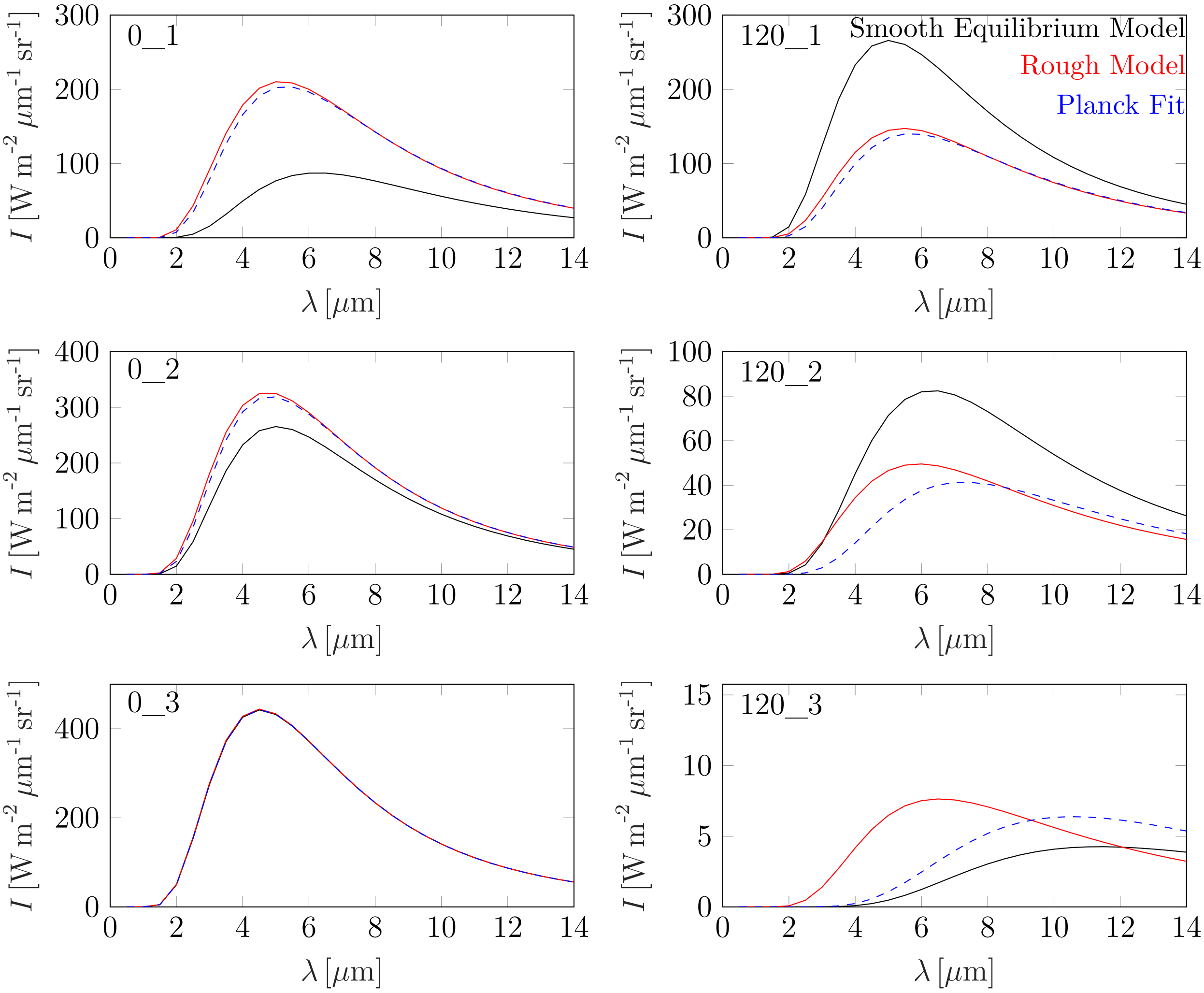

Figure G.4. Simulated thermal emission of Mercury for two phase angles g at an arbitrary solar distance of 0.387 AU. This model assumes a variable $\bar{\epsilon}_{\mathrm{h}}$ and a rescaled albedo A_{dh}. Left: Simulated Mercury disk for $g = 0°$. The plots show the spectral radiance at the indicated locations. Right: Simulated Mercury disk for $g = 120°$. The plots show the spectral radiance at the indicated locations. Modified version of Figure 5.12 based on Wohlfarth et al. [2023].

Appendix H

Addendum: Particle size distribution of submicroscopic iron

This section explores the optimal size range for microphase iron to simulate space weathering effects, as previously noted in Section 6.3.2. As seen in Figure 6.3 (top), very small npFe^0 particles ($d = 1\,\mathrm{nm}$) cause spectral reddening. Larger spherical iron particles of a fixed size (d = 10–500 nm) cause unnatural oscillations between $0.5\,\mu\mathrm{m}$ and $1.5\,\mu\mathrm{m}$ in the simulated spectra. Backed by TEM studies such as Noble et al. [2011] and Pieters and Noble [2016], it is more realistic to assume a distribution of multiple particle sizes such that the oscillation effects even out. This distribution of larger particles is then summarized to an effective iron endmember and termed microphase iron (mpFe^0). Unfortunately, the precise particle size distribution that constitutes the microphase iron remains unknown, and devising an inverse problem to estimate the distribution is out of the scope of this work. For simplicity, this work assumes that the particle sizes follow a uniform distribution over a finite (ordered) set $\{d_{\mathrm{min}}, \ldots, d_{\mathrm{max}}\}$ of particle sizes, where d_{min} is the minimal and d_{max} is the maximal particle size. The particle sizes d_{min} and d_{max} that define the particle size distribution can then be estimated through an optimization procedure, which follows three steps. First, iron particles are simulated for a finite set of seventeen particle sizes ranging from $d = 20\,\mathrm{nm}$ to $d = 340\,\mathrm{nm}$ in steps of 20 nm. Secondly, every possible set of consecutive particle sizes is determined. Here, consecutive particle sizes mean any set of particle sizes with at least two elements that follow one another, for example, $\{40\,\mathrm{nm}, 60\,\mathrm{nm}, 80\,\mathrm{nm}\}$, $\{180\,\mathrm{nm}, 200\,\mathrm{nm}\}$, or $\{140\,\mathrm{nm}, \ldots\ 220\,\mathrm{nm}\}$. A combinatorial analysis shows that 136 such uniform sets exist. Thirdly, the space weathering simulation of the M^3 spectra is carried out with three endmembers: The immature soil, the nanophase iron ($d = 1\,\mathrm{nm}$), and the microphase iron modeled with the uniform distribution of particles with sizes $\{d_{\mathrm{min}}, \ldots, d_{\mathrm{max}}\}$. A Levenberg-Marquardt [Marsland, 2009] minimizes the RMSE between the simulated space weathering spectrum and the mature soil spectrum and provides the endmember abundances. The particle size distribution that yields the lowest RMSE values is chosen as the distribution that models the microphase iron. For lunar mare sites, a uniform particle size distribution with particle sizes from $\{20\,\mathrm{nm}, 40\,\mathrm{nm}, \ldots, 200\,\mathrm{nm}\}$ is optimal, and for lunar highlands, a distribution with $\{40\,\mathrm{nm}, 60\,\mathrm{nm}, \ldots, 240\,\mathrm{nm}\}$ yields the best fits.

Tables H.1 and H.2 list the RMSE for the best thirty particle size distributions averaged over the mare or highland samples, respectively.

size range [nm]	RMSE $\times10^{-3}$	size range [nm]	RMSE $\times10^{-3}$	size range [nm]	RMSE $\times10^{-3}$
$\{20,\dots,200\}$	4.613	$\{40,\dots,240\}$	4.746	$\{80,\dots,160\}$	4.746
$\{40,\dots,200\}$	4.617	$\{60,\dots,240\}$	4.796	$\{60,\dots,260\}$	4.796
$\{20,\dots,220\}$	4.633	$\{80,\dots,200\}$	4.806	$\{80,\dots,240\}$	4.806
$\{40,\dots,220\}$	4.638	$\{80,\dots,180\}$	4.841	$\{100,\dots,180\}$	4.841
$\{60,\dots,200\}$	4.656	$\{80,\dots,220\}$	4.856	$\{100,\dots,200\}$	4.856
$\{60,\dots,220\}$	4.683	$\{20,\dots,160\}$	4.872	$\{20,\dots,280\}$	4.872
$\{20,\dots,180\}$	4.692	$\{40,\dots,160\}$	4.874	$\{40,\dots,280\}$	4.874
$\{40,\dots,180\}$	4.694	$\{60,\dots,160\}$	4.890	$\{100,\dots,160\}$	4.890
$\{60,\dots,180\}$	4.723	$\{20,\dots,260\}$	4.916	$\{20,\dots,140\}$	4.916
$\{20,\dots,240\}$	4.742	$\{40,\dots,260\}$	4.920	$\{60,\dots,140\}$	4.920

Table H.1. RMSE between the modeled space weathering spectrum and the measured M^3 spectrum, assuming different particle size ranges. The RMSE is the average over the best-fit results at all eighty M^3 mare sites presented in Section 6.4.2. The table shows the first thirty results out of 136 with the best RMSE. A uniform distribution of particle sizes from 20–200 nm produces the best fits for $mpFe^0$.

size range [nm]	RMSE $\times10^{-3}$	size range [nm]	RMSE $\times10^{-3}$	size range [nm]	RMSE $\times10^{-3}$
$\{40,\dots,240\}$	2.889	$\{20,\dots,260\}$	3.267	$\{100,\dots,220\}$	3.267
$\{60,\dots,240\}$	2.889	$\{80,\dots,260\}$	3.326	$\{100,\dots,240\}$	3.326
$\{20,\dots,240\}$	2.976	$\{60,\dots,200\}$	3.558	$\{100,\dots,260\}$	3.558
$\{40,\dots,220\}$	3.026	$\{40,\dots,200\}$	3.559	$\{100,\dots,200\}$	3.559
$\{60,\dots,220\}$	3.027	$\{20,\dots,200\}$	3.622	$\{60,\dots,300\}$	3.622
$\{80,\dots,240\}$	3.052	$\{80,\dots,200\}$	3.636	$\{40,\dots,300\}$	3.636
$\{20,\dots,220\}$	3.098	$\{60,\dots,280\}$	3.688	$\{60,\dots,180\}$	3.688
$\{80,\dots,220\}$	3.162	$\{40,\dots,280\}$	3.694	$\{40,\dots,180\}$	3.694
$\{60,\dots,260\}$	3.166	$\{20,\dots,280\}$	3.793	$\{80,\dots,180\}$	3.793
$\{40,\dots,260\}$	3.169	$\{80,\dots,280\}$	3.830	$\{20,\dots,300\}$	3.830

Table H.2. RMSE between the modeled space weathering spectrum and the measured spectrum, assuming different particle size ranges. The RMSE is the average over the best-fit results of thirty M^3 highland sites presented in Section 6.4.1. The table shows the first thirty results out of 136 with the best RMSE. A uniform distribution of particle sizes from 40–240 nm produces the best fits for $mpFe^0$.